Université de Toulouse

THÈSE

En vue de l'obtention du

DOCTORAT DE L'UNIVERSITÉ DE TOULOUSE

Délivré par :

Université Toulouse 3 Paul Sabatier (UT3 Paul Sabatier)

Présentée et soutenue par :
Tania JAHANBIN
le 13 Novembre 2014

Titre :

Conception et développement in vitro d'agents de contraste hautement efficace en IRM. Apport de la dynamique moléculaire sur le signal RMN

École doctorale et discipline ou spécialité :

ED GEET : Radio-physique et Imagerie Médicale

Unité de recherche :

INSERM U825, Imagerie Cérébrale et Handicaps Neurologiques

Directeur(s) de Thèse :

Soraya BENDERBOUS

Jury :

Mme. Isabelle BERRY	Président du Jury
M. Jean-Marc CONSTANS	Rapporteur
M. Peter SPEARMAN	Rapporteur
M. Stephane CHAUSSEDENT	Examinateur
Mme. Hafsa KORRI-YOUSSOUFI	Examinateur
Mme. Soraya BENDERBOUS	Directeur de thèse

Acknowledgement

First, I would like to express my gratitude to my supervisor, Prof Soraya Benderbous, for her guidance, and advice she has provided throughout my thesis. I would also like to thank the director of laboratory of INSERM U825, Dr Pierre Celsis, for his support during my PhD.

My thesis work has been performed in collaboration with three laboratories including laboratory of bioorganic and biononorganic of university of paris sud under directory of Dr Hafsa Korri Youssoufi and Dr Helen Dorizon, laboratory of ITODAYS of the university of paris 7 under directory of Prof Souad Ammar Merah, and the laboratory of photonic of Angers under directory of Prof Stephane Chaussedent. I do greatly appreciate for their kind guidance, caring, patience, and providing me with an excellent atmosphere for doing research. I would like to express my deepest gratitude to Prof Francois Sanchez, director of photonic laboratory of Angers, for his warm welcome in the laboratory and his support. Moreover, I am grateful to all the people who have been (and are) working in the lab of photonic and of bioorganic and nonbioorganic, for the great atmosphere and for the helpful attitude.

Finally, I would like to acknowledge with gratitude, the support of all my friends in laboratory Paris sud, Paris 7 and laboratory of photonic of Angers.

I would like to dedicate this dissertation to my beloved Family

Contents

Symbols and Abbrevations

Chemical formulas

AOT	Dioctyl sodium sulfosuccinate
BF_3	Boron trifluoride
CH_2Cl_2	Dichloromethane
CTAB	cetyl trimethyl-ammonium bromide
DHLA	dihydrolipoic acid
Fe(TMPyP)	Iron meso-tetrakis (N-methyl-4-pyridiniumyl) porphyrin
Gd-Dota	Gadolinium-tetraazacyclododecanetetraacetic acid
Gd-DOTP	Gd(III) 5- (1, 4, 7, 10-tetra-azacyclododecane- tetrakis(methylenephosphonic acid)
Gd(TPyP)	Gadolinium meso-tetrakis(4-pyridyl) porphyrin
H_2O	Water
HSA	Human serum albumin
MAA	Mercaptoacetic
MeOH	Methanol
MnS	Manganese sulphide
Mn(TSPP)	Manganese meso-tetrakis (4-sulfonatophenyl) porphyrin
MnZnS	Manganese zinc sulphide
MPA	Mercaptopropionic
NaOH	Sodium hydroxide
PEG	Polyethylene glycol
RCO_2H	Carboxylic acids
SDS	sodium dodecyl sulphate
TFA	trifluoroacetic acid
$TMPyPH_2$	Meso-tetrakis (N-methyl-4-pyridiniumyl) porphyrin
TOPO	Trioctylphosphine oxide
TPP	Sodium triphosphate pentabasic
$TPyPH_2$	Meso-tetrakis (4-pyridyl) porphyrin
ZnS	Zinc sulphide

Experimental techniques

ATR-FTIR	Fourier transform infrared spectroscopy equipped with Attenuated total reflectance
DLS	Dynamic light scattering
FS	Fluorescence spectroscopy
^{1}H NMR	Hydrogen nuclear magnetic resonance
ICP-MS	Inductively coupled plasma mass spectrometry
MALDI-TOF	Matrix-assisted laser desorption/ionization Time-of-flight mass spectrometry
MRI	Magnetic resonance imaging
SEM-EDX	Scanning electron microscopy-equipped with
SQUID	Superconducting quantum interference device magnetometer
TEM	Transmission electron microscopy
XRD	X-ray diffraction
XRF	X-ray fluorescence spectroscopy
UV-vis	Ultraviolet-visible spectroscopy

Symbols

a	Distance of closest approach of bulk water at outer sphere
A_{ij}	Buckingham potential parameter
B_0	Magnetic field
$B_1(t)$	oscillating magnetic field perpendicular to B_0
C_{ij}	Buckingham potential parameter
CA	Contrast agents
[CA]	Contrast agents concentration
CN	Coordination number

CNs	Chitosan nanoparticles
C_{OS}	Outer sphere constant
CS	Coordination sphere/shell
D	Diffusion Coefficient
D	Dissociation of bond energy
Eth	Ethanol
Fe	Iron
FOV	Field of view
Gd	Gadolinium
H	Hydrogen
ħ	Planck's constant divided by 2π
HD	Hydrodynamic diameter
J(ω)	non-Lorentzian spectral density
K	Kelvin
K	Force constant of spring potential
Kbar	Kilo bar
K_B	Boltzmann constant
M	Magnetization
M_{xy}	Magnetization perpendicular
MDs	Molecular dynamic simulation
MHz	Mega Hertz
$mM^{-1}.s^{-1}$	$(millimole.second)^{-1}$
min	Minute
Mn	Manganese
ms	Millisecond
N_A	Avogadro's number
NPT	Isothermal–isobaric ensemble
NVE	Microcanonical ensemble
NVT	Canonical ensemble
O	Oxygen
Pa	Pascal
PL	Photoluminescence
q	Number of coordinated water molecules
QDs	Quantum Dots
RDF	Radial distribution function
RF	Radiofrequency
r_1,r_2	Longitudinal and transverse relaxivity
r_{ij}	Distance between atom *i* and *j*
rmp	Rounds per minute
ROI	Region of interest
r_{MH}	Distance between proton and paramagnetic ions
S	Electronic spin
S	Sulphur
S(t)	Signal intensity at
SNR	Signal to noise ratio
SPIO	Superparamagnetic iron oxide
T	Tesla
T	Absolute temperature
$T_{1,2}^{SC}$	Scalar relaxation time
$T_{1e,2e}$	Electronic relaxation time
$\frac{1}{T_{1m,2m}}$	Longitudinal and transverse relaxivity
$\frac{1}{T_{1,2(dia)}}$	Longitudinal and transverse relaxivity of solvent

TE	Time echo
TR	Time repetition
T1	Longitudinal relaxation time
T_{1e}	Longitudinal electron spin relaxation time
T2	Transverse relaxation time
T_{2e}	Transverse electron spin relaxation time
τ_R	Rotational correlation time for metal-proton vector
τ_{S0}	Electron spin relaxation time at zero field
$\tau_{S1,S2}$	Electronic relaxation time
τ_{SC}	Correlation time for scalar interaction
τ_v	Correlation time for the modulation of ZFS
u_{ij}	Potential energy
USPIO	Ultrasmall superparamagnetic iron oxide
ω	Angular frequency
$\Delta\omega$	Chemical shift difference between bound and bulk water
ω_H	Larmor frequency of the proton
ω_S	Larmor frequency of the S spin
ZFS	Zero field splitting
Δ	Amplitude of transient ZFS
γ	Nuclear gyromagnetic ratio
μ_B	Bohr magneton
μ_0	Magnetic constant
λ_{max}	Maximum wavelength
ρ_{ij}	Buckingham potential parameter
Θ_0	Equilibrium value of the angle of three core body potential
θ_{ijk}	Angle between A_{ij}-B-A_{jk} atoms

List of Figures

List of Tables

Chapter I: Introduction

A. General introduction

In medical diagnostics, visualizing molecular processes with cellular resolution is required for early diagnosis and therapeutic approaches. Thereby, considerable efforts have been devoted toward developing various imaging modalities. Each available imaging modality has its own strengths and weaknesses in terms of sensitivity, spatial resolution, target-to-background contrast or potential in clinical applications. After the first visualization of the human body via magnetic resonance imaging (MRI) in 1977 [1], [2] , MRI has become the most widespread clinical diagnostic imaging technique in cancer therapy. MRI offers several significant advantages over other modalities such as high spatial resolution, noninvasiveness, absence of ionizing radiation, and capability to elicit both anatomic and physiologic information simultaneously [3].

However, MRI is emerging an advantageous technique; overriding challenge with MRI is its relatively low sensitively (insufficient contrast) for label detection. In order to better distinguish targeted tissue from surrounding tissue, contrast of the images needs to be enhanced. The contrast of MRI could be affected either by intrinsic (T1, T2 T_2^*, proton-density, flow, chemical environment, diffusion and perfusion) or extrinsic (pulse sequence, acquisition parameters (TE and TR, flip angel, etc.), strength of applied field and contrast agents) parameters. One common approach to overcome the lack of MRI sensitivity is applying the contrast agents to provide additional contrast. A tremendous effort has been spent on designing contrast agents which exhibits high relaxivity, low toxicity, specificity, and suitable long intravascular duration and excretion time.

Macrocyclic ligands are widely utilized as the metal chelators owing to high thermodynamic and kinetic stability [4]. Among the studied macrocyclic chelator, porphyrin has attracted much attention in cancer diagnosis and treatment due to its feature preferential uptake by tumor cells (including sarcomas, carcinomas, and atheromatous plaque) [5] while the reasons for this selectivity remain obscure till now. After the first report about high efficiency of water soluble Mn(II)-mesoporphyrin as a tumor targeting MRI contrast agent [6], numerous works have been devoted to study the potential of various water soluble Mn(II) and Fe(II) mesoporphyrins as MRI contrast agents. Nonetheless, low stability of Gd(III)-mesoporphyrins has prevented in development of these complexes. Metallated meso-tetra-pyridyle porphyrin is considered as an axial-ligand stretch due to the coordination of the metal with one nitrogen atom coming from the adjacent porphine molecules which can improve its stability [7]. One way to improve water solubility, is by encapsulating in or covalently attaching the CA on the

surface of nanocarriers, leading to improving simultaneously stability, biocompatibility, and the release of paramagnetic ions. Over the last decades, numerous nanocarriers have been explored as platforms for paramagnetic-labeling and/or encapsulation, including polymers, proteins, dendrimers, micelles, and vesicles. Among the studied polymers, chitosan has been receiving much attention in drug delivery and molecular imaging owing to its characteristic properties, including biocompatibility, biodegradability, nontoxicity, and mucoadhesive properties [8], [9]. Hence, conjugation/or encapsulation of metallated- meso-tetra-pyridyle porphyrin with chitosan could be considered as a novel contrast agent.

On the other hand, developing favorable multifunctional imaging probes becomes increasingly more demanding these days in order to obtain complementary physiological and anatomical information and improving the detection of tumor tissues. Nanoparticles offer an ideal platform for developing dual modality probes in molecular imaging techniques owing to their high surface to volume ratio and the possibility to perform surface modification, functionalization and bioconjugation. In this context, quantum dots (QDs) doped with paramagnetic metal ions have been extensively investigated as dual magneto optical cancer probes. Mn-doped QDs are some of the most investigated QDs in medical imaging. Although, research has been mostly focused on the potential of manganese-doped QDs as a fluorescent bio-label [10], its efficiency as an MRI contrast agent is less well studied. Moreover, the majority of Mn-doped QDs as both a MRI contrast agent and a fluorescence label are core/shell structured nanoparticles. While doping of metal ions on the surface of QDs could be a new approach to design the dual agents (i.e. fluorescence and MRI agents) which offers an opportunity to improve the relaxivity of QDs.

Besides the experimental studies, the computational studies allow to gain detailed information about the structure of the paramagnetic substance, solvent, intramolecular interactions of the paramagnetic species in aqueous solution and dynamics of molecules in system [11]. Molecular dynamic simulation (MDs) is one of the most utilized numerical techniques to approximate macroscopic properties of the system. MDs is widely used to understand the dynamic and thermodynamic properties of materials and living matter by observing the position of certain number of atoms/particles over given period. Thus, modeling the contrast agents surrounded with water molecules via molecular dynamic simulation permits us to obtain reliable insight through interaction between a paramagnetic ion and solvation water, while the long-term goal is understanding the relaxation mechanism.

B. Objective of thesis

The main aim of my work is developing two new paramagnetic complexes as magnetic resonance imaging longitudinal MRI contrast agents in the form of macromolecular and nanoparticular contrast agents.

1. Developing Gd-meso-tetra-pyridyle porphyrin conjugated with chitosan nanoparticles, which exhibit the high efficiency as MRI contrast agents with a great potential in biomedical applications owing to interesting chitosan properties such as biocompatibility, biodegradability, and mucoadhesive.
2. Developing Mn-doped ZnS quantum dots with high Mn dopant concentrations, in which the majority of Mn lies close to or on the surface of ZnS to extend their application as MRI contrast agents. In order to obtain significant insight about Mn:ZnS interaction with surrounding water molecules, molecular dynamic simulation is carried out for better understanding the relaxation mechanisms of Mn-doped ZnS dispersed in water. Then the simulated results correlate with experimental r1 relaxivity as a function of Mn dopant concentration.

C. Thesis outline

The theory of relaxation mechanism is described in Chapter 2. It provides the necessary basics of MRI and relaxation mechanism of paramagnetic contrast agents. In Chapter 3, the literature related to the objective of thesis is reviewed. Owing to the interdisciplinary character of this work, the literature review chapter is composed of four major parts. The first part provides an overview of metalloprphyrin complexes and their *in-vitro* and *in-vivo* efficiency as MRI contrast agents. The second part describes the potential of different developed macromolecular contrast agents. Afterwards, the third part of the literature review deals with the potential of quantum dots as MRI contrast agents. Finally, the numerical simulation background of nanoparticles in particular those used for evaluating/interpreting the dynamic of QDs in aqueous solution will be explained. Chapter 4 concerns methodological and characterization of both developed paramagnetic complexes. Meantime, molecular dynamic simulations procedure and the potential parameters are explained. Chapter 5 deals with the results and discussion of physicochemical characterization of two novel developed contrast agents and their efficiency as MRI contrast enhancers. The simulated results of Mn:ZnS QDs

in vacuum and in aqueous media (water) are then described in the last section of Chapter 5. Finally in the Chapter 6, the contributions of my thesis work is summarized by providing some helpful prospectives to future research directions.

Chapter II: Relaxation mechanism

A. Basic principle of MRI

Magnetic Resonance Imaging (MRI) is based on the magnetic properties of water protons (hydrogen) and on the water protons interaction with both applied magnetic field and radiofrequency producing highly detailed images of the human body. The hydrogen atom has a net magnetic moment. Therefore, in the absence of an external magnetic field, protons are randomly orientated. The protons tend to align with or against the magnetic field and precess around it. The frequency of precession is described by Larmor's equation

$$\Omega=\gamma B \quad (1)$$

where ω is the frequency precession and γ is the gyromagnetic ratio, which is a constant, and B is strength of applied field. During application of an external magnetic field (B_0), the majority of protons align along the field direction into the low energy state, giving rise to a net magnetization in the direction of B_0. The second weaker magnetic field, radiofrequency (RF) pulse, is applied in a perpendicular direction to the first field and oscillated at a Larmor frequency. This causes the magnetic moment (M) to tilt away from B_0 and flip about an angle dependent on the pulse duration and amplitude as presented in Fig. 1. After the termination of the RF pulse, the magnetization will not precess perpetually around the B_0-field but will return to its equilibrium position along the *z*-axis (direction of B_0).

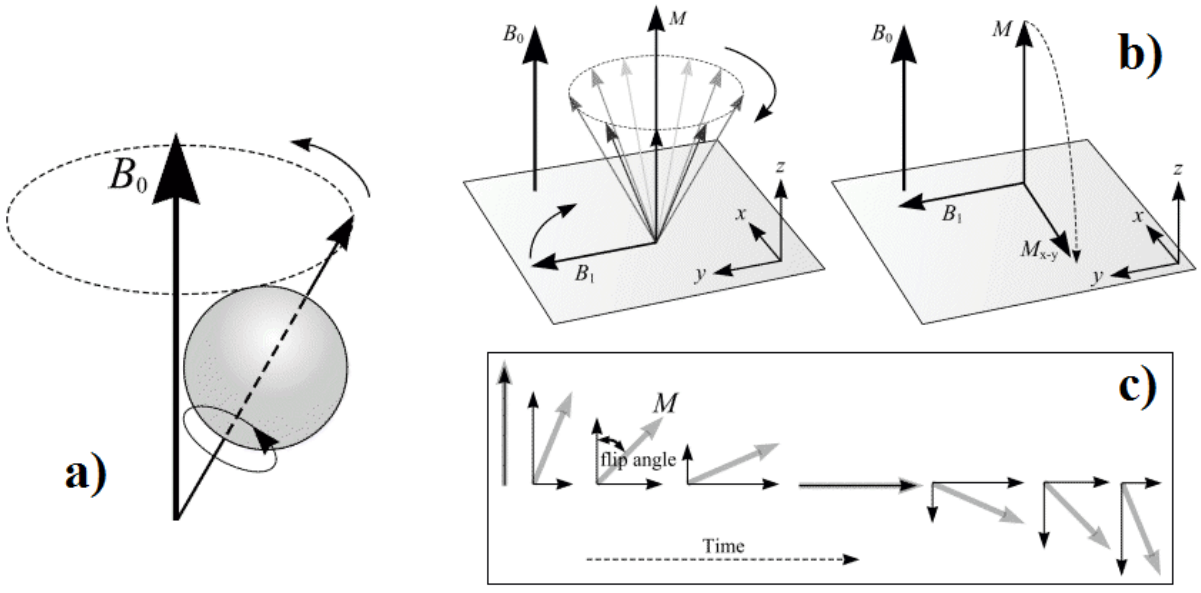

Figure 1. Schematic represents a) precession of magnetic moment around B_0, b) effect of RF radiation on net magnetic momentum which is tilted from its original orientation (z-axis) into transverse plane (x-y), and c) flip angle [12].

During relaxation, the nuclei lose energy by emitting their own RF signal. This signal is referred to free-induction decay (FID) response signal, which could be observed thanks to the induced current in a detector coil. After a 90° RF pulse, the amplitude of the signal detected by the coil does not rapidly drop down to zero. The loss of transverse magnetization with time because of spin dephasing is referred to as Free Induction Decay (FID). The Larmor frequencies of distinctive nuclei and their respective contributions are obtained by Fourier transform of this signal.

B. Relaxation time

The return of magnetic moment to its equilibrium state is expressed as relaxation. T1 relaxation (also known as spin-lattice or longitudinal relaxation) is the realignment of spins (M) with the external magnetic field B_0 (z-axis). T2 relaxation (also known as T2 decay, transverse relaxation or spin-spin relaxation) is the decrease of the M_{xy} component.

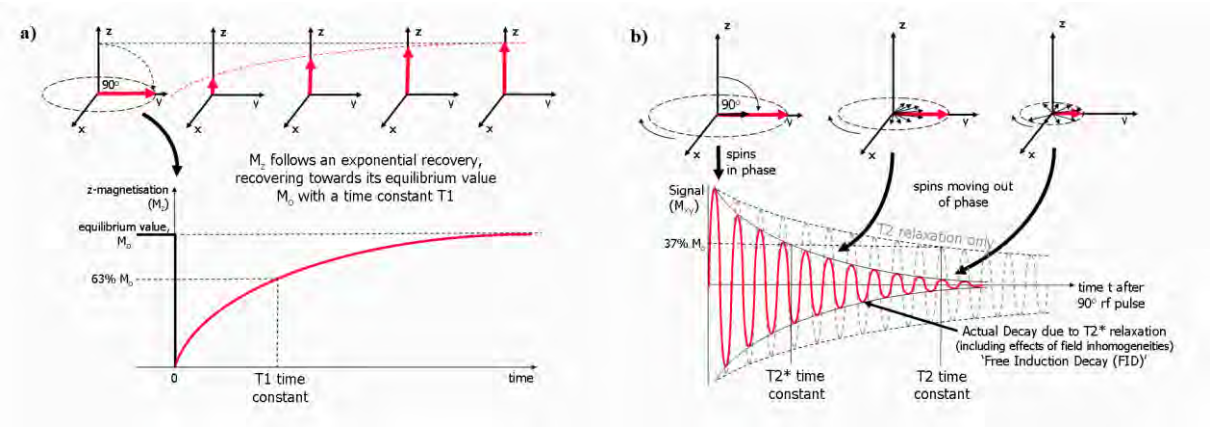

Figure 2. a) Longitudinal and b) Transverse relaxation time of magnetic moment after termination of RF [13]

B.1. Longitudinal relaxation time

After the RF pulse, nuclei will dissipate their excess energy as heat and revert to their Boltzman equilibrium position. Realignment of the nuclei along z-axis (B_0), through a process known as recovery, leads to a gradual increase in the longitudinal magnetization. The time taken for a nucleus to relax back to its equilibrium state is called longitudinal relaxation time. The process of equilibrium restoration is described as follows

$$M_z(t) = M_z(0).(1 - e^{-\frac{t}{T1}}) \quad (2)$$

where T1 is the time taken for the longitudinal magnetization to be restored.

B.2. Transverse relaxation time

After applying a RF pulse, all the individual spins magnetic moments precess coherently around the *z*-axis, creating a magnetization component in the *xy*-plane. The magnetic moments interact with each other causing a decrease in transverse magnetization. The transverse relaxation time corresponds to the time taken for disappearance of magnetization in the *xy*-plane. The transverse relaxation time is described by the following equation

$$M_{xy}(t) = M_{xy}(0).e^{-\frac{t}{T2}} \quad (3)$$

while T2 is the time taken that the transverse magntizations decay to 37% of its initial value. The relaxation time of water could be shortened by nearby paramagnetic or superparamagnetic particles due to their large electronic magnetic moments (dipoles) in the presence of external magnetic field. Gd (III) with seven and Mn (II) and Fe (II) with five unpaired electrons are the most widely used paramagnetic ions for increasing proton relaxation rate of water molecules.

The efficiency of paramagnetic ions to affect the relaxation times of water protons is evaluated by relaxivity (r1 or r2) which are defined as the increase of relaxation rate (1/T1 or 1/T2) produced by 1mmol per liter of paramagnetic substance (expressed $mmol^{-1}.s^{-1}$). The r1 and r2 relaxivities are the main physicochemical parameters in development and design of contrast agents.

$$\frac{1}{T_{i(obs)}} = \frac{1}{T_{i(dia)}} + r_i C \quad i=1,2 \quad (4)$$

where $\frac{1}{T_{i(obs)}}$ corresponds the relaxation rate of aqueous system (s^{-1}) , $\frac{1}{T_{i(dia)}}$ relaxation rate of the solvent (s^{-1}), C concentration of paramagnetic ion ($mmol^{-1}$) and r_i the relaxivity ($mmol^{-1}.s^{-1}$).

C. Paramagnetic relaxation time

A quantitative theoretical model has been developed to demonstrate the relaxivity of contrast agents [14]. The paramagnetic relaxation of water protons originates from the dipole-dipole interactions between proton nuclear spins of water molecules and the fluctuating local magnetic field, which is produced from unpaired electron spins of the paramagnetic ions [15]. The paramagnetic relaxation is explained by inner, second, and outer sphere contributions [16], as shown in Fig. 3. The inner sphere contribution arises from interaction of water molecule(s) in the first coordination sphere with paramagnetic ions which transmitted to bulk via chemical exchange [17]. Besides the inner sphere coordinated water, there are some water molecules that may be bonded to the ligand (hydrogen-bonded) or to the inner sphere water molecule(s). These water molecules also contribute to overall paramagnetic relaxation, identifying as second sphere contribution [17]. The bulk water molecules, which have diffused around the paramagnetic center, also experience the paramagnetic effect. This relaxation mechanism is defined as outer sphere contribution. Thereby, total paramagnetic relaxation rate can be expressed as follows

$$\frac{1}{T_{ip}} = \left(\frac{1}{T_{ip}}\right)_{IS} + \left(\frac{1}{T_{ip}}\right)_{SS} + \left(\frac{1}{T_{ip}}\right)_{OS} \quad i = 1,2 \tag{5}$$

where IS, SS and OS stand from inner, second and outer sphere, respectively.

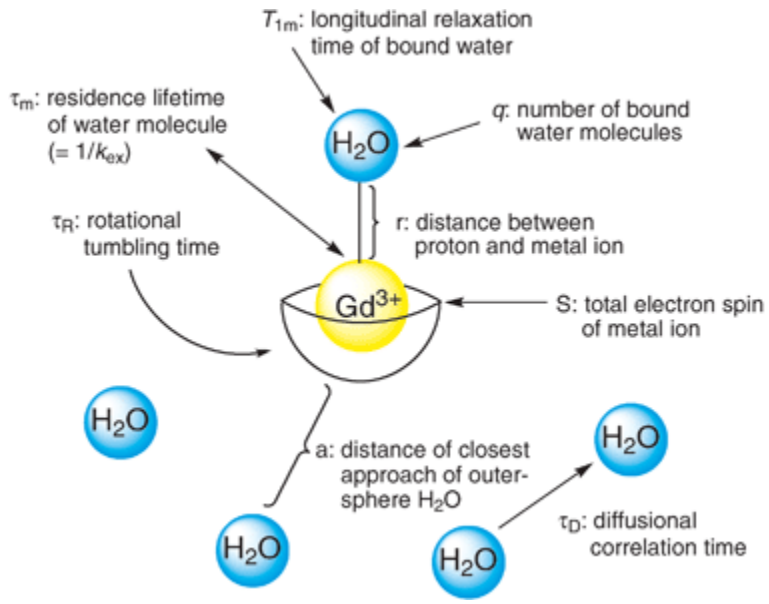

Figure 3. Schematic representation of the inner, second and outer sphere contributions on relaxation time [18]

C.1. Inner Sphere Proton relaxivity

The relaxivity of bulk water is based on exchange of coordinated water with paramagnetic ions, defined as

$$R_{1p} = \frac{q/[H_2O]}{T_{1m} + \tau_m} \tag{6}$$

$$R_{2P} = \frac{1}{\tau_m}\left[\frac{T^{-1}{}_{2m}(\tau_m^{-1} + T^{-1}{}_{2m}) + \Delta\omega_m^2}{(\tau_m^{-1} + T^{-1}{}_{2m}) + \Delta\omega_m^2}\right] \times \frac{q}{[H_2O]} \tag{7}$$

Where $\frac{1}{T_{1m}}$ and $\frac{1}{T_{2m}}$ are longitudinal and transverse relaxivities, $\Delta\omega_m$ is the chemical shift difference between coordinated water and bulk water, τ_m is lifetime of coordinated water in first sphere, and q is the number of coordinated water moolecules. The relaxation of a coordinated water proton is governed by dipole-dipole coupling (dd) between the paramagnetic ion and hydrogen of water [19], scalar relaxation (sc) [19], and curie spin (cs) relaxations [20]. It is noteworthy that at high magnetic field of 1.5T and higher, only dipolar relaxation contributes to longitudinal relaxation rate while all three mechanisms can contribute to transverse relaxation rate.

$$\frac{1}{T_1^{DD}} = \frac{2}{15}\left(\frac{\mu_0}{4\pi}\right)^2 \frac{\gamma_H^2 g_e^2 \mu_B^2 S(S+1)}{r_{MH}^6}\left[\frac{7\tau_{c2}}{1+\omega_S^2\tau_{c2}^2} + \frac{3\tau_{c1}}{1+\omega_H^2\tau_{c1}^2}\right] \tag{8}$$

$$\frac{1}{T_1^{SC}} = \frac{2(S(S+1))}{3}\left(\frac{A}{\hbar}\right)^2 \frac{\tau_{SC}}{1+\omega_S^2\tau_{SC}^2} \tag{9}$$

$$\frac{1}{T_1^{CS}} = \left(\frac{\mu_0}{4\pi}\right)^2 \frac{2\omega_H^2 g_e^4 \mu_B^4 S^2(S+1)^2}{(3K_BT)^2 r_{MH}^6}\left[\frac{3\tau_2}{1+\omega_H^2\tau_2^2}\right] \tag{10}$$

Moreover, transverse relaxivity arises from inner sphere contribution is defined as follows

$$\frac{1}{T_2^{DD}} = \frac{1}{15}\left(\frac{\mu_0}{4\pi}\right)^2 \frac{\gamma_H^2 g_e^2 \mu_B^2 S(S+1)}{r_{MH}^6}\left[4\tau_c + \frac{13\tau_{c2}}{1+\omega_S^2\tau_{c2}^2} + \frac{3\tau_{c1}}{1+\omega_H^2\tau_{c1}^2}\right] \tag{11}$$

$$\frac{1}{T_2^{SC}} = \frac{1}{3}\left(\frac{A}{\hbar}\right)^2 (S(S+1))\frac{\tau_{SC}}{1+\omega_S^2\tau_{SC}^2} \tag{12}$$

$$\frac{1}{T_2^{CS}} = \frac{1}{5}\left(\frac{\mu_0}{4\pi}\right)^2 \frac{\omega_H^2 g_e^4 \mu_B^4 S^2 (S+1)^2}{(3K_B T)^2 r_{MH}^6}\left[\frac{4\tau_2}{1+\omega_H^2\tau_2^2}\right] \quad (13)$$

Where γ is the nuclear gyromagnetic ratio, g electron factor, μ_B Bohr magneton, r_{MH} the electron spin-proton distance, τ_c correlation time, and ω_I and ω_H are the nuclear and electron Larmor frequencies, respectively. The correlation time (τ_c) is defined as

$$\frac{1}{\tau_{ci}} = \frac{1}{\tau_m} + \frac{1}{\tau_R} + \frac{1}{T_{ie}} \qquad i=1,2 \quad (14)$$

while τ_R is the rotational correlation time and T_{1e} and T_{2e} are longitudinal and transverse electron spin relaxation time.

C.1.1. Dipolar interaction

The interaction between two magnetic moments causes the field fluctuation. The alignment of spin to magnetic field influence the local dipolar field of neighboring spin (as shown in Fig. 4). This interaction is known as dipole-dipole or dipolar coupling. The interaction could be heteronuclear or homonuclear, between different nuclei or the same sort, respectively. The dipolar interaction plays a main role in the relaxation mechanism, especially for the higher spin system.

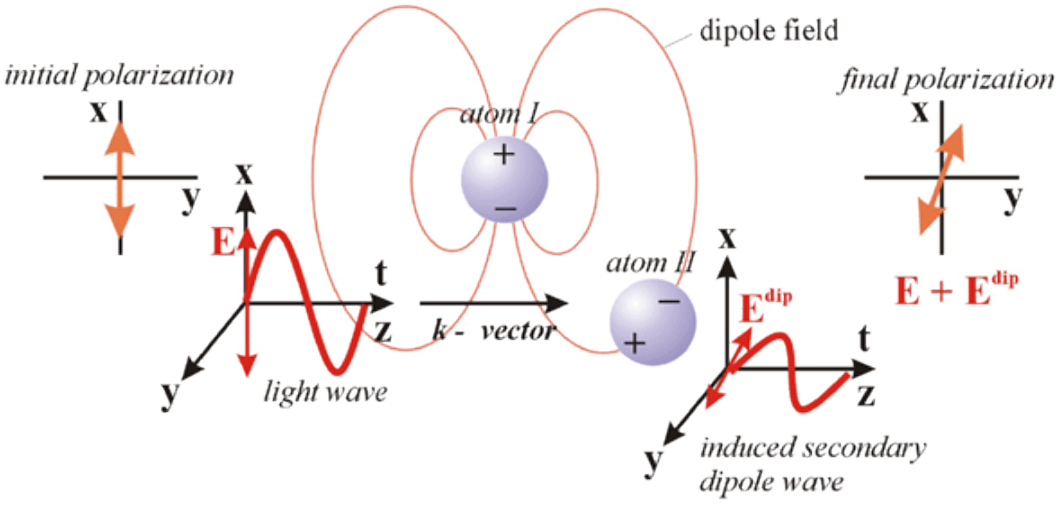

Figure 4. Orientation-dependent dipolar field experienced by a neighboring spin

C.1.2. Scalar interaction

The scalar interaction occurs when the nucleus-electron distance is about the nucleus radius. Thereby, the nuclei bound directly to the paramagnetic specie undergoing the scalar interaction. The scalar interaction is mainly influenced by electron spin relaxation and by water exchange rates and remains unaffected by orientation of the molecule. The correlation time of scalar interaction is given by

$$\frac{1}{\tau_{SCi}} = \frac{1}{T_{ie}} + \frac{1}{\tau_M} \quad i=1,2 \tag{15}$$

For the CAs composed of paramagnetic ions with S>1/2, electron spin relaxations are interpreted in terms of Zero Field Splitting (ZFS) interaction. The electronic relaxation is field dependent. For Gd(III) complex the rates are interpreted as follows

$$\frac{1}{T_{1e}} = \frac{2}{50}\left[4S(S+1)-3\right]\Delta^2\tau_v\left[J(\omega_S,\tau_v)+4J(2\omega_S,\tau_v)\right] \tag{16}$$

$$\frac{1}{T_{2e}} = \frac{1}{50}\left[4S(S+1)-3\right]\Delta^2\tau_v\left[3J(0,\tau_v)+5J(\omega_S,\tau_v)+2J(2\omega_S,\tau_v)\right] \tag{17}$$

$$\Delta^2 = \frac{5}{\left[4S(S+1)-3\right]\tau_v\tau_{S0}} \tag{18}$$

Where τ_v is correlation time for modulation of ZFS interaction, Δ amplitude of transient ZFS and τ_{S0} electron spin relaxation time at zero field.

C.1.3. Curie relaxation

In paramagnetic system, due to the Boltzman distribution there is a difference in the populations of electron spin energy levels, which induce a magnetic moment. This perturbation can influence the relaxation mechanism which is known as curie relaxation.

Referring equations 6 to 18, numerous parameters have an impact on protons relaxivity from inner sphere contributions.

1. Rotational coordination time (τ_R): reorientation of vector between paramagnetic ion and the water molecule proton.

2. Electronic relaxation time (T_{1e}, T_{2e}): the process of returning to equilibrium state of magnetization associated to electrons during transitions between electronic levels of paramagnetic center.
3. Number of coordinated water molecules (q)
4. Distance between proton and paramagnetic ions (r_{MH}) have sixth-power dependence and influence significantly the dipolar relaxation rate.
5. Residence time of coordinated water (τ_M): exchange between water molecules surrounding the complex and water coordinated to the metal ion. The residency time should be long enough to increase the probability of relaxation to occur meanwhile short enough to exchange the relaxed water molecule with the bulk water [21].

C.2. Second sphere relaxivity

The second sphere relaxation pathway in principle depends on the same parameters as the inner sphere term. The contribution is enhanced by slowing down rotational correlation time, increasing the number of hydrogen-bonded waters and their residency lifetime. The distinguishing contribution of the second sphere from the outer sphere term is very difficult. The effect of second sphere term on relaxivity has been reported for $[Gd\text{-}DOTP]^{5-}$ (q=0) with human serum albumin (HAS). The relaxivity enhancement of $[Gd\text{-}DOTP]^{5-}$ in the presence of (HAS) has been attributed to the presence of exchangeable protons on proteins close to the interaction site of the complex and from hydrogen-bonded water molecules in the second sphere shell.

C.3. Outer sphere relaxivity

Outer sphere theory demonstrates the relaxation induced by diffusion of water molecules within the magnetic field gradient around the paramagnetic hydrated ion [22]. This mechanism may contribute to the relaxivity of paramagnetic complexes at the imaging fields, arising from modulation of dipolar interaction of the paramagnetic ions with water molecules which are diffusing next to the surface of the complex. The component relaxivity arising from the outer sphere has been estimated by a expression derived by Freed [23].

$$r_{ip}^{OS} = C^{OS}\left(\frac{[CA]}{aD}\right)\left[7J_2(\omega_S) + 3J_1(\omega_H)\right] \quad (19)$$

$$J(\omega) = \mathrm{Re}\left[\frac{1 + \frac{1}{4}(i\omega\tau_d + \frac{\tau_d}{T_{je}})^{1/2}}{1 + (i\omega\tau_d + \frac{\tau_d}{T_{je}})^{1/2} + 4/9(i\omega\tau_d + \frac{\tau_d}{T_{je}}) + 1/9(i\omega\tau_d + \frac{\tau_d}{T_{je}})^{3/2}} \right] \quad j=1,2 \qquad (20)$$

Where a is the distance of closest approach, D diffusion constant, and τ_D translational correlation time equal to a^2/D, constant C^{OS} (5.8×10^{-10} $m^6 mol^{-1} s^{-2}$) and J(ω) is the non-Lorentzian spectral density. At the imaging field, the outer sphere relaxivity depends on distance of closest approach, which attributes to the molecular dimension and charge distribution of complex, and on the relative diffusion coefficient of solute and solvent.

Chapter III:Literature review

Over decades, much effort has been focused on developing the MRI contrast agents with high efficiency. However, until now only some of these agents are clinically approved. The Gd-based contrast agents available for clinical use, presented in Fig. 5 and summarized in Table 1, are nine coordinated complexes, binding with eight ligand sites and one water molecule, with molecular weight less than 1000 Da. Among the listed CAs, [Gd(DTPA)(H_2O)], first approved contrast agent [24], [Gd(DOTA)(H_2O)], [Gd(BOPTA)(H2O)] and MS-325 are ionic CAs while the rest are neutral CAs.

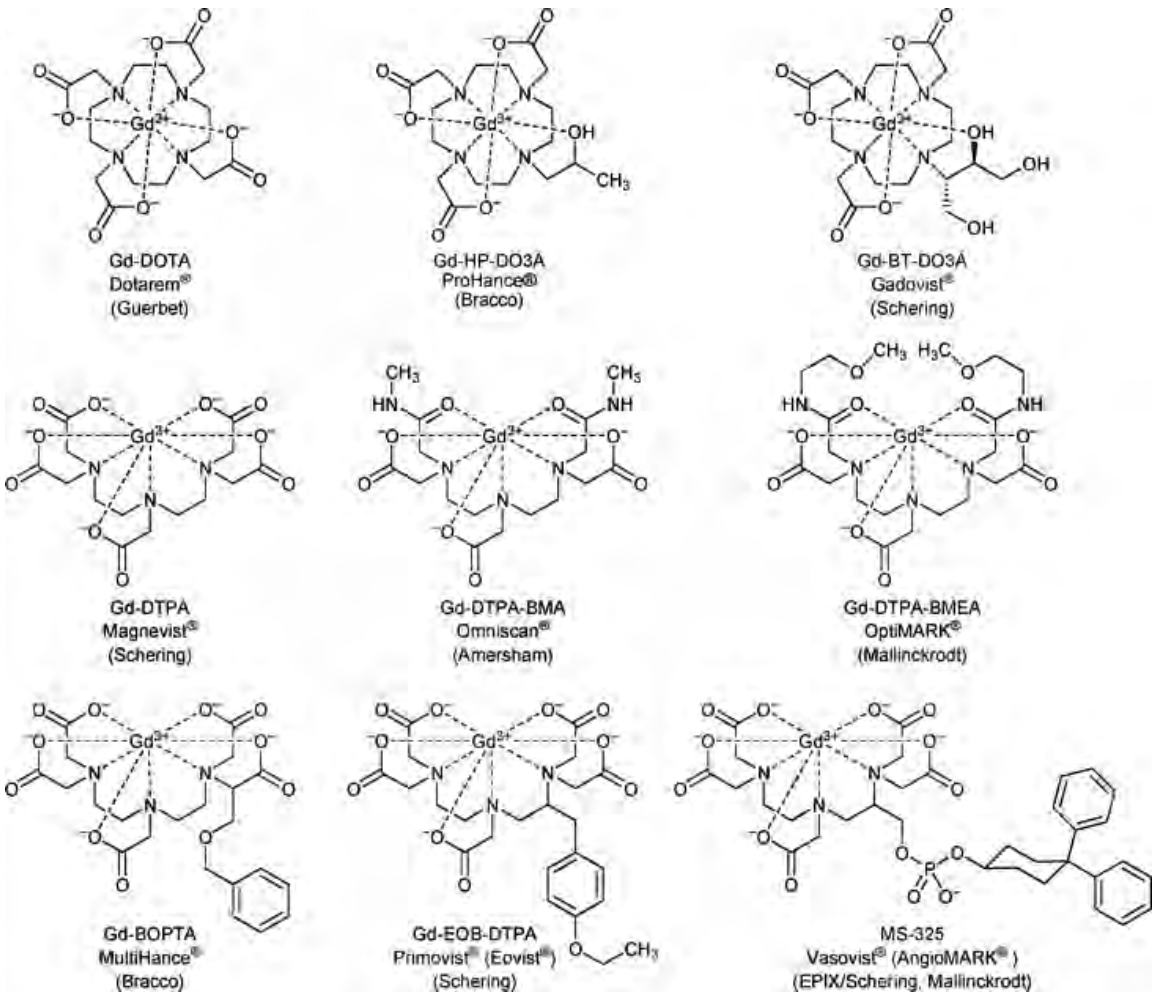

Figure 5. Schematic of commercial Gd-based clinical approved MRI contrast agents [25]

The first generation of currently available clinical contrast agents is non-specific extracellular MRI CAs. They distribute into the intravascular and interstitial space. This allows us to evaluate the physiological parameters, including renal function and status or existence of blood brain barriers [26]. Non-specificity of conventional CAs causes their poor performance for early diagnosis and imaging of specific organs. However, CAs with preferential uptake to

a particular tissue would improve the diagnostic accuracy. This type of CAs has been named as targeted CAs or second generation CAs.

Table 1. Available commercial Gd-based MRI contrast agents

Chemical name	Generic name	Brand name	Charge	Company	Relaxivity ($mM^{-1}s^{-1}$)
(Gd(DTPA)(H_20)]	Gadopentetate dimeglumine	Magnevist	2-	Schering(Germany)	$^{+}$r1=4.9, r2=6.3
[Gd(DOTA)(H_20)]	Gadoterate meglumine	Dotarem	1-	Guerbet (France)	r1=3.4, r2=4.8, B0=1.0T
[Gd(DTPA-BMA)(H_20)]	Gadodiamide	Omniscan	0	Amersham	*r1=5.4
[Gd(HP-D03A)(H_20)]	Gadoteridol	ProHance	0	Bracco (Italy)	*r1=5.4
[Gd(D03A-butrol)(H_20)]	Gadobutrol	Gadovist	0	Schering(Germany)	r1=3.6, B0=1.0 T
(Gd(DTPA-BMEA)(H_20)]	Gadoversetamide	OptiMARK	0	Mallinckrodt (U. S.)	
♦[Gd(BOPTA)(H2O)]	Gadobenate Dimeglumine	MultiHance	2-	Bracco spa (Italy)	$^{+}r_1$ = 9.7, r_2 = 12.5
♦Gd-EOB-DTPA	Gadoxetic acid	Primovist	2-	Schering (Germany)	*r_1 = 6.9, r_2 = 8.7
MS-325	Gadofosveset trisodium	Vasovist	3-	EPIX/Schering, Malinckrodt	r_1=27.7, r_2=72.6, 1.5T

+ In heparinized human plasma, at 39°C
* In citrated human plasma, at 37°C
♦ Second generation of CAs

Gd[BOPTA] and Gd-EOB-DTPA are classified as second generation contrast agents. Second generation CAs exhibit responsive behavior to physiochemical environments such as pH of solution, temperature, redox potential, metal ion concentration (Zn, Ca, Cu), and enzyme activity. These agents have shown the selectively uptake by a particular kind of cell. For instant, $[Gd (BOPTA)]^{2-}$ has shown great efficiency in the imaging of liver and myocardium [27]. Moreover, it has been used in applications of perfusion cardiac MRI for the diagnosis of coronary artery disease, cardiac tumors, inflammations and different types of cardiomyopathies [27]. $[Gd(EOB-DTPA)]^{2-}$ is applied for detection of liver metastases [28]. Nowadays, much research has been focused on designing targeted CA.

A. Tumor-Targeting contrast agents

In actively growing tumor cells with volume greater than 2 mm^3, delivery of nutrients and oxygen become limited. In order to supply oxygen and nutrients to tumor cells, new blood vessels form around tumor cells with enlarge gap junction of 100 nm to 2μm [29]. These new vessels are irregular and poorly organized which shows leaky fenestrations. This leads the extravasations of small macromolecules and nanoparticles smaller than 100 nm, which are out

of vasculature, into tumor cells [30]. Moreover, tumor cells show higher compound retention time compared with healthy tissues because of their inefficient lymphatic drainage [31], [32]. These two features provide an enhanced permeability and retention (EPR) effect in tumor cells that is playing an important role for passive targeting and accumulation of contrast agents in tumor interstitium [29]. The accumulation of targeting agents in tumor cells passively or actively is schematically presented in Fig. 6.

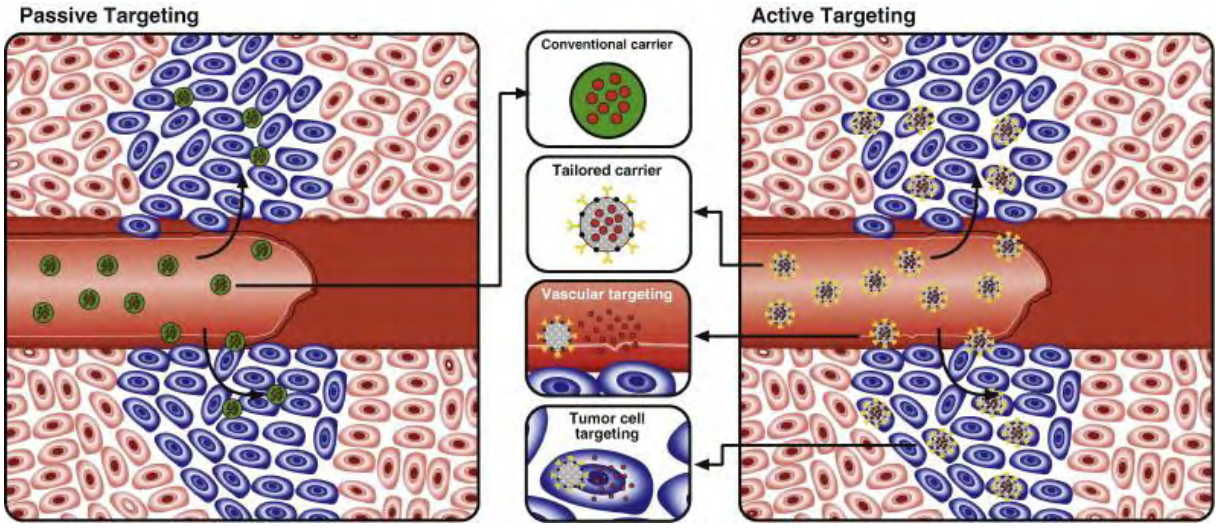

Figure 6. Schematic of targeted CAs in tumor cells passively and actively [33]

Furthermore, one method to increase the accumulation of CAs in tumor tissues is surface conjugation of CAs with appropriate ligands to targeting either cell surface or receptor targeting. These CAs have the ability to recognize cellular membrane of specific molecular sites. Thus, by administration of targeting CAs, the concentration of CAs in targeted tissue is much greater than in non-targeted tissue, which enhances the selective tissue's relaxation and may increase contrast between specific tissue and its surrounding. Whilst some complexes such as porphyrins have shown the intrinsic uptake by tumor cells [34], [35].

A.1. Macrocyclic chelator

Among the available commercial CAs, non-macrocyclic chelators such as DTPA shows a releasing Gd(III) which causes nephrogenic systemic fibrosis disease [4]. Thus, complexes with high stability to chelate the paramagnetic ions are desirable. The advantages of using macrocyclic complexes as chelators is their high thermodynamic, kinetic stability, and ability

to tune their coordination environment [4]. In Fig. 7, the most common macrocyclic chelators used as imaging agents are presented.

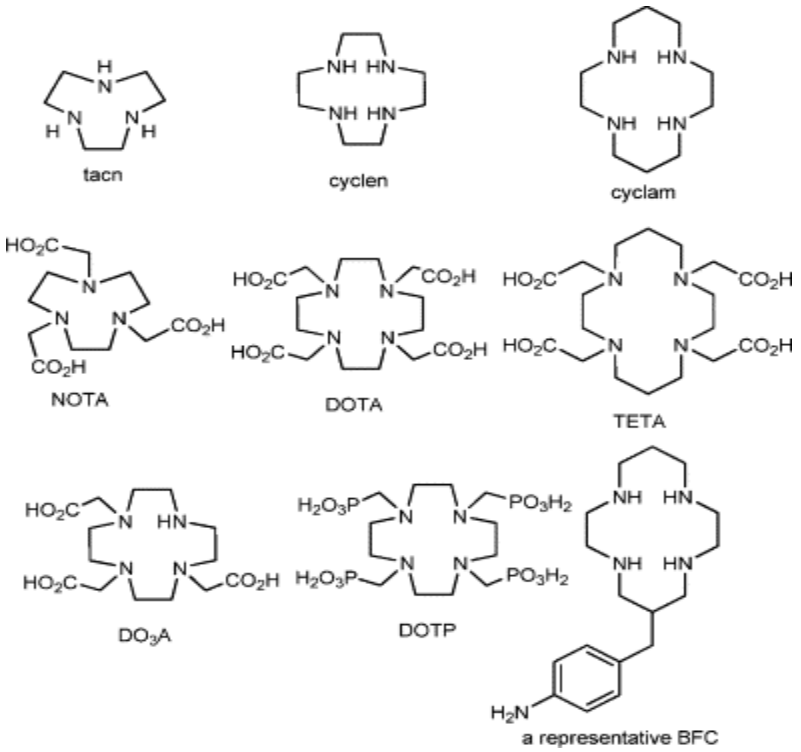

Figure 7. Developed macrocyclic chelators for biomedical application [4]

On the other hand, the developed macrocyclic ligands have been modified to target specific tissue or cellular receptors in order to enhance the contrast of MR imaging. For instance, conjugation of macrocycle Gd-Dota to polyarginie oligomers and stilbene derivatives could help Gd-Dota become a targeting MRI CA [36]. Meade and his colleagues succeeded in attaching progesterone derivatives to Gd-DO3A which could be applied as breast cancer prognostic marker, presented in Fig. 8a [37]. In other research, Gd-DO3A have been functionalized with an alkyl group as MRI targeting contrast agents, shown in Fig. 8b [38]. Gd(III) cyclen macrocycle has also been modified for using as bone imaging and therapy by addition of phosphate group in the macrocycle [39].

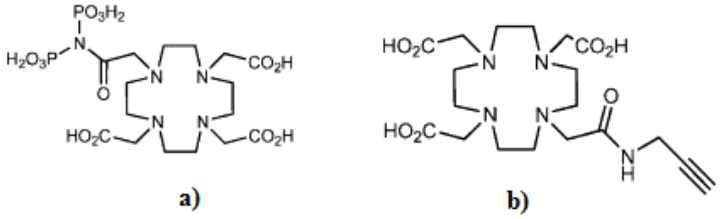

Figure 8. Structure of Macrocycle chelator as targeting MRI CAs

As described before, macrocyclic complexes have been chemically modified to be used as targeting agents. Furthermore, porphyrin is a macrocyclic chelator which has a natural tendency to penetrate into tumor cells.

A.1.1. General reviews of Porphyrins

Porphyrin stems from the Greek word porphura due to its intense purple color. The utility of naturally occurring porphyrin compounds is aa strong incentive for widespread attention in porphyrin chemistry. Porphyrin plays an important role in the metabolism of living organisms. For instance in mammalian blood, hemoglobin is iron substituted porphyrin derivatives. Cytochrome is hemeproteins, which transfer electron to cell respiration. Adenosylcobalamin or vitamin B_{12} is another naturally occurring porphyrin, which is made of cobalt/corrin complex. Corrin is similar to the porphyrin ring while it contains one less methine bridge causing loss of planarity and aromaticity within the macrocycle. While this complex in the body helps in methylation of DNA and producing hemoglobin. Chlorophyll, which is responsible for transfer of photonic energy to the reaction center in plants and plays an important role in photosynthesis, is the other example of a naturally occurring porphyrin derivative.

The simple structural feature of porphyrin (porphine) consists of four pyrrolic units connected through one-carbon methine bridges. The bridging of pyrrole units results in a large and planar macrocyclic structure with unsaturated atomic center. The porphyrin compounds follow Huckel's rule [40], which estimates the aromatic properties of planar rings. Due to this rule, the number of π electrons in a cyclic ring equals to (4n+2) while *n* is zero or a positive integer. In porphyrin, *n* equals to 4 thereby there are 18 π conjugated electrons. It is noteworthy that there are 22 π electrons in porphyrin while just 18 π electrons are delocalized [40]. High stability and astonishing photophysical properties of porphyrin complexes arise from this strong conjugation. The porphyrin can be substituted in different positions. Positions 5,10,15,20 are four meso-substituted positions while 2, 3, 7,8,12,13,17,18 are the eight β-substituted positions, as shown in Fig. 9. The rest are the eight possible α-substituted positions. β- and meso positions can be substituted by functional groups. Among the various porphyrin derivatives, meso-substituted porphyrins have received great attention in many fields including solar cell, biomedical, chemical sensor and photodynamic therapy.

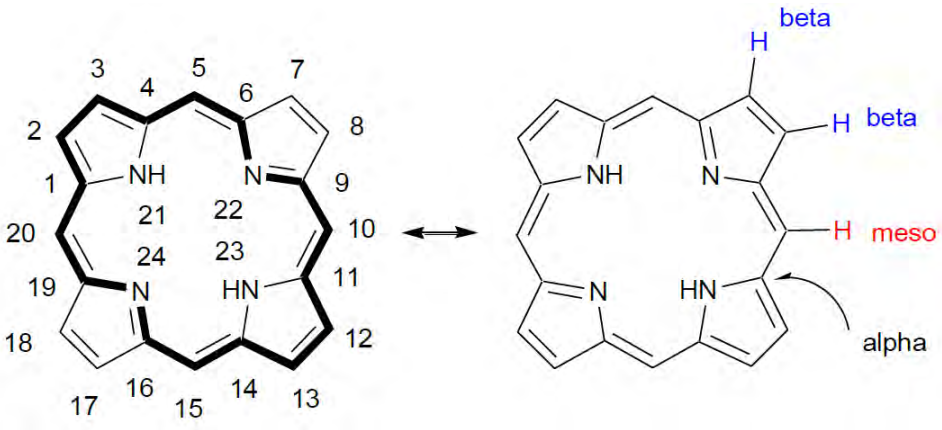

Figure 9. Schematic of porphine and peripheral position of atoms in porphine structure

As presented in Fig. 9, two pyrrolenine nitrogen atoms in porphyrin rings are capable of accepting protons while two NH groups are capable of losing protons. The losing proton results in the formation of dianion species which makes it suitable to insert metal ions in the core of porphyrin. Free base porphyrin can bind with almost all metals and some semi-metals to form metalloporphyrin complexes. Referring to the position of metal ions in metalloporphyrin, they can be categorized as in plane, out-of-plane or in bimetallic complexes.

A.1.2. Synthesis of meso-substituted porphyrin complex

The arrangement of diverse substituents in specific patterns is the main theme in the synthesis of porphyrins [41]. Control over this arrangement enables us to design and tailor different types of porphyrins for specific applications [41]. Meso-tetraphenylporphyrin has been successfully synthesized for the first time by Rothemund in 1936 [42]. Rothmund has reported the formation of meso-substituted porphyrin in one step using pyrrole and benzaldehyde under acidic conditions in a sealed flask at 150°C for 24h [43] (Fig. 10). The low yield, irreproducible and harsh experimental conditions are the limitation of this set up [44], [45].

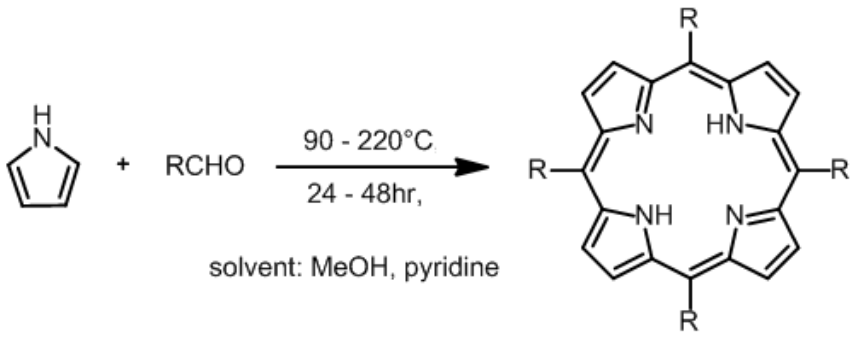

Figure 10. The Rothemund synthesis of meso-substituted porphyrin

In Rothemund synthesis, the character of substituent on the phenyl ring affects the yields of tetraphenylporphyrin [46]. The reaction and yields of tetrraphenylporphyrin can be accelerated by electron-accepter substituents while electron donor substituents can retard the reaction and reduce the yields [47]. This retardation is attributed to preferable polymerization of pyrrole to obtain polypyrrole.

In 1967, Alder, Longo and coworkers reexamined and modified the Rhotemund method [48]. They reacted benzaldehyde and pyrrole by condensation in refluxing propionic acid in glassware open to the atmosphere [48] (Fig. 11) under 141°C for 30 minutes. Performing the reaction on the large scale is the advantage of Alder's method. Moreover, this method is much milder than Rothemund's synthesis conditions and it is compatible with a variety of aldehydes with yields of 20%.

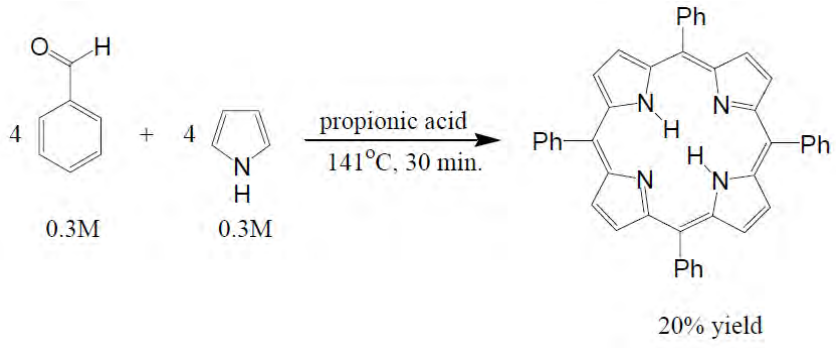

Figure 11. The Aldler-Longo method for preparing meso-substituted porphyrin

However, while the Alder method works better than Rothemund method, it has a limitation such as failing reaction with benzaldehydes, no crystallization of porphyrin , purification problem, and low and often irreproducible yields [49].

The Alder method was optimized by Lindsey and coworkers in 1987[50], [51]. In this method, a new strategy for the synthesis of meso-substituted porphyrin has been used. The reaction has been performed using acid-catalyzed pyrrole-aldehyde condensation in the presence of $CHCl_3$ for one hour at room temperature. The first step has been monitored to obtain maximum porphyrinogen which can be oxidized rapidly to porphyrin with addition of 3 equivalents of quinon oxidant in the 2nd step [52], as shown in Fig. 12. The reaction was carried out under gentle conditions to achieve equilibrium during condensation and to avoid any side reaction. The oxidation of porphyrinogen in the Lindsey method has been carried out by adding p-chloranil, 2,3-dichlor-5,6dicyano-1,4-benzoquinone (DDQ) which require one hour for a complete reaction. This method also has its own limitation such as expensive cost, destroying some porphyrinogen during adding DDQ, requiring large volume of solvent (pyrrole and aldehyde), and difficult purification of porphyrin [53].

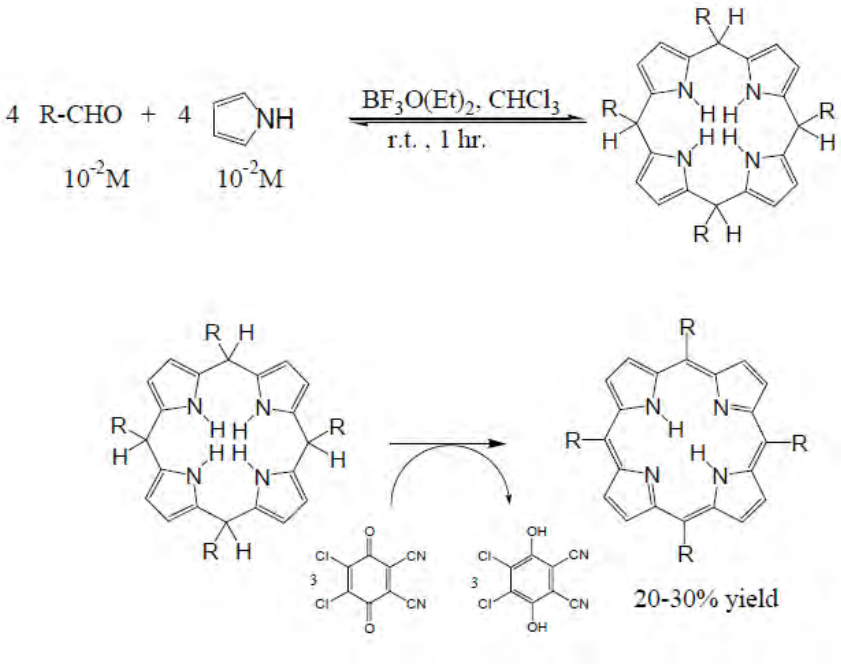

Figure 12. Two steps synthesis of porphyrin at room temperature

In the MacDonald method, different meso-substituted trans-porphyrins can be prepared by condensation of a 5-disubstituted dipyrromethane with aldehyde as shown in Fig. 13 [54] . The drawback of this method can be referred to modest yields of porphyrin (10-30%), and condensation in dilute solutions (10 mM). Sometimes the dipyrromethane-aldehyde condensation is not desirable to produce trans-A_2B_2-porphyrin because of obtaining the mixture of porphyrins which are difficult to separate [47].

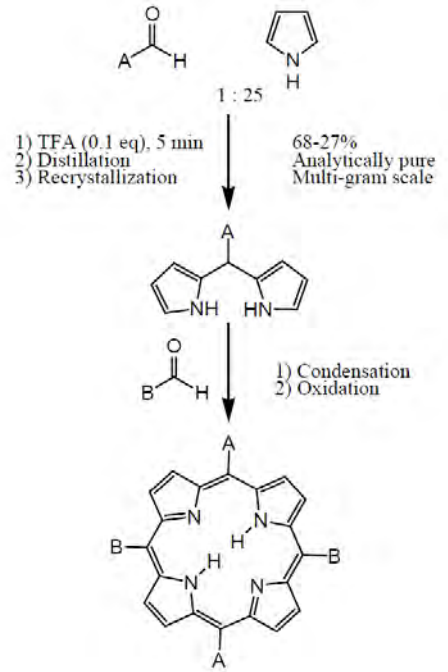

Figure 13. The MacDonald type 2+2 condensation method

A.1.3. Electronic absorption Spectrum of porphyrin

For the first time in 1960, the absorption spectrum of porphyrin was successfully explained in terms of four orbital models. Due to four orbital models of Martin Gouterman [55], absorption bands in porphyrin complex originate from transition between two highest occupied molecular orbital (HOMO and HOMO-1 , π orbitals) and two lowest unoccupied molecular orbital's (LUMO and LUMO+1, π* orbitals) as presented in Fig. 15. For metalloporphyrin with 4-fold symmetry, the LUMOs are degenerate (labeled as e_{gx} and e_{gy}) whereas HOMOs are nearly degenerate (labeled as a_{1u} and a_{2u}). Excited states comes from the transition between $a_{1u,2u} \rightarrow e_{gx,gy}$ (x-polarization) and those between $a_{1u,2u} \rightarrow e_{gy,gx}$ (y-polarization). These polarized excited states are mixed and split into two states in energy, lower energy (labeled as Q_x and Q_y) and higher energy (labeled as B_x and B_y) states. Lower energy (with less oscillator strength) and higher energy (with greater oscillator strength) give rise to a Q band and Soret band, respectively. In the case of free base porphyrin, 2- fold symmetry results in nondegeneracy of LUMOs and splitting of Q_x and Q_y as well as B_x and B_y transition. Transition between HOMOs and LUMOs in free base porphyrin produces four excited states.

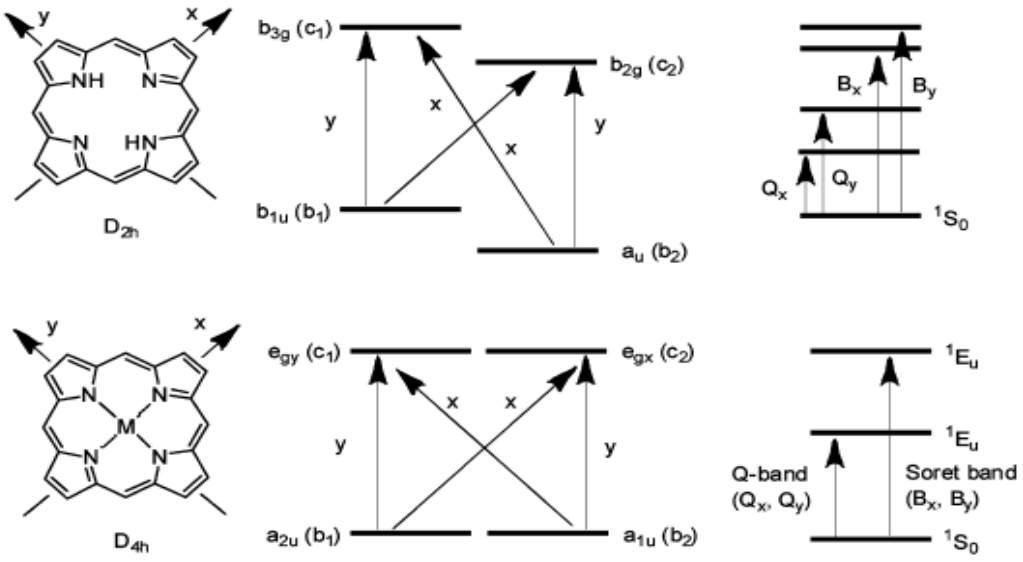

Figure 14. The Gouterman's four orbital models for D_{2h} symmetry free-base porphyrin (top) and for D_{4h} symmetry metalloporphyrin [56]

As explained, the electronic absorption spectrum of porphyrin contains two distinct regions. The first region, which involves the transition from ground state to the second excited state, is called the Soret band. The Soret band of porphyrin is in the range of 380-500 nm depending on the type of porphyrin- whether meso- or β-substituted. The second region, in the range of 500-700 nm, is called Q band, which involves the weak transition from ground state to the first excited state. Protonation of two inner nitrogen atoms during metallation of porphyrin causes strong changes to the visible absorption spectrum. This change is attributed to more symmetry in protonated (metallated porphyrin) than the free base one that simplifies the Q band pattern.

Based on relative intensities of four Q bands, four basic spectra have been identified in UV-visible spectra of porphyrin, presented in Fig. 14. If the relative intensities of Q bands are in the order of IV>III>II>I, the spectrum is called etio type. This type of spectrum can be observed in β-substitued porphyrin while six or more positions are substituted with groups such as alkyl without any π-electrons. Rhodo type of spectrum could be observed while β-positions of porphyrin have been substituted with groups such as carbonyl or vinyl groups which has π-electrons. This causes a change in the relative intensity of Q bands (III>IV>II>I) and shifting the spectrum to the longer wavelength (redshift). Substituting of two electron-withdrawing groups on opposite pyrrole rings causes a change in maxima absorption

intensities follow the order III>II>IV>I, has been called oxo-rhodo-type spectrum. And the fourth spectra observed when substitution of meso positions causes to obtain maxima intensities in order of IV>II>III>I, which is called phyllo-type spectrum [57].

As described above, metallation of porphyrin changes the absorption spectrum by reducing four Q bands to two Q bands, designated by α and β, and Soret band around 400 nm. Whereas the intensity of metalloporphyrin's α and β bands depends on the coordination of metal with the ligand. While metal forms a stable square-planar complex with the porphyrin ring, the intensity of α band is higher than β band.

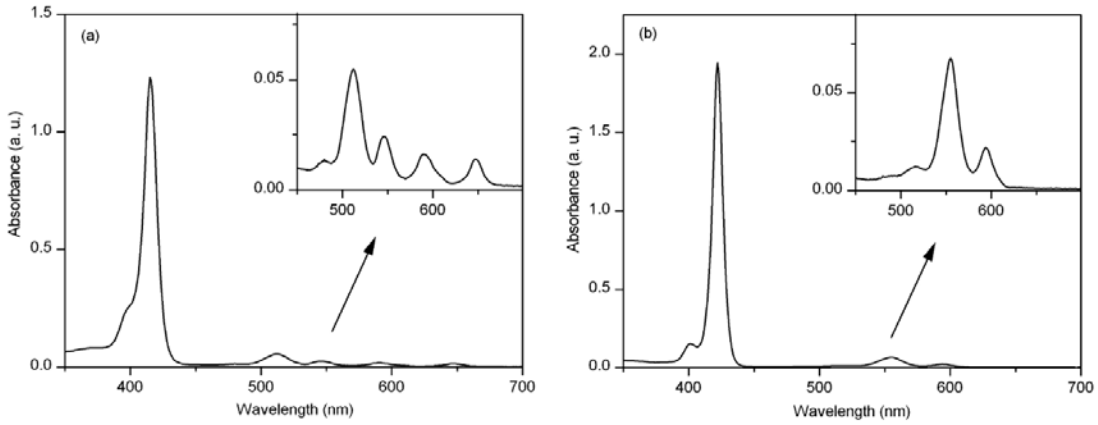

Figure 15. Typical UV-visible spectra of a) free-base and b) metallated porphyrin

Porphyrins have been widely studied due to their characteristic optical properties. The UV-visible spectrum of porphyrin contains two main regions. One intense absorption peak around 400 nm that is named Soret band following low intense peaks, Q band, in the region of 450 nm-700 nm. The intensity and position of peaks depends on the solvent, concentration as well as nature of porphyrin side chains and their positions.

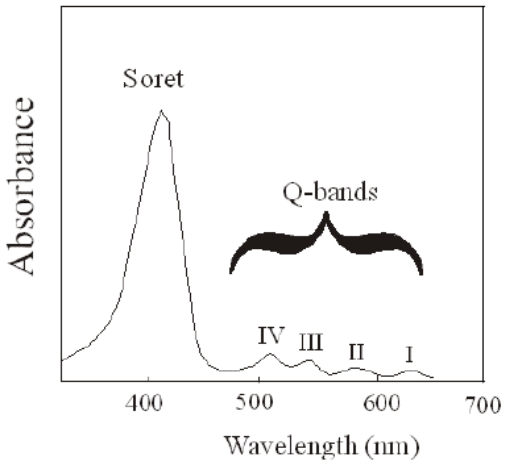

Figure 16. UV-visible absorption spectrum of porphyrin with its typical Soret and Q bands

A.2. Application of porphyrin in cancer therapy and imaging

A.2.1. Photodynamic Therapy

Porphyrins have been extensively utilized as photosensitizers [58]. Exciting with UV-visible light, photosensitizers induce photochemical reactions using irradiating energy. Singlet oxygen is produced during photochemical process. Combination of photosensetizers with oxygen induce the lethal cytotoxic agents which results in cell death and tissue destruction [59]. These agents can be applied in photodynamic therapy (PDT). For the first time, Raab in 1900 reported the chemical sensitization of tissue by light [60]. In 1903, Tappeiner and Jesionek [61] have successfully treated skin cancer by applying topically eosin and light [62]. Later, Raab and Tappeiner discovered that certain dyes could destroy the cell in the presence of light [63]. Afterward, certain attention has been focused on using PDT for malignant lesions in human. With administration of photosensitizers to cancer cells, either intravenous or intraperitoneal injection, the cancer cells could be irradiated with light. During returning the photosensitizer to its ground state, the singlet oxygen could be produced from transferring released energy to triplet molecule. This singlet oxygen is the trigger for tumor destruction in PDT, as presented in Fig. 17. The lifetime (1-320 ns) and diffusion distance (10-55 nm) of singlet oxygen in cells are very short. Thus, the damage of PDT is highly depending on the sub cellular localization of photosensitizers.

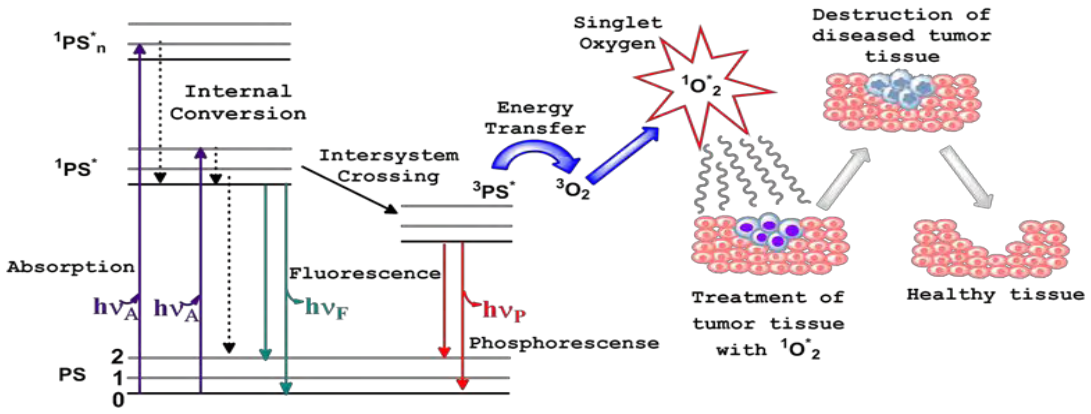

Figure 17. Schematically presents the photodynamic therapy using photosensitizers [64]

The ideal photosensitizers should be retained by diseased tissue in order to minimize the damage of healthy tissues during photochemical reaction. In order to obtain the satisfactory results, photosensitizers should localize in target tissue. This could improve the efficacy of cell destruction to obtain effective PDT. The majority of successful and effective photosensitizers are based upon tetrapyrrole chromophore such as porphyrin, chlorine, and bacteriochlorin complexes. Most photosensitizers in PDT are based upon porphyrin or porphyrin-related derivatives due to their preferential localization in tumor tissues and their characteristic optical properties.

A.2.2. Fluorescence Imaging

Referring to characteristic optical properties of porphyrins, they can also be used as imaging agents. Porphyrins emit light at high wavelength (red or near-infrared wavelengths) during their irradiation. The emission at high wavelength could be useful in cellular imaging studies. Due to preferential localization of porphyrinic complexes into tumor tissues and their characteristic fluorescence features, it is possible to visualize the tumor cells using porphyrin complexes as fluorescence agents. The history of fluorescence imaging of tumor tissues goes back to 1924. First fluorescence emission (red/brown) from tumor cells was observed by Policard [65], [66]. Lforth *et al.* have reported the localized fluorescence emission of different porphyrin and metalloporphyrin complexes from tumor tissues [67], but not from healthy tissue [58].

Fluorescence imaging and PDT modalities are based on the same principles while the outcome is different. Fluorescence imaging has shown no/low cytotoxicity which is attributed

to using low fluence rate to generate light activation. Whereas in PDT, the aim is using the cytotoxic effect of photosensitizers, high fluence rate have been applied to generate singlet oxygen to destroy the tumor cells. Thereby, the porphyrinic complexes could be applied as imaging and therapeutic agents at the same time.

A.2.3. Magnetic Resonance Imaging

In 1984, for the first time the efficiency of water soluble metalloporphyrin as MRI contrast agents has been suggested by Chen *et al.* [68]. They have studied the potential of three water soluble metalloporphyrins such as Mn(III), Fe(III), Cu(II) tetra-(4-sulfanatophenyl) porphyrin (TSPP) to shorten the relaxation time of nearby water protons [68]. Among these three metalloporphyrins, Mn ($TSPP_4$) and Cu($TSPP_4$) have exhibited respectively the highest (r1=10.36 $mM^{-1}.s^{-1}$, 20 MHz) and the lowest (r1=0.139 $mM^{-1}.s^{-1}$, 20 MHz) relaxivity. In order to examine the effect of another ligand upon relaxivity of water protons, Fe($TSPP_4$) has been added to the solution of 0.2 M pyridine in water [68]. The reduction of r1 from 3.9 $mM^{-1}.s^{-1}$ to 0.2 $mM^{-1}.s^{-1}$ was observed which was attributed to a decrease in the high spin form of Fe(III) complex in the presence of pyridine [68]. Subsequently, Furmanski and Longley in 1988 have investigated the *in-vitro* and *in-vivo* efficiency of Gd(III) and Mn(III) meso-tetra n-methyl-4-pyridyl porphyrin (TMPyP) as MRI CA at 10.7 MHz [69]. Gd(TMPyP) has exhibited the low r1 of 5.19 $mM^{-1}s^{-1}$ which is less than the r1of free Gd(III) (14.67 $mM^{-1}s^{-1}$)which was ascribed as chelating of Gd(III) with porphyrin causing the loss of available proton coordination site [69]. In another research, Lyon and co workers have investigated relaxivity of Gd(III), Mn(III), and Fe(III)-tetraphenylporphine sulfonate, Gd(TPPS), Mn(TPPS), Fe (TPPS), where the porphyrin is substituted by sulfonato group in aromatic ring [70]. The relatively high r1 of Gd(TPPS) (22.8 $mM^{-1}.s^{-1}$) was obtained while this compound was found to dissociate rapidly in solution which was an obstacle for further studies [70]. Gd-hematoporphyrin (Gd-H) and Gd-boronated porphyrin,1, 6, 11, 16-tetra (3-*o*-carboranyl- methoxy) phenyl-porphyrin (Gd-TCP)) are two other Gd-mesoporphyrins which have been studied as MRI contrast agents [71]. Gd-TCP in aqueous solution has possessed the higher r1 of 31.4 $mM^{-1}s^{-1}$ at 7T and 23°C [71], additionally; it has exhibited the significant uptake in tumor tissues compared with Gd-H [72]. One significant obstacle for going further with water soluble Gd-meso-porphyrin derivatives as MRI contrast agents is the low stability of the complexes because of the large size of Gd(III). After observing the low stability of Gd-mesoporphyrin, a new class of Gd-porphyrin with high stability has been

synthesized. Bis-triethylen glycol gadolinium texaphyrin diacetate (Motexafin gadolinium), extended porphyrin, and exhibited a high relaxivity (16.9 $mM^{-1}.s^{-1}$ at 50 MHz) and high stability [73]. Furthermore, the potential of gadolinium complex conjugated with porphyrin has been also investigated as a MRI contrast agent. One of the developed complexes is Gdophrin-2, Gd (III) mesoporphyrin-IX-13,17-bis [2-oxo-4,7,10,10-tetra (carboxylatomethyl)-1,4,7,10-tetraazadecyl]-Diamide. It shows high r1 of 8.3 $mM^{-1}.s^{-1}$ at 0.47T [74]. This compound was recognized as a positive enhancing myocardium- and necrosis- targeted MRI contrast agent [75]. In 2011, Guo-Ping Yan et al. synthesized porphyrin containing polyaspartamide gadolinium complex by the incorporation of water soluble 5-(4'-aminophenyl)-10,15,20-tris (4'-sulfonatophenyl) porphyrin, trisodium salt (APTSPP) as the tumor targeting groups and DTPA into poly-α,β-[N-(2-hydroxyethyl)-L-aspartamidel] (PHEA) [76]. They observed that r1 of the new complex was around 14 $mM^{-1}s^{-1}$ however the relaxivity of the commercial Gd-DTPA CAs is 3.68 $mM^{-1}s^{-1}$ [76].

Table 2. List of studied metalloporphyrins and their relaxivities

Metalloporphyrin	R1($mM^{-1}s^{-1}$)	Condition	Ref.
Gd-porphyrin derivatives			
Gd(TMPyP)	5.19	10.7 MHz, 37°C in 37% dimethyl sulfoxide/water	[69]
Gd(TSPP)	22.8	0.25 T, 37°C	[68]
Gd-H	16.3	7T and 23°C	[71]
Gd-TCP	31.4		
Gd-MP	9	1T	[77]
Gd-DTPA-APTSPP- PHE	14		[76]
Gd-Motexafin	16.9	50 MHz, 25°C	[73]
Gdophrin-2	8.3	0.47T, 39°C	[74]
Mn-porphyrin derivatives			
Mn(II)(TCP)	16	1T	[78]
Mn-uroporphyrin	4.8	300 MHz, in plasma	[79]
Mn(TPPAS)	20	20 MHz	[80]
$Mn(TPPS)^{3+}$	10.3		
Mn(TPP)	13	20 MHz	[77]
Mn-TE-2PyP	~9		[81]
Mn-Tn-Hex-2-PyP	~13		
$Mn(TSPP_4)$	10.36	37°C,20 MHz, in water	[68]
$Mn(TSPP_4)$	7.6	37°C,20 MHz, in pyridine	
Mn(TMPyP)	11.53	10.7 MHz, 37°C in water	[69]

After observing the low stability of Gd-mesoporphyrins, an increasing interest has been devoted to study the potential of Mn-porphyrins as MRI contrast agents. The manganese(III)-tetraphenyl-porphyrin-sulfonate have been studied by some researchers due to its *in-vitro* high stability and simultaneously preferential localization in mitochondria [70]. Although, the relatively high toxicity of TPPS4 (LD_{50}=0.5 mmol/kg) is reduced after metallation with Mn(III), Mn(TPPS4) is reported as a toxic complex [82], [83]. Besides Mn(TPPS4), the relaxivity of less sulfonated compounds such as Mn(TPPS3) and Mn(TPPS2) were also screened by Fiel et al. [84]. Among them, Mn(TPPS3) showed the best tissue contrast with r1~10.3 $mM^{-1}s^{-1}$ at 20 MHz [84]. Moreover, Mn-mesotetraphenylporphyrin, Mn (TPP), has shown high r1 of 13 $mM^{-1}s^{-1}$ at 20 MHz in aqueous solution [77]. In another research, the potential of two Mn-mesoporphyrins substituted with different polyhydroxylamides, Mn(III) 5,10,15,20-tetrakis{[4-carboxylic acid-(2,3-dihydroxyisopropyl)amide phenyl) porphyrin (Mn(TPPIS)) and Mn(III) 5,10,15,20-tetrakis(4-carboxylic acid-(1,3-dihydroxyisopropyl)amide phenyl) (Mn(TPPAS)), as MRI contrast enhancement has been studied [80]. It has been observed that Mn(TPPAS) has the higher relaxivity (almost two times) than r1 of Mn(TPPS) (10.3 $mM^{-1}s^{-1}$) which has been attributed to two water molecules in the inner sphere instead of one for Mn(TPPS) porphyrin [80]. Although, Mn(TPPAS) has shown great signal enhancement at heart, liver, lungs and gastrointestinal tract, this compound exhibited significant toxicity [80]. The more basic porphyrin derivatives, protoporphyrin IX (Mn(PPIX)) has shown the lower relaxivity compared with those of Mn(TPPS) which was attributed to its aggregation in dilute phase [85]. The relaxivity of Mn-boronated protoporphyrin has been also reported of 4.43 $mM^{-1}s^{-1}$ at 10.7 MHz [86]. The relaxivity of two Mn-mesoporphyrins such as: Mn(III) meso-tetrakis(N-ethylpyridinium-2-yl)porphyrin (MnTE-2-PyP(5+)) and Mn(III) mesotetrakis(N-hexylpyridinium-2-yl)porphyrin (MnTnHex-2-PyP(5+)) have revealed the high efficiency r1 of almost two and three-fold respectively higher than r1 of Gd-DTPA, of these two complexes as MRI CA [81].

A.2.4. In-vivo MRI studies of metalloporphyrin

In-vivo MRI studies of Mn $(TPPS_3)_2$ has been performed by Cheng *et al*. [87], presented in Fig. 18. After tail vein injection of Mn $(TPPS_3)_2$ at rat (25 μmol.kg), strong T1 contrast (bright signal) enhancement in cardiovascular systems has been observed [87]. After 10 min of $Mn(TPPS_3)_2$ injection, the reduction of T1 of blood from 1700 ms to 200 ms has been

reported, moreover, T1 effect still could be observed after 24 h [87]. Meantime, the Mn $(TPPS_3)_2$ shows the long retention of 1h in rats without any significant T1 changes which results in increasing the temporal imaging window [87].

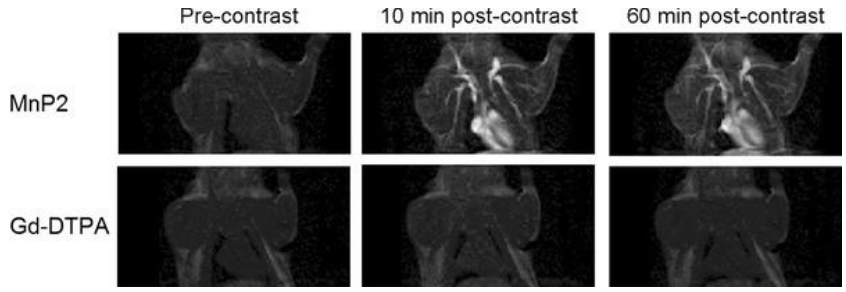

Figure 18. T1 weighted images of healthy rats after postinjection of Mn $(TPPS_3)_2$ from spin echo sequences at 3T compared with those of after postinjection of conventional CAs Gd-DTPA as reference [87]

The biodistribution of $Mn(TSPP_4)$, Mn-TCP, and $Mn(TSPP_3)_2$ in rats have been studied by Cheng *et al.*, Fig. 19 [78]. Significant signal enhancement has been observed after 0.05 mmolMn/kg administration of Mn-porphyrins, specially in kidney and bladder, within 10 min of postinjection [78]. After 1h, the majority of signal enhancement in kidney has been relocalated into bladder and fully disappeared after 24h. Among those three Mn-porphyrins studied, Mn-TCP was the one which was rapidly cleared via renal filtration [78]. The signal intensity of kidney remains high after 60 min of postinjection of Mn(TPPS). While, $Mn(TSPP_3)_2$ showed significant T1 enhancement in the liver whereas after 3 days no bladder enhancement was observed. Due to strong T1 enhancement after postinjection of $Mn(TSPP_3)_2$ in blood vessel and heart, it has been suggested that this compound could be applied as blood pool CAs [78].

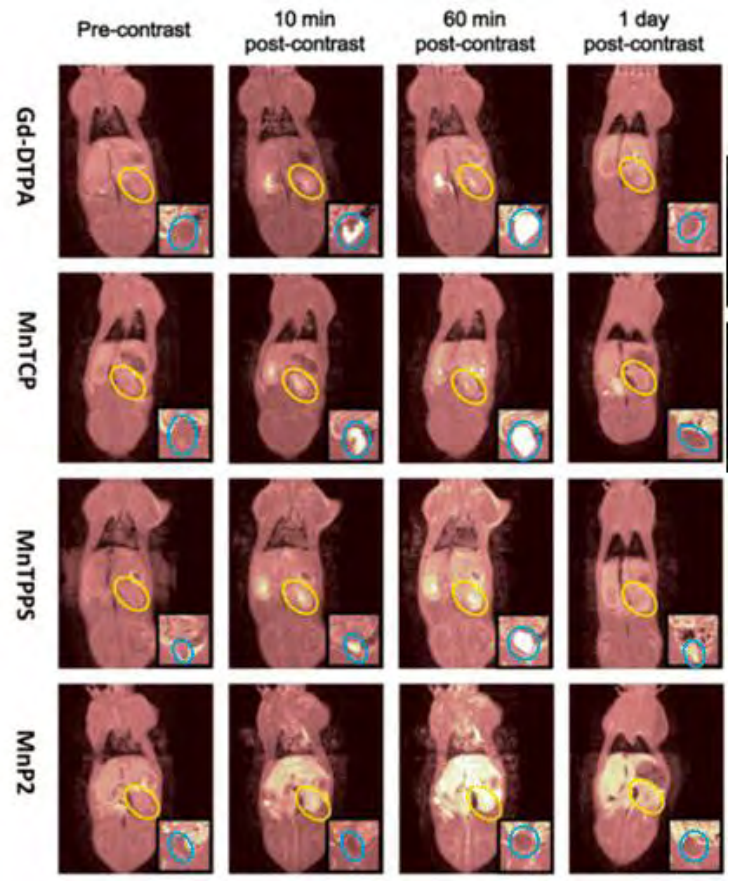

Figure 19. T1 weighted spin echo of rat after pre and postinjection of Mn-porphyrins such as Mn-TCP, Mn(TPPS) and MnP2 ($Mn(TPPS_3)_2$) in comparison with Gd-DTPA as a reference at 3T. yellow circle: left kidney, blue circle: bladder [78]

The signal enhancement of Gd-TCP, Gd-H porphyrins in different tissues including kidney, liver, spleen and tumor tissues of mice and their biodistributions in melanoma xenograft have been studied and compared with those one of GdCl3 and Gd-DTPA [88]. The signal intensity in tumor tissues after postinjection of Gd-porphyrins were higher than those using a commercial one which confirms the specific accumulation of Gd-porphyrins in tumor tissues [88], as shown in Fig. 20.

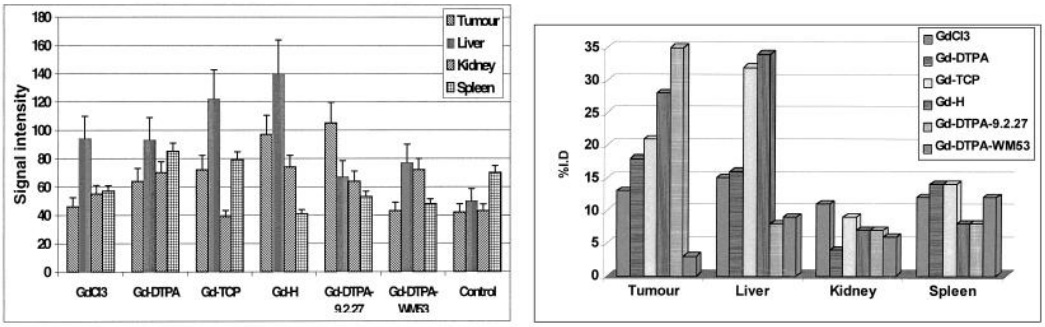

Figure 20. MRI signal intensity after postinjection of different Gd(III) compounds and their distribution in melanoma xenografts in nude mice after 24h [88]

Over recent decades, conjugation/encapsulation of CA with/within macromolecules is becoming an approach to improve the efficiency of CAs. In the next section, the developed macromolecular CA and their relaxivities will be reviewed.

B. Macromolecular Contrast agents

Conventional CAs mostly exhibit rapid extravasate from vasculature and distribute in extracellular space nondiscriminatively because of their low molecular weight as shown in Fig. 21, providing a short time window for imaging. For instance, the Gd-DTPA-BMA CA administered in rat has exhibited the distribution of 4.6±1.7 and elimination half-life of 18±2.8 min [89]. Thus, it is required to develop CAs with long blood pool retention as well as providing a wider time window for cardiovascular and oncological MRIs [89].

Recently, macromolecular CAs have been developed in order to prolong blood pool retention times. Macromolecular CAs (MCAs) could be defined as CAs with high molecular weight (>1 kDa) and long half-life in blood circulation (>10 min). Meantime, chelating of paramagnetic ions with macromolecules can affect the relaxivity of CAs due to retarding the rotational motion of the complex and increase τ_R. Thereby, high relaxivity and prolonged pharmacokinetics could help to minimize administration of MMCAs, reducing the risk of nephrogenic systemic fibrosis [90], [91]. The other advantages of MMCAs over CAs with low molecular weight is their ability to be adapted as a targeted CAs, drug carrier and their flexibility for labeling due to their inherent multivalency [92].

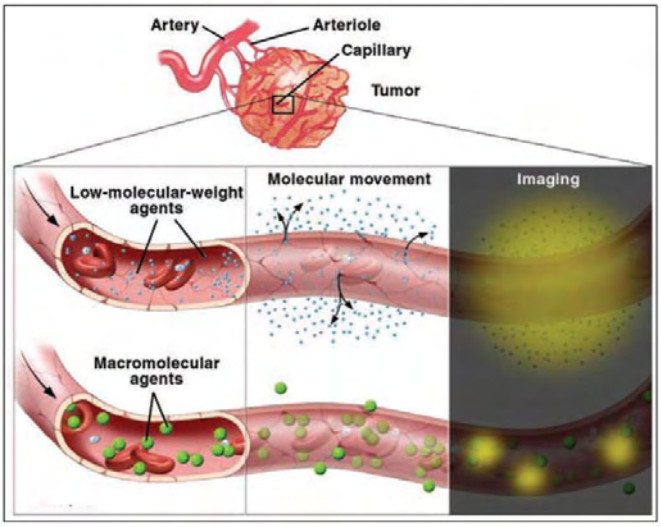

Figure 21. Schematic presents diffusing of A) low molecular weight and B) macromolecular CAs from tumor vessels into the interstitial space [93]

For instance, conjugation of Gd-DTPA with poly-L-lysine with the molecular weight of 3.3-102 kDa enhance the r1 up to 2.5 times higher than Gd-DTPA (at 2.4T and 37°C) in aqueous solution [94]. In another work, Gd-DTPA conjugated onto rigid poly(propylene imine) (PPI) dendrimers has shown r1 and r2 of 19.7 $mM^{-1}s^{-1}$ and 27.8 $mM^{-1}s^{-1}$ (1.5T and 20°C), respectively, which is almost 5 times higher than those of Gd-DTPA [95]. Conjugation of Gd-DTPA onto flexible polyethylene glycol (PEG) has shown a slight enhancement of relaxivity [96]. The Gd-DTPA-PEG with molecular weight in the range of 10-83 kDa possesses r1 of 6 $mM^{-1}s^{-1}$ at 20 MHz and 37°C. This negligible enhancement has been attributed to the flexibility of linear copolymer PEG that could not significantly retard rotational motion of the complex.

However, sometimes conjugation of CAs with polymer could not significantly enhance the relaxivity of CAs due to reduce the number of coordinated water and slower the water exchange rate. For instance, conjugation of dendrimer-Gd-DOTA with PEG has shown r1 of 13.7 $mM^{-1}s^{-1}$ due to decrease hydration number and slower water exchange rate [97]. However, water soluble Gd-DOTA dendrimer with molecular weight of 61.8 kDa possesses an r1 of 18.8 $mM^{-1}s^{-1}$ at 25MHz [97]. It has been observed that by PEGylation of non-polyaminocarboxylate Gd chelate the number of coordinated water decreases from 2 to 1. Thereby, the PEGylation causes either negligible increase of r1 or reduction of r1. Additionally, it has been observed that by PEGylation of dendrimer-Gd-DOTA the blood elimination half-lives increased up to 1219 min and seven-day liver uptake dropped to 8% of

the administered dosage, compared with dendrimer-Gd-DOTA with blood half-lives of maximum 115 min and seven-day liver retention of over 40% [97]. In the following section, we will focus on a literature review of different developed macromolecular contrast agents.

B.1. Macromolecular Contrast agents classification

Different varieties of Macromolecular Contrast agents (MMCAs) have been synthesized during the past decades. MMCAs have been classified as block, and nano-polymeric MMCAs [98]. The block MMCAs are made of paramagnetic chelates that are located in the polymer backbones such as DTPA di-ester or DTPA-bisamide copolymers. Thus, insertion of paramagnetic chelates in the backbone of polymers restricted the CAs rotation which enhances relaxivity.

Over two recent decades, nanotechnology has created new opportunities in the medical area, including drug delivery, cancer therapy, and molecular imaging. Using nanoparticles in the range of 10nm-500 nm has shown a significant impact on drug delivery. In this context, polymer nanoparticles have shown particular promise as unique biomedicine vehicles. The large surface to volume ratio of polymeric nanoparticles offers the high capacity to absorb large amount of drug or imaging agents [99], [100].

B.1.1. Block macromolecular contrast agents

Series of copolymers of diethylenetriaminepentaacetic acid (DTPA) and poly(ethylene glycol) (PEG) diamines have been used as chelater of Gd, resulting in molecular weight in the range of 10.8 to 83.4 kDa [101]. While, the highest r1 (10.1 $mM^{-1}s^{-1}$, 20 MHz and 40°C) was observed for Gd complex with molecular weight of 13.6 kDa [101]. Referring to high molecular weight of complex, the r1 was not as high as expected. The flexibility of PEG could prevent the enhancement of the complex relaxivity.

In another work, Gd-DTPA coupled with *L*-tartaric acid, with two different degrees of polymerization of n=12 (Gd4(H_2O)) and n=19 (Gd10(H_2O)) as presented in Fig. 22, have exhibited r1 of 4.7 and 4.4 $mM^{-1}s^{-1}$, respectively, at 400 MHz and 310 K [102]. However, the per molecule r1 of Gd4(H_2O) and Gd10(H_2O) were reported as high as 51 and 80 $mM^{-1}s^{-1}$, respectively, which provides a substantial 16- and 25-times higher r1 compared with that of

Gd-DTPA-BA [102]. The low relaxivity values per Gd ions has been referred to the internal flexibility of the complex and slow water exchange rate of Gd-DTPA [103].

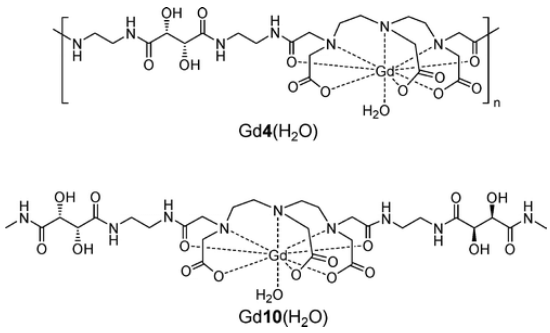

Figure 22. Structure of coupling *L*-tartaric acid to Gd-DTPA with two degree of polymerization of n=12 (Gd4(H_2O)) and n=19 (Gd10(H_2O))

In the other studies, the relaxivity of two linear polymerizations of DTPA with 1,6-hexanediamine (HMD) and trans-1,4-cyclohexanediamine (CHD) have been investigated by Duarte and colleagues [104]. They observed that r1 of Gd-DTPA-CHD was slightly higher than Gd-DTPA-HMD, as presented in Fig. 23, which were two times higher than Gd-DTPA. From the relaxometry studies, rigidity of cyclic diamide linking has been referred as an obstacle to enhance the relaxivity of the complexes. Compared with the MMCAs, their relaxivities were not high. Moreover, the short length of linking groups could prevent the hydrophobic interaction between polymer chains [104]. Referring to evaluated rotational correlation time, presented in Fig. 23, it has been deduced that substantial residual flexibility and long residence time of water molecules in the inner sphere could block the increase of r1 [104].

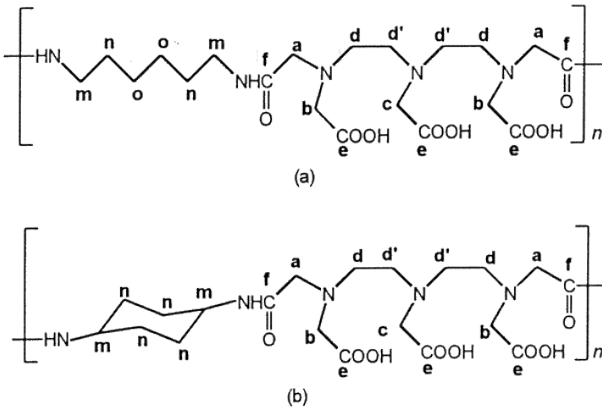

Parameters	Gd-DTPA-HMD	Gd-DTPA-CHD
Mw	4900	6400
r1($mM^{-1}s^{-1}$)	7.8*	8.1*
τ_R $(ps)^+$	580	997
τ_M $(\mu s)^+$	1.33	1.45
τ_V $(ps)^+$	21	32
τ_{SO} $(ps)^+$	120	140

* at 9MHz and 298K

\+ r_{Gd-O}=0.31 nm, D=3.5x10^{-9} m^2s^{-1}, and q=1

τ_R: rotational correlation time

τ_V: correlation time modulating electric relaxation

τ_M: residence time of inner sphere water molecule

τ_{SO}: electronic relaxation time

Figure 23. Structure a)DTPA-HMD and b)DTPA-CHD linear polymers and evaluated the relaxometry properties of two Gd complexes [104]

Gd-DTPA-cytine copolymer (GDCP), and Gd-DTPA-cytine diethyl estercopolyemrs (GDCEP) with different molecular weights have been synthesized by Zong and coworkers, summarized in Fig. 24 [105]. GDCP exhibited more prolonged and contrast enhancement in blood pool and liver which was ascribed as higher molecular weight of GDCP, compared with those of GDCEP [105].

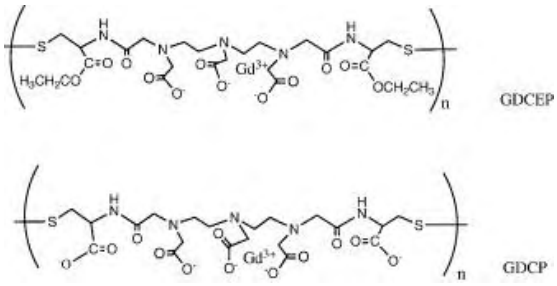

	GDCEP			GDCP		
Mw (kDa)	73	48	34	62	46	22
Gd content (wt.%)	16.9	17.7	16.9	16.7	17.1	16.4
Relaxivity ($mM^{-1}s^{-1}$)*	4.5	4.8	4.6	6.9	5.8	5.4

* at 3T and room temperature

Figure 24. Structure and physicochemical parameters of GDCP and GDCEP [105]

Furthermore, relaxivity of GDCP conjugated with different molecular weight of PEG has been studied [106]. It was observed that PEG chain length did not significantly alter r1 of GDCP. PEG_{2000}-GDCP exhibited the highest r1 of 8.73 $mM^{-1}s^{-1}$ at 3T [106]. The grafting of GDCP with PEG did not enhance the r1, which was attributed to high density of PEG chains [106].

B.1.2. Nano-polymeric macromolecular contrast agents

Different varieties of polymer carriers, either natural or synthetic, have been used as a platform for synthesis of various types of tumor imaging CAs or tumor therapy nanoparticles. Depending on the preparation route, the CAs or drug could either be entrapped in or covalently conjugated to the surface of the polymer platform, presented in Fig. 25. The synthetic polymer nanocarrires include polyethylene glycol (PEG), polyglutamic acid (PGA), poly-D,L-lactide-co-glycolide (PLGA), polylactic acid (PLA) and *N*-(2-hydroxypropyl)-methacrylamide copolymer (HPMA) [107]. The drawback of the majority of synthetic polymers is their non-biocompatibility, non-biodegradability and expensive cost in fabrication. The natural polymers which have been extensively used include chitosan, dextran,

albumin, heparin, and Sodium alginate [107]. Among the abundant natural polymeric nanocarriers, much attention has been focused on chitosan and its derivatives [108], [109].

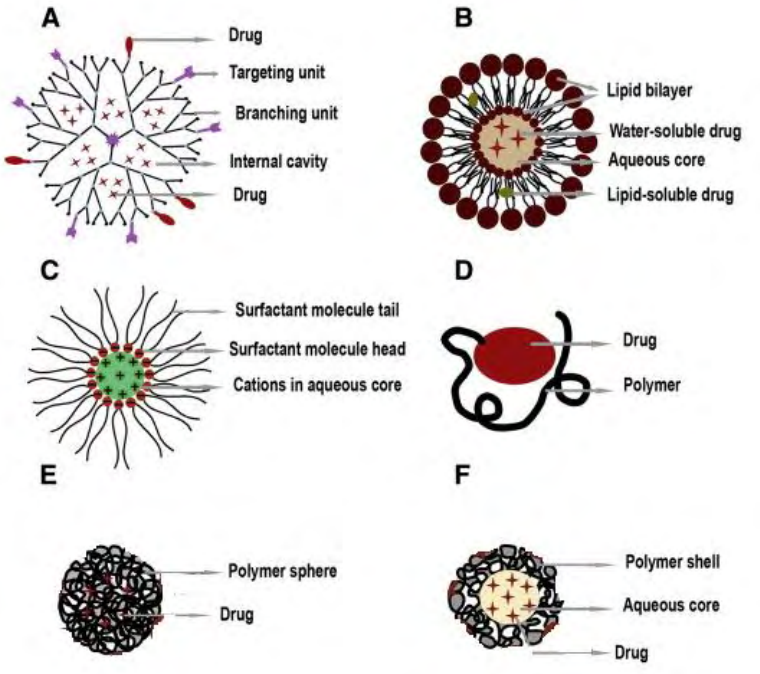

Figure 25. The classification of developed polymeric nanocarries A) dendrimer, B) liposomes, C) polymer-CAs conjugated, D) polymeric nanosphere, E) polymer core-shell nanoparticles [110]

B.1.2.1. Chitosan

Chitosan is one of the most promising polymers for pharmaceutical and biomedical area [108], [109]. Chitosan is a natural liner polysaccharide, composed of β-(1-4)-linked-2-amino-2-deoxy-β-D-glucopyranose and 2-acetamido-2-deoxy-β-D-glycopyranose, derived through partial deacetylation of chitin[111]. Chitosan nanoparticles (CNs) have been intensively investigated for drug delivery administration due to their unique properties such as biocompatibility, biodegradability, nontoxicity, antibacterial, and mucoadhesive properties [8], [9]. As mentioned before, chitosan can be obtained by modulation of the deacetylation degree of chitin. Therefore, chitosan with different molecular weight and deacetylation degree can be obtained while both of these parameters have an effect on their physicochemical and biomedical applications. By introducing hydrophobic moieties in to the chitosan backbone, it is possible to obtain an amphiphilic compound [112], which is useful to form the

nanoparticles. Thereby, the hydrophilic core of chitosan nanoparticles can efficiently encapsulate the drug.

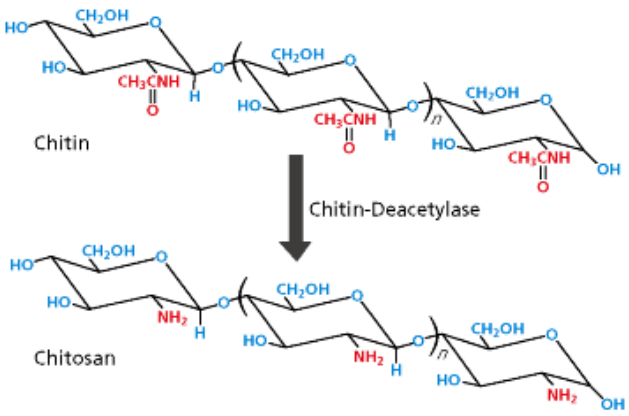

Figure 26. Fabrication of chitosan from chitin by modulation of deacetylation degree

The size, polydispersity, charge, as well as capacity for drug encapsulation of chitosan nanoparticles depend on the preparation method and chitosan structure such as molecular weight and deacetylation degrees. Thereby, due to the important role of physicochemical properties of the nanoparticle on its biomedical applications, in the next section the method used for synthesis of chitosan nanoparticles will be briefly described.

B.1.2.2. Protocol of chitosan nanoparticles preparation

For the first time, Ohya and colleagues demonstrated the intravenous delivery of an anticancer drug via chitosan nanoparticles which were synthesized via emulsification and cross-linking [113]. Thenceforward, much attention has focused on preparation of chitosan nnaoparticles. The methods employed to prepare CNs were emulsion-droplet coalescence, emulsion solvent diffusion, reverse micellar route, ionic gelation, and desolvation [114], as summarized in Table 3.

Table 3. Methods employed for fabrication of chitosan nanoparticles (CNs) [114]

Method	Matrix	Ref.
Emulsification and cross-lining	Chitosan, glutaraldehyde	[113]
Emulsion droplet coalescence	Chitosan	[115], [116]
Reverse micellisation	Chitosan, glutaraldehyde	[117]–[119]
Emulsion solvent diffusion	Chitosan	[120]
Ionic gelation	Chitosan, glutaralde	[109], [121]
Modified ionic gelation	Chitosan, acrylic acid, methacrylic acid, polyethylene glycol, polyether	[122], [123]
Desolvation	Chitosan	[124]–[126]

The ion gelation method is one of the most commonly used methods to fabricate chitosan nanoparticles due to its mild preparation conditions, hydrophilic environment, no organic solvents, and no high shear forces [114]. Referring to high protonation degree of amine groups of chitosan, the chitosan could form hydrogels in the presence of polyanion. Thereby, chitosan nanoparticles can be produced from inter and intra-molecular cross-linkage of bulk chitosan by ionic molecules. Calvo and coworkers have developed a very mild ionic gelation method to fabricate chitosan nanoparticles [109]. They have used polyanion tripolyphosphate (TPP) as ionic molecules to interact with positively charged amino groups of chitosan in acidic media. After adding TPP in the chitosan solution under mild stirring, the chitosan nnaoparticles are immediately formed. After 10 min of stirring, the reaction has fully completed and the suspension centrifugated to separate the nanoparticles from unreacted chitosan and TPP. In order to obtain small and monodispersed chitosan nanoparticles, there are some parameters such as stirring pattern, centrifugation condition, temperature, concentration of chitosan and cross-linker, and volume of resuspension, should be optimized [127]. Additionally, other factors also play an important role in the size of CNs [109], [121], [127]. For example, it has been reported that the size of CNs increase with chitosan concentration [123], and contrarily the cross-linker concentrations [128]. The recent work has shown that maintaining the reaction temperature below 4°C has significantly effect on average particle size of CNs [121]. This has been attributed to the reduction of CNs collision polarity due to the formation of hydration layer around nanoparticles via reducing temperature. This results in increasing hydrogen bonds between water molecules and chitosan polar groups, leading to the formation of hydration layer around the CNs [121].

B.1.2.3. Biodegradability, biocompatibility, biodistribution and toxicity of chitosan composites

As mentioned before, the unique features of chitosan which attracted much attention is its biocompatibility, biodegradability and biodistribution. Herein, these three key features of chitosan will be briefly discussed and reviewed.

The molecular weight of polymer for renal clearance should be in the range of 30 kDa – 40 kDa, while polymer with higher molecular weight should tolerate degradation either chemically or enzymatically [129]. Chemical degradation is attributed to acid catalyzed degradation. While enzymatical degradation depends on the structure of the polymer, for instance chitosan could be degraded via enzyme able to hydrolyze the linkages of glucosamine–glucosamine, glucosamine–Nacetyl-glucosamine and N-acetyl-glucosamine–N-acetylglucosamine [129]. Furthermore, for chitosan degradation, redox reactions and free-radical degradation could occur while they are unlikely to affect *in-vivo* degradation of chitosan [130]. Chitosan is known as a biodegradable polymer, predominantly via lysome and some colon bacterial enzymes [131]. The rate and extent of *in-vivo* chitosan biodegradability increase with decrease of chitosan deacetylation degree [132]. In General, chitosan in appropriate conditions and given enough time would sufficiently degrade. The degradation, distribution and elimination mechanism of chitosan are dependent on molecular weight of chitosan [133]. The two possible degradation sites for chitosan are referred to liver and kidney [129]. Oral administration of chitosan has revealed certain degradation in gastrointestinal tract [129].

Due to clinical tests of chitosan biocompatibility in normal conditions, no inflammatory or allergic reactions have been observed following implantation, injection, topical application or ingestion in human body [133]. Its *in-vitro* biocompatibility has been already proven in myocardial endothelial and epithelial cells [134], hepatocytes [135], and keratinocytes [136]. Furthermore, i*n-vivo* biocompatibility of chitosan for humans and mammals has also been proven [133].

Biodistribution of chitosan in body also depends on molecular weight, deacetylation degree, and the size of chitosan platform. For chitosan nanoparticles, the biodistribution and kinetics could be tuned via the size and charge of nanoparticles and not by chitosan chemical structure [129]. The chitosan with high molecular weight would be excreted without any absorption. Intraperitoneal administration of FITC-labeled chitosan has been studied [137]. It has been observed that the labeled chitosan predominately localized in kidney and they were absorbed

in peritoneal cavity [137]. Moreover, biodistribution of FITC-labeled chitosans with two different molecular weights of 3.8 kDa and 230 kDa have been studied [138]. it was observed that no uptake has been observed for higher molecular weight [138].

Furthermore, chitosan in known as one of the non-toxic, biologically compatible polymers [139]. No determinal toxicity of chitosan in mice has been reported by Rao and his coworkers [140]. As well, Richardson *et al.* have also reported the non toxicity of chitosan with different concentration and deacetylation degree [141]. LD50 of paclitaxel chitosan micelles in mice has been reported of 72.2 mg/kg, additionally; no anaphylaxis has been observed in guinea pigs [142]. In oral administration of 100 mg/kg chitosan (80 kDa and 80% DD) to mice, no toxicity has been observed [143].

B.1.2.4. Chitosan based MRI contrast agents

Referring to the high biocompatibility and biodegradability of chitosan compound, they have been extensively investigated for biomedical applications such as drug delivery, gene delivery, tissue engineering, antimicrobial and antiviral activity. Moreover, chitosan has an ability to prolong residence time in gastrointestinal tract via mucoadhesion. These properties as well as its cellular permeability property are the major factors for using chitosan in biomedcine. Since conjugation of contrast agents to chitosan composites could also extend CAs applications, in the following section the efficiency of chitosan-based CA for *in-vitro* and *in-vivo* application will be reviewed.

B.1.2.5. *In-vitro* MRI studies of chitosan-based contrast agent

The potential of chitosan-based CA as MRI contrast enhancement has been studied by some researchers. For instance, ultra-small $Mn_{1-x}Zn_{x}Fe_2O_4$ series ($0 <= x <= 1$) coated with chitosan have shown high r2 that increased from 69.4 $mM^{-1}s^{-1}$ to 118.2 $mM^{-1}s^{-1}$ with Mn content concentrations varied between x=0 to x=1 [144]. Chitosan-substitution with diethylenetriaminepentaacetic acid (DTPA) has been used as a Gd chelator to enhance the stability of complex on liposome surface [145]. The complex has exhibited high r1 of almost 6 $mM^{-1}s^{-1}$ at 3T which is attributed to the high number of Gd ions anchored on the liposome surface which improved water and Gd(III) interactions [145]. In another study, the efficiency of Gd-DTPA-CS as MRI CAs has been studied via Huang and his colleagues [146].

They have reported that r1 of Gd-DTPA-CS (11.65 $mM^{-1}s^{-1}$ at 32 °C and 0.5) is almost 3 times higher than r1 of Gd-DTPA [146]. The increase of r1 relaxivity has been ascribed to increase the number of inner sphere coordinated water molecules, the decrease of rotational correlation rate by attachment to chitosan, and the increase of water exchange rate [146]. Furthermore, the conjugated Gd- 1,4,7,10-tetraazacyclododecane-1,4,7,10-tetraacetic acid 1-(2,5-dioxo-1-pyrrolidinyl)ester (DOTA-NHS) to the surface of a water-soluble glycol chitosan (GC) has possessed high r1 of 9.1 $mM^{-1}s^{-1}$ at 1.41 T [147], [148]. On the other hand, the conjugation of Gd ions to the surface of CNs through diethylenetriamine pentaacetic acid (DTPA), using N-(3-dimethylaminopropyl)-N'-ethylcarbodiimide hydrochloride (EDC) and N-hydroxysuccinimide (NHS), showed r1 of 7.509 $mM^{-1}s^{-1}$ at 3T [149]. Furthermore, conjugation of Gd-based CNs to another macromolecular polymer has shown great potential as MRI CAs. For instance, poly-γ-glutamic acid (PGA)-folic acid conjugated to chitosan–Gd complex has shown a high efficiency (T1 of 244 ms at 1.5 T) [150]. The potential of chitosan functionalized with β- and γ-cyclodextrins (CDs) conjugated to DTPA-Gd has been reported as high as r1 of 8.9 $mM^{-1}s^{-1}$ at 20 MHz and 298K[151]. The significant enhancement of relaxivity has been reported for Lectin-DTPA–Gd conjugated with CNs with r1 of $1.47x10^{5}$ $mM^{-1}s^{-1}$ at 1.5T and 20°C [152]. In this complex, chitosan as well as protein complexes carrying paramagnetic chelates which reduced molecular mobility, leading to prolonged rotational correlation time that causes enhancement of proton relaxivity [153], [154]. The incorporated / conjugation of Mn-based CAs to chitosan have also been studied. For instance, Mn-DTPA-CNs in aqueous solution has showen high r1 relaxivity of 7.21 $mM^{-1}s^{-1}$at 0.5T and 32°C compared with those of Mn-DTPA [155]. The efficiency of iron oxide-coated with chitosan has been also reported. Efficiency of ferrite coated with chitosan have been evaluated via NMR spectroscopy while chitosan based nanoparticles possess r1 of 0.00291 $ppm^{-1}s^{-1}$ and r2 of 0.0691 $ppm^{-1}s^{-1}$ [156]. Further studies on conjugation of iron oxide on chitosan has been performed by Tsai et al. [157]. r1 and r2 relaxivities of iron oxide conjugated with chitosan have been evaluated of 22 $mM^{-1}s^{-1}$ and 202 $mM^{-1}s^{-1}$, respectively, via MRI 3T scanner [157]. The only published research regarding to efficiency of metalloporphyrin conjugated with CNs has been reported that water-soluble tetra(carboxyl phenyl)Mn(II)-porphyrin-CNs possessed a r1of 6.11 $mM^{-1}s^{-1}$[158].

B.1.2.6. *In-vivo* MRI studies of chitosan based contrast agents

The developed GC-NH2-GdDOTA (0.03 mmol/kg Gd) have been intravenously administered in nude mice with T6-17 flank tumors, shown in Fig. 27 [147]. Less than 4 hours after injection, great contrast enhancement was observed with the maximum after 2h postinjection while no contrast or very little was observed after 24h of postinjection [147]. No discernible enhancement within tumor in T1-weighted images revealed any tumor specificity of GC-NH2-GdDOTA [147]. The signal changes have been evaluated to study the relative signal intensity enhancement pre- and post-contrast T1-W MR images. After 2h of postinjection of GC-NH2-Gd-DOTA, signal intensity enhanced as high as 2.4 times [147]. Thereby, conjugation of Gd-DOTA to chitosan enhanced the signal and contrast of T1-weighted images.

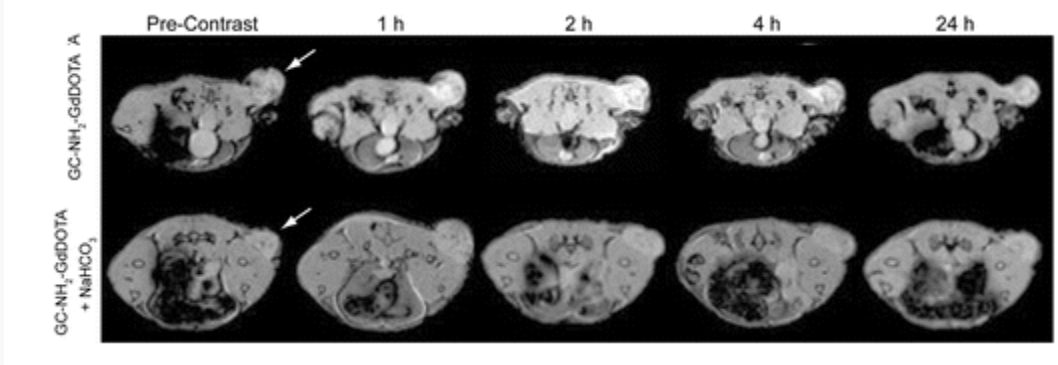

Figure 27. *In-vivo* MR images of mice with T6-17 flank tumors [147]

In another research, the efficiency of Gd-DTPA conjugated with chitosan as contrast enhancement in liver and kidney of rat has been studied [146]. It was observed that after short time of post intravenous injection of Gd-DTPA, contrast enhancement could be observed in rats' liver meanwhile after 30 min the signal intensity of liver decreased, conversely to the signal intensity of kidney [146]. This indicates the poor blood circulation and fast clearance of Gd-DTPA from kidney. Additionally, liver parenchyma blood vessels were not clearly observed after administration of Gd-DTPA [146].

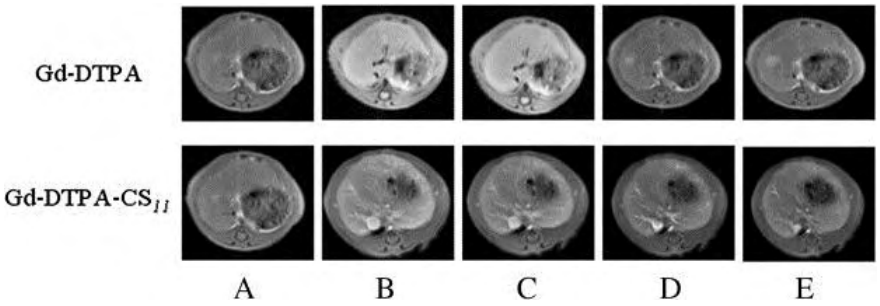

Figure 28. T1-weighted of rat liver postinteravenous injection of Gd-DTPA-CS (0.08 mmol/kg Gd) and Gd-DTPA (tail vein) into rat after A) 0 min, B) 5 min, C) 15 min, D) 30 min and E) 90 min [146]

As presented in Fig. 28, after short time of administration of Gd-DTPA-CS, signal intensity enhanced and the blood vessel of liver was visible [146]. It was observed that after 90 min still no contrast enhancement has revealed in kidney due to no excretion from liver into kidney in this period, Fig. 29 [146]. Thereby, conjugation of Gd-DTPA with chitosan enhances the blood circulation of CAs and increases the contrast and signal intensity in liver [146].

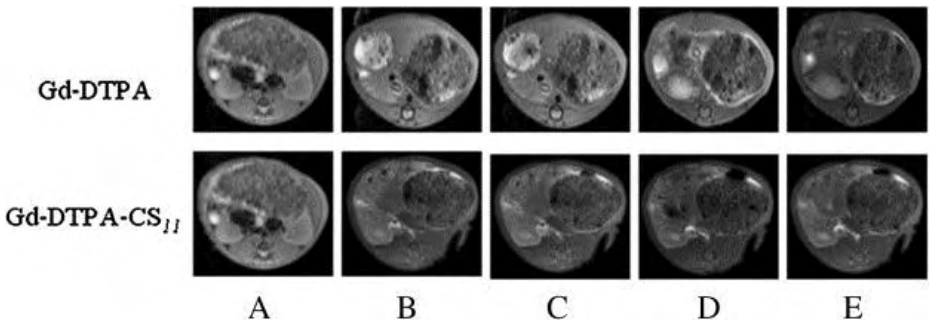

Figure 29. T1-weighted of rat kidney postinteravenous injection of Gd-DTPA-CS (0.08 mmol/kg Gd) and Gd-DTPA (tail vein) into rat after A)0 min, B) 5 min, C) 15 min, D) 30 min and E) 90 min [146]

C. Quantum Dots

Over the last two decades, experimental and theoretical research on quantum dots (QDs) has increased significantly in order to explore their characteristic properties. In 1982, Efros and Ekrimov were first to report the synthesize of QDs [159]. It was found that the band gap energy of QDs is size-dependent while bulk semiconductors band gap energy depends on their composition [160]–[162] as presented in Fig. 30. Thereby, controlling the size of QDs has an important impact on their fluorescence emission wavelength.

Quantum dots (QDs) are semiconductor nanoparticle clusters, which exhibit quantum confinement effects. They are composed of atoms from groups II-VI, or IV-VI of periodic Table with the size in the range of 2-20 nm. Their composition and small size, consisting of 100 to 100000 atoms per nanoparticles [163], give them extraordinary optical and electrical properties.

These compounds are highly florescent due to their excitation states/ band gaps. The quantum confinement of QDs enables them to emit light at different wavelength, which depends on the diameter of their core. The small gap of larger particles causes the emission of red light, while small particles emit blue light due to their large band gaps. Moreover, small particles act as a single molecule while all constituent atoms are excited and emitted light together. Hence, the intensity of resultant signals increase. Compared to organic florophores, small QDs particles exhibit high florescence efficiency as well as lack of photobleaching due to their long florescence lifetime (10-40 ns).

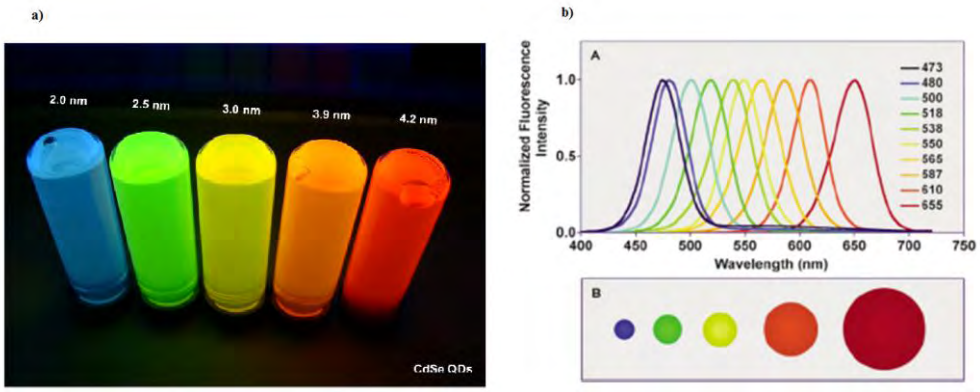

Figure 30. a) Different sized CdSe colloids irradiated with UV-visible light and emit different color light b)Emission wavelength of QDs at different particle size[164]

C.1. Importance of QDs

QDs possess characteristic properties, including high quantum yields, broad absorption band, high molar extinction, large effective Stoke shifts, narrow and symmetric emission bands, and high resistance to photobleaching and chemical degradation [165], [166]. Meantime, their electrical and optical properties can be tuned up by changing their size [167]–[169] and their compositions [170], [171]. By modifying the surface of QDs, they can also be applied as

active targeting, diagnostic or therapeutic agents [172]–[174]. They have attracted a great deal of interest in optical imaging and other imaging modalities such as PET and MRI. Controlling the shape and size with the desired geometries are the main challenge for the synthesis of QDs.

C.1.1. Synthesis of QDs

Several methods have been developed to synthesize QDs. Electron beam lithography, reactive-ion and wet chemical etching [175] are common methods to prepare QDs with diameter of about 30 nm while focused ion and laser beams have been utilized to fabricate zero-dimension dots [176]. The main drawbacks of the wet chemical and reactive-ion etching are the impurities incorporation into the QDs and structural imperfections [175].

Focused ion beam (FIB) technique makes possible to fabricate the QDs with extremely high lateral precision [175]. The surface of semiconductor substrate could be sputtered by highly focused beams from a molten metal source (e.g., Ga, Au/Si, Au/Si/Be, or Pd/As/B). Thus, the ion beam has play a major role on the shape, size and inter-particle distance of the synthesized QDs with a minimum beam diameter of 8–20 nm which allows obtaining the QDs with dimension of less than 100 nm [177].

Electron beam lithography followed by etching or lift-off processes is another method for fabrication of QDs [175]. The advantage of this approach is its high flexibility to design the nanostructure systems with any shape, precise separation and periodicity [175]. The III-V and II-VI QDs with diameter less than 30 nm have been successfully fabricated with this method [175].

Wet-chemical methods mainly pursue the conventional precipitation one while the solution or mixture of solution is carefully controlled during the synthesis. During the precipitation process, both nucleation and growth of nanoparticles is controlled. Wet chemical methods enable us to control the size, composition and shape of QDs [175]. Some parameters such as temperature, stabilizers or micelle formation, concentrations of precursors, ratios of anionic to cationic species and solvent have a strong effect on fabrication of QDs with wet chemical method [175].

Sol-gel technique is one of the most used method to synthesize small nanoparticles. In general, a metal precursor (e.g. alkoxides, acetates or nitrates) in an acidic or basic medium is prepared (sol) [175]. Hydrolysis, condensation (sol formation) and growth (gel formation) are the main three steps in sol-gel process [175]. CdS [178], ZnO [179]–[182], PbS [183] QDs

have been prepared via sol-gel method. Although, these methods have some advantages such as simplicity, low cost and suitable for scale-up, broad size distribution and a high concentration of defects are two main disadvantages of this method [183].

Microemulsion processes, categorized as normal microemulsion, *i.e.*, oil-in-water, or as reverse microemulsion, *i.e.*, water-in-oil, are popular methods for synthesizing QDs. In the reverse micelle process, two immiscible liquids (polar water and nonpolar alkane) are mixed and stirred to form emulsion [175]. Using surfactants such as Aerosol OT (AOT), cetyl trimethyl-ammonium bromide (CTAB), sodium dodecyl sulphate (SDS) or triton-X would lead to disperse nanometer water droplets in *n*-alkane solution [175]. The II-VI core and core/shell QDs, such as CdS [184], CdS:Mn/ZnS [184]–[187], ZnS/CdSe [188], CdSe/ZnSe [189], ZnSe [190] and IV-VI QDs have been successfully synthesized with reverse microemulsion technique[191]. Same as the other methods of fabrication, sol-gel technique shows some advantages such as the control of the QDs size with a narrow distribution, and its dispersion and disadvantages include low yield and incorporation of impurities and defects [175].

In 1993, Bawendi and colleagues for the first time explained the procedure of pyrolysis route for the production of QDs (~300°C) [192]. Precursors, such as alkyl [14], acetate [191], carbonate [191] and oxides [164,191] were mixed with phosphene or bis(trimethyl-silyl) precursors. In this method, trioctyl-phosphine oxide (TOPO, a coordinating solvent) dry at 200–350 ºC under vacuum (1 Torr) in a three-neck round flask. A mixture of precursor and tri-*n*-octyl-phosphine (TOP) selenide were simultaneously injected under vigorous stirring at ~300 ºC, which results in formations of homogeneous nucleation of QDs. The stabilizing of QDs dispersion is relating to TOPO solvent [175]. The majority of II-VI [193]–[197], IV-VI [198] and III-V QDs [199] have been synthesized via this technique. The size and shape of prepared QDs depends on some parameters including reaction time, temperature, precursors, solvents, type of coordinating agents and its purity degree [175]. Although, the relatively slow growth of the particles, the size series of QDs can be obtained from the same precursor bath [175]. Some of the disadvantages of this method are the high cost of fabrication, the toxicity of the organometallic precursors, and generally low dispersivity in water [175].

C.1.2. Ligand exchange approaches towards biologically compatible probes

Unfortunately, QDs are soluble only in nonpolar organic solvents, such as chloroform and hexane [200]. Various approaches have been developed to solublizing QDs. One of the most common method to water-solubilization of QDs is substitution of hydrophobic surface groups with hydrophilic one which is commonly achieved by replacing of the TOPO with bifunctional ligands which should possess the surface-anchoring group such as thiol [201], [202] and a hydrophilic end group such as carboxyl or hydroxyl [200]. Mercaptoacetic (MAA), mercaptopropionic (MPA) acids, and thiol-containing zwitterionic molecules, such as cysteine are the common ligands for functionalization of QD surface [200]. Regardless of the simplicity of thiol exchange procedure, the main challenge of using thiol as ligand is their tendency to quench fluorescence of QDs as well as its instability [203].

Liu et al. have accomplished to improve the stability of QDs (~11.4 nm) by using di-thiol ligands dihydrolipoic acid (DHLA) conjugated to poly(ethylene glycol) (PEG) [204]. However, they found that the fluorescence efficiency of obtained QDs decreased. Afterward, Sukhanova and co-workers have achieved to solubilize CdSe/ZnS core/shell nanocrystals in water with DL-Cysteine and improved its stability with poly(allylamine) [205]. Furthermore, Jiang et *al.* have enhanced the stability of ZnS-capped CdSe encapsulated with mercaptoundecanoic acid shell by covalently cross-linking neighboring molecules with lysine [206]. While, they have observed that the hydrodynamic radius of QDs colloids have dramatically increased from 8.7 to 20.3 nm due to shell cross-linking conjugation [206].

Using multifunctional and multidentate polymer ligands for coating CdTe QDs (with coating thickness in the range of 5.6 and 9.7 nm) leads to enhance its colloidal stability and photobleaching problem [207]. It has been found that grafting of balanced composition of thiol and amine coordination group into polymer chains could improve QDs colloids stability and overcome photobleaching as well as enhancing fluorescence quantum yields [207].

In another work, Gerion and colleagues have successfully embedded CdSe/ZnS core/shell QDs in siloxane shell and functionalized with either thiol or amine group [208]. In this procedure, silica/siloxane shell with thickness between 1-5 nm leads solublizing particles in polar solvent. Afterward, siloxane shell has been coated with bifunctional methoxy compounds, which shows highly stability against flocculation and great solubility in aqueous buffer. The only drawback of this approach is precipitation and gel formation of QDs colloids at neutral pH due to residual silanol groups on the QD surface[208].

Another alternative approach to transfer TOPO capped QDs from organic to aqueous solution is encapsulating of QDs with amphiphilic molecules, including polymers or phospholipids [209], [210]. Several QDs such as $CoPt_3$, CdSe/ZnS, and Fe_2O_3 have been successfully water-soloublized via this method [210]. Although the water-solublized of QDs via this method is stable with maintained optical efficiency, the hydrodynamic radius of nanoparticles dramatically increases because of deposition of several organic layers [211].

Ligand exchange method often yields compact probes which exhibit low stability and fluorescence efficiency, whereas polymer-encapsulation approach causes to have high stable and bright QDs with the large particle size [200]. With water solubilization of QDs, the number of QDs have already used in biomedical research. While up to now, no method can satisfy all the design criteria imposed by researcher [200].

C.2. QDs application in bioimaging

Over decades, a significant amount of research is focused at using QDs in biological imaging [212]–[219]. Previously, most of optical bioimaging was based on traditional organic dyes [220]. Instability of organic dye is a major obstacle in bioimaging. Furthermore, conventional dye molecules have a narrow absorption and excitation band which makes difficult the simultaneous excitation of multiple dyes [221], [222]. Quantum dots offer several advantages over organic fluorophores which were commonly used for *in-vitro* labeling [223]. Comparing with organic dyes, QDs absorb light more efficiently, and an individual QD is 10–20 times brighter than organic fluorophores. Moreover, QDs are more photostable (about thousands of times), more resistant photobleaching (about more than 30 min of continuous high-energy illumination) than organic dyes. Overall, QDs generally exhibit broad excitation windows but narrow emission peaks and less toxicity than conventional organic dyes; QDs have replaced conventional organic dyes for *in-vitro* and *in-vitro* imaging and diagnostic of live cell [205], [224], [225]. Referring to properties of QDs, QDs have shown great potential in bioimaging applications.

C.2.1. Application of Quantum dots as contrast enhancement of MR images

Referring to aims of my project, the potential of reported metal-doped QDs as MRI contrast agents will be reviewed in this section. Among the paramagnetic ion doped quantum dots (QDs), Mn-doped QDs have attracted much attention as MRI CAs while the majority of them are core/shell QDs. The potential of 3-5 nm of Mn-doped CdTe/ZnS colloids as MRI contrast agents has been studied by evaluating their relaxivities [226]. The r1 of Mn:CdTe/ZnS in aqueous solution at 3T increased from 5.4 $mM^{-1}s^{-1}$ to 10.68 $mM^{-1}s^{-1}$ with increase the Mn dopant concentration from 4.7% to 9.7%, respectively [226]. Furthermore, r1 of ultra small CdSe/Mn:ZnS QDs has been reported in the range of 11-18 $mM^{-1}s^{-1}$ at 7T and ambient temperature [227]. The high relaxivity of these complexes have been attributed to location of Mn ions on the shell of nanoparticles which causes slowing of the tumbling rotation and enhancing the interaction between Mn ions and water molecules [227]. It has been observed that r1 increased with the thickness of shell which was attributed to probability of higher Mn concentration localized in the shell [227]. Iron oxide-Mn:ZnS encapsulated with poly(lactic-co-glycolic acid) has been also studied as MRI contrast agents at 3T [228]. The signal T*2 of MR images decreased with increasing PLGA concentration while the concentration of Mn and Fe were constant [228]. Meantime, the signal intensity (T*2) decreased more rapidly with increasing iron oxide concentration at lower TE [228]. The r*2 of nanoparticles have been evaluated as high as 523 $mM^{-1}s^{-1}$ [228]. In the other study, the hollow MnO particles has shown the highest r1 of 0.2 $mM^{-1}s^{-1}$ and r2 of 7.48 $mM^{-1}s^{-1}$ [229]. While after coating with iridium $SiO_2$the relaxivity decrease to r1 of 0.17 $mM^{-1}s^{-1}$ and r2 of 1.67 $mM^{-1}s^{-1}$ [229]. By coating the MnO, the accessibility of water molecules diminished [229]. The MnO/SiO_2 grafted with PEG complex has showen high r1 of 13 $mM^{-1}s^{-1}$ at 0.81 MHz [230]. The high relaxivity of the compound was ascribed to high molecular weight of PEG for coating and its large size of 9.2 nm [230].

The efficiency of QDs doped with other metal ions has been also studied. For instance, 20 nm of ZnO-doped Er, Yb, Gd_x (x=1, 2, 3%) has shown great efficacy as MRI CAs with r1 varied between 23-168 $mM^{-1}s^{-1}$ for Gd(III) increased from 1% to 3% [231]. The high relaxivity of prepared nanoparticles has been attributed to the porous structure of nanoparticles which enhances the accessibility of water molecules to metal ions [231]. The potential of Gd doped ZnO as MRI contrast agents has been reported by Liu et al. [232].The strong T1 contrast

enhancement of Gd-doped ZnO colloids has been reported with r1 of 16 $mM^{-1}s^{-1}$ at 1.5T [232]. Furthermore, incorporation of Gd to CdS:Mn/ZnS has been yielding enhancement of relaxivity (r_1=20 $mM^{-1}s^{-1}$ and r_2=151 $mM^{-1}S^{-1}$ at 4.7 T), attributing to contribution of Gd and Mn as well as grafting QDs with rigid macromolecules to avoid free rotation [233]. Doping Gd into InP/ZnS quantum dots extend its application as MRI contrast agents as well as florescence agents [234]. *In-vitro* MRI studies of novel nanoparticles have proven its high efficiency as MRI contrast agents with the high r1 of 12.2 $mM^{-1}s^{-1}$ at 35 MHz [234]. Moreover, ZnS:Tb,Gd and ZnS:Er,Yb,Gd nanoparticles have shown high relaxivity of 39.4 $mM^{-1}s^{-1}$ and 57.8 $mM^{-1}s^{-1}$[235]. On the other hand, conjugation of Gd-complex on $CulnS_2$/ZnS quantum dots have exhibited the r1 of 3.72 $mM^{-1}s^{-1}$ at 7.0T [236]. The *in-vitro* MRI studies of silica nanohybrids composed of $CuInS_2$/ZnS and magnetite nanoparticles exhibited a high spin-spin relaxivity of 214 $mM^{-1}s^{-1}$ [237]. Europium doped gadolinium sulfide QDs synthesized via sonochemistry has been studied as photoluminescence and MRI contrast agents [238]. The nanoparticles in aqueous solution have shown r1 of 13.48 $mM^{-1}s^{-1}$ at 4.7T [238]. Computer simulations have been carried out in our work to understand the assemblies of Mn-ZnS molecules dispersed in water in terms of their structure and microscopic interactions between water molecule and Mn molecules.

D. Molecular dynamics simulation

The two main familiar computer simulation techniques are molecular dynamic (MDs) and Monte Carlo (MC) simulation. The MDs show great advantages over MCs due to gathering dynamical information of systems as well as high accuracy. Molecular dynamic has emerged as one of the indispensable numerical techniques since 1957. Alder and Wainwright firstly introduced MD technique to investigate interaction of hard sphere [239]. Later on, liquid argon was simulated using a realistic potential by Rahman in 1964. In 1974, Rahman and Stillinger for the first time simulated the realistic system (liquid water) with molecular dynamic simulation [240]. Since then, MDs become a valuable tool in many disciplines such as physics, chemistry, materials science, etc. MDs can be categorized in two main families such as classical and quantum mechanics. In classical mechanics, the atom is considered as a ball, which is bonded together with elastic sticks and dynamics of the system is simulated by applying classical mechanics laws. The second category, quantum mechanics, the quantum nature of chemical bonds is taken into account. In this method, quantum equations are carried

out to determine the bonding in system whereas dynamics of ions is calculated using classic equations. MD is a numerical method for particle tracking by generating the trajectories of the system. For tracking of particles, appropriate interatomic potential and suitable initial and boundary conditions are required. Then, trajectory of N particles is obtained from integration of Newton's equations of motion. The simple algorithm of MD is presented in Fig. 31.

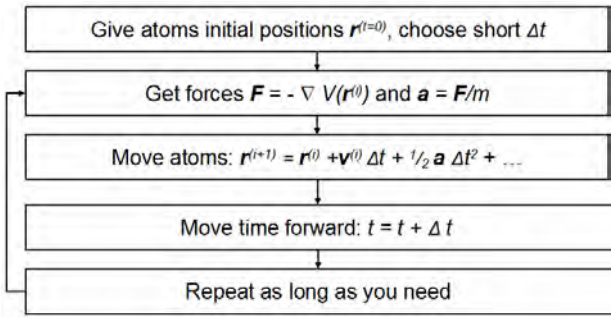

Figure 31. Algorithm of molecular dynamic simulation

Figure 32 represents the MDs system contains N particles. At any instant, the particle coordinates' are defined as $r^{3N} \equiv \{r_1(t), r_2(t), \ldots, r_N(t)\}$ while r_I is the coordinates of atom i. At time $t=t_0$, the system is in its initial configuration. As the simulation runs, particles in system evolve through a sequence of timesteps (Δt), typical values $\sim 10^{-15}$ s. The internal energy of system is defined as follows

$$E = K + U = \sum_{i=1}^{N} \frac{1}{2} m_i \left| \dot{x}_i(t) \right|^2 + U(x^{3N}(t)) \tag{21}$$

After running simulation, the system reaches the desired condition. Then properties of system such as radial distribution, thermal condition, energy, etc of the system averages over time. One of the most important results extracted from MDs is radial distribution. Radial distribution is the probability of finding particles at a distance r from a reference particle. The RDF of the system is calculated as follows

$$g_{ab}(r) = \frac{\sum_{k=1}^{M} N_k(r_{ab}, \Delta r)}{M(\frac{1}{2}N)\rho V(r_{ab}, \Delta r)} \tag{22}$$

While N_k is number of atoms at time k in a spherical shell dr, and ρ is average of density. From integration of RDF over dr, average coordination number of particle from reference particle can be evaluated.

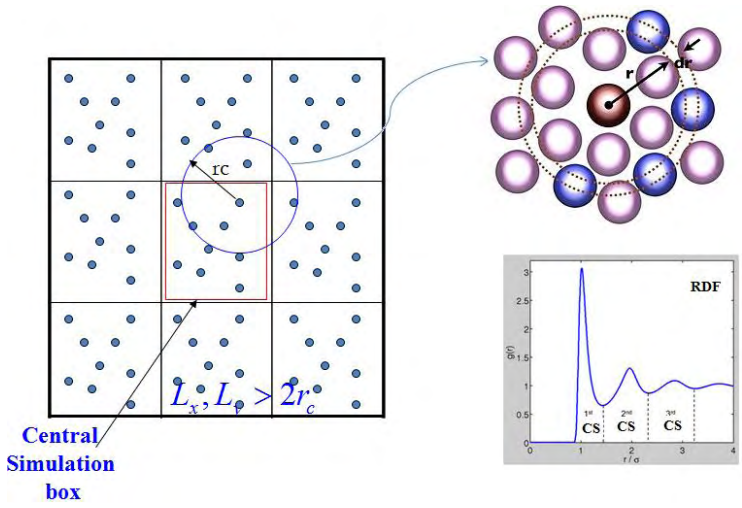

Figure 32. Schematic explicits simulation box and radial distribution evaluated

D.1. Simulation Set-up and procedure

Among all available softwares for MDs, DL_POLY and LAMMPS are the most popular ones. The five important gradients required for MDs can be listed as follows, initial condition, boundary condition, force evaluation, and integrator/ thermodynamic ensemble. The first step is initialization of atoms and choosing the suitable boundary conditions. Two main boundary conditions are isolated and periodic boundary conditions. Isolated is ideally suited for cluster while periodic boundary is used mostly for liquids and solids. Particles in isolated boundary condition interact among themselves and no interactions with outside. In periodic boundary, particles are kept track in a super cell while surrounded by infinite replicas. Thus, some particles might not interact with particles in same super cell, they interact with particles in an adjacent image of the super cell.

Secondly, interaction should be identified by applying the appropriate force field. The interaction between atoms can be determined as inter and/or intratomic interactions. The interatomic potential is a critical parameter in MDs. It controls the simulation and accuracy of results obtained. The major challenge in MD is finding the appropriate potential for

describing the interaction between atoms of the system. The energy of the system can be considered as follows

$$E = \sum V_1(r_i) + \sum V_2(r_i, r_j), \sum V_3(r_i, r_j, r_k) + ... + \sum V_N(r_i, r_j, r_k, ..., r_N) \quad (23)$$

While r_i, r_j, r_k,…,r_N are the particle positions and V_1,V_2,V_3,…, V_N are m-body potentials. The most used inter and intratomic potentials in DL_POLY are listed in Table 4.

Thermodynamic ensemble is playing an important role for MDs. The ensemble is the group of atoms, which have same macroscopic state but in different microscopic states. The microstate of group of atoms can be defined in terms of thermodynamic quantities such as number of atoms N, pressure P, temperature T, volume V, etc. The common ensemble used in MDs are microcanonical ensemble (NVE), canonical ensemble (NVT), isobaric isothermal ensemble (NPT). In NVE, the system is isolated while total energy, number of atoms, and volume of ensemble are constant. This thermodynamic ensemble is commonly used to represent the possible atom states without controlling pressure or temperature of system. The canonical ensemble (NVT) is applied to control temperature of the system during simulation. The volume and number of atoms remain constant throughout the run. Finally, NPT allows us to control pressure and temperature of system.

In the next step, we have to choose an appropriate algorithm for integration of Newton's motion equations for positions and velocities at time t and after t+Δt (Δt is the timestep, in the range of 10^{-15}s). Many numerical algorithms have been developed for integration of the Newton's equation; Velvert being the most popular. Positions, velocities and accelerations of particles is approximated in Velvert algorithm scheme via Taylor series expansion

$$\begin{aligned} r(t+\Delta t) &= r(t) + \dot{r}(t)\Delta t + \frac{1}{2}\ddot{r}(t)\Delta t + ... \\ v(t+\Delta t) &= \dot{r}(t) + \ddot{r}(t)\Delta t + \frac{1}{2}\dddot{r}(t)\Delta t^2 + ... \\ a(t+\Delta t) &= \ddot{r}(t) + \dddot{r}(t)\Delta t + \frac{1}{2}\ddddot{r}(t)\Delta t^2 + ... \end{aligned} \quad (24)$$

While r, Δt, v, $\dot{r}$ are position, timestep, velocity and acceleration, respectively. $\dddot{r}, \ddddot{r}$ are the third and fourth time derivation of position. For Leapfrog velvert, velocity leaps over the positions and vice versa. Thereby, positions and velocities are not known at the same time. The velocities are explicitly calculated. However, positions, velocities and accelerations in velocity velvert algorithm are newly calculated at each time.

Table 4. List of most used potential developed in DL_POLY

Intramolecular potential		
Core-shell		$U(r)=\frac{1}{2}kr_{ij}^2$
Tethering potential	Harmonic	$U(r)=\frac{1}{2}k(r_i-r_i^{t=0})^2$
Bond potential	Harmonic	$U(r)=\frac{1}{2}k(r_{ij}-r_0)^2$
	Morse	$U(r)=E_0\{1-\exp(-k(r_{ij}-r_0))\}^2-1$
	12-6	$U(r)=(\frac{A}{r_{ij}^{12}})-(\frac{B}{r_{ij}^6})$
	Lennard-Jones	$U(r)=4\varepsilon\left[(\frac{\sigma}{r_{ij}})^{12}-(\frac{\sigma}{r_{ij}})^6\right]$
	Buckingham	$U(r)=A\exp(-\frac{r_{ij}}{\rho})-\frac{C}{r_{ij}^6}$
	Coulomb	$U(r)=k^{Electrostatics}(r_{ij})(=\frac{k}{4\pi\varepsilon_0\varepsilon}\frac{q_iq_j}{r_{ij}})$
Angle Potential	Harmonic	$U(r)=\frac{1}{2}k(\Theta_{ij}-\Theta_0)^2$
Dihedral Angle Potentiel	Cosine	$U(\phi)=A[1+\cos(m\phi-\delta)]$
	Harmonic	$U(r)=\frac{1}{2}k(\phi_{ij}-\phi_0)^2$
Intermolecular Potential		
Van der Wals	Tabulated	
	Buckingham	$U(r)=A\exp(-\frac{r_{ij}}{\rho})-\frac{C}{r_{ij}^6}$
	12-6	$U(r)=(\frac{A}{r_{ij}^{12}})-(\frac{B}{r_{ij}^6})$
	Morse	$U(r)=E_0\{1-\exp(-k(r_{ij}-r_0))\}^2-1$
Metal	EAM (embedded-atom method)	Tabulated potential
Three body potential	Harmonic	$U(r)=\frac{1}{2}k(\Theta_{ij}-\Theta_0)^2$
Four body potential	Harmonic	$U(r)=\frac{1}{2}k(\phi_{ij}-\phi_0)^2$
External Filed	Electric	$F=qE$
	Magnetic	$F=q(vxH)$

The system should be relaxed from its initial condition to its natural equilibrium condition by choosing appropriate force field, and long enough time of simulation, and thermodynamic ensembles. After reaching the equilibrium condition of the system, the results obtained can be treated and visualized.

D.1.1. Molecular dynamic simulation of ZnS and ZnS-doped nanoparticles

ZnS is one of the most extensively investigated semiconductor materials. ZnS in nature can be found in two crystal structures such as zinc-blend (cubic) and/or wurzite (hexagonal) phases while solid-solid phase transition can occur under different conditions, including pressure [241], temperature [242], environment [243], and aggregation [244]. At standard temperature (~30°C) and pressure, ZnS structure remains sphalerite (cubic). In the sphalerite phase, both Zn and S atoms are coordinated tetrahedrally with three-layer repeat ABC. On the other hand in wurzite structure, which is more stable at high temperature (1020°C) due to high internal energy, ZnS dimers are close packed with a ABAB arrangement [245]. Physical, mechanical and opto-electrical properties of ZnS nanoparticles change with transformation of phase. Hence, study and/ or prediction of ZnS stability structure under different conditions have been investigated to shed light on dominant factors on phase transformation. In order to support the experimental results and obtain stepwise observations, classical MD simulations have been performed to investigate ZnS structure.

In 1995, Wright and Jackson have developed shell potential to simulate ZnS nanoparticles [246]. The interatomic potentials used to describe ZnS atomic interactions were shell and Buckingham potentials. Firstly, they assumed S atoms have a neutral shell connecting to a core with atomic charges of -2 (M1). Secondly, both Zn and S atoms were assumed to have a core and a shell (M2). Thirdly, both S and Zn have core and shell and three-body potential was added to improve the results obtained (M3), summarized in Table 5.

All three methods show good results, whilst the closest to experimental results has been obtained from M3. From M3 potential parameters, it is possible to reproduce ZnS polymorphs, sphalerite, and wurzite phases. Defect and activation energy of atomic migration of sphalerite ZnS structure have been calculated by Wright *et al.* [247]. It has been observed that the surface {110} of sphalerite has the lowest energy and type III surface such as {111} could be stabilized by introducing point defects [247]. Moreover, they have reported that Zn diffusion occurred because of the interstitial mechanism whilst S atoms diffuse because of vacancies in host lattice. Referring to higher defect formation energy of wurzite compared with sphalerite one, wurzite phase has shown much higher activation energy [247].

Table 5. Potential parameters developed by Wright and Jackson for model ZnS structure and comparing experimental and calculated structural results [246]

Potential		(M1)	(M2)	(M3)	(M1)	(M2)	(M3)	(M1)	(M2)	(M3)
Buckingham		A			ρ			C		
	Zn-S	613.356	539.45	528.899	0.399	0.4099	0.4111	0	0	0
	S-S	1200	1200	1200	0.149	0.149	0.149	120	120	120
		K								
Shell	S-S	12.7	18.8	16.86						
	Zn-Zn	0	3.52	2.181						
		K			Θ					
Three-body	S-Zn-S	----	----	0.713	----		----			109.47

Results (sphalerite)	*a*(Å)	*V*(Å^3)	C_{11} (MPa)	C_{12} (MPa)	C_{44} (MPa)
Experimental	5.41	158.297	9.42	5.68	4.36
Simulated (M3)	5.407	158.10	9.17	5.82	4.4

Further investigation on aggregation, coursing and transformation in ZnS nanoparticles have been performed by Zhang and Banfield in 2004 [248]. For this purpose, 3 nm unrelaxed ZnS nanoparticles have been placed in the corner of tetrahedron and one in the center with the distance of 30.5 Å, presented in Fig. 33I. During the simulation, these nanoparticles have been randomly oriented with respect to the interatomic potential developed by Wright and Jackson [247]. The system after 1.1 ns did not reach the equilibrium state, Fig. 33II. After 10 ps, nanoparticles relaxed due to surfaces atom rearrangement. After relaxation of nanoparticles, the nanoparticles aggregation started to form because of translational and/or rotational movement of nanoparticles, up to 235 ps. Furthermore, atomic diffusion crystallization of nanoparticles upon each other causes coarsening of particles. The size of particles after coarsening becomes 5 nm in diameter with a close-packed periodic layer on the surface and wurzite structure in center, Fig. 33III. They have reported that during last 1 ps the majority of Zn or S atoms moved while the fast moving atoms were located on the surface of particle, Fig. 33IV. They have observed that diffusion of atoms on the surface is much faster than in the bulk which affect the structural transformation, aggregation, and coarsening of particles [248].

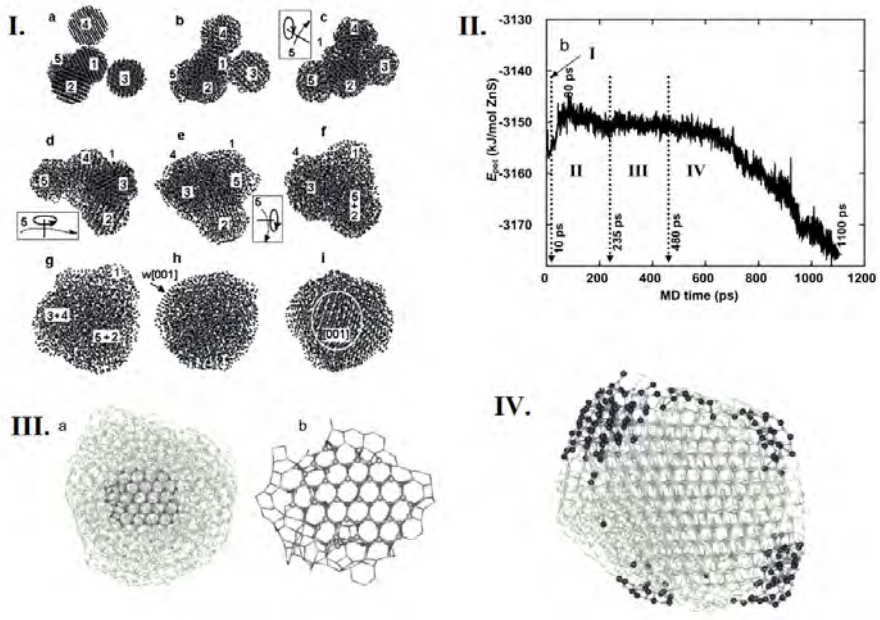

Figure 33.I. Snapshot of particle during simulation: a) 0 ps, b) 13.8 ps, c) 16.3 ps, d) 28.8 ps, e) 41.3 ps, f) 78.9 ps, g) 167 ps, h) 479.5 ps, i) 1100 ps, II. Potential energy of system during MDs time, III. Enlargened snapshot of particle at 479.5 ps, IV. Black balls are atoms with high mobility in the last 1 ps [248]

Wrigth and Gale have developed the more complicated potential to model $Zn_xCd_{x-1}S$ with sphalerite and wurzite structures [249]. The interatomic potentials used to model CdZnS structure in wurzite and sphalerite phases are listed in Table 6. They have reported that four-body potential is a crucial potential to correct the phase stability of ZnS and it is impossible to stabilize sphalerite over wurzite phase in the absence of tortional potential [249]. Sphalerite is the most favorable crystal structure of ZnS in standard condition, while for CdZnS hexagonal is more stable. In solid solution of $Zn_xCd_{1-x}S$, transition from hexagonal to sphalerite has occurred at x=0.6. In 2009, Wright has described the potential parameters for ZnS nanoparticles doped with Cd, Mn and Fe ions in vacuum [250], as listed in Table 6. The atomistic simulation technique based on Born model has been carried out to describe the interaction between ions in system. From simulation, the impurities have a great tendency to replace at Zn sites rather than interstitially entering to system. They reported that the impurity could be located as isolated ion at low concentration causing slightly lower the defect energy especially when the dopant atoms are distant from each other. Above 30% concentration, the impurities are mostly located at adjacent sites. Moreover, concentration of Fe and Mn dopant atoms has no impact on surface energy of crystal structure. However, surface energy increases with Cd concentration especially at surfaces with high density of Zn sites such as (111) and

(110) surfaces. At surfaces with low ZnS site density, large Cd atoms have more space which is the reason to observe less enchantment of surface energy [250].

Table 6. Interatomic potential values used for study incorporation of Cd, Mn, and Fe ions into ZnS sphalerite [249],[250]

Potentials	parameter values	Atomic pairs				
Buckingham		Zn-S*	Cd-S*	Mn-S	Fe-S	S-S
	A (eV)	672.288	1240.9518	750.686175	782.4698	1200
	ρ (Å)	0.39089	0.371852	0.390889	0.385720	0.149
	C (eV/Å^6)	0	0	0	0	0
	Cut-off	12	12	12	12	12
Three-body		S-Zn-S*		S-Cd-S*		
	K (eV/rad^2)	9.42834x10^6		3.59468x10^7		
	Θ (°)	109.47		109.47		
	ρ_1/ ρ_2	0.3		0.3		
Torsion		Zn-S-Zn-S*				
	K (eV)	0.005				
	m/n	+1/+3				
	r_{min}(Å)	2.5				
	r_{max}(Å)	3				
Core-shell		S-S*				
	K (eV/Å^2)	13.302743				

* Potential parameters used to model CdZnS bulk structure

D.1.2. Molecular dynamic simulation of ZnS and ZnS-doped nanoparticles in solution

Classical molecular dynamic simulations are a common numerical method to investigate the system in aqueous solution over long time scales (over nanoseconds). However, this method is still at an early stage. Study of the interaction of nanoparticles with water molecules in many biological processes is received much attention due to the importance of understanding nucleation of nanoparticles from water solution. Semiconductor nanoparticles and their interaction with water molecules have already been studied via molecular dynamic simulation.

For instance, stability of different sized ZnS nanoparticles (2, 2.5, 3, 4 and 5 nm) with sphalerite and wurzite initial structures surrounded with different number of water molecules have been studied numerically and experimentally [244]. The numerical simulation of ZnS has been performed by using the shell model plus Buckingham and three-body potentials at 300 K using Nose-Hoover algorithm with time step of 0.5 fs. Different models such as shell, CVFF (consistent values from force field), and SPC/E (extended simple point charge model) have been used for water molecules MDs. Among these models, they have reported that the

shell model presented best compatibility with shell ZnS model. From MDs of model particles, loss of initial configurations in vacuum was observed while crystallinity increased following water binding, as presented in Fig. 34. The increase of crystallinity with lower water coverage was referring to the strong water interactions with surface of ZnS. From MDs results, they reported that binding polar water molecules to Zn or S ions in the surface would increase crystallinity and showing residual surface stress [244].

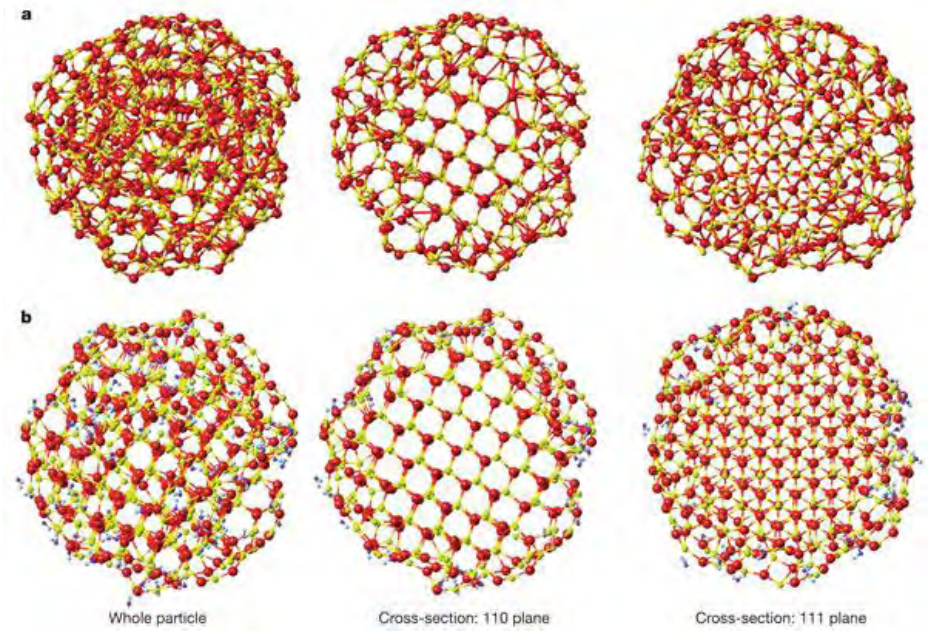

Figure 34. 3D snapshot of ZnS 3 nm MDs a) in vacuum, and b) with surface-bound water S atoms yellow, Zn red, O blue, H light blue [244]

Formation of cluster ZnS in aqueous solution has been studied by Said *et. al* using molecular dynamic simulation [251]. They have investigated the influence of temperature and water concentration on formation of ZnS clusters. The Zn and S ions randomly placed in the box of water (ρ~0.977 g/cm^3) at room temperature. The pre-equilibration was achieved after 40 ps while Zn and S ions are fixed and water molecules moved. Afterward, all atoms in the system are free to move during 20 ps to reach the equilibrium condition. The ZnS interatomic potential was the same as reported by Zhang [244]. The additional thermostat to control the temperature of system is applied with introducing the friction constant of 15 au/ps. For formation of ZnS cluster, temperature increased to 3000 K for 50 ps then decreased every 10 K to reach 300 K [252]. The interaction between water and ZnS clusters was modeled using Buckingham and Lennard-jones potentials. At 300K, every Zn atom coordinated with 6 water molecules. On the other hand, S atoms do not form a stable complex by interacting with water

molecules. However, Zn-S pair in a distance of 4.6 Å forms a stable complex in solution. Forming cluster of ZnS has been observed while some atoms jump the barrier. After first cluster formation, growing cluster is easy. Due to results obtained from simulation, the most stable ZnS cluster forms at $(ZnS)_6$-$(ZnS)_{47}$ which forms a hollow cluster.

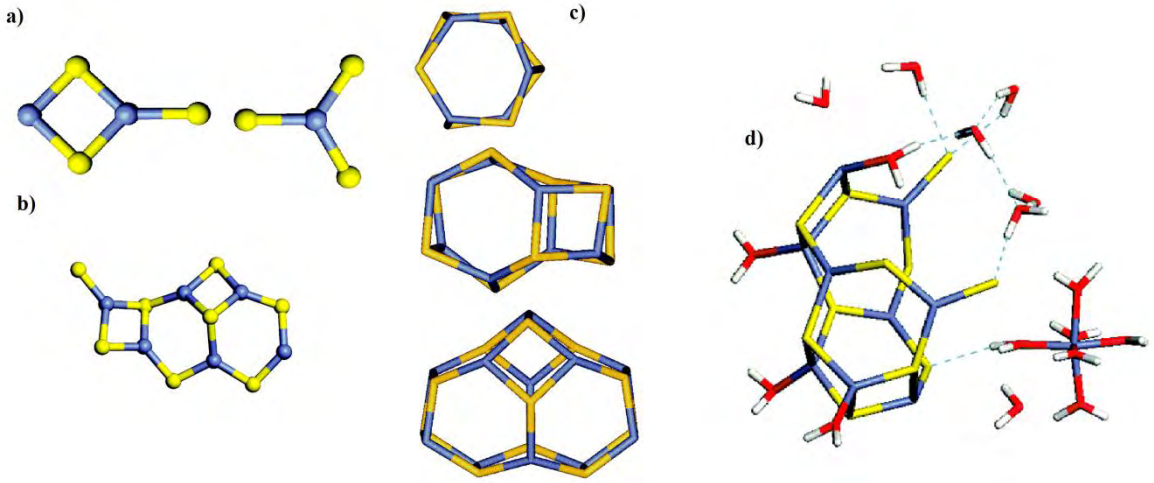

Figure 35. a) ZnS_3 and Zn_2S_3 first cluster formed, b) Zn_6S_8 cluster after 1.5 ns, c) cluster formation at 500 K, d) Zn_9S_{11} bubble cluster after 6 ns. Yellow stick : S; blue stick : Zn; red sticks : O; and white sticks : H [251].

Chapter IV: Material and Methods

In this chapter, firstly synthesis and characterization of metallated porphyrin is presented. Secondly, conjugation of metallopoprhyin with chitosan nanoparticles via passive loading and chemical conjugation is described following with characterization. For the second thematic part of the thesis, synthesis and characterization of Mn:ZnS QDs will be explained in detail. Finally, the simulation procedures for modelling of MnZnS nanaoparticles in aqueous solution (water) will be indicated.

A. Synthesis of Porphyrin

A.1. Chemical materials

Pyrrole (reagent grade, 98%), benzaldehyde (≥99.5%), dichloromethane, boron trifluoride diethyl etherate (≥46% BF_3 basis), trifluoroacetic acid (99%), 4-chloroaniline (98%), 2,3-dichloro-5,6-dicyano-1,4-benzoquinone (98%), manganese meso-tetrakis (4-sulfonatophenyl) porphyrin Mn(TSPP) (cat. No. 441813), silica gel, gadolinium acetylacetonate hydrate (99.9%), and 1,2,4-trichlorobenzene analytical standard were purchased from Sigma-Aldrich. The Gd-Dota (Gd-1,4,7,10-tetraazacyclododecane-1,4,7,10-tetraacetic acid) was obtained from laboratory Andre Guerbet, France.

A.2. Metallation of meso-tetrakis(4-pyridyl)porphyrin with Gadolinium (Gd(TPyP))

Meso-tetrakis (4-pyridyl) ($TPyPH_2$) free-base porphyrin was synthesized and purified following the Lindsey procedure [50]. The gadolinium meso-tetrakis(4-pyridyl) porphyrin were synthesized according to the method developed by Adler [253]. The solution of ($TPyPH_2$) (0.26 g, 0.3 mmol) was heated with an excess of gadolinium acetylacetonate hydrate (0.34 g) in 190 mL of 1-,2-,4- trichlorobenzene under argon at 245°C. The reaction was followed and stopped after 80% disappearance of the visible Qv peak (513 nm) by checking the UV-visible spectra of the metal ion porphyrin. The product was filtered with alumina gel and then purified by column chromatography with alumina gel and eluted with the mixture of dichloromethane and methanol varied between 0 to 5%.

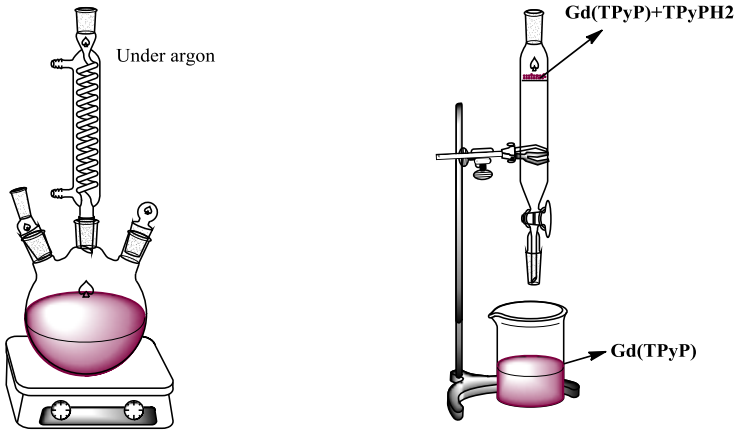

Figure 36. Schematic of Gd(TPyP) synthesis procedure

A.3. Colloid preparation

In order to prepare the colloids of metalloporphyrin complexes, different weighted amount of commercial Mn(TSPP), and Fe(TMPyP) were dissolved in 1mL of deionized water while synthesized Gd(TPyP) were dispersed in 1mL of ethanol because of its scarcely water solubility. Referring to Table 7, concentrations of Fe(TMPyP) and Mn(TSPP) were in the range of 1mM to 10 mM and 0.1 mM to 1 mM, respectively. The Gd(TPyP) concentration varied between 0.1 mM up to 1mM.

Table 7. Weighted amount and concentration of metalloporphyrins

Product	Mn(TSPP)				Fe(TMPyP)				Gd(TPyP)							
Weighted amount (mg)	0.1	0.3	0.5	1	0.9	1.8	3.1	9.1	0.09	0.18	0.27	0.36	0.45	0.54	0.72	0.9
Concentration (mL)	0.1	0.3	0.5	1	1	2	3	10	0.1	0.2	0.3	0.4	0.5	0.6	0.8	1

Dilution of commercial Gd-Dota 500 mM solution was performed in dionised water and in the mixture of ethanol/water. It has been known that ionic contrast agents such as Gd-DTPA and Gd-Dota were crystallized when mixing with 100% ethanol [254]–[256]. Thus, in order to avoid crystallization, Gd-Dota was diluted with 94% ethanol and 6% water in glass vials, as described in [255]. After dilution, the glass vials were placed in an ultrasonic bath for 20 minutes. The concentrations of diluted Gd-Dota in water and in the mixture were in the range of 0.6 -30 mM and 1-9 mM, respectively.

A.4. Characterization

A.4.1. UV-visible spectroscopy

The metallation of TPyPH2 was studied using ultraviolet- visible spectroscopy (UVIKON XL spectrometer). The small quantity of TPyPH2 and Gd(TPyP) porphyrins were dispersed in ethanol. One milliliter (mL) of porphyrin colloid was put in the rectangular quartz cuvette with 1 cm pathlength.

A.4.2. Matrix assisted laser desorption/ionisation (MALDI)-TOF mass spectrometry

Molecular mass of synthesized Gd(TPyP) was investigated by Matrix-Assisted Laser Desorption/Ionisation time-of-flight mass spectrometry (MALDI TOF, Applied Biosystem Voyager-De Str). Dichloromethane was chosen as a matrix solvent.

A.4.3. Fourier transmission infrared spectroscopy

Fourier transmission infrared spectroscopy (FT-IR, Bruker IFS 66 spectrometer) of $TPyPH_2$, and Gd(TPyP) powder were carried out over the range of 4000-800 cm^{-1} using 10 scans.

A.4.4. NMR relaxometry

r1 and r2 of prepared Gd(TPyP), Mn(TSPP) and Fe(TMPyP) colloids were evaluated via the Minispec NMR spectrometer (Bruker instruments, Mq20, Germany) at 20 MHz (B_0=0.47 T). The temperature of system was fixed at 40°C. Data were acquired via minispec mplus software. The longitudinal relaxation times (T1) were measured using an inversion-recovery sequence. Ten inversion recovery times ranging from 10 ms to 5T1 of solution (10-1500 ms). T2 relaxation times have been determined by employing the Carr-Purcell Meiboom Gill sequence. The acquisition parameters were set as follows: pulse separation (τ)=1 ms, recycle delay=1.5 s, and number of echoes= 1000 with an echo time of 2ms. The tubes filled with metalloporphyrin colloids were preconditioned in a bath reservoir for 20 minutes in order to equilibrate the temperature at 40°C. The real temperature of the probe head sample (37°C) was measured by a calibrated thermometer. Data processing was performed with XWIN-NMR Bruker. The T1 and T2 of metalloporphyrin and Gd-Dota in aqueous media were

determined by monoexponential fitting of NMR free induction decay (FID) signal intensity to equations 26 and 27, respectively

$$S = S_0(1-2\exp(-\frac{t}{T_1})) \tag{25}$$

$$S = S_0 \exp(-\frac{t}{T_2^*}) \tag{26}$$

r1 and r2 relaxivities have been obtained from the linear least square regression of inverse of relaxation time versus the concentration of paramagnetic ions as bellow

$$\frac{1}{T_{i(obs)}} = \frac{1}{T_{i(dia)}} + r_i C \quad i=1,2 \tag{27}$$

Where $T_{i(obs)}$ and $T_{i(dia)}$ are respectively the relaxation times of aqueous solution (s^{-1}) and relaxation times of the solvent (s^{-1}), C is the concentration of paramagnetic ion ($mmol^{-1}$) and r_i is the paramagnetic relaxivity ($mmol^{-1}.s^{-1}$).

A.4.5. Magnetic Resonance Imaging

Magnetic resonance imaging (MRI) of metalloporphyrins and Gd-DOTA colloids were acquired with MRI scanner (Philips ACHIEVA 3.0T TX) at 3T and 25°C. The longitudinal and transverse relaxivities of prepared colloids were evaluated from obtained images. The T1 weighted images were obtained from spin echo sequence by keeping the echo time TE of 8 ms and varying repetition time TR (100-400 ms). For T2 weighted images, the spin echo sequence was used keeping the long repetition time TR=1500 ms and varying echo time TE (7ms - 40 ms).The other parameters were optimized such as: field of view (FOV)= 154x154x5, slice thickness=5 mm, flip angle=90°, number of signal averages= 7, and voxel=1x1x5 mm^3. The high resolution T1 and T2 weighted images were obtained from spin echo sequence (TR=400 ms and TE=8 ms) and (TR=1500 ms, TE=40 ms), respectively. After image acquisition, the magnitudes of signal intensities within region of interest (ROI) were inferred manually by ImageJ software. The MRI signal intensity was fitted on a voxel basis with a monoexponential function $S_I = S_0.(1-\exp(-\frac{TR}{T1}))$ and $S_I = S_0.\exp(-\frac{TE}{T2})$ to evaluate T1 and T2 relaxation times, respectively. The slop of inverse T1 and T2 relaxation times versus concentration of paramagnetic ions was defined as r1 and r2 relaxivity, respectively.

B. Loading of Gd(TPyP) into Chitosan nanoparticles

The insolubility of Gd(TPyP) in water is the major obstacle to introduce this product as a MRI contrast agent. It has been assumed that its solubility could be enhanced by encapsulating the complex in chitosan nanoparticles (CNs). Since physicochemical properties of CNs depend strongly on the condition of formation, we tried to optimize the procedure of CNs synthesis to obtain small nanoparticles with narrow distribution. The chitosan concentrations and processes such as stirring speed and stirring time, which could have an impact on size and polydispersity of final prepared nanoparticles, were optimized. Secondly, we investigated the feasibility of incorporation of Gd(TPyP) into chitosan nanoparticles via chemical conjugation and passive absorption methods.

B.1. Chemical Materials

Chitosan (from shrimp shells, medium molecular weight, deacetylation degree ≥85%), chitosan (high purity, low molecular weight (M_v=60-120 kDa), deacetylation degree≥ 93%), and sodium triphosphate pentabasic (TPP) (purity ≥98%) were purchased from Sigma-Aldrich. All other reagents used were of analytical grade without further purification.

B.2. Synthesis of Chitosan Nanoparticles (CNs)

CNs were prepared by following the reported method by Fan et al. [257] with slight modifications. Different concentrations (0.5, 0.7, 1, and 1.7 mg/mL) of chitosan were dissolved in 70 mL of acid acetic (1%) under magnetic stirring overnight. The pH of solution was adjusted to 4.7 by adding dropwise 20% wt NaOH aqueous solution under magnetic stirring. 125 mg of TPP was dissolved in 100 mL of deionised water. Chitosan and TPP solutions were filtered through syringe filter (pore size 0.22 μm, Milipore). To prepare CNs, 3 mL of the chitosan solution was heated for 10 minutes in the water bath at 60°C. The heated solution was mixed with 1 mL of TPP solution (4°C) under magnetic stirring in the cooled chamber (6°C). The transparent solution became opalescent after mixing of TPP and chitosan (Fig. 37), followed by sonication (bioblock scientific, 32 Hz) for 3 min in a glass beaker. CNs suspension were centrifuged at 12,500 rpm at 4°C for 15 min and washed 3 times with distilled water. The nanoparticles were collected after freeze drying over night at 2°C.

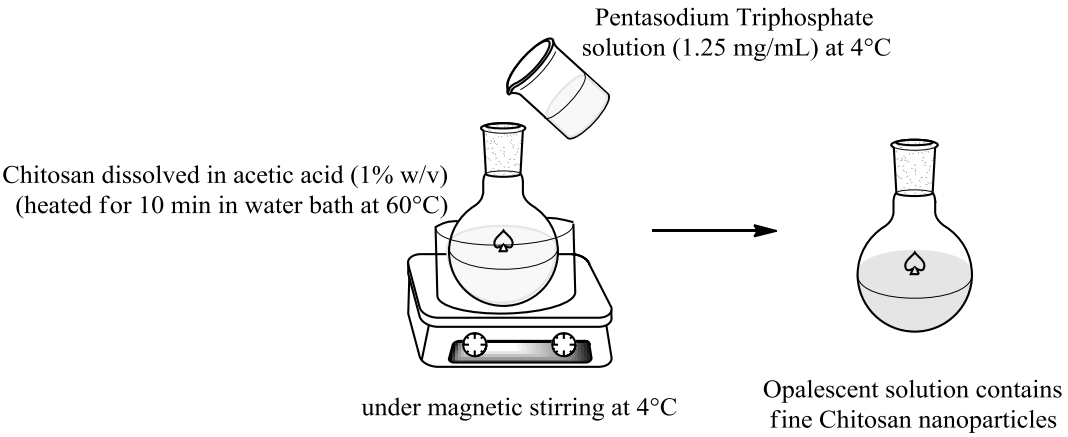

Figure 37. Procedure of CNs preparation

B.3. Preparation of Gd(TPyP) loaded chitosan nanoparticles

Loading of Gd(TPyP) into CNs was done via chemical conjugation and passive absorption routes. In chemical conjugation, Gd(TPyP) was directly added to chitosan solution or to TPP solution. Thus, for active loading (chemical conjugation) of Gd(TPyP) into CNs, 1 mM of Gd(TPyP), dispersed in ethanol, was added into TPP or chitosan solution, as depicted in Fig. 38. Then the procedure of CNs synthesis was followed.

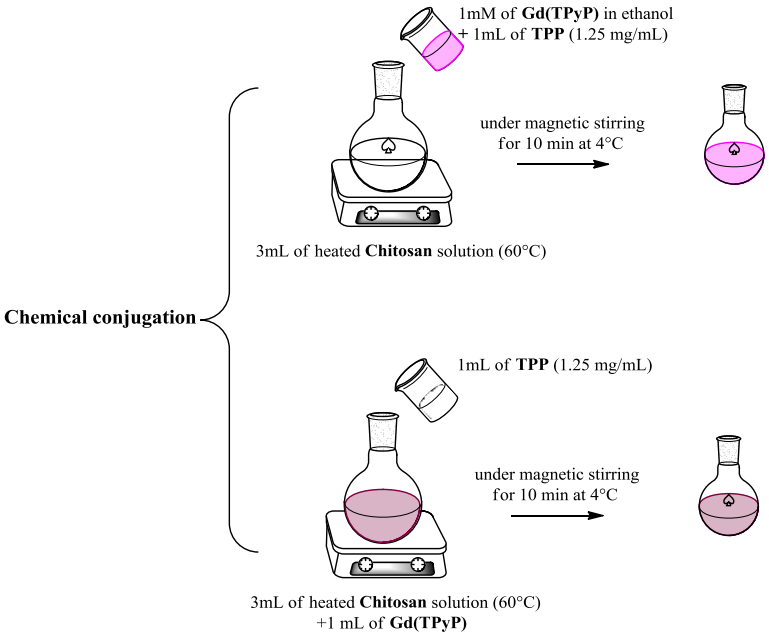

Figure 38. Chemical conjugation of Gd(TPyP)-CNs

The passive loading was performed by dry mixing of CNs with metalloporphyrin for 15 min. After 15 minutes mixing, the mixture was dissolved in distilled water under magnetic stirring for 15 min at 4°C, following sonication. In order to prepare different concentrations of Gd(TPyP)-CNs, four different quantities of Gd(TPyP) (2, 4, 8, 12 mg) were mixed with 4 mg of CNs. The centrifugation has been used to separate free Gd(TPyP) from Gd(TPyP)-CNs (Fig. 39).

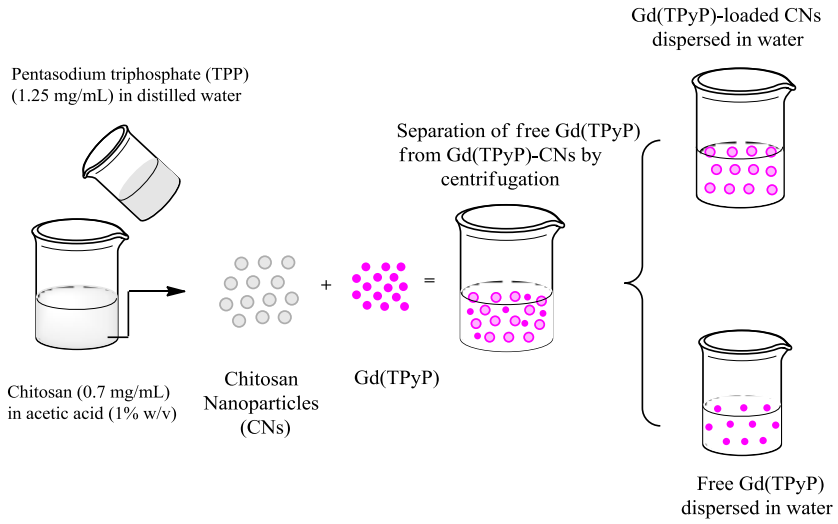

Figure 39. Passive loading of Gd(TPyP)-CNs

B.4. Characterization of CNs and Gd(TPyP)-CNs

B.4.1. Dynamic light scattering

The physicochemical properties of prepared CNs and Gd(TPyP)-CNs such as particle size and polydispersity have been studied by dynamic light scattering ZetaSizer-NanoZS (Malvern Instrument, UK) equipped with a standard 633 nm laser. The size distribution of dispersed samples in 1mL of distilled water was calculated from autocorrelation function of light scattered from particles at 20°C. The homogeneity of solution was determined from polydispersity index (PdI) which varies between 0 to 1. A value below 0.3 indicates high homogeneity while those greater than 0.3 indicate heterogeneous dispersion.

B.4.2. Microscopic imaging of CNs and Gd(TPyP)/CNs

Surface morphology of CNs and Gd(TPyP)-CNs were examined using scanning electron microscopy (SEM) (cambridgeS260, UK). A small drop of nanoparticles suspension was sprinkled on the golden surface and dried at the room temperature. The quantitative analysis of Gd(TPyP)-CNs was examined by SEM coupled with energy dispersive X-ray spectroscopy (EDX).

B.4.3. UV-visible spectroscopy of Gd(TPyP)-CNs

Due to the characteristic property of porphyrin complex, the ultraviolet-visible absorption spectroscopy has been used to study the porphyrin structure of Gd(TPyP)-CNs via different methods and to determine the Gd(TPyP) concentration in Gd(TPyP)-CNs. The UV-vis spectra were recorded by UV-visible spectroscopy (UVIKON XL spectrometer) in the range of 350-700 nm at room temperature using quartz cuvettes (1cm optical path).

B.4.4. Fourier transmission infrared spectroscopy

Fourier transmission infrared spectroscopy (FTIR) of bulk chitosan, CNs, Gd(TPyP), and Gd(TPyP)-CNs were carried out by FTIR spectroscopy over the range of 4000-800 cm^{-1}.

B.4.5. Inductively coupled plasma mass spectrometry (ICP-MS)

The concentration of Gd(TPyP) loaded into CNs has been confirmed via inductively coupled plasma mass spectroscopy (Agilent 7700). The original solutions were all diluted 100x for the ICP measurements. The concentration from ICP-Ms has been compared with concentration measured from Soret band absorption.

B.4.6. Magnetic resonance imaging

The magnetic resonance imaging (MRI) studies of Gd(TPyP)-CNs dispersed in water were performed at 3T and 25°C. The longitudinal and transverse relaxivity of prepared colloids were evaluated from obtained T1 and T2 weighted images. The T1 weighted images were

obtained from spin echo sequence by keeping the echo time TE of 8 ms and varying repetition time TR (100-400 ms). The T2 weighted images were obtained from the spin echo sequence keeping the long repetition time TR=1500 ms and varying echo time TE (7ms - 40 ms).The other parameters were optimized such as: field of view (FOV)= 160x160x5, slice thickness=5 mm, flip angle=90°, number of signal averages= 7, and voxel=2x2x5 mm^3. The presented high resolution T1 and T2 weighted images were obtained from spin echo sequence (TR=400 ms and TE=8 ms) and (TR=1500 ms, TE=40 ms), respectively, with voxel=1x1x5 and field of view (FOV)= 160x160x5, slice thickness=5 mm, flip angle=90°, number of signal averages= 7. After image acquisition, T1 and T2 relaxation times have been evaluated as described previously in section A.4.5.

B.4.7. Determination of entrapment efficiency, loading capacity and yield of Gd(TPyP)/CNs

Gd(TPyP)-CNs was ultracentrifuged at 18000 rpm for 20 min at 4°C. The amount of free Gd(TPyP) in supernatant after ultracentrifugation was measured by UV-visible spectrometry (UVIKON XL spectrometer) at room temperature. The colorless solution was collected and the concentration of free Gd(TPyP) in solution was determined by UV-visible spectroscopy. Afterward, freeze-drying is employed to dry nanoparticles. The entrapment efficiency, loading capacity and yield percentage of Gd(TPyP)/CNs were calculated as follows:

$$\text{Entrapment efficiency (\%)} = \frac{(A-B)}{A} \times 100 \quad (28)$$

$$\text{Loading capacity (\%)} = \frac{(A-B)}{C} \times 100 \quad (29)$$

$$\text{Yield (\%)} = (W_1/W_2) \times 100 \quad (30)$$

while A, B and C correspond respectively to initial amount of Gd(TPyP), the amount of free Gd(TPyP) in the supernatant after centrifuge, and weight of CNs. W_1 and W_2 is the weight of dried Gd(TPyP)-CNs recovered after freeze-drying and the sum of initial amount of CNs and Gd(TPyP).

C. Synthesis of ultra small Mn (II) doped ZnS nanoparticles

C.1. Chemical material

Zinc acetate dehydrate (99.9%, Sigma-Aldrich), manganese (II) acetate (99.9%, Sigma-Aldrich), thiourea (99%, Alfa-Aesar), diethyleneglycol (Acros), tri-octylphosphine oxide

(99%, Acros) and mercaptoacetic acid, thioglycolic acid, (98%, Acros) are used as purchased with no further purification.

C.2. Synthesis of Manganese Zinc Sulphide particles

$Mn_xZn_{1-x}S$ nanoparticles were synthesized by the polyol method using the protocol described elsewhere [258] and adjusting the nominal zinc and manganese precursors concentration to vary x between 0.1 to 0.3. Light brown powders of $Mn_xZn_{1-x}S$ ($0.1 \leq x \leq 0.3$) were recovered by centrifugation at 23 000 $tr.min^{-1}$. The different particle sizes of $Mn_{0.3}Zn_{0.7}S$ were collected from different speeds of centrifugation.

C.3. Particle Characterization of $Mn_xZn_{1-x}S$ (x=0.1, 0.2, and 0.3)

C.3.1. X-ray diffraction

The x-ray diffraction of prepared powder was recorded using x-ray diffractometer (PANalytical X pert-pro diffractometer) with Cu Kα radiation (λ = 1.54 Å). The crystal size of MnZnS powder were determined via MAUD software which is based on the Rietveld method combined with Fourier analysis.

C.3.2. Microscopy imaging

The microstructure and crystallinity of prepared MnZnS were further studied by high-resolution transmission electron microscopy (TEM) (HRTEM, JEOL-2100F). The particle size distribution was obtained from these micrographs by SAISAM software (Microvision Instruments). The chemical composition of powders was verified using EDX mounted on a JEOL-JSM 6100 scanning electron microscope (SEM).

C.3.3. Magnetic property

The magnetic properties of the prepared samples were investigated via Super Quanducting Interference Devices (SQUID) magnetometer (Quantum Design MPMS-5S). The

magnetization measurements were performed at 310K and applied magnetic field varying between 0-50 kOe.

C.4. Colloid Preparation

Different quantities of Mn:ZnS nanoparticles were dispersed in cyclohexane (0.62 mg/mL) by sonication. 4 mL of the resulting solution was mixed with 4 mL of water. Afterward, 200µL of mercaptoacetic acid was added dropwise to the solution under sonication for 15 min. After aging for another 15 min, MnZnS nanoparticles were successfully transferred into water. The excess of mercaptoacetic acid was removed from the aqueous colloid by dialysis.

C.5. Colloid Characterization

C.5.1. Quantitative analysis of Mn(III)

The quantitative analysis of Mn doped in ZnS was analyzed by x-ray fluorescence spectroscopy (MINIPAL4 XRF spectrometer) equipped with a rhodium X-ray tube operating at 30 kV and 87 µA current emissions. For this purpose, the fluorescence intensity of 15 µl of MnZnS suspension which was deposited on the cellulose membrane was compared with the fluorescence intensity of standard solution.

C.5.2. Fluorescence spectroscopy

A fluorescence spectroscopy (model Fluorolog Horiba Jobin–Yvon) was used for photoluminescence (PL) measurements, which were carried out at room temperature using a Xenon arc lamp as an excitation source. The photoluminescence emission spectra of the colloids were recorded at λ_{exc}=405 nm.

C.5.3. Magnetic resonance imaging

The relaxation time of prepared $Mn_xZn_{1-x}S$ colloids in water was studied by Philips ACHIEVA 3.0 T MRI scanner at 25°C. The T1 weighted images were acquired using spin-echo pulse sequence maintenance the echo time (TE) at 8 ms and time repetition (TR) varied between 100 ms- 1000 ms. The other acquisition parameters were optimized such as: field of

view (FOV)=154x154 mm^2, slice thickness=5 mm, flip angle=90°, matrix size= 80x80, number of averages=7, and voxel=2x2x5 mm^3. The acquisition parameters for $Mn_{0.3}Zn_{0.7}S$ colloids in water with different particle size have been optimized as follows: field of view (FOV)=170x170 mm^2, slice thickness=5 mm, flip angle=90°, matrix size= 96x96, number of averages=7, and voxel=2x2x5 mm^3. After image acquisition, the magnitudes of image signal intensities were inferred manually within regions of interest (ROIs) by ImageJ software and following the procedure described previously.

D. Molecular dynamic simulation

D.1. ZnS structure

A few interatomic potentials have been developed for the molecular dynamic simulation of ZnS [259]–[261] . In this work, the empirical ZnS shell model which has been developed by Wright and Jackson [260] was employed to simulate ZnS crystal structure. In the core-shell model of sphalerite ZnS, Zn and S atoms in molecule have been modeled by a massless shell (or very light) connected to a core, which contains all the atomic mass, via a harmonic spring. The sum of core and shell charges should be equal to the total charge of atoms. The spring potential is described as follows

$$u_{ij} = \frac{1}{2} K r_{ij}^2 \tag{31}$$

With the force constant of K and r_{ij} is the distance between atom i and j. The short range interaction between atom i and atom j was demonstrated via Buckingham potential

$$u_{ij} = A_{ij} \exp(-\frac{R_{ij}}{\rho_{ij}}) - \frac{C_{ij}}{r_{ij}^6} \tag{32}$$

Where r_{ij} is the distance between two atoms i and j, and A_{ij}, ρ_{ij}, C_{ij} are three model parameters. For the nearest S-Zn-S atoms, three-body potential has been considered

$$u_{ij} = \frac{1}{2} K_{ijk} (\theta - \theta_{ijk})^2 \tag{33}$$

Where θ_{ijk} is the angle formed by atom S_i and Zn_j (in center) and S_k, θ is the equilibrium value of the angle (109.4°), and k is the model parameter. These potential parameters are listed in Table 8.

The molecular dynamics simulation (MDs) has been conducted via DL_POLY_4 [262]. The initial configuration of ZnS atoms were constructed from atomic coordination of bulk sphalerite ZnS reported by Wyckoff [263]. The MD cell contains 5x5x5 unit cells that contain 500 ZnS molecules. The MD procedure was as follows: time step of 0.5 fs, pressure of 1.0 atm, applying periodic boundary condition, and using the canonical NPT and NVT with equilibration of 100 ps. We used the Nose-Hoover algorithm with thermostat and barostat relaxation times of 0.5 ps in both NPT and NVT ensembles to keep our simulations consistent. Afterward, the final data are collected from NVE ensemble simulation. After reaching the equilibrium, the bulk crystal cleaved to form nanosphere particles with desire diameter of 2.5 nm.

Table 8. The potential parameters for simulation of ZnS

Buckingham Parameters				
Atomic Pair	A (eV)	ρ(Å)	C(eVÅ^6)	Cutoff(Å)
Zn-S	513.356	0.3999	0.0	12.0
S-S	1200.0	0.149	120.0	12.0
Three body Parameters				
Atomic Pair	K(eVrad^{-2})	Θ_0(deg)	ρ(Å)	Cutoff(Å)
SS-Zn-SS	0.713	109.47	0.0	6.0
Shell model Parameters				
Atomic Pair	Mass	Charge	K(eVÅ^{-2})	
S(core)	31.80	0.0	--	
S(shell)	0.20	-2.0	16.86	
Zn(core)	64.2	0.0	--	
Zn(shell)	0.8	2.0	2.181	

D.2. MnZnS crystal structure

Wright has already reported the potential parameters for incorporation of impurities into ZnS crystal structure [264]. In our study, we used the potential parameters reported by Wright to model sphalerite MnZnS structure, listed in Table 9. The simulation procedure was the same as ZnS simulation.

Table 9. The potential parameters for MnZnS solid structure simulation

Buckingham Parameters				
Atomic Pair	A (eV)	ρ(Å)	C(eVÅ^6)	Cutoff(Å)
Mn-S	750.686175	0.390889	0.0	12.0
S-S	1200.0	0.149	0.0	12.0
Zn-S	528.8990	0.4110	0.0	12.0
Three body Parameters				
Atomic Pair	K(eVrad^{-2})	Θ_0(deg)	ρ_1/ρ_2(Å)	Cutoff(Å)
SS-Zn-SS	9.4283e-6	109.47	0.3	6.0
Shell model Parameters				
Atomic Pair	Mass	Charge	K(eVÅ^{-2})	
S(Core)	30.0	1.357	--	
S(Shell)	2.0	-3.357	13.302743	
Mn	54.0	2.0	--	
Zn	65.0	2.0	--	

D.3. Molecular dynamic simulation of water molecule

In order to study the interaction of MnZnS nanoparticles with water, two different water models, including TIP3P (transferable intermolecular potential 3P) [265], and SPC/E (extended simple point charge) [266] have been employed for MD simulation of water molecules. For simulation of liquid water, we simulated a box containing 2376 water molecules with initial density of ~1.0 g/cm^3. The simulation was made under the NPT and NVT ensembles. Berendsen algorithm generates in both NVT and NPT ensembles with thermostat and barostat relaxation times set at 0.1 (ps). Equilibrium was reached in 50 ps, and simulation after the attainment of equilibrium was continued for 200 ps in steps of 0.1 fs. Final data were collected from NVE ensemble. The Newton equations of motion were integrated using the Verlet algorithm.

D.4. Molecular dynamic simulation of ZnS nanoparticle surrounded with water molecules

Interaction of 1877 water molecules with 228 ZnS molecules was studied. The box of water molecules with lattice constant of 39.034 Å was cut off and ZnS nanoparticles have been located in the center of vacancy space. Buckingham potential [267] has been applied for

describing ZnS molecules interaction with water molecules for this modalling as listed in Table 10.

Table 10. Buckingham potential [267]

Atomic pair	A(eV)	r(Å)	C(eVÅ^6)
S-O	41399.49	0.2039	0
S-H	4268.15	0.3686	965.33
Zn-O	14974.51	0.186011	0.0

The simulation conditions were carried out using the NPT and NVT generating Berendsen algorithm with thermostat and barostat relaxation times of 0.5 (ps) in timesteps of 0.1 fs. Final data were collected from NVE ensemble.

D.5. Interaction of MnZnS molecules with water molecules

In order to achieve simulating MnZnS nanoparticles surrounded with water molecules, we need to describe the interaction between Mn atoms and water molecules. We used the Buckingham potential to describe Mn-O pair potential with potential parameters such as A=25974.51 (eV), ρ=0.188011 (Å), and C=20 (eVÅ^6). Finally, the interaction of $Mn_xZn_{1-x}S$ nanoparticles (x=0.1, 0.2, 0.3) with water molecules has been simulated using MnZnS, Zn-O, S-H, S-O, Mn-O, and H_2O potential parameters, following the same procedure applied for simulation of liquid water.

Chapter V: Results and discussion

A. Metallated Porphyrin Complexes Results

A.1. UV-visible Characterizing of ($TPyPH_2$) and Gd(TPyP)

The UV-vis spectra of $TPyPH_2$ and metallated Gd(TPYP) are presented in Fig. 40, consistent with those reported one [268], [269]. The absorption spectrum of $TPyPH_2$ in ethanol has an intense Soret band at 416 nm and four Q bands in the visible spectral region at 513, 542, 588 and 642 nm. As presented in Fig. 40, the absorption spectrum slightly changes after metallation with Gd(III). Upon the metallation, the Soret band shifted from 419 nm to 422 nm while Q band underwent major changes and simplified. $TPyPH_2$ has an intense peak at 554 nm while in Gd(TPyP) this peak has almost disappeared and an intense peak has been observed at 515 nm. On going from freebase to metallated porphyrin, porphyrin deprotonates and the symmetry of the planar macrocyclic fragment increases leading to doubly degenerate molecular orbitals. This degeneration accounts for the reduction in the number of peaks in the Q band [270]. Referring to the UV-vis spectroscopy studies, $TPyPH_2$ porphyrin is successfully metallated with Gd(III) ions.

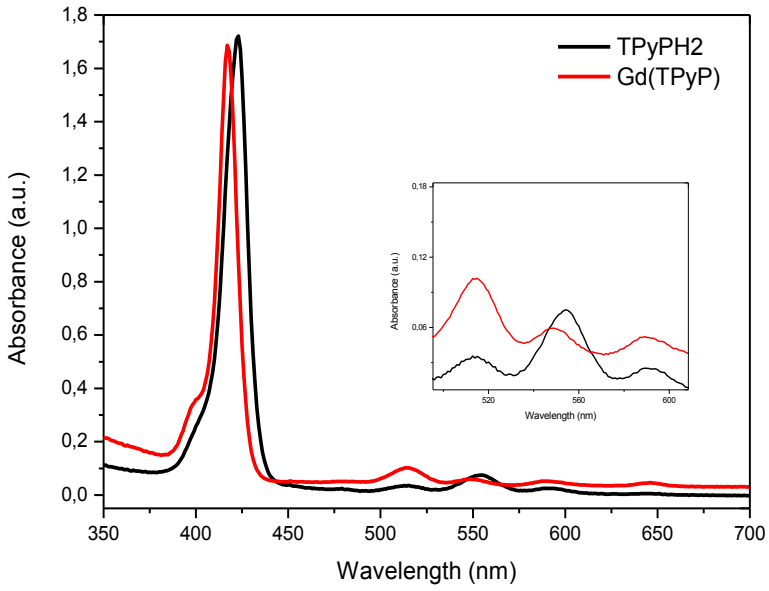

Figure 40. UV-visible absorption spectra of $TPyPH_2$ and Gd(TPyP) dispersed in ethanol at ambient temperature

A.2. ATR-FT-IR spectroscopy of Gd(TPyP) and $TPyPH_2$

Compared with transmission IR techniques, attenuated total reflectance-Fourier transform infrared (ATR-FT-IR) spectroscopy is a useful technique for measuring the infrared spectrum of solids and liquids as well as probing adsorption on particle surfaces. ATR-FT-IR allows us to study the structure of thin films, powders, surface layers of bulk materials, polymers, and various chromophores and dyes. Herein, we studied the structure of developed Gd(TPyP) complex by ATR-FT-IR spectroscopy.

Figure 41 illustrates the FT-IR spectrum acquired from Gd(TPyP) powder in comparison with the spectrum corresponding to $TPyPH_2$. FT-IR peaks and their main assignments are listed in Table 11. The spectrum of Gd(TPyP) is quite similar to the one of $TPyPH_2$ and both spectra exhibit the typical IR band of the porphyrin macrocycle.

Table 11. FT-IR peaks of $TPyPH_2$ and Gd(TPyP)

Assignments	Wavenumbers (cm^{-1})	
	$TPyPH_2$	Gd(TPyP)
γ N—H	3309	----
—OH stretching	----	3255
C═C stretch of phenyl	1591	1594
C═N stretch of pyrrole	1352	1334
C—H bend of pyrrole	1068	1070
C—H out of plane of pyrrole	785	790

$TPyPH_2$ spectrum contains C═C stretching of phenyl group at 1591 cm^{-1}, C═N bandstretching of pyrrole at 1352 cm^{-1}, and C—H vibration of pyrrole at 785 cm^{-1}, which are in good agreement with those reported in [271]. By coordination of Gd(III) with 4 nitrogens of the porphyrin ring, these typical peaks slightly shifted, including 1594 cm^{-1} (C═C stretching of phenyl), 1334 cm^{-1} (C═N bend) and 790 cm^{-1}(C—H vibration of pyrrole). Moreover, ($TPyPH_2$) has shown a peak at 3309 nm, corresponding to N—H, while this peak disappeared in the spectrum of Gd(TPyP). This is attributed to the coordination of metal ion with porphyrin nitrogen atoms. The wide band observed in the range of 3400-3000 cm^{-1} in IR spectrum of Gd(TPyP) is attributed to stretching vibration of hydroxyl group. On the other hand, peaks in the range of 1400-1500 cm^{-1} of Gd(TPyP) spectrum can be ascribed to IR of carboxylate (—COO^-) overlapping with the C═C stretching of porphyrin [272]. Comparing

FT-IR spectrum of $TPyPH_2$ with the Gd(TPyP) one, it could be deduced that Gd ions have coordinated with nitrogen atoms of the porphyrin ring and one acetate ligand.

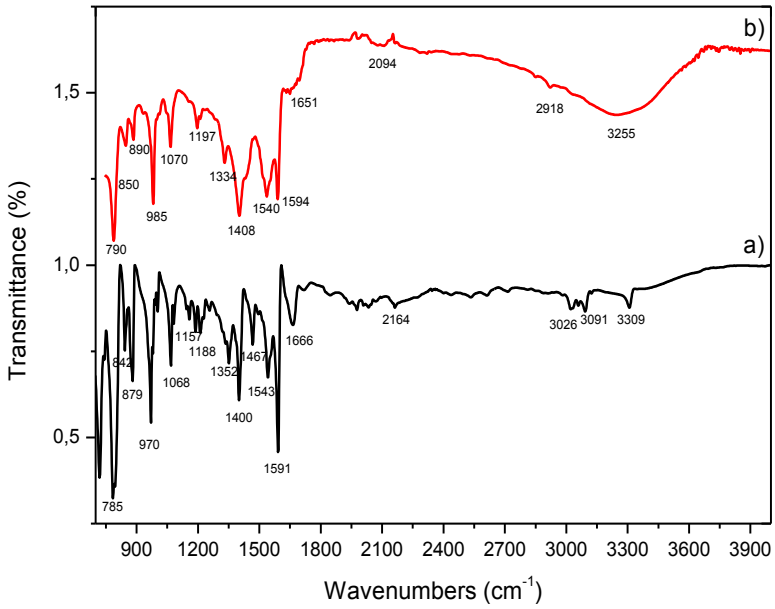

Figure 41. FTIR spectra of a) $TPyPH_2$ and b) Gd(TPyP)

A.3. Proton Nuclear Magnetic Resonance Relaxometry studies

Metalloporphyrins have exhibited the ability to enhance relaxivity of water protons [70], [273] which is one of the most important parameters to enhance the contrast of MR images. In order to evaluate the efficiency of the synthesized Gd(III) porphyrin as a MRI contrast agent, longitudinal (T1) and transverse (T2) relaxation times of Gd(TPyP) colloids were measured by ^1H NMR relaxometry at 20 MHz (0.47T) and 37°C. Meantime, its efficiency has been compared with two water soluble metalloporphyrins such as Mn(III)-tetra-[4-sulfanatophenyl] porphyrin (Mn(TSPP)) and Fe(III)-meso-tetrakis[4-N-methylpyridiniumyl]porphyrins (Fe(TMpyP)) and commercial Gadoterate meglumine (Gd-Dota).

A.3.1. T1 and T2 relaxation times of Fe(TMPyP) and Mn(TSPP) at 20 MHz

Relaxation times of Mn(TSPP) and Fe(TMPyP) measured via ^{1}H NMR relaxometry are listed in Table 12. From Table 12, T1 and T2 relaxation times of Mn(TSPP) and Fe(TMPyP) in water decrease with increasing concentration of paramagnetic ions. At the same paramagnetic concentration of 1mM, Fe(TMPyP) has shown longer T1 (~ two times) and T2 (~five times) than those one of Mn(TSPP). The relaxivity of Mn(TSPP) and Fe(TMPyP) are presented in Fig. 42 and Fig. 43, respectively.

Table 12. Longitudinal and transverse relaxation time (T1 and T2) of Mn(TSPP) and Fe(TMPyP) dissolved in distilled water at 20 MHz and 37°C

Relaxation time of Mn(TSPP) in water			Relaxation time of Fe(TMePyP) in water		
Concentration of Mn(III) (mM)	T1 (ms)	T2 (ms)	Concentration of Fe(III)(mM)	T1 (ms)	T2 (ms)
0.1	1190±0.2	428.4±0.001	1	244±0.03	225.9±0.001
0.3	467±0.04	148.5±0.001	2	149.9±0.002	137.3±0.002
0.5	283±0.03	87.56±0.007	3.5	81.6±0.003	74.67±0.001
1.0	147±0.01	46.21±0.004	10	27.11±0.009	24.43±0.003

r1 of Fe(TMPyP) in the literature has been reported in the range of 4.4-1.3 $mM^{-1}.s^{-1}$ (at 10 MHz) which decreased by pH varied between 1-10 [274]. The dependency of Fe(TMPyP) complex's r1 to pH was related to its spin moments. This complex possesses typical high spin moments S=5/2 at pH < 5, and dropped to lower spin S=1/2 at higher pH>7 due to the formation of Fe-O-Fe and dimerization of Fe(TMPyP) which causes the decrease of the relaxivitiy [274]. The equilibrium behavior of Fe(TMPyP) in aqueous media as a function of pH has been studied by Gandini *et al.* using UV-visible spectroscopy [275]. They have observed five different Fe coordinations in the equilibrium state such as: Fe-H_2O (Fe1), H_2O-Fe- H_2O (Fe2), H_2O-Fe-OH^- (Fe3), μ-oxo dimer Fe-O-Fe (Fe4) and OH^--Fe-OH^- (Fe5).

Our results are in the range of the reported values. The relaxivity of Fe(TMpyP) arises from inner sphere contribution such as hydration number and the residency of water molecules [276]. As explained above the hydration number of Fe(TMpyP) depends on the pH of solution which can be followed by UV-visible spectroscopy. Thus, in order to understand the coordination of Fe ions with water molecules in our study, small quantities of Fe(TMPyP) have been dispersed in distilled water and examined, with UV-visible spectroscopy. As shown in Fig. 42, the spectrum of Fe(TMPyP) in water contains an envelope Soret band at 401 nm

(shoulder at 418 nm) which is consistent with the spectrum of Fe1 species reported by Gandini *et al.* [275]. Furthermore, due to positively charged nitrogen in ortho positions of Fe(TMPyP), the complex has a tendency to withdraw electrons which strengthens the metal-axial water bonds. This strengthening could cause the long water residency time which has been reported as long as 1.3 s at room temperature [276]. One molecule of water in inner sphere with long residency time could cause the r1 of 3.7 $mM^{-1}s^{-1}$ at 0.47T for Fe(TMPyP).

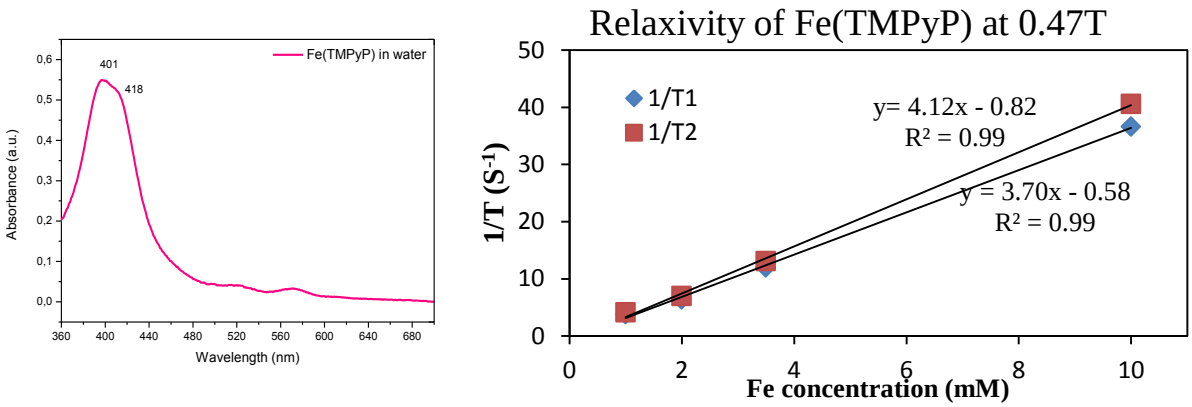

Figure 42. Right: UV-vis spectrum of Fe(TMPyP in water and Left: r1 and r2 of Fe(TMPyP) in water at B_0=0.47 T and T=37°C

In comparison with relaxivities of Fe(TMyP), Mn(TSPP) exhibits higher r1 of 6.63 $mM^{-1}.s^{-1}$, consistent with those of previous reported values [82], [277], presented in Fig. 43. High relaxivity of anionic Mn(TSPP) complex also comes from the inner sphere contribution [277]. Mn(III) ion coordinates axially with two water molecules [277]. Additionally, due to the strong electron donor of peripheral 4-sulfonatophenyl substituent of Mn(TSPP), electron density at the center of the complex is high which could labialize metal-axial water bonding and promote the limiting dissociative water-exchange mechanism. This labialization causes short water residency time, reported as short as 36 ns at room temperature [277]. Furthermore, the short distance between Mn ions and coordinated water (~2.26Å) could also increase the dipolar interaction, improving r1 [278]. Thus, one more water molecule in inner sphere with short water residency time are the reasons that Mn(TSPP) possesses higher relaxivity than r1 of Fe(TMPyP).

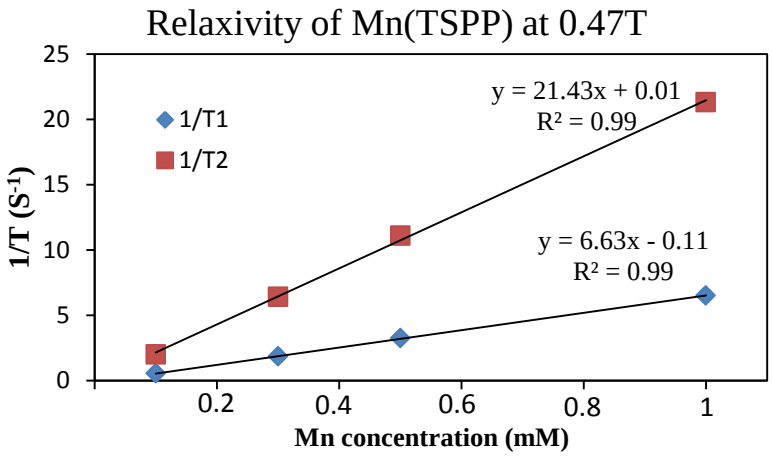

Figure 43. Longitudinal and transverse relaxation rates [($1/T_1$) and ($1/T_2$)] of Mn(TSPP) versus the Mn(III) concentration in water at B_0=0.47 T and T=37°C

A.3.2. T1 and T2 relaxation times of Gd-DOTA at 20 MHz

Relaxation times and relaxivities of commercial Gd-Dota diluted in water and in the mixture of water and ethanol are tabulated in Table 13 and in Fig. 44, respectively.

Table 13. T1 and T2 relaxation times of Gd-DOTA diluted in water and in the mixture of water/ethanol at 20 MHz and 37°C

Relaxation time of Gd-Dota in water			Relaxation time of Gd-Dota in ethanol+water		
Concentration of Gd(III) (mM)	T1 (ms)	T2 (ms)	Concentration of Gd(III) (mM)	T1 (ms)	T2 (ms)
0.6	450±0.07	395.8±0.002	1	446±0.06	381.8±0.002
3	92±0.01	98.9±0.003	----	----	----
4	71.8±0.005	68.6±0.001	----	----	----
5	43.1±0.002	44.17±0.006	5	75.3±0.002	53.7±0.006
7	35.6±0.002	31.6±0.003	7	48.8±0.002	39.4±0.003
9	27.3±0.002	22.23±0.004	9	32.1±0.002	27.35±0.004

Gd-Dota diluted in the mixture has shown r1 of 3.51 $mM^{-1}.s^{-1}$ which is slightly lower than the one of Gd-Dota (4.1 $mM^{-1}.s^{-1}$) in water which is in good agreement with the reported one [255]. This small difference could be related to the structure of ethanol. In the mixture of ethanol/water, there are four chemically distinctive sites that are occupied by hydrogen such as methyl (CH_3), methylene (CH_2) and bonding to oxygen in ethanol and in water. It has been reported that the resonance frequency offset of methyl and methylene results in chemical shift displacement which causes the relaxation time enhancement [255].

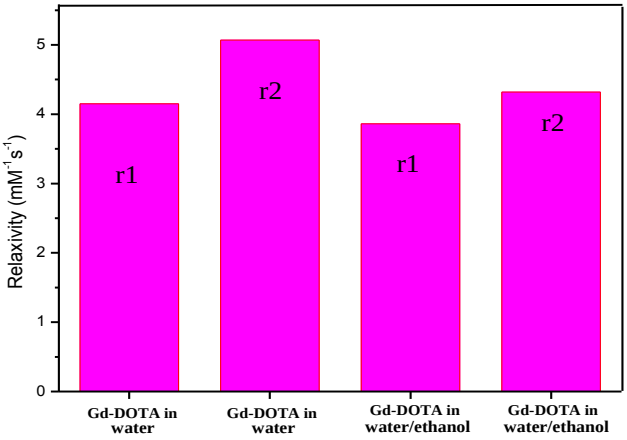

Figure 44. Longitudinal and transverse relaxivities r1 and r2 of Gd-DOTA in water and in the mixture of water/ ethanol at B_0=0.47 T and T=37°C

A.3.3. T1 and T2 relaxation times of developed Gd(TPyP) at 20 MHz

As listed in Table 14, T1 and T2 of Gd(TPyP) in ethanol are varied between 194-33 ms and 167-15 nm, respectively, with the Gd(III) concentration in the range of 0.1-1 mM. T1 and T2 values of Gd(TPyP) are much smaller than those of manganese and iron porphyrins and Gd-Dota. The order of longitudinal relaxation time of these three metaloporphyrins at 1mM from least to greatest is Gd(TPyP) with T1=33 ms, Mn(TSPP) with T1=147 ms and Fe(TMPyP) with T1=244 ms. Comparing with relaxation times of Gd-Dota, Gd(TPyP) at the concentration almost 10 times lower exhibits much shorter T1 and T2 ($\leq$ 11 times). r1 and r2 of Gd(TPyP) in ethanol are presented in Fig. 45. Gd(TPyP) in ethanol has shown a high r1 of 26 $mM^{-1}.s^{-1}$ and r2 of 68 $mM^{-1}.s^{-1}$ at 20 MHz.

Table 14. Longitudinal (T1) and transverse (T2) relaxation times of Gd(TPyP) at 20 MHz and 37°C

Relaxation time of Gd(TPyP) in ethanol at 0.47 T		
Concentration of Gd(III) (mM)	T1 (ms)	T2 (ms)
0.1	194±0.09	167.7±0.005
0.2	92±0.06	82.6±0.003
0.3	66±0.04	55.4±0.004
0.4	56±0.03	43.6±0.004
0.5	62±0.02	32.7±0.002
0.7	45±0.02	22.4±0.001
0.9	37±0.01	17.82±0.001
1	33±0.01	15.69±0.003

The coordination geometry of Gd(TPyP)(acac) (acac=acetylacetonate) has already been studied via extended x-ray absorption and molecular dynamic simulations [7]. It has been reported that three oxygen atoms are coordinating with Gd(III) of Gd(TPyP)(acac) at the average distance of 2.41 Å, one from water and two from acetylacetonate), referring to its octacoordinated structure [7], [279]. Due to the similar structure of Gd(TPyP)(acac) with Gd(TPyP)(OAc), we could suppose that Gd(III) of Gd(TPyP)(OAc) is also coordinated with one water molecule and one molecule of acetate at a distance of 2.41 Å. The coordination of one acetate molecule with Gd(III) of Gd(TPyP)(OAc) has been confirmed by measuring its molecular weight (833 g/mol) using MALDI-TOF spectroscopy.

One coordinated water at the distance of 2.41 Å and owing the molecular weight of 833 g/mol are not the only reasons that Gd(TPyP)(OAc) possesses this high relaxivity. Some other parameters such as water residency time, well-located metal ion in the center of chelate [280], [281], high isotropic structure of complex [280], [281], and rigidity of linking between metal ions and chelate [282] could also contribute to this high relaxivity. It has been reported that well-located metal ion in the center of the complex causes the tumbling of such carrier transfer to the rotation of metal-water proton which decreases the longitudinal relaxation time [280]. Furthermore, rigidity of linking plays an important role in determining the relaxivity. The flexible linking allows the metal-water proton vector rotate independently and faster than the whole complex, resulting in the decrease of r1[281], [283]. It is known that Gd(III) of Gd(TPyP) could coordinate with one nitrogen of another porphyrin molecule, resulting in modifying its structural environment, and stretching of macrocycle. The coordination with nitrogen of another porphyrin could reduce the flexibity of the complex, which results in improving r1.

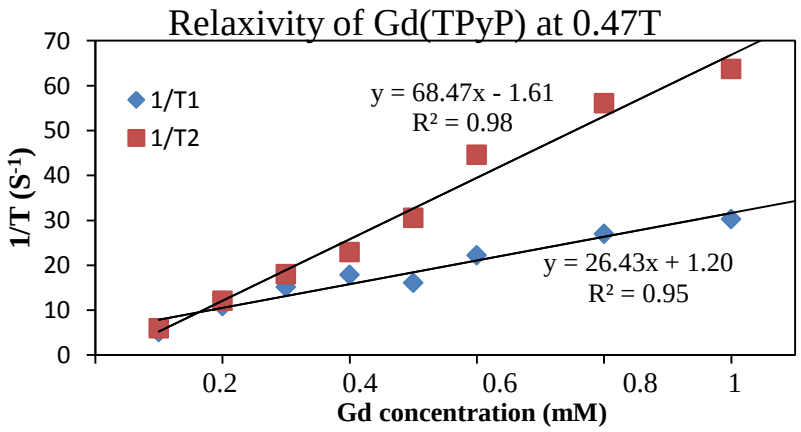

Figure 45. r1 and r2 of Gd(TPyP) in ethanol at B_0=0.47 T and T=37°C

One of developed Gd-porphyrin, which possesses high relaxivity (r1=16.9 $mM^{-1}.s^{-1}$ at 50 MHz) and high stability, is Gd-texaphyrin (Motexafin gadolinium). Texaphyrin is pentaaza, expanded porphyrin [284], which contains five nitrogen atoms in their central core. It has been reported that Gd(III) ion of Gd-texaphyrin coordinated with four water molecules [285], [286]. Gd-texaphyrin with higher molecular weight (1148.4 $g.M^{-1}$) and coordinated with 4 water molecules possesses lower r1 (16.9 $mM^{-1}.s^{-1}$ at 50 MHz and 25°C) compared with r1 of developed Gd(TPyP) (r1=26 $mM^{-1}.s^{-1}$ at 20 Mhz) in our work.

The other commercially developed Gd(III)-porphyrin as MRI CA is Gadophrin-2 (bis-Gd-DTPA-mesoporphyrin). Gd(III) Mesoporphyrin-IX-13,17-bis[2-oxo-4,7,10,10-tetra(carboxylatomethyl)-1,4,7,10-tetraazadecyl]-Diamide, Gadophrin-2, is composed of two Gd-DTPA which are covalently linked to the mesoporphyrin. This compound of chelated porphyrin derivatives contains two Gd^{3+} ions per molecule. The coupling of porphyrin with DTPA increases the molecular weight of the complex (1697.25 g/mol) which leads to an increase in the correlation time (τ_c), and enhanced r1 relaxivity [287]. This complex in aqueous solution has shown r1 of 8.3 $mM^{-1}.s^{-1}$ at 0.47T and 39°C [74], which is much lower (almost 3-fold) than r1 of Gd(TPyP). The evaluation of NMR relaxivity permits us to assume the potential of the developed Gd(TPyP) as MRI CA. Further studies in the efficiency of metalloporphyrins as MRI CA have been conducted using MRI at 3T.

A.4. In-vitro Magnetic Resonance Imaging studies at 60 MHz

T1 and T2 weighted images of Mn(TSPP) and Fe(TMPyP) are presented in Fig. 46. The signal intensity on T1 weighted images of both Mn(TSPP) and Fe(TMPyP) solution increases with concentration of paramagnetic ions, and conversely on the signal intensity on T2 images. From Fig. 46, T2 effect of Mn(TSPP) solution at lower concentration (~10-fold) is much more pronounced compared with those of Fe(TMPyP).

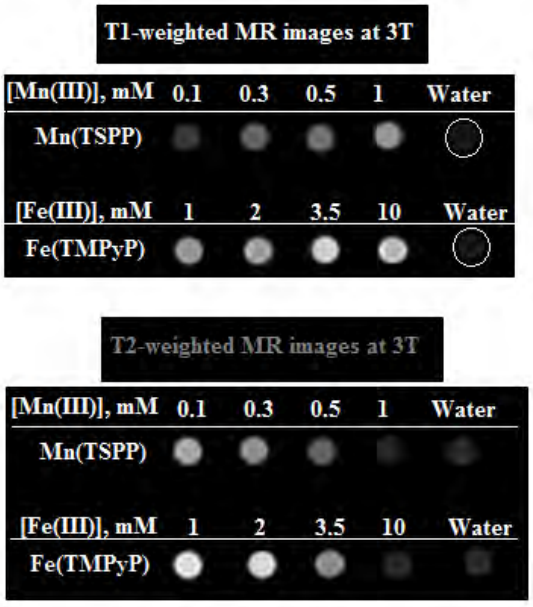

Figure 46. T1 (TR=400 ms, TE=8 ms) and T2 (TR=1500 ms, TE=40 ms) weighted spin echo MR images of different concentration of Mn(TSPP) and Fe (TMePyP) in water at 3T and 25°C

Figure 47 represents T1 and T2 weighted images of Gd(TPyP) and Gd-Dota in aqueous media. The signal intensity on T1 images increased progressively with Gd concentrations in Gd(TPyP) and Gd-Dota solution, and conversely for those on T2 images . We observed (Fig. 47) that Gd(TPyP) with lower concentration produces brighter T1 and darker T2, compared with those of both Gd-DOTA solutions. These images confirm the efficiency of Gd(TPyP) in contrast enhancement of MR images.

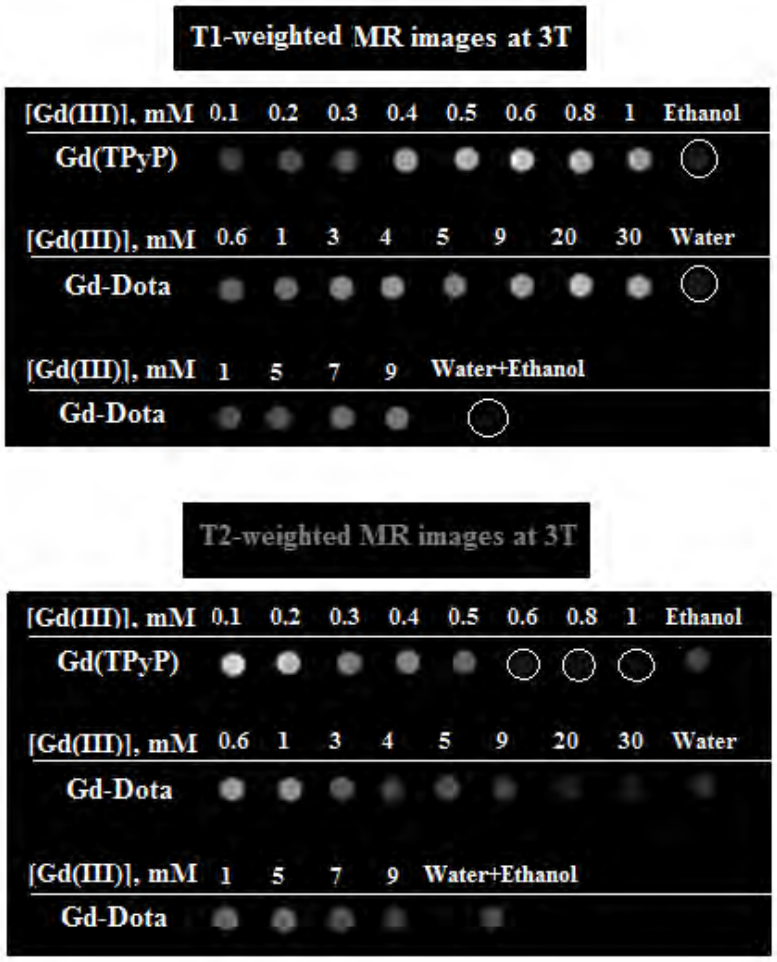

Figure 47. T1 (TR=400 ms and TE=8 ms) and T2 (TR=1500 ms, TE=40 ms) weighted spin echo MR images of different concentration of Gd(TPyP) in ethanol and Gd-Dota in water and Gd-Dota in water/ethanol at 3T and 25°C

A.5. Relaxivity of metalloporphyrins and Gd-Dota solution at 3T

Relaxivity depends on external parameters such as applied field and temperature [288]. Thereby, r1 and r2 relaxivities of three metalloporphyrins in aqueous media have been evaluated from treating MR images at 3T. The evaluated r1 and r2 of Mn(TSPP) and Fe(TMPyP) via MRI and NMR relaxometry are summerized in Fig. 48. It can be observed that the values of r1 and r2 obtained from MR images are respectively smaller and larger compared with those values measured via NMR relaxometry.

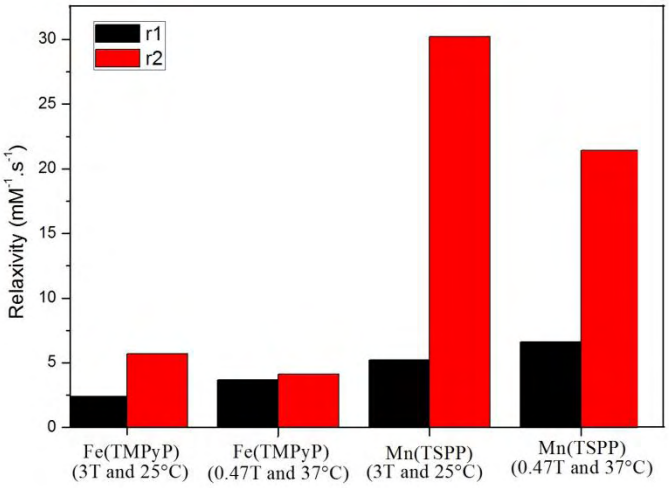

Figure 48. r1 and r2 relaxivities of Mn(TSPP) and Fe(TMPyP) colloids measured via MRI at 3T and 25°C and NMR relaxometry at 0.47T and 37°C

The evaluated r1 and r2 relaxivites of Gd(TPyP) and Gd-DOTA via MRI and NMR relaxometry have been presented in Fig. 49. As presented in Fig. 49, the evaluated r1 and r2 of Gd(TPyP) using NMR and MRI did not significantly change.

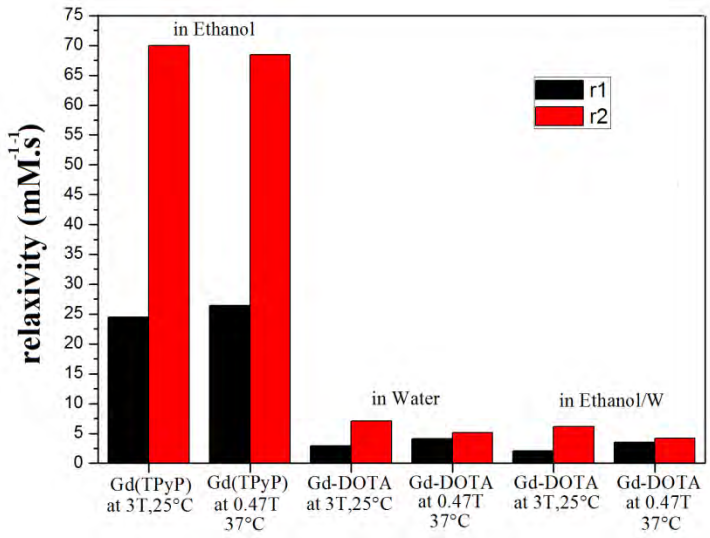

Figure 49. The r1 and r2 relaxivity of Gd(TPyP) and Gd-DOTA solution at 3T and 25°C and 0.47T and 37°C

In our study, we have observed that r1 of all three metalloporphyrins and Gd-DOTA solution measured using MR images are slightly lower than those measured by NMR relaxometry, and

in the opposite sense for r2 relaxivity. Among all the complexes, the difference between measured r2 relaxivity of Mn(TSPP) via NMR and MRI is much more pronounced.

The relaxivity of Gd-based MRI contrast agents at multiple field strengths has already been studied by other researchers. For instance, magnevist ($[Gd(DTPA)(H_2O)]^{2-}$), exhibited a modest longitudinal relaxivity of 4.70 $mM^{-1}.s^{-1}$ at 0.47T, which decreased to 3.80 $mM^{-1}.s^{-1}$ with increasing applied field to 1.5T [289]. Whereas, its transverse relaxivity increased drastically from 5.60 $mM^{-1}.s^{-1}$ at 0.47T to 18.80 $mM^{-1}.s^{-1}$ at 1.5T [289]. Serum albumin binding of Gd-phostriamine contrast agent has also shown a decrease in longitudinal relaxivity with field strength [288], [290]. The effect of applied field on relaxivity of Mn and Fe-based contrast agents has also been investigated; for instance, r1 and r2 of Resovist (magnetite) in water have been studied at three different magnetic fields (0.47, 1.5 and 9.4T) [291]. r1 of magnetite decreased from 8.30 to 5.14 $mM^{-1}.s^{-1}$ whereas r2 drastically increased from 9.27 to 15.7 $mM^{-1}.s^{-1}$ with increasing field strength from 1.4T to 9.4T [291]. r1 of ultrasmall iron oxide (USPIOs) in water decreased from 14.152 to 2.097 $mM^{-1}.s^{-1}$ meanwhile its r2 increased from 10.71 to 84.57 $mM^{-1}.s^{-1}$ with magnetic field varied between 10 mT-14.1 T [292]. Nonetheless, Troughton *et al.* has reported the reduction of r1 and r2 of Mn(EDTA) with applied field [293]. The decrease of r2 of Mn(EDTA) with magnetic field was attributed to the short residence time of water (5 ns at 20°C) in Mn(EDTA) solution [293].

The decrease of r1 relaxivity above 1.5T is related to negligible contribution of electronic relaxation time at high magnetic field (above 1.5T) [294]. Thereby, the contribution from rotational correlation time and water residency time play the major role in r1 relaxivity of paramagnetic-based agents at high magnetic field [294]. While, increase of r2 with magnetic field is due to linear increase of the metal complex magnetization which results in greater susceptibility contrast at higher fields [288].

Temperature can also have a dramatic effect on the relaxivity of contrast agents. It is known that relaxation rate decreases with the temperature [295], [296]. Based on Stokes-Einstein-Debye equation, the drop of r1 relaxivity is related to the relation between rotational correlation rate and temperature [297]. The rotational correlation time increases with temperature, thereby it causes the relaxivity to decreases [298]. Another temperature dependent parameter contributing to relaxivity is water exchange rate. The relaxivity would be limited at low temperature while the water-exchange rate is fast enough [295]. Thus, the slow water exchange rate could also lead to a decrease in relaxivity with temperature. Thereby, in our study, temperature could also influence the relaxivity of Mn(TSPP),

Fe(TMPyP), Gd(TPyP), and Gd-DOTA. The relaxivity of all solutions were measured at two different magnetic fields with different temperature. Thus, the reduction of r1 relaxivity could be attributed to decreasing the temperature and simultaneously increasing the magnetic field.

B. Gd(TPyP) conjugated with Chitosan nanoparticles

Chitosan is one of the most promising polymers for pharmecutical and biomedical area due to its unique properties such as biocompatibility, biodegradability, nontoxicity, and mucoadhesive properties [141], [299], [300]. It was observed that encapsulation of the poorly water-soluble drug through CNs could enhance the drug solubility [301]–[303]. In our study, CNs are considered as suitable polymeric carriers to enhance the water-solubility of Gd(TPyP). Firstly, we tried to optimize the preparation procedure of CNs to obtain the small particle with narrow size distribution. Afterward, the loading of Gd(TPyP) into CNs was investigated.

B.1. Physicochemical Characterization of Chitosan nanoparticles

The important role of chitosan and TPP concentrations in forming CNs has been reported by several researchers [109], [257]. They have reported that the microparticles could form at chitosan concentration above 1.5 mg/mL and TPP concentration above 1.0 mg/mL [257]. Above 1.5 mg/mL chitosan concentration, there are plenty of chitosan molecules involved in cross linking of a single particle which leads to form the micro particles. Some researchers have studied the aggregation behavior of chitosan in aqueous media [304]–[307]. They confirmed that the critical aggregation concentration is about 1 mg/mL [308]. Herein, the different chitosan concentrations less than 2mg/mL have been prepared to study the effect of chitosan concentration on average particle size.

The particle size and PdI of CNs obtained from different bulk chitosan concentrations have been measured via dynamic light scattering (DLS) and the results obtained were listed in Table 15. As listed in Table 15, size and PdI of CNs decrease with increasing concentration of chitosan solution from 0.5 mg/mL to 0.7 mg/mL. For CNs obtained from bulk chitosan with medium molecular weight (MM_v), mean particle size decreased from 9.1 μm for 0.5 mg/mL chitosan solution to 305 nm for 0.7 mg/mL chitosan solution. The same trends have been observed for CNs obtained from bulk chitosan with low molecular weight (LM_v), decreasing

from 8.9 μm to 120 nm. Afterward, for further increasing of chitosan concentration, the mean diameter of CNs obtained from MM_v and LM_v increases from 305 nm-24 μm and 120 nm-12 μm, respectively. The increase of particle size for higher chitosan concentration than 1 mg/mL could be related to the aggregation formation of chitosan in solution which has been previously reported [308]. The smallest CNs with narrow size distribution was obtained from chitosan concentration of 0.7 mg/mL for both MM_v and LM_v.

Table 15. Mean particle size (nm) and PdI values of CNs in distilled water from different chitosan concentration (mg/mL) with two different deacetylation degree (85% and 93%), TPP=1.25 mg/mL, T=20°C

Chitosan Concentration (mg/mL)	Bulk Chitosan DD=85%. MM_v		Bulk Chitosan DD=93%. LM_v	
	PdI	Average Size CNs (nm)	PdI	Average Size CNs (nm)
0.5	0.319	9158	0.289	8991
0.7	***0.201***	***305***	***0.139***	***120***
1.0	0.789	980	0.687	684
1.7	1	23860	1	12230

The effect of chitosan concentration on particle size of CNs was investigated by Fan *et al*. [257]. They succeeded to prepare CNs with mean hydrodynamic diameters of 138 nm and PdI of 0.026 from chitosan (LM_v and DD=91%) concentration of 0.5 mg/mL and TPP concentration of 0.5 mg/mL. Due to the modification performed during the synthesis of CNs, we achieved a reduction in the hydrodynamic radius of CNs to 120 nm. The difference between PdI value obtained and Fan's result might be related to the purity and different deacetylation degree of bulk chitosan used.

Referring to the results obtained, particle size and size distribution of CNs depends on chitosan solution concentration as well as molecular weight and/ or deacetylation degree of bulk chitosan. It has been reported that the average diameter and dispersity of CNs increased with the molecular weight of chitosan [308], [309]. The effect of chitosan concentration with different molecular weights on the average diameter and homogeneity of CNs has been studied by some researchers. The effect of chitosan concentrations with high (HM_v), medium (MM_v) and low (LM_v) molecular weights on particles size has been studied by Gan *et al.* [308]. They observed that the particle size of CNs linearly increased with chitosan concentration. They observed that the size of CNs obtained from HM_v chitosan was significantly affected with increasing chitosan concentration [308]. The smallest particle size (~152 nm) with high zeta potential (+31 mV) was obtained from LM_v chitosan at 0.5 mg/mL concentration [308]. In aother work, the effect of chitosan concentration and chitosan

molecular weight, in the range of 140–160, 240–270 and 280–320 kDa, on the diameter of chitosan microspheres has been studied by He *et al.* [310]. They also reported that at the same chitosan concentration the particle size increased with molecular weight unlike the zeta potential [310]. Referring to these studies, our results are consistent.

As listed in Table 15, size and polydispersity values of CNs from LM_v chitosan are much lower than MM_v at the same concentration. This could be attributed to the effect of molecular weight on the conformation of chitosan chains in solution [311], [312]. Tsaih and Chen suggested that the occurrence of conformational transition of chitosan related to their molecular weight could be attributed to the difference in intramolecular hydrogen bonding and/or the difference in charge distribution [311]. Considering Tsaih's study, the high molecular weight chitosan have more intermolecular hydrogen bonding and chitosan molecules could entangle with each other easily which leads to the formation of large particles. While for the small molecular weight, the conformational of chitosan in solution is stiff and extended which could lead to smaller particle size.

The other parameter, which could also affect the particle size of CNs, is acetylation degree of chitosan. There are a lot of contradicting results have been published about the effect of acetylation degrees of chitosan on chain conformation of chitosan. Some researchers have reported that the stiffness of chitosan chains increased with increasing acetylation degree [306], [313], [314] whereas Errington and coworkers have described the opposite effect [315]. Wang has also reported that the stiffness of chitosan chain decreased with decreasing acetylation degree of chitosan [316]. On the other hand, other researchers indicated that the rigidity of chitosan chain does not depend on the acetylation degree of chitosan [317]–[319].

The effect of acetylation degree on chitosan solution have systematically studied by Schatz *et al.* [305], [320] and Sorlier *et al.* [312], [321]. They defined three distinct groups of acetylation degree (DA) to demonstrate the behavior of chitosan in solution. First group is chitosan with DA less than 20% which displays a polyelectrolyte. The hydrophilic and hydrophobic interactions are moderate for chitosan with DA between 20 and 50%. For higher acetylation degree, the hydrophobic interaction will arise.

The electrostatic, hydrophobic interaction, hydrogen bonding, and strict interaction could change with changing deacetylation degree of chitosan [322]. The rigidity of the chain may increase at higher content of acetyl groups. Hence, more hydrophobic interaction and hydrogen bonding could be formed. Meantime, it has been reported that the higher charged polycation could be formed at lower acetylation degree. The accumulation of charges causes expansion of polymer chains [323]. The acetylation degrees of chitosan used in our study

were 7% and 15% (deacetylation degree (%)=1-acetylation degree (%)). Hence, referring to Schatz studies, we could suppose that the both chitosans display polyelectrolyte behavior in solution. Therefore, the higher deacetylation degree (lower acetylation degree) could cause the formation of smaller CNs due to its higher charged polycation, causing the expansion of polymer.

After optimization of the chitosan concentration, the impact of stirring rate and time of stirring on the formation of CNs has been studied: The particle size and PdI of CNs obtained at different stirring rates and timing have been studied via DLS, listed in Table 16. It has been observed that the increase of stirring rate up to 700 rpm leads to a decrease in CNs average diameter while further increase leads to larger particle with higher PdI which could be attributed to the formation of CNs aggregates. The aggregation at high stirring rate might be caused by the destruction of the repulsive force between particles which leads to the aggregation [257]. Fan *et al.* have observed the same trend that the CNs particle size decreases with increasing stirring rate varied between 200-800 rpm, further increase causes larger particle [257].

Table 16. Effect of stirring rate and time of stirring on average CNs particle size and PdI

Stirring rate (rpm)	particle size (nm)	PdI	Time of stirring (min)	particle size (nm)	PdI
300	705	0.593	5	225	0.463
500	323	0.407	10	120	0.139
700	120	0.129	20	164	0.29
1000	147	0.265	30	194	0.320
1200	198	0.35	60	1600	0.791

It has been reported that the time of reaction also affecte the particle size and polydispersity of CNs [324]. The DLS results represent small particles with low PdI after 10 min of magnetic agitation. Above 15 min of agitation, the hydrodynamic radius of CNs and its PdI increases referring to the formation of CNs aggregation. Yang *et al.* has also reported the aggregation of particles with increasing time of interaction [324].

Compared with high molecular weight chitosan, low molecular weight chitosan shows better solubility, biocompatibility, biodegradability and even less toxicity [325], [326]. Furthermore, referring to the main aim of our work to prepare small nanoparticles, further studies have been performed on CNs obtained from chitosan (LM_v) concentration of 0.7 mg/mL and TPP concentration of 1.25 mg/mL.

B.1.1. Morphology of Chitosan nanoparticles

The morphology of optimized chitosan nanoparticles (CNs) was examined using SEM. SEM images of CNs before and after sonication are presented in Fig. 50. From these images, nanoparticles exhibited a spherical shape with a narrow size distribution in the range of 35-45 nm. CNs aggregation could be observed before sonication while using sonication leads to destruction of the aggregates, as presented in Fig. 50. The discrepancy in size measured with DLS and SEM can be attributed to the different measurement techniques. In DLS, we measured the hydrodynamic radius of particles while SEM gives an actual diameter of nanoparticles in their dry state.

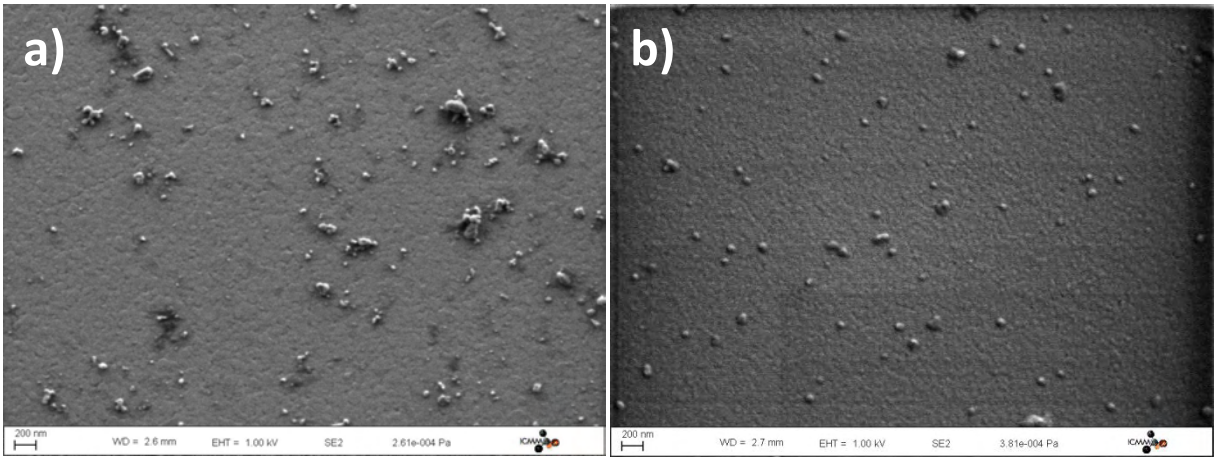

Figure 50. CNs SEM images a) before and b) after sonication. Particle preparation conditions: LM_v chitosan concentration = 0.7 mg/mL. TPP concentration=1.25 mg/mL

B.1.2. FT-IR spectroscopy of bulk chitosan (93%) and CNs

In acidic solution, chitosan is protonated and can interact with negatively charged counter ions of TPP dissociated in water. Thereby, NH_3^+ of chitosan ionically reacts with OH^- and $P_3O_{10}^{5-}$ ions of TPP in solution which leads to the formation of CNs. The FT-IR spectra of bulk chitosan and CNs were recorded to investigate the interaction between chitosan and sodium tripolyphosphate (TPP), presented in Fig. 51. FT-IR spectrum of bulk chitosn contains the feature sharp peak of amide II (N-H bending vibration) at 1581 cm^{-1} and low intensity peak of amide I (–CO stretching vibration) at 1643 cm^{-1} which could confirm the high deacetylation degree of bulk chitosan [327], [328]. Moreover, IR spectrum of bulk chitosan contains the peak of amino group ($–NH_2$ and –OH) stretching vibration at 3340 cm^{-1} [327],

[328], [329]. Whereas in IR spectrum of CNs, this characteristic peak becomes wider and shifts to 3230 cm^{-1}, indicating that the majority of amino groups of bulk chitosan participate in the electrostatic interaction with TPP [327]. The flattening of $–NH_2$ and –OH band has already been observed in FT-IR spectra of prepared CNs via ionic gelation method [309], [327], [330], [331].

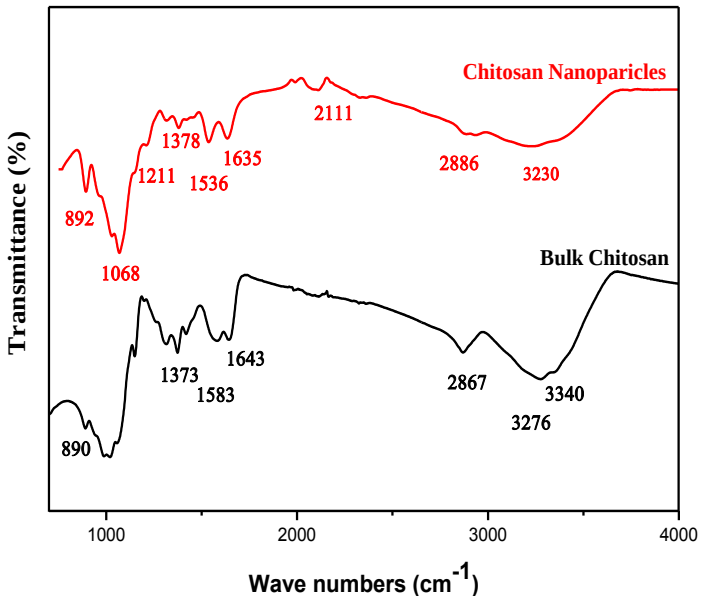

Figure 51. FT-IR spectra of bulk chitosan (M_w=60-120 kDa, degree of deacetylation≥93%), and Chitosan nanoparticles

Moreover, –CO stretching vibration peak of bulk chitosan disappears in the IR spectrum of CNs which could be ascribed to the linkage between phosphoric and ammonium group of chitosan [332]. Similar results were observed for CNs prepared via ionic gelation in different studies [328], [330], [332]–[334]. The new peak at 1211 cm^{-1} in IR spectrum of CNs could be assigned to the P═O stretching. The appearance of P=O stretching peak in CNs could confirm the interaction between positive charged amino groups of chitosan with negative charged phosphate group of TPP.

B.2. Gd(TPyP)-encapsulated through Chitosan nanoparticles

After optimization the procedure of CNs synthesis to obtain small chitosan nanoparticles, the encapsulation of Gd(TPyP) into chitosan nanoparticles has been studied.

B.2.1. UV-Vis spectroscopy of Gd(TPyP)-loaded Chitosan nanoparticles via active and passive routes

Firstly, we studied the loading of Gd(TPyP) into CNs by chemical conjugation. As described in Chapter IV, chemical conjugation of Gd(TPyP) with CNs has been performed by adding 1 mL of Gd(TPyP) either to acetic acid (NPs-1) or to TPP solution (NPs-2). UV-visible spectra of prepared nanoparticles (NPs-1) and (NPs-2) are presented in Fig. 52, comparing with Gd(TPyP) spectrum in ethanol. As presented in Fig. 52, the spectrum of NPs-2 is similar to the spectrum of NPs-1 with slight shift and broader Soret band. The spectrum of NPs-1 contains the intense Soret band at 445 nm followed by 3 Q bands (522 nm, 552 nm and 588 nm) while the spectrum of prepared NPs-2 contains a broad and low intense Soret band at 416 nm followed by 3Q bands (516, 556, and 587 nm).

The disappearance of the characteristic Q band of Gd(TPyP) at 554 nm and the growth of characteristic Q band of ($TPyPH_2$) at 517 nm in both NPs-1 and NPs-2 has been observed that could be marked as a structural deformation of Gd(TPyP). According to the large ionic radii of Gd(III), Gd(III) can not fit in the central cavity of porphyrin and thus it locates out of the porphyrin plane. Hence, the complex could be easily demetallated in acidic media. For example, the demetallation of Sn(TPyP) in acidic solution has been studied by UV-visible spectroscopy [269]. It has been observed that the Soret band of Sn(TPyP) shifted from 424 nm to 417 nm with changing the solvent from dimethylformamide (DMF) to hydrochloric acid solution HCl-H2O following with four Q bands. Referring to the demetallation probability of Gd(TPyP) during chemical conjugation of Gd(TPyP) to CNs, chemical conjugation would not be an appropriate method for encapsulation of Gd(TPyP) into CNs.

From Fig. 52, electronic absorption spectrum of Gd(TPyP) conjugated with CNs via passive method is similar to Gd(TPyP) in ethanol. The nanoparticles' spectra display an intense sharp Soret band at 419 nm followed by a typical Q band at 552 nm. The slight observed shift should be related to the solvent. The absorption spectrum of the chemical species in solution strongly depends on the solvent-solute interaction and solvent nature (polarity of solvent) [335]. The intermolecular solvent-solute interaction alters the energy difference between ground and excited state of chemical species [336]. Thus, the solvent nature has an impact on the UV-visible spectrum of chemical species.

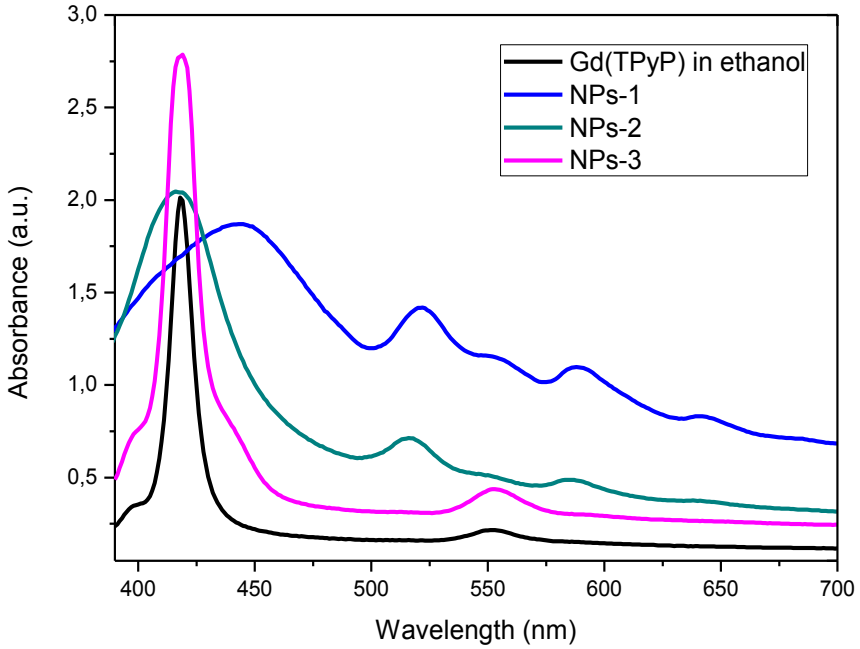

Figure 52. UV-Vis spectra of Gd(TPyP) in ethanol, NPs-1 and NPs-2: Gd(TPyP)-CNs via chemical conjugation, NPs-3: Gd(TPyP)-CNs via passive method

B.2.2. Evaluation of Gd(III) concentration loaded into Chitosan nanoparticle

Different quantities of Gd(TPyP) were conjugated through CNs via passive method. As presented in Fig. 53, all samples showed high water solubility and purple color which increased with the Gd(TPyP) concentration. Sample 1, 2, 3, and 4 referred respectively to the CNs:Gd(TPyP) ratio of 1:0.5 , 1:1, 1:2 and 1:3 which were dispersed in 4 ml of distilled water. UV-visible spectroscopy was used to determine the concentration of Gd(TPyP) into nanoparticles. Figure 53 exhibited the electronic absorption of Gd(TPyP)-CNs after adsorption of different quantities of Gd(TPyP) to CNs. It can be seen that the Soret band intensity of Gd(TPyP)-CNs enhances with the concentration of Gd(TPyP) except for sample 4. In order to prepare the clear solution for UV-visible measurements, sample 1 to 3 was diluted by adding 40µl of prepared colloids to 960 µl of distilled water. While for sample 4, regarding to its high absorption intensity (≥2.5%), 20 µl of solution were added to 980 µl of distilled water.

The concentration of analyte in solution could be determined by measuring the absorbance at the fixed wavelength by applying Beer-Lambert law. From Beer Lambert law, absorbance of solution is directly proportional to the concentration of analyte as follows

$$A = \varepsilon.c.L \tag{34}$$

While L is the path length through the sample, c is the molar concentration of species in the solution and ε is the molar absorptivity (extinction coefficient).

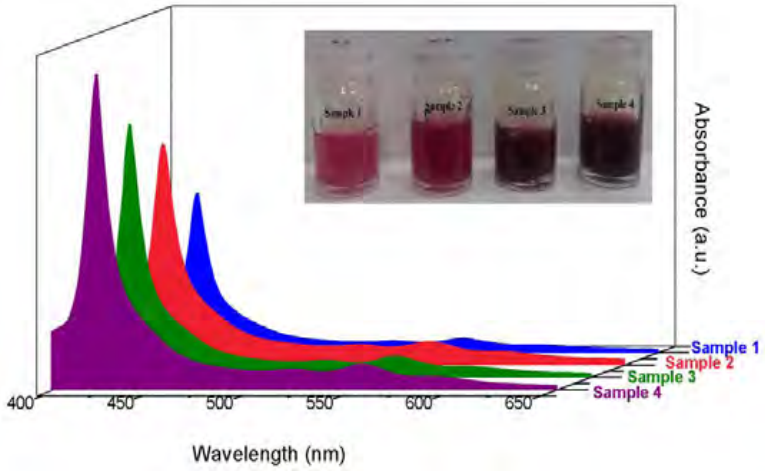

Figure 53. UV-visible spectra of Gd(TPyP)-CNs with different concentration of Gd(TPyP)

The Soret band intensity of all four samples (at 419 nm) was measured from UV-visible spectra. It is required to evaluate the molar absorptivity of Gd(TPyP) in water to determine precisely the concentration of Gd(TPyP) in the prepared nanoparticles.

The molar absorptivity of Gd(TPyP) in water, however, is an obstacle due to the poor solubility of Gd(TPyP) in water. Thus, 1 mg of Gd(TPyP) was first dissolved in 1 mL of ethanol. Afterwards, 50 µL of Gd(TPyP) solution was diluted with 1.95 mL of distilled water. Next, a series of concentrations was prepared from the main solution. From Beer-Lambert law and their UV-visible spectra, the molar absorptivity of Gd(TPyP) in water was calculated. The details are summarized in Table 17.

Table 17. The concentration of Gd(TPyP) in water and UV-visible absorbance (a.u.)

Final concentration of Gd(TPyP) (µM)	Absorbance at 419 nm (a.u.)
4.5	0.486
6	0.873
9	1.283
10.5	1.467

The molar absorptivity of Gd(TPyP) in water at 419 nm was determined by a linear fit of absorption intensity as a function of Gd(TPyP) concentrationwhich is 1.582×10^5 $L.mol^{-1}.cm^{-1}$ as presented in Fig. 54.

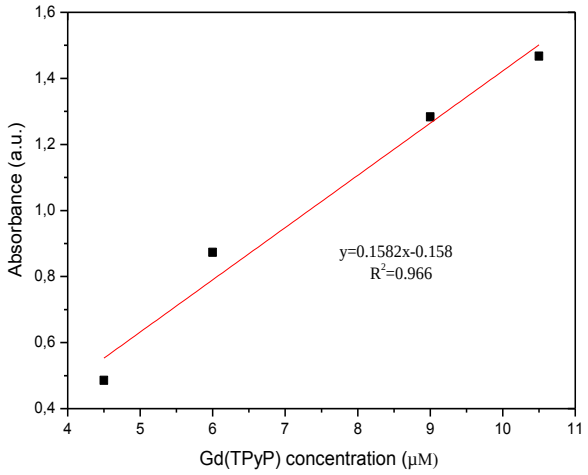

Figure 54. Evaluate molar absorptivity of Gd(TPyP) in water at 419 nm

Referring to evaluated molar absorptivity of Gd(TPyP) in water, we are able to calculate the concentration of conjugated Gd(TPyP) in the nanoparticles from their UV-visible spectra. Furthermore, quantitative measurements with inductively coupled plasma mass spectrometry (ICP-MS) were performed for the same samples. This method gives the real value of Gd loaded in CNs. The two analytical methods show the increase of the amount of Gd(TPyP) adsorbed into chitosan nanoparticles from sample 1 to 4. A one-to-one linear correlation between the values obtained via UV-vis and ICP-MS was observed, Fig. 55.

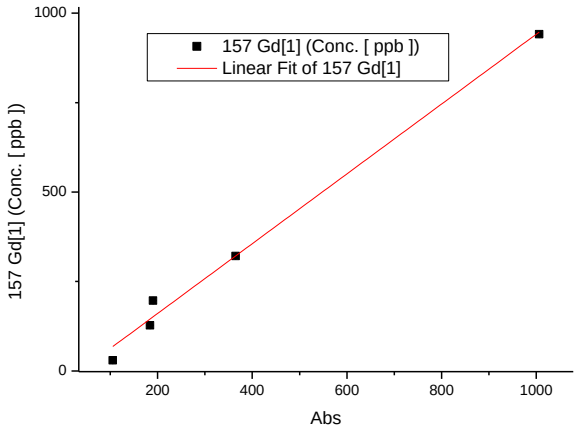

Figure 55. ICP results versus absorbance of Gd(TPyP)-CNs after conjugation of different quantities of Gd(TPyP) with CNs

Entrapment efficiency (EE), loading capacity (LC) and yield percentage of prepared samples were evaluated, as described in the experimental section (B.4.7). The effect of different

concentrations of Gd(TPyP) on EE, LC and yield (%) of Gd(TPyP)-CNs is presented in Fig. 56. It can be observed that the maximum EE (87%) was achieved at CNs:Gd(TPyP) ratio of 1:2 while LC (%) and yield (%) reach their maximum values at the ratio of 1:3.

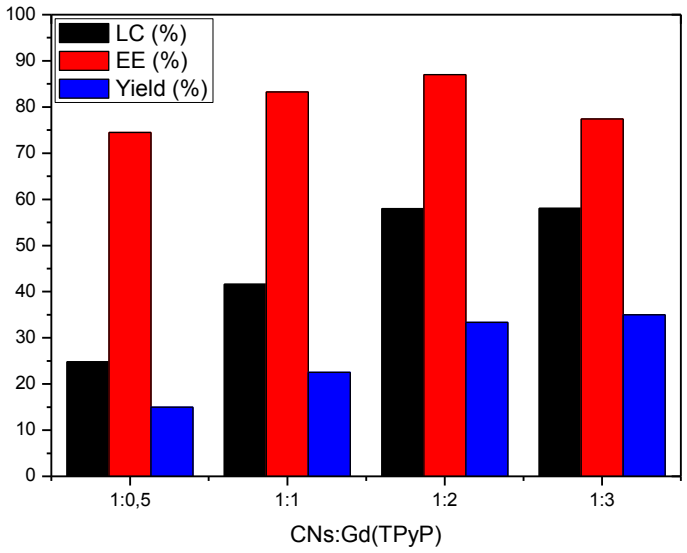

Figure 56. Entrapment efficiency (EE), loading capacity (LC) and yield % for different CNs: Gd(TPyP) ratios

B.2.3. Physicochemical properties of Gd(TPyP)-loaded CNs

The morphology of Gd(TPyP)-CNs has been analyzed via SEM, presented in Fig. 57. From SEM images, Gd(TPyP) -CNs are of uniform spherical shape and the absorption of Gd(TPyP) into CNs does not cause any changes in the shape of CNs. The particle size of Gd(TPyP)-CNs from SEM images is determined in the range of 45-65 nm.

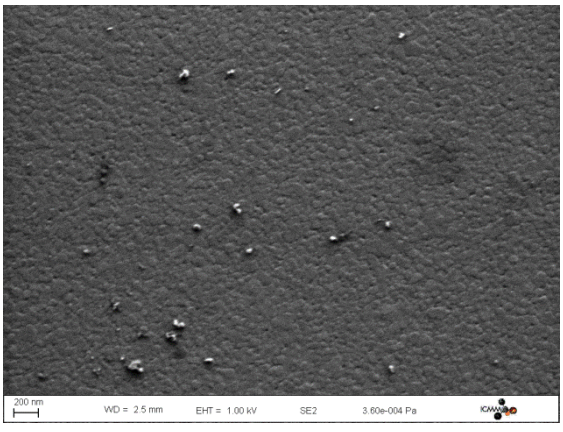

Figure 57. SEM image of Gd(TPyP)-CNs with ratio of 3:1

The hydrodynamic radius and polydispersity of prepared Gd(TPyP)-CNs have been studied via DLS. The typical size distribution by scattering intensity graph of CNs and Gd(TPyP)-CNs are presented in Fig. 58. The size distributions of CNs and Gd(TPyP)-CNs in water consist of a single peak with maximum at 120 and 412 nm, respectively. It is noteworthy to indicate that the size of Gd(TPyP)-CNs measured either by SEM or by DLS remains unchanged for nanoparticles with different Gd(TPyP) concentrations. The increase of the average particle size can be attributed to the association of the macrocycle to the chitosan nanoparticles.

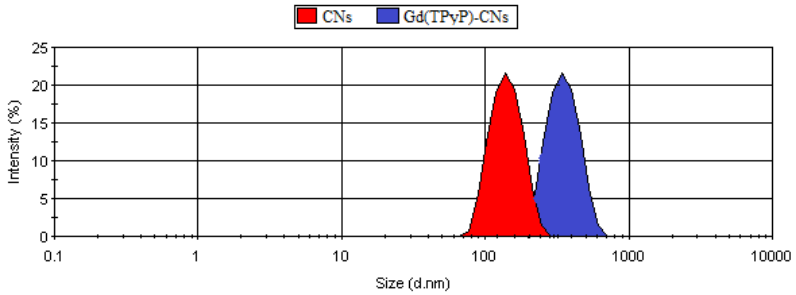

Figure 58. DLS results of optimized chitosan nanoparticles and Gd(TPyP)-CNs with ratio of 3:1

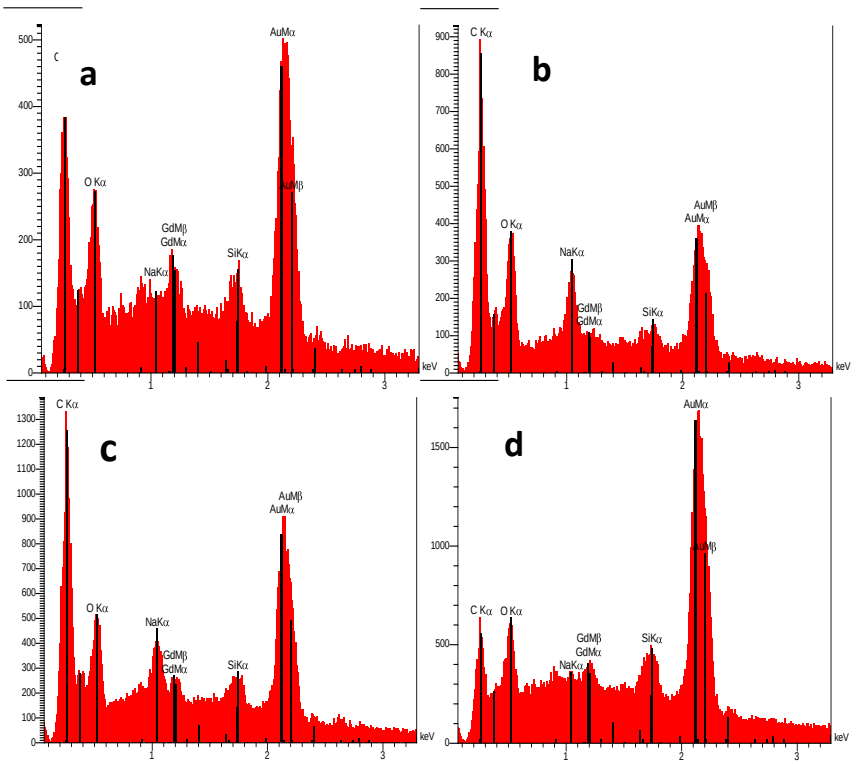

Figure 59. EDX spectra of Gd(TPyP)-CNs with different ratio of Gd(TPyP):CNs a) sample 1 (0.5:1 mg), b) sample 2 (1:1 mg), c) sample 3 (2:1 mg) and d) sample 4 (3:1 mg)

The presence of Gd(III) in prepared Gd(TPyP)-CNs was investigated using EDX-SEM. As presented in Fig. 59, EDX spectra confirm the existence of Gd(III) in all four Gd(TPyP)-CNs particles.

B.2.4. Fourier Transform Infrared Spectroscopy of prepared CNs-Gd(TPyP)

FT-IR studies of Gd(TPyP) and Gd(TPyP)-CNs were performed to characterize the chemical structure of Gd(TPyP)-CNs nanoparticles. The infrared spectra of prepared Gd(TPyP)-CNs, Gd(TPyP), and CNs are shown in Fig. 60. The FT-IR spectrum of Gd(TPyP)-CNs is similar to the CNs spectrum with additional peaks referring to IR of Gd(TPyP). The IR spectrum of Gd(TPyP)-CNs contains a peak at 1641 cm^{-1} due to carbonyl vibration of CNs. Moreover, the typical pyridyl vibration peak of Gd(TPyP) at 1540 cm^{-1} disappears in the IR spectrum of the Gd(TPyP)-CNs. This could demonstrate the interaction of chitosan with the pyridyl following hydrogen binding. Furthermore, after conjugation of Gd(TPyP) with CNs, IR band of CNs amido group C═O was shifted from 1631 to 1641 cm^{-1} which could be related to coordination between chitosan and Gd(TPyP).

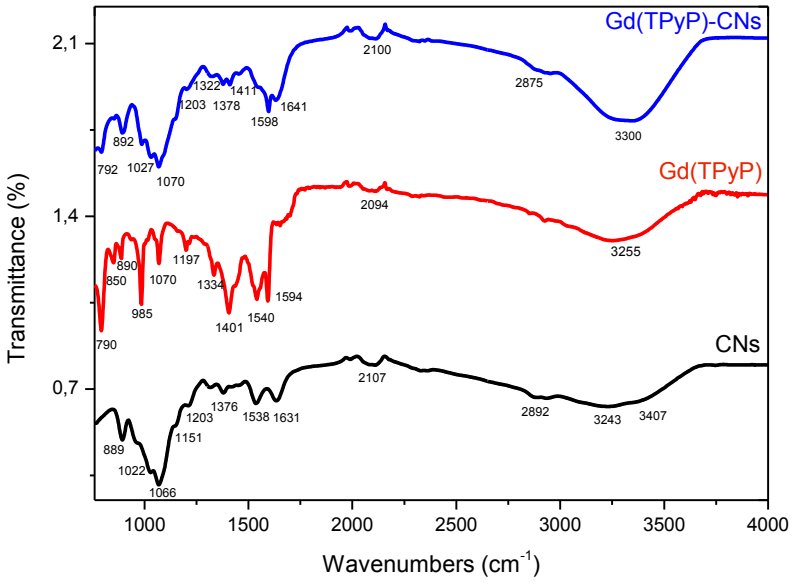

Figure 60. FT-IR spectra of a) CNs, b) Gd(TPyP), c)Gd(TPyP)-CNs

B.2.5. Magnetic Resonance Imaging of Gd(TPYP)-CNs

The potential of Gd(TPyP)-CNs in water as MRI contrast enhancement was studied via MRI at 3T and 25°C. T1 and T2 weighted images of Gd(TPyP)-CNs solution are presented in Fig. 61. T1 signal intensity increases with increasing the loading amount of Gd(TPyP) as well as the Gd(III) concentrations, and conversely for the T2 signal intensity.

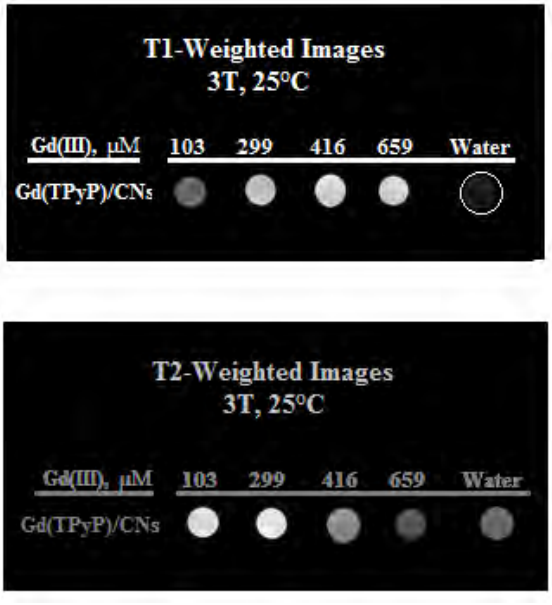

Figure 61. T1 (TR=400 ms, TE=8 ms) and T2 (TR=1500 ms, TE=40 ms) weighted spin echo MR images of different concentration of Gd(TPyP)-CNs in water at 3T and 25°C

The longitudinal and transverse relaxivities (r1 and r2) of Gd(TPyP)-CNs were evaluated and represented in Fig. 62. r1 of Gd(TPyP)-CNs in water (38.35 $mM^{-1}.s^{-1}$) is 56% higher than Gd(TPyP) in ethanol (r1=24.5 $mM^{-1}.s^{-1}$) while its r2 (33.43 $mM^{-1}.s^{-1}$) decreases by 52% compared with the one of Gd(TPyP) in ethanol (r2=69.97 $mM^{-1}.s^{-1}$) at 3T and 25°C. The measured r1 of Gd(TPyP)-CNs is ~12 times greater than the r1 of Gd-Dota at 3T.

The relaxivity enhancement of contrast agents conjugated to CNs has already been reported in some works. It was found that r1 of Gd-DTPA improved with conjugation to CNs from 3.62 $mM^{-1}.s^{-1}$ to 11.62 $mM^{-1}.s^{-1}$ at 0.5T and 32°C [146]. In another examlpe, Mn-DTPA-CNs in aqueous solution showed high r1 of 7.21 $mM^{-1}.s^{-1}$ at 0.5T and 32°C [155]. In the other research, Gd-Dota attached to bimodal chitosan nanoparticles with small size (22 nm) exhibited high r1 of 41.1 $mM^{-1}.s^{-1}$ at 4.7T [337]. Gd-phostriamine (MS-325) chelated with chitosan– β –cyclodextrins (CD) in aqueous solution also showed higher r1 of 27.5 $mM^{-1}.s^{-1}$

compared with the one of MS-325 binding toward β-CD monomers (11.5 $mM^{-1}.s^{-1}$) at 0.47T and 25°C [338].

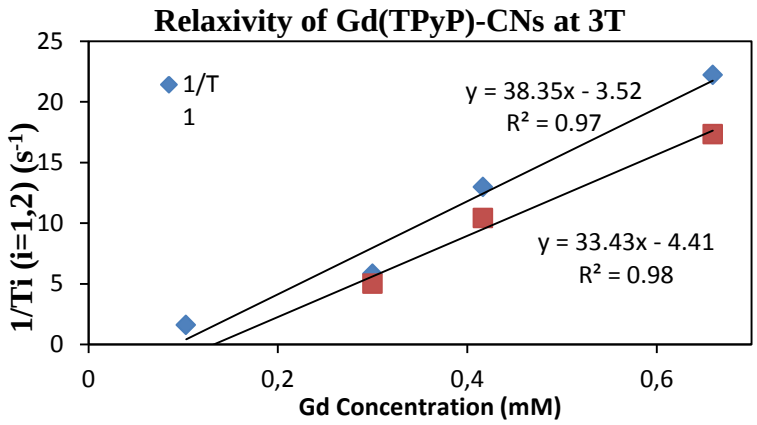

Figure 62. Longitudinal and transverse relaxation rates [$(1/T_1)$ and $(1/T_2)$] of Gd(TPyP)-CNs versus the Gd(III) concentrations in water at B_0=3T and T=25°C

Thereby, the enhancement of r1 relaxivity with conjugation of Gd(TPyP) to CNs, as presented in Fig. 63, is consistent with published values. The enhancement of relaxivity with conjugation of agent to CNs could be explained as a result of a combination of factors: i) a decrease in rotational correlation time by attachment of the complex to the CNs, ii) an increase in the exchange rate of nearby coordinated water molecules and iii) an increase in the amount of paramagnetic ion loaded into the nanoparticles [152].

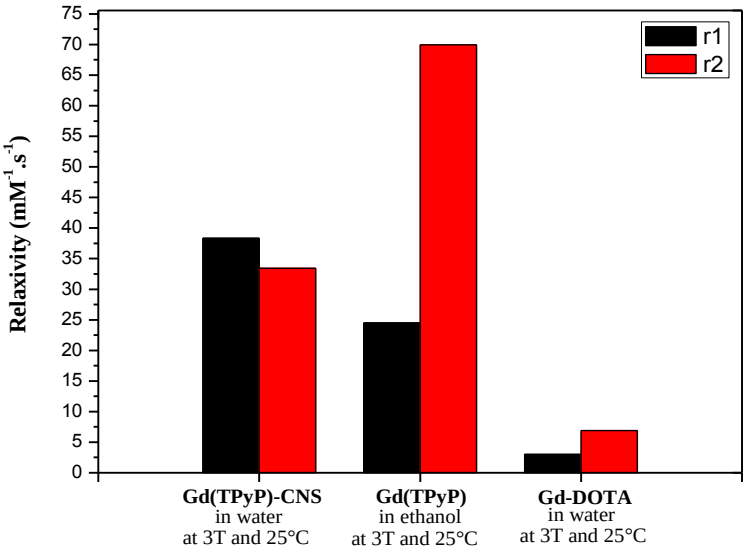

Figure 63. r1 and r2 relaxivity of Gd(TPyP) encapsulated with chitosan nanoparticles, Gd(TPyP) and Gd-DOTA at 3T and 25°C

It has been found that the water diffusion in the presence of particles with hydrophilic shells decreased which causes r2 to increase [339]. Additionally, we could assume that more than one Gd(III) has been loaded into nanoparticles, leading to an increase in r2. Nonetheless, our obtained result is inconsistent with these explanations. We observed that the r2 decreased from 69.97 $mM^{-1}.s^{-1}$to 33.43 $mM^{-1}.s^{-1}$ after conjugation of Gd(TPyP) with CNs. The problem of Gd(TPyP) solubility in organic solvent can lead to the formation of aggregates. It is known that r2 relaxivity is very sensitive to the aggregation in which r2 relaxivity increases with aggregation [340]. Thus, the high r2 of Gd(TPyP) in ethanol could be ascribed to its aggregation during measurements. Whereas, loading of Gd(TPyP) to CNs with great water solubility leads to prevent the formation of the aggregates.

C. Mn-doped ZnS ultrasmall Nanoparticles

ZnS is recognized as one of the most promising materials for a number of optoelectronic applications. Thus, different transition metal (TM) ions can be introduced into their lattices, which not only serve as the luminescent centers to bring new emissions, but also make QDs exhibit ferromagnetic properties [341], [342]. ZnS:TM quantum dots have exhibited their potential in a number of promising applications in biomedicine, including magnetic resonance imaging, luminescence labeling, therapeutic for hyperthermia and targeted drug delivery. In this section, we demonstrate the physicochemical, photoluminescence and relaxivity results of developed Mn:ZnS with different dopant concentrations.

C.1. Structural and Elemental analysis of $Mn_xZn_{x-1}S$ (x=0.1, 0.2, 0.3)

The structural characterization of MnZnS QDs with different Mn contents was performed using X-ray diffraction (CuK_α radiation). The recorded X-ray powder diffraction (XRD) pattern of $Mn_xZn_{1-x}S$ nanoparticles are represented in Fig. 64. The diffraction patterns of MnZnS are consistent with the JCPDS data of ZnS (card No. 05-0566). From Fig. 64, XRD patterns contain three main broad peaks corresponding to the (111), (220) and (311) planes in which the strongest peak corresponds to (111) plane. MnZnS nanoparticles possess a single-phase cubic crystal structure with $F\bar{4}3M$ symmetry. This indicates that the doping Mn^{2+}ions has no effect on the crystal structure of ZnS. No additional peak corresponding to any other crystallographic phase or unreacted ingredient was observed. Moreover, the broad peak

clearly indicates the small nanocrystal sizes. The mean diameter of particle size was determined via MAUD software (Table 18). The average particle sizes of $Mn_xZn_{x-1}S$ ($0.1 \leq x \leq 0.3$) are in the range of 1.6 - 1.9 nm.

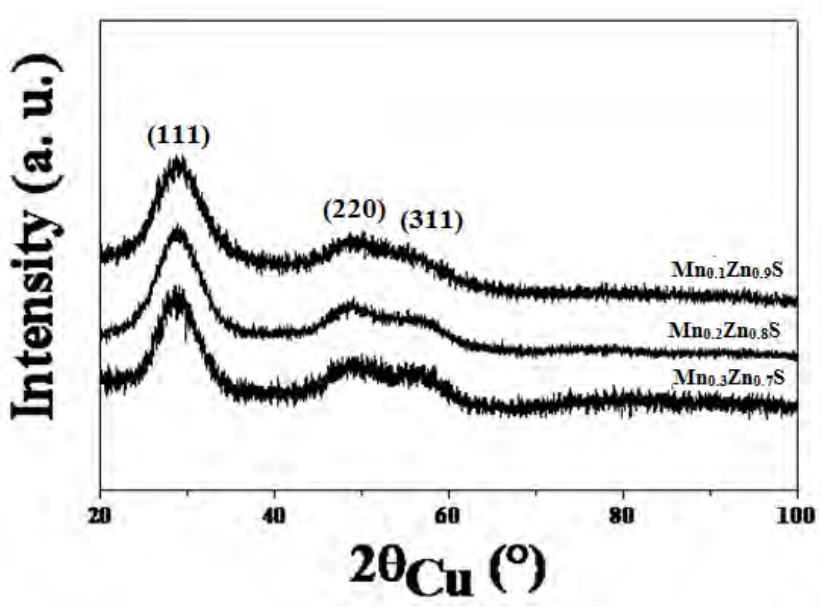

Figure 64. The XRD patterns of the as-prepared $Mn_xZn_{1-x}S$ (x=0.1, 0.2, and 0.3)

The microstructures of the Mn-doped ZnS nanoparticles were characterized by TEM. Figure 65 shows the TEM images of Mn:ZnS with different Mn(II) content. TEM images exhibit spherical nanoparticles with nearly uniform size of ~1.55 nm, which is consistent with the XRD results with slight differences. The evaluated particle size from TEM images are listed in Table 18. The inset of Fig. 65 shows the representative selected area electron diffraction pattern, confirming the crystalline planes of MnZnS. The electron diffraction of the selected area shows two rings which correspond to the (111) and (220) planes of cubic ZnS.

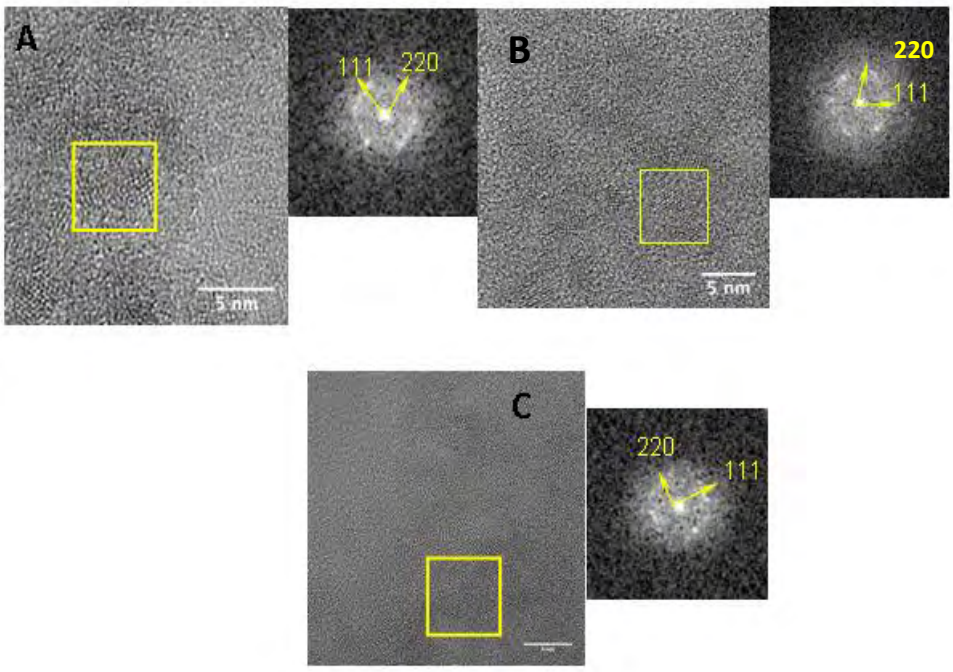

Figure 65. TEM image of Mn-doped ZnS nanoparticles with different Mn content

In addition, EDX and XRF measurements were carried out to determine the overall composition and spatial distribution of Mn ions in Mn:ZnS as listed in Table 18. EDX of all three samples confirmed the presence of Mn (II) and the evaluated weight percent (wt%) are very close to the nominal value. Moreover, the concentration of Mn(II) content in Mn:ZnS was precisely investigated with XRF. The percent composition of Mn and Zn in Mn:ZnS are listed in Table 18. The measured Mn contents in all three samples by XRF are consistent with the EDX results.

Table 18. Physico-chemical characteristics of $Mn_xZn_{1-x}S$ such as chemical composition from EDX and XRF analyses, and the average crystal size $<L_{XRD}>$ from XRD and $<D_{TEM}>$ the average particle diameters from statistical analysis of TEM images

Samples	Mn/(Zn+Mn) at.-%		Zn/(Zn+Mn) at.-%		Nanoparticles size	
	EDX	XRF	EDX	XRF	$<L_{XRD}>$ (nm)	$<D_{TEM}>$ (nm)
$Mn_{0.1}Zn_{0.9}S$	10	9.2	90	90.8	1.6	1.54 ± 0.15
$Mn_{0.2}Zn_{0.9}S$	20	17.0	80	83	1.8	1.63 ± 0.26
$Mn_{0.3}Zn_{0.7}S$	30	26.0	70	74	1.9	1.55± 0.25

C.2. Optical properties of $Mn_xZn_{1-x}S$(x=0.1, 0.2, and 0.3)

Room temperature photoluminescence (PL) emission spectra of all three MnZnS samples are presented in Fig. 66. From Fig. 66, all three samples exhibited a broad blue emission band with a distinct peak around 465 nm.

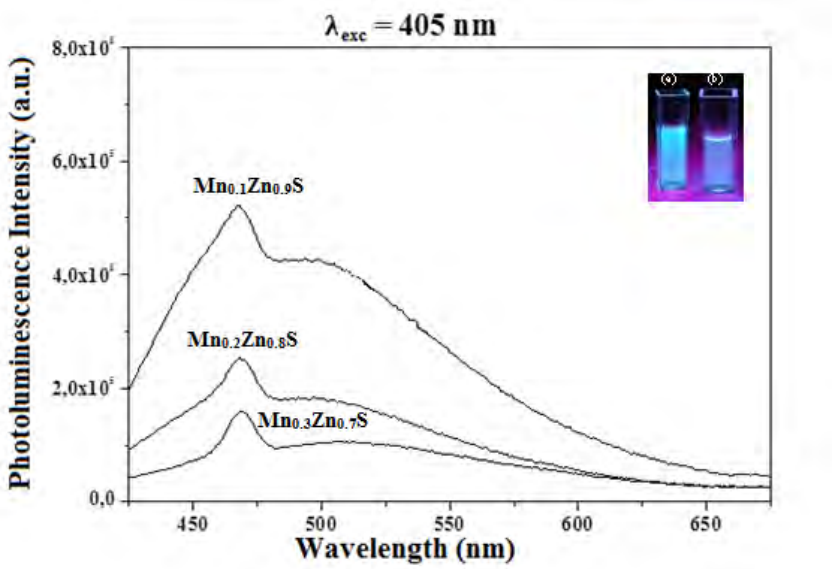

Figure 66. Photoluminescence emission spectra of $Mn_xZn_{1-x}S$ ($0.1 \leq x \leq 0.3$) recorded for λ_{exc}=405 nm at room temperature , inset the emission observed from a) $Mn_{0.1}Zn_{0.9}S$ and b)ZnS at 325 wavelength

The PL emission of Mn:ZnS with different concentration of Mn [343]–[352] and at different excitation wavelengths [343], [345], [346] has been extensively studied by many groups. Due to the literature review, the entire PL spectrum of Mn-doped ZnS nanoparticles is dominated by two-emission bands, blue in the range of 400-500 and yellow emissions around 580-600 nm. The blue emission should be associated with the emission of defect of ZnS host [353], [354] while yellow emission is associated with $^4T_1 - {}^6A_1$ transition within 3d Mn(II). Due to Bhargava and Gallagher studies [355], yellow-orange emission in MnZnS is ascribed to the energy transfer from ZnS host to Mn(II) ions. As illustrated in Fig. 67, during PL process, the electron from valence band of ZnS crystal is excited across the band gap. Due to recombination processes, the photoexcited electron subsequently decays. With doping Mn in the ZnS host lattice, Mn(II) occupies a tetrahedral site and the photoexcited electron may be captured by Mn(II) ions. Thereby, the transition of $^4T_1 - {}^6A_1$ is partially possible due to the mixing of s-p electrons of ZnS with d electrons of Mn(II) ions, resulting in characteristic

emission of Mn(II) [356]. In comparison with the reported emission spectrum of Mn-doped ZnS, in all three PL emissions of Mn:ZnS, we observed just one broad peak at ~470 nm with no yellow emission. The luminescence emission includes band-edge emission and trap-state emission – which originate in defects containing vacancies and interstitials. The Peak emission around 465 nm, can be attributed to dangling Sulphur bonds that there are the Zn and S interstitial transitions and S or Zn vacancies – which would lie close to the band edge.

Lü *et al.*[345] have been studied the PL spectrum of ZnS:Mn nanoparticles at different excitation wavelength. They have observed that the intensity of blue emission peak was stronger than intensity of yellow emission peak after the excitation wavelength reached 340 nm and the yellow emission band vanished at the excitation wavelength of 376 nm. Meanwhile, Zhang *et al.*[343] have also observed that Mn emission could be observed at excitation wavelength in the ultraviolet region (280 nm$\leq\lambda_{exc}\leq$370 nm). Referring to their studies, the maximum emission intensity of Mn(II) was observed at excitation wavelength of 320 nm [343]. The PL emission of Mn:ZnS has also been studied Marandi *et al.* [352]. They found that the irradiation time during fluorescence studies has an effect on PL spectrum of Mn:ZnS. They have reported that the PL emission of Mn(II) at 585 nm emerged at longer irradiation times ($\geq$2 min) [352]. Moreover, they observed that the emission peak of Mn increased by increasing Mn:Zn ratio up to 1% and after that the luminescence decreased and vanished at higher Mn:Zn ratios (at 10%) [352]. Furthermore, it has been accepted that thiol ligands is a PL quencher [357], [358]. The highest occupied molecular orbital (HOMO) of thiol ligands has the higher energy level compared with quantum dots (QDs) valence bands which results in transfering of photoexcited holes from top of QDs valence band to HOMO level of thiol ligands [359], [360]. Thereby, thiol ligands act as the hole scavengers which could lead to reduced PL emission intensity.

Due to the above discussions, PL emission of Mn:ZnS could be influenced by the following issues: i) the excitation wavelength, ii) the irradiation time during florescence studies, iii) concentration of Mn dopant, and iv) the effect of thiol ligands. Furthermore, location of Mn(II) could also affect the photoluminescence properties of Mn:ZnS. Theoretically, Mn(II) ions should incorporate in the ZnS nanocrystals and occupy Zn^{2+}ion sites in the host lattice (ZnS) regarding to their similar sizes and charges [361]. It has been reported that a part of Mn(II) ions could be located on the surface of ZnS nanocrystal [362]–[364]. Sooklal *et al.* have found that Mn(II) ions incorporated into ZnS lattice or on the surface of ZnS would yield the orange and ultraviolet emission, respectively [365]. They have observed the blue emission

at 390 nm for MnZnS nanoparticle when Mn(II) distributed on the surface of ZnS [365]. Photographs of PL emission of $Mn_{0.1}Zn_{0.9}S$ and ZnS under UV excitation (325 nm) are presented in inset of Fig. 66. Remarkably, we observe the blue emission of Mn:ZnS which indicates the incorporation of Mn(II) on the surface of ZnS. Thereby, no orange-yellow emission in PL spectra of all three prepared Mn:ZnS in our study could be referred to the distribution of Mn(II) partially on or close to the surface of ZnS.

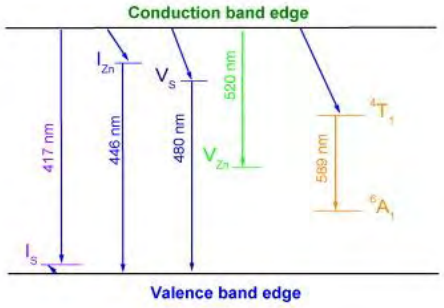

Figure 67. The schematic diagram of energy-level of Mn doped ZnS nanoparticles corresponding to photoluminescence spectra[348]

C.3. Magnetic properties of $Mn_xZn_{x-1}S$ (x=0.1, 0.2, 0.3)

Figure 68 shows the magnetization of $Mn_xZn_{x-1}S$ ($0.1 \leq x \leq 0.3$) versus magnetic field. The M-H curves of all Mn-doped ZnS reveals no saturation magnetization up to 50kOe with zero coercivity and remanence values. All three samples exhibited characteristic paramagnetism at room temperature.

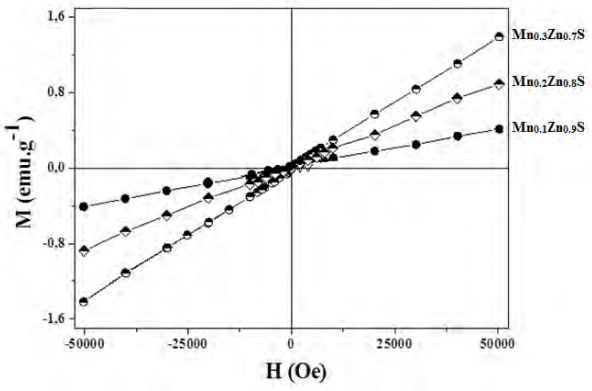

Figure 68. Magnetization versus magnetic field up to 50 kOe for $Mn_xZn_{1-x}S$ nanoparticles with different Mn contents (x=0.1, 0.2, and 0.3) at 300K

The magnetizations of as prepared Mn-doped ZnS ($0.1 \leq x \leq 0.3$) are much higher than the magnetization of bulk Mn-doped ZnS[366]. We observed that the magnetization of Mn:ZnS increased with Mn dopant content. From M-H curves of Mn doped ZnS, magnetization increased linearly from 0.24 emu.g^{-1} to 1.44 emu.g^{-1} (Fig. 68) with increasing Mn doping concentrations from 0.1 to 0.3, respectively. This enhancement is attributed to the enhanced exchange interactions referring to higher density of Mn^{2+} in samples [367].

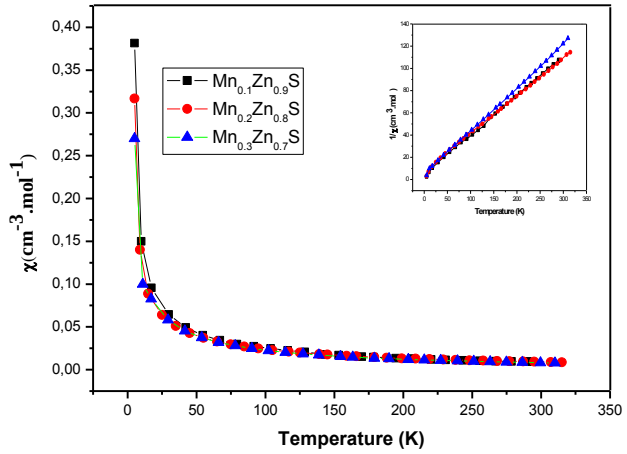

Figure 69. Susceptibility versus temperature and in the inset the temperature dependence of inverse magnetic susceptibility of Mn-doped ZnS with different dopant concentrations ($0.1 \leq x \leq 0.3$) at 2kOe

The susceptibility of Mn:ZnS with different Mn(II) contents was investigated at different temperatures under an applied magnetic field of 2 kOe. As shown in Fig. 69, all three samples exhibited the smooth and featureless curves. Moreover, susceptibility decreases with increasing temperature which is the characteristic paramagnetic behavior.

The magnetic properties of Mn-doped ZnS crucially depend on Mn doping concentration. At low Mn content, Mn atoms replaced the host lattice cations, while at high Mn concentration the Mn atoms cannot be considered as isolated one. At higher Mn concentrations, Mn clusters can form which could cause the antiferromagnetic behavior [368]. Thereby, the stable states of electron spins have opposite directions with nearest neighbors, which causes the antiferromagnetic behavior. This feature was observed for Mn:ZnSe nanoparticles [368]. They have observed the linear dependency of M-H at 5K which is paramagnetism attitude, meanwhile, the negative paramagnetic curie temperature has been obtained [368]. Bulk MnZnS with Mn(II) concentration of 0.28% also showed a negative Curie-Weiss temperature -31K which suggests the presence of antiferromagnetism [366]. In our study, a small negative curie constant was obtained which could be due to the existence of Mn-Mn clusters.

C.4. Magnetic Resonance Imaging of $Mn_xZn_{x-1}S$ (x=0.1, 0.2, 0.3) colloids

The capability of prepared MnZnS colloids on enhancing MRI signal has been studied using a 3T MRI. T1 and T2 weighted images of prepared Mn:ZnS colloids (in water) are presented in Fig. 70. From Fig. 70, Mn-doped ZnS shows appreciable signal enhancement on T1 weighted images compared to ZnS solution. The signal intensity on T1-weighted images of Mn:ZnS increased with increasing Mn(II) concentration. From T2 images, no significant T2 effect could be observed, and T2 images of $Mn_{0.3}Zn_{0.7}S$ were bright compared to those of $Mn_{0.1}Zn_{0.9}S$ and $Mn_{0.2}Zn_{0.8}S$.

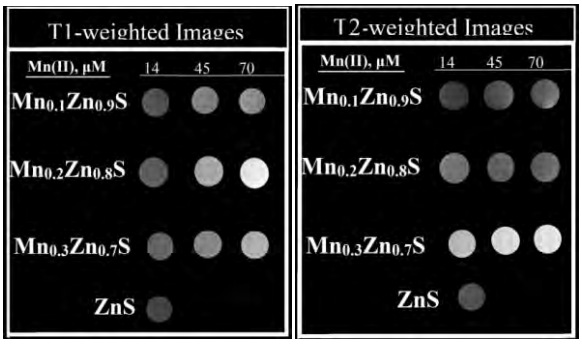

Figure 70. T1 (3T, TR=400 ms and TE=8 ms) and T2(3T.,TR=1500 ms and TE=40 ms) weighted images of ZnS as reference and $Mn_xZn_{1-x}S$ ($0.1 \leq x \leq 0.3$) at 3T and 25°C

Relaxivity is one of the most important parameter to evaluate the efficiency of contrast agents. Thus, longitudinal and transverse relaxation times (T1 and T2) of $Mn_xZn_{1-x}S$ (x=0.1, 0.2, and 0.3) solutions were evaluated from their T1 and T2 weighted images. Figure 71 displays the evaluated relaxivities of $Mn_xZn_{1-x}S$ ($0.1 \leq x \leq 0.3$) in aqueous media. r1 relaxivity increased from 20.34 $mM^{-1}.s^{-1}$ to 86.08 $mM^{-1}.s^{-1}$ and slightly decreased to 75.5 $mM^{-1}.s^{-1}$ with increasing Mn-dopant. The same trend has been observed for r2, increasing from 37.37 $mM^{-1}.s^{-1}$ to 54.95 $mM^{-1}.s^{-1}$ and decreased to 40.4 $mM^{-1}.s^{-1}$ for further increase of Mn content (Mn=0.3).

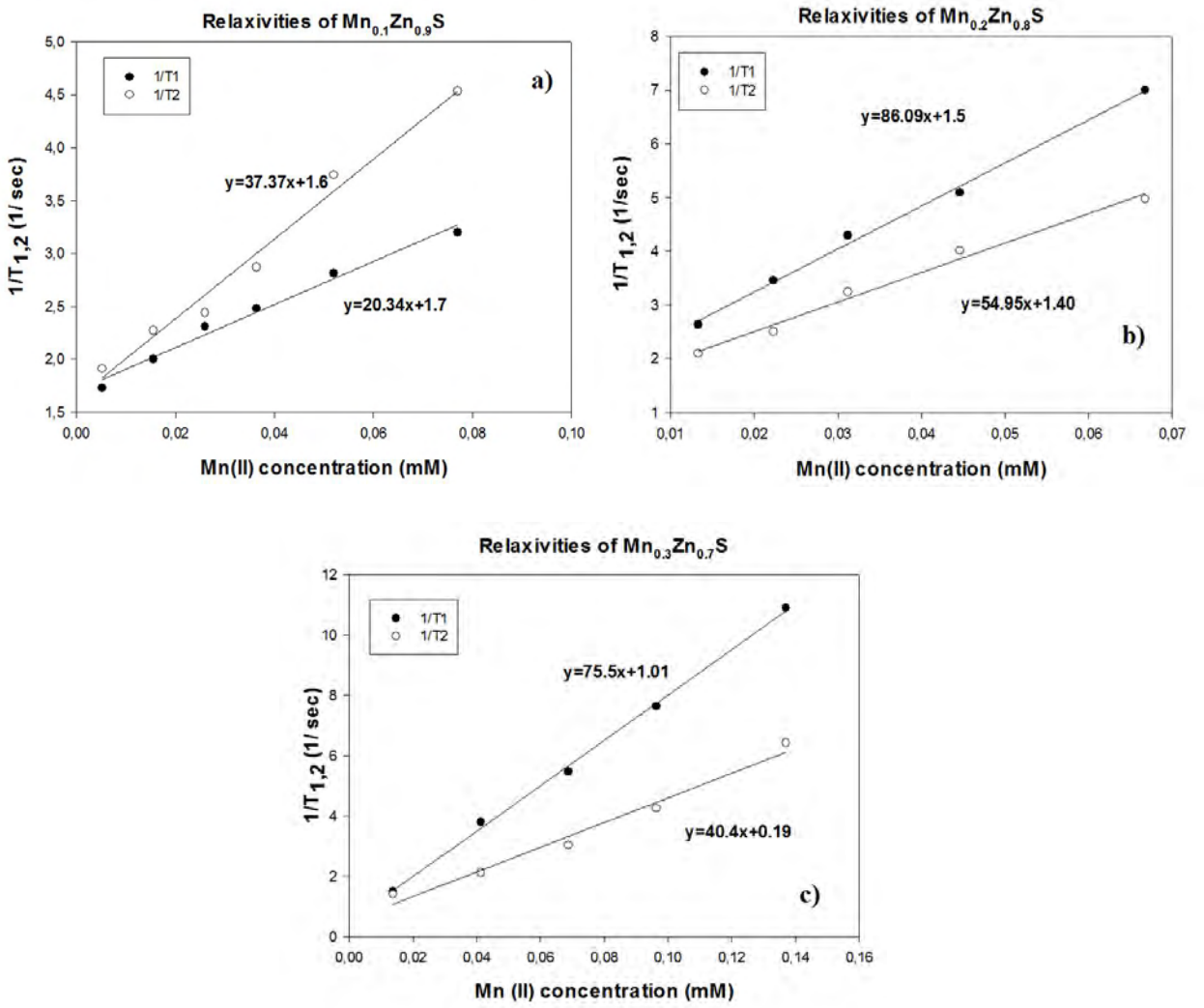

Figure 71. Longitudinal and transverse relaxation rates ($1/T_1$) of a) $Mn_{0.1}Zn_{0.9}S$, b) $Mn_{0.2}Zn_{0.8}S$ and c) $Mn_{0.3}Zn_{0.7}S$ versus the Mn(II) concentrations in aqueous solution at B_0=3T and T=25°C

Relaxivity of paramagnetic-based nanoparticles is attributed to three key parameters, including the number of unpaired spins, paramagnetic properties of metal ions and high surface to volume ratio of nanoparticles [369]. The main advantage of paramagnetic nanoparticles compared to macromolecular chelates is their large surface to volume ratio which causes the majority of paramagnetic ions to accumulate on the surface of the particles [369]. Thereby, the development of the paramagnetic nanoparticles has attracted much attention in clinical imaging technique. For instance, MnO nanoparticles coated via D-glucuronic acid, with average particle diameter in the range of 2 nm to 3 nm and hydrodynamic radius of 5 nm, has shown high r1 and r2 relaxivity of 7.02 $mM^{-1}.s^{-1}$ and 47.97 $mM^{-1}.s^{-}1$, respectively, at 1.5 T [369]. Its high r1 was ascribed to high surface to volume ratio (~0.35), high value of S=5/2 and its paramagnetic characters [369].

Beside the size of particles, the coating of nanoparticles is considered as an important factor on enhancing the relaxivity of paramagnetic-based nanoparticles. For example in the other studeis, MnO (with average diameter of 20 nm) coated with dopamine and human serum albumin (HAS) bilayer induced larger r1 of 1.97 $mM^{-1}.s^{-1}$ (almost 5 times) than r1of the phospholipid coated one (r1=0.37 $mM^{-1}.s^{-1}$) [370]. Both dopamine and HAS are known as hydrophilic ligand which allows for efficient water penetration, causing the r1 enhancement of MnO.

In our study Mn:ZnS exhibits high r1, varying between 20.34-75.5 $mM^{-1}s^{-1}$ with increasing Mn dopant contents. The measured r1 of Mn-doped ZnS is much higher than those of clinically approved Mn contrast agents such as Mn(II) dipyridoxyl diphosphate (Mn-DPDP) (Teslascan®, r1=2.1 $mM^{-1}.s^{-1}$ at 1.5T and 20°C) [371] and $MnCl_2$ (r1=8 $mM^{-1}.s^{-1}$ at 0.47T and 40°C) [372] in aqueous solution. Comparing with the r1 of CdTe/Mn:ZnS with the Mn dopant concentration of 10%, the $Mn_{0.1}Zn_{0.9}S$ in our study shows higher r1 of 20.34 $mM^{-1}.s^{-1}$. The high r1 of $Mn_xZn_{1-x}S$ could be attributed to the ultrasmall size of nanoparticles which caused the accumulation of Mn ions on the surface of ZnS (supported by PL studies of Mn:ZnS), increasing relaxivity. The localization of Mn(II) on or close to the nanoparticle surface would cause the reduction of the distance between paramagnetic ions and bound water molecule which leads to enhanced r1. On the other hand, the coating could also have an impact on relaxivity. The sulphur head of mercaptoacetic acid group coordinates with zinc ions at the surface of MnZnS and its exterior, carboxylic acid group, links to water molecules which lets MnZnS to be soluble in water (as shown in Fig. 72). The hydrophilic mercaptoacetic acid allows water to become accessible to the inner sphere of Mn:ZnS [373], enhancing r1 relaxivity. Thus, mercaptoacetic acid could play a role in obtaining this high relaxivity.

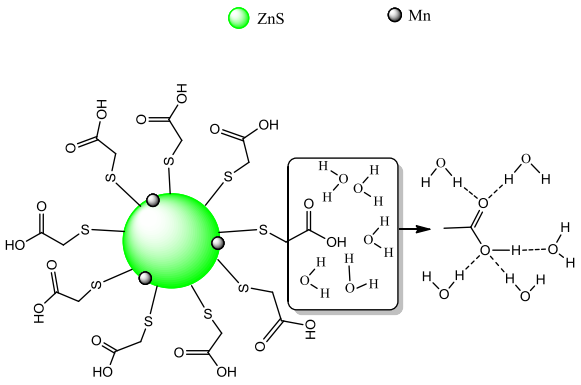

Figure 72. Schematic of Mn:ZnS capped with mercaptoacetic acid and enlarge carboxylic acid interaction with water molecules

Furthermore, second and outer sphere contributions have a significant fraction of total relaxivity for the complex with low molecular weight [276]. Notable second sphere contribution on relaxivity has been studied for 20 different Gd-DOTA derivatives [374]. Each compounds had one water molecule in the inner sphere and in order to promote hydrogen bonding with the second sphere water molecule, nitrogen of amide group of Gd-DOTA was substituted with different groups. The highest r1 (58.1 $mM^{-1}.s^{-1}$ at 0.47 T in serum albumin) was obtained for the compound in which the nitrogen of the amide group was substituted with carboxylate [374]. This high relaxivity was attributed to strong bonding of carboxylate with water molecules in the second sphere which enhances r1 [374]. In other words, the high r1 of Mn:ZnS in our study could be attributed to second sphere contributions. Carboxylic group of mercaptoacetic acid with a high number of strong dipoles is considered as a highly polar organic functional group [375]. Hence, it favorably participates and forms strong H-bonding with water molecules [376]. These strong interactions lead to increase the water residency time in the second sphere [376]. Thereby, the carboxylic group of mercaptoacetic acid can promote the second sphere contribution and resulting in enhancement of the relaxivity of Mn:ZnS.

We observe that r1 and r2 increase with Mn dopant content up to 20% then decrease for further increase. Some researchers have reported this drastic change of relaxivity. For instance, r1 of zeolite GdNaY nanoparticles of 37.7 $mM^{-1}.s^{-1}$ reduces to 11.4 $mM^{-1}.s^{-1}$ at 60 MHz and 37°C with increasing Gd loading into zeolite [377]. The authors have ascribed the relaxivity reduction to a lower number of water molecules per Gd ions inside the zeolite cavity at higher Gd loading and reduction in outer sphere hydration contributions [377]. In other research, r1 of Gd-incorporated mesoporous silica drastically decreased from 23.6 $mM^{-1}.s^{-1}$ to 7.2 $mM^{-1}.s^{-1}$ with increasing incorporation of Gd(III) from 1.6% to 3.1% [378]. This reduction has been attributed to shortening electronic relaxation due to enhancing the dipole-dipole interaction between Gd ions at high loading [378]. In our work, the decrease of relaxivities upon Mn content of 0.3 could be related to significant dipole-dipole interaction at this Mn dopant concentration (0.3) which is shortening electronic relaxation times and reduce the overall relaxivity.

After observing the decrease of r1 and r2 of $Mn_{0.3}Zn_{0.7}S$ compared to those of $Mn_{0.1}Zn_{0.9}S$ and $Mn_{0.2}Zn_{0.8}S$, different particle sizes of $Mn_{0.3}Zn_{0.7}S$ have been synthesized to study whether by increasing the particle size the dipole-dipole interaction of Mn(II) atoms at this concentration could be reduced.

C.5. Physicochemical characterization of $Mn_{0.3}Zn_{0.7}S$ with different particle sizes

The different particle sizes of $Mn_{0.3}Zn_{0.7}S$ nanoparticles have been synthesized and collected from ultrahigh speed centrifugation. The average crystallite sizes of $Mn_{0.3}Zn_{0.7}S$ were estimated from TEM image and XRD spectra. The evaluated results are listed in Table 19. The diameter of different $Mn_{0.3}Zn_{0.7}S$ particles evaluated from TEM images agree well with the XRD data.

Table 19. Particle size of $Mn_{0.3}Zn_{0.7}S$ evaluated from TEM images and XRD spectrum

Sample	Particle size by TEM	Particle size by XRD
$Mn_{0.3}Zn_{0.7}S$ (S1)	1.55	1.8
$Mn_{0.3}Zn_{0.7}S$ (S2)	1.85	1.9
$Mn_{0.3}Zn_{0.7}S$ (S3)	2.1	2.3
$Mn_{0.3}Zn_{0.7}S$ (S4)	2.6	2.5

Figure 73 shows the magnetization of $Mn_{0.3}Zn_{0.7}S$ with different core diameters varied between 1.8-2.5 nm versus magnetic field. M-H curves of all four samples reveal the linear dependency of M with H with zero coercivity and remanence values and no saturation magnetization. All samples exhibited paramagnetic properties at room temperature.

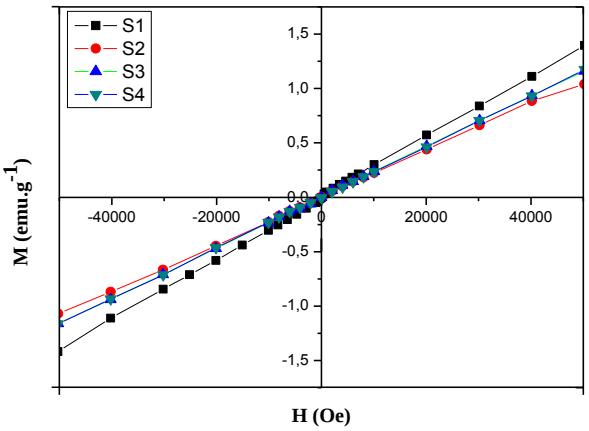

Figure 73. Magnetization versus magnetic field up to 50 kOe for $Mn_{0.3}Zn_{0.9}S$ nanoparticles with different particle sizes at 300K

C.6. Size dependent r1 and r2 relaxivities of $Mn_{0.3}Zn_{0.7}S$ nanoparticles

T1 and T2 weighted images of four samples (S1, S2, S3, and S4, as listed in Table 19) in aqueous solution at 3T are presented in Fig. 74. As shown in Fig. 74, $Mn_{0.3}Zn_{0.7}S$ induced a signal intensity enhancement on T1 weighted images with increasing the Mn(II) concentrations. It is noteworthy that at the same imaging parameters and same concentrations of Mn(II) ions, the signal intensity on T1 weighted images increase with particle size of nanoparticles. Moreover, the signal intensity on T2 weighted images increases with Mn(II) concentration until 70 μM. Signal intensity loss on T2 weighted images could be observed for samples with concentration of 100 μM which increases with particle size.

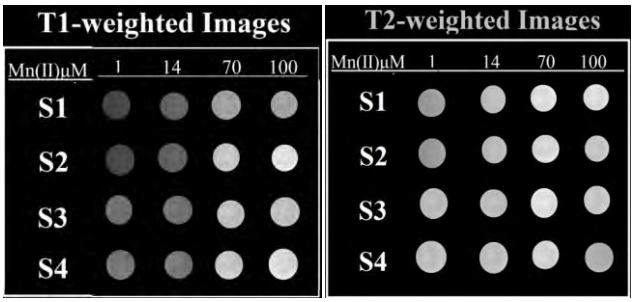

Figure 74. T1 (TR=400 ms, TE=8 ms) and T2 (TR=1500 ms, TE=50 ms) weighted spin echo MR images of different concentrations of $Mn_{0.3}Zn_{0.7}S$ with different particle size in water at 3T and 25°C

r1 and r2 relaxivities of the different particle sizes of $Mn_{0.3}Zn_{0.7}S$ are presented in Fig. 75. r1 relaxivity decreased dramatically with increasing the particle size from a value of 75.5 $mM^{-1}.s^{-1}$ for S1, with diameter of 1.55 nm, to 42.81 $mM^{-1}.s^{-1}$ for S4 with average diameter of 2.5 nm. Simultaneously, r2 decreased from 40.4 to 31.4 and subsequently, it remained unchanged with further increase of particle size.

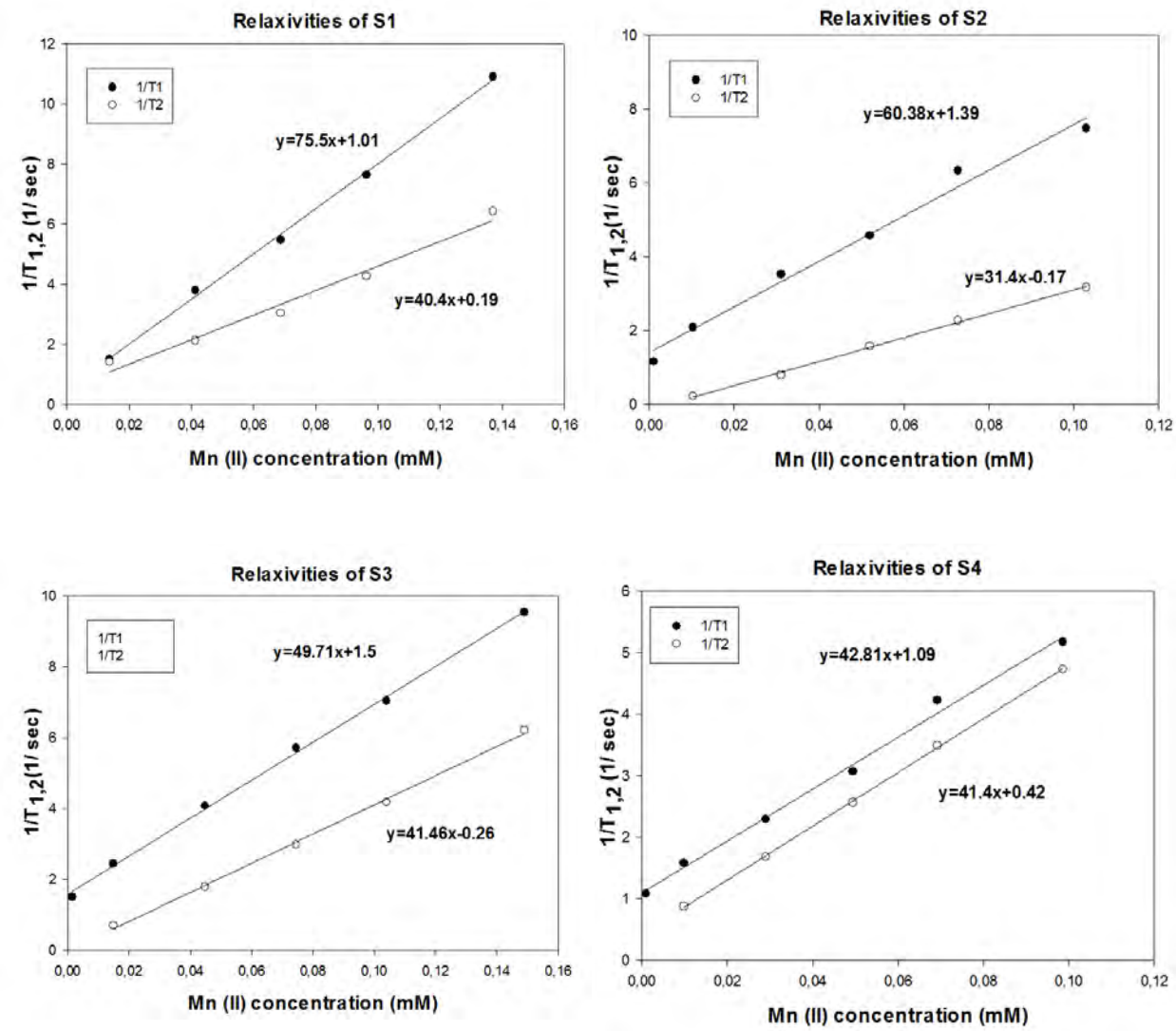

Figure 75. The longitudinal and transverse relaxation rates (1/T1 and 1/T2) of $Mn_{0.3}Zn_{0.7}S$ with different particle sizes versus the Mn(II) concentration in water at B0=3 T and T=25°C

The number of paramagnetic ions cooperated on the surface of nanoparticles are responsible for shortening of T1 relaxation time [379]. Thus, the surface of nanoparticles plays an important role on relaxivity r1. Hyeon and co-workers have observed that longitudinal relaxivity of MnO nanoparticles decreases from 0.37 to 0.12 $mM^{-1}s^{-1}$ with increase in particle size [380]. The decrease of r1 relaxivity with increasing diameter of Gd_2O_3 nanoparticles has also been reported. The small Gd_2O_3 with diameter of 3 nm exhibited r1 of 2.64 $mM^{-1}.s^{-1}$ at 20 MHz and 37°C while it decreased to 1.86 $mM^{-1}.s^{-1}$ for aggregated nanoparticles with hydrodynamic radius of 105 nm [381]. Moreover, Rahman *et al.* found that r1 of Gd_2O_3 increased with decreasing particle size until the nanoparticle size reached 2.3 nm afterward a

further reduction in the particle size caused a reduction of r1 [382]. On the other hand, r1 of different cobalt nanoparticles coated with polymer have also been investigated [383]. It was reported that r1 of largest cobalt nanoparticles (28 nm) in water was almost doublet (7.4 $mM^{-1}s^{-1}$) than the one (3.9 $mM^{-1}s^{-1}$) of smaller nanoparticles (13 nm) at 1.5T whilst their r2 relaxivities were the same [383]. In our study, r1 of $Mn_{0.3}Zn_{0.7}S$ decreased with increasing particle size, with coating thickness of 0.5 nm, consistent with previous reported ones. The decrease of surface area by increasing particle size could be responsible for the decrease of r1 relaxivity.

Due to size dependency of r1 and r2 relaxivities, r2 changes are less pronounced than r1 in our study. The decrease of r2 from 40 $mM^{-1}s^{-1}$ (S1) to 31 $mM^{-1}s^{-1}$ (S2) could be attributed to the decrease of surface to volume ratio with increasing particle size. Meanwhile, r2 of S3 and S4 did not change. Roohi *et al.* has also observed the same trend for relaxivity of SPIO [384]. They have reported that r2 of SPIO changes with increasing the hydrodynamic radius of SPIO up to 60 nm while for larger particles r2 remains constant [384].

D. Molecular Dynamics simulation (MDs)

Molecular dynamics give us the ability to study the real dynamics of the system during time of simulation. Thus, in order to obtain better understanding of the microscopic behavior of MnZnS in aqueous solution (water), the structure of MnZnS in vacuum and in water have been estimated via molecular dynamic simulation.

D.1. ZnS and MnZnS zincblende structure

As mentioned in the previous chapter, shell model of ZnS [260] has been adopted for numerical simulation of ZnS structure. Figure 76 displays the simulated radial distribution function (RDF), and the snapshot of its crystal structure. The characteristic RDF peaks and their corresponding coordination number (CN) of Zn-Zn and Zn-S pairs have been tabulated in Table 20. RDF of Zn-S and Zn-Zn pairs contain sharp peaks which demonstrate the crystal structure of ZnS. Zn-Zn RDF exhibits four peaks at 3.78 Å, 5.42 Å, 6.62, and 7.57 Å with corresponding integration number of 12, 18, 42, and 54. Moreover, RDF of Zn-S pairs exhibits four peaks at 2.32, 4.425, 5.82, and 6.92Å. Referring to Zn-S RDF, Zn atoms

coordinated with 4, 12 and 12 atom of S at 1st, 2nd and 3rd coordination shells, respectively. Benkabou *et al.* have simulated ZnS crystal structure using MD simulation while the interaction between atoms were described by tersoff potential [261]. They reported the 1st, 2nd, and 3rd RDF of ZnS zincbelnde structure at 2.31, 3.81, and 4.46 Å, respectively [261], consistent with our results.

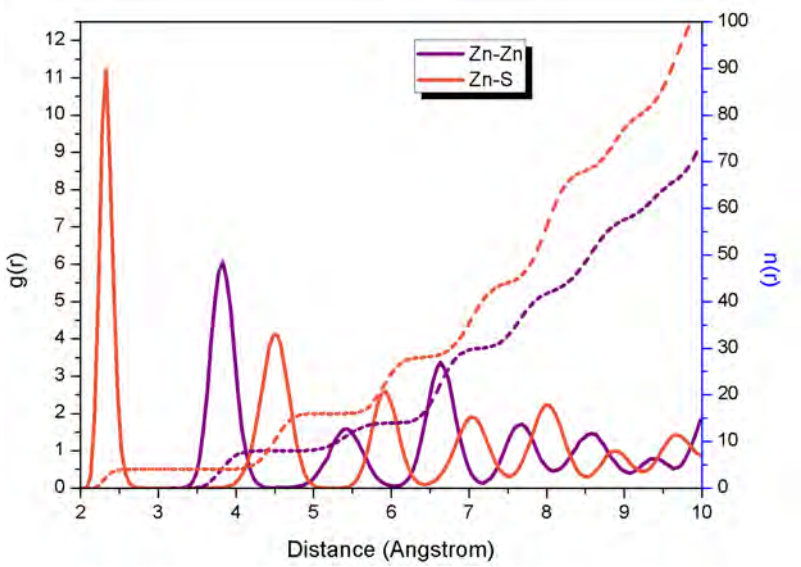

Figure 76. Radial distribution of Zn-Zn and Zn-S and associated coordination numbers

The lattice constant and cell volume of simulated ZnS are calculated as listed in Table 20 which are 1.04% smaller than the experimental one. These two crystal parameters have been theoretically studied by some researchers using force field modeling [249] and linearized augmented planewave (LAPW) method [385]. The unit volume and lattice constant of ZnS using LAPW and force field methods have been reported of v=152.80 Å^3 and a=5.345 Å, and v=161.93 Å^3 and a=5.45Å, respectively [249],[385]. In comparison with experimental and other theoretical studies, it could be deduced that ZnS crystal structure is successfully reproduced.

Next step, incorporation of Mn atoms into ZnS lattice is simulated from developed potential by Wright [250], as mentioned in previous chapter (section D.4). RDF and corresponding integration of sphalerite MnZnS have been presented in Fig. 77 and summarized in Table 20.

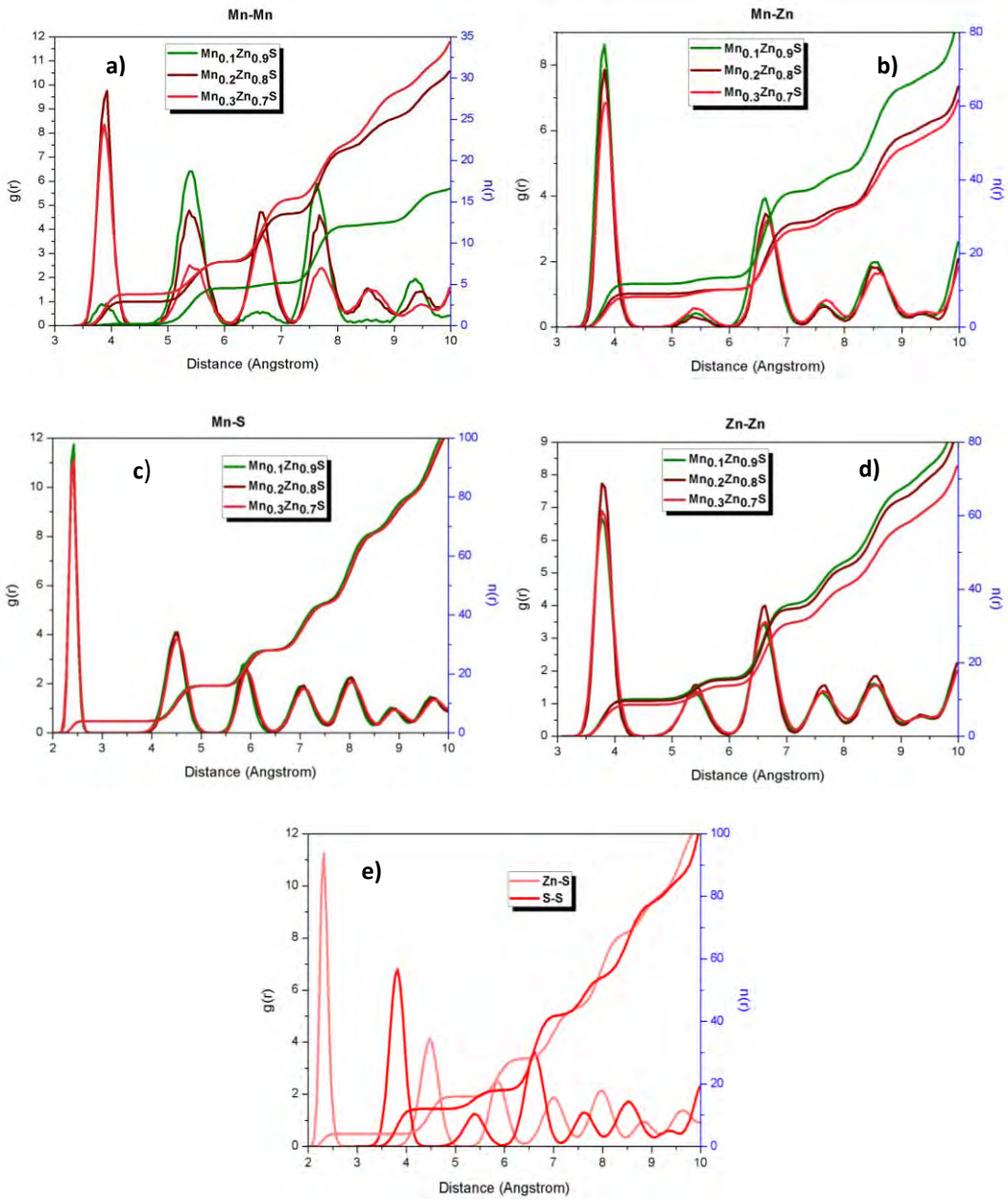

Figure 77. RDFs and corresponding coordination number of a) Mn-Mn, b) Mn-Zn, c) Mn-S, d) Zn-Zn and e) Zn-S, S-S of $Mn_xZn_{1-x}S$ (x=0.1, 0.2, 0.3) at 300 K and 1 bar

As listed in Table 20, the shortest Mn-S interaction is occurs at the distance of 2.42 Å, which is in good agreement with the reported Mn-S distance measured by X-ray absorption spectroscopy (2.43-2.45 Å) [264]. From simulated Mn:ZnS crystal structure with different Mn dopant concentrations (10 to 30%), the first interaction of Mn-Mn atoms is at 3.87 Å. Referring to the calculated RDF, incorporation of Mn atoms into ZnS lattice affect the crystal structure of ZnS and causes the expansion of the tetrahedron structure of ZnS. This expansion has an effect on lattice constant.

As listed in Table 20, the lattice constant increases from 5.394 Å ($Mn_{0.1}Zn_{0.9}S$) to 5.429 Å ($Mn_{0.3}Zn_{0.7}S$) with increasing Mn concentration. Wright *et al.* has studied the crystal structure of Mn impurity incorporated within ZnS sites [250]. They have reported the shortest Mn-S distance at 2.41 Å and an increase of lattice constant of about +0.00064 Å per MnS% for substitution of one Mn atom in $(ZnS)_4$ [250]. While for incorporation a second Mn into ZnS_4, they have reported the first coordination of Mn-Mn pairs at the distance of 3.87 Å and less distortion of crystal structure [250]. The Mn-Mn first coordination in our study is at the distance of 3.87Å, consistent with the reported values by Wright *et al* [250]. Thereby, the increase of lattice constant with Mn dopant concentrations in our study is reliable and reasonable and in agreement with Wright and coworkers studies [250]. Moreover, some experimental studies have also reported the increase of lattice parameter and cell volume of Mn:ZnS with Mn dopant. For instance, Van *et al.* have reported an increase of lattice constant from 5.41 to 5.43 Å for the fabricated MnZnS with Mn dopant of 1%-15% [386]. The increase of lattice constant from 5.37-5.373 Å and cell volume from 154.9-155.15 $Å^3$ of synthesized Mn-doped ZnS with different Mn concentrations in the range of 1% to 10% have also been reported by Mote *et al.* [387]. Due to the reported crystal parameters of Mn:ZnS either from simulations or from characterization, our simulated MnZnS nanoparticles with different Mn dopant concentrations are consistent.

Table 20 . Characteristic sphalerite structure of MnZnS and ZnS from simulation and experiments

	$Mn_{0.1}Zn_{0.9}S$		$Mn_{0.2}Zn_{0.8}S$		$Mn_{0.3}Zn_{0.7}S$		ZnS		Expt.	
Pair atoms	1^{st} g(r)	1^{st} n(r)	1^{st} g(r)	1^{st} n(r)	1^{st} g(r)	1^{st} n(r)	1^{st} g(r)	1^{st} n(r)	1^{st} g(r)	1^{st} n(r)
Mn-Mn	3.87	0.22	3.87	2.90	3.87	3.80	----	----		
Mn-Zn	3.82	11.77	3.82	9.09	3.82	8.19	----	----		
Mn-S	2.42	4	2.42	4	2.42	4	----	----		
Zn-S	2.32	4	2.32	4	2.32	4	2.32	4	2.34	4
Zn-Zn	3.77	10.08	3.77	9.67	3.77	8.62	3.78	12	3.82	12
a (Å)	5.394		5.407		5.429		5.39		5.409	
Unit cell Volume ($Å^3$)	156.99		158.10		160.04		156.68		158.34	

*Expt. Results [249]

Visualization of MD simulation was performed using the Aten software [388]. The structure of [110] surface of ZnS and MnZnS after relaxation are illustrated in Fig. 78. As observed in Fig. 78, S atoms are in upward in position compared with either Zn or Mn atoms in both structures. The movement of Zn and S atoms after relaxation of ZnS crystal structure has been studied by Wright *et al.* [247] and Duke *et al.* [389]. Both have reported the upward movement of S atom compared with downward movement of corresponding Zn atom. The

movement of atoms was attributed to the relative spacing changes between layers and atoms [247].

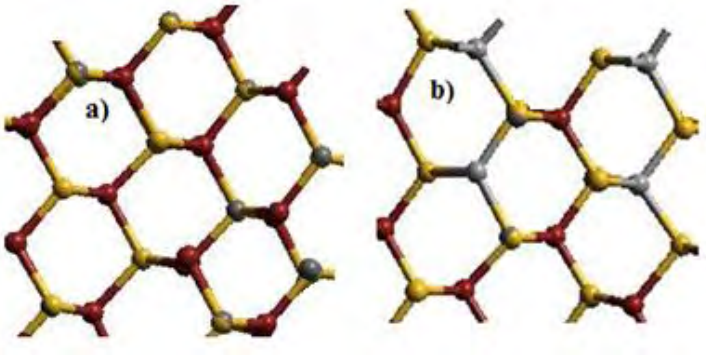

Figure 78. Surface [110] crystal structure of a) ZnS and b) MnZnS, yellow : S atom, red : Zn, and grey color : Mn

Energy time-dependent of ZnS and MnZnS systems are presented in Fig. 79. It can be observed that the energy of all systems slightly fluctuates, with difference less than 0.05 eV, during simulation time, which infers all systems are fully relaxed. Employing the shell model developed by Wright *et al.* [246], the energy of ZnS system fluctuates around -30.15 eV, with reported values of -32.64 eV [248] and -33.46 eV [249]. While the incorporation of Mn atoms into ZnS system, the energy of the system per ZnS reduces to -33.61 (Mn=10%), -33.53 (Mn=20%) and -33.43 eV (Mn=30%) with increasing Mn. In order to investigate the effect of Mn incorporation on the energy of system, we employed the complicated potential parameters used to simulate MnZnS structure. We observed that ZnS energy is fluctuating around -33.31 eV, which is close to those reported values [248], [249]. By comparing the simulated energy of ZnS and MnZnS using same potential parameters, it can be induced that the incorporation of Mn atoms in ZnS sites did not affect the energy of system. Referring to these results, reliability and accuracy of the generated sphalerite MnZnS structure can be demonstrated.

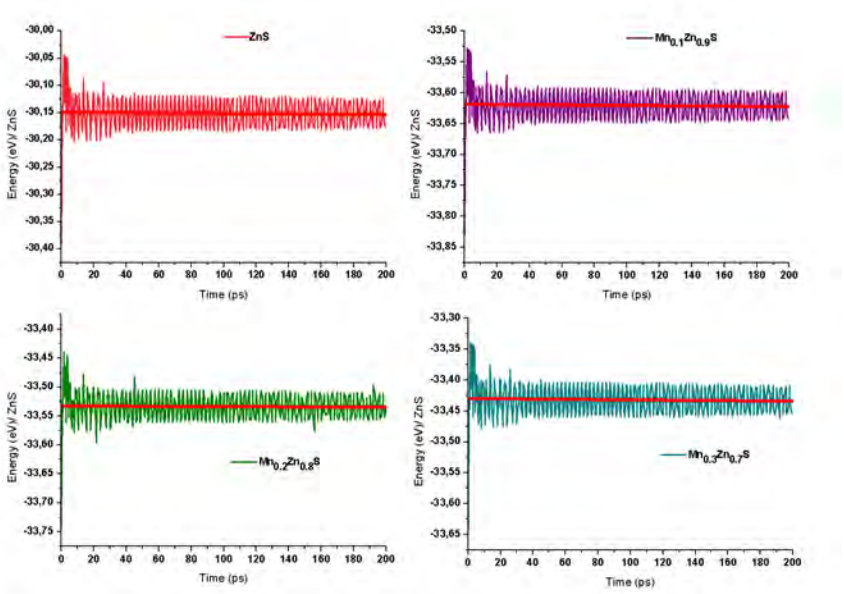

Figure 79. Time-dependent of potential energy (eV) of simulated ZnS and $Mn_xZn_{1-x}S$ (x=0.1, 0.2, 0.3) crystal structure at 300K and 1bar

D.2. Molecular dynamic simulation of water molecule

The RDFs of water molecules are displayed in Fig. 80. As observed, the RDF of liquid is quite different from solid one. The RDF of liquid possesses broad peak and non-zero values at all separations compared with sharp peaks and zero minimum of crystal structure. RDF of O-O for SPC/E and TIP3P models shows respectively a first broad peak at 2.98 and 3.23 Å followed by a second peak at 5.65 and 6.13 Å. Referring to Fig. 80, O-O RDF of liquid water does not exhibit distinct minima after the first peak in both models. This suggests that there is interaction between water molecules in first and second coordination spheres which could facilitate the exchange of water molecules between those coordination shells. Due to RDF of water, oxygen coordinated with two hydrogen atoms at distance of 0.95Å (SPC/E) and 0.98 Å (TIP3P).

The diffusion coefficient of liquid water is one of the interesting properties. As presented in Table 21, the calculated diffusion coefficients of water from TIP3P and SPC/E models are respectively 38% and 2.7% lower compared to the experimental value of 2.30 ($10^{-5}cm^2/s$). Additionally, density of simulated water molecules are 1.021($g.cm^{-3}$) for TIP3P and 0.997 ($g.cm^{-3}$) for SPC/E models which are very close to the experimental density of 0.997 $g.cm^{-3}$ 298 K.

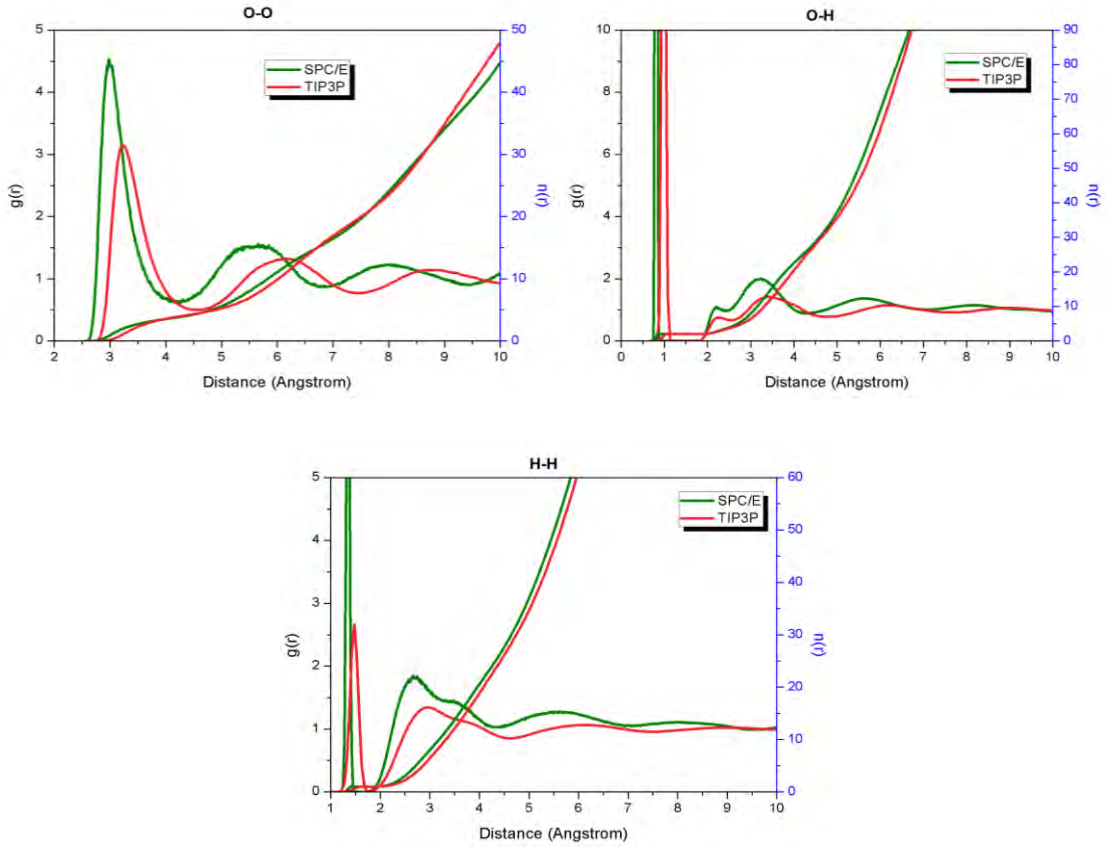

Figure 80. Radial distributions $g_{O\text{-}O}(r)$, $g_{O\text{-}H}(r)$, and $g_{H\text{-}H}(r)$ with corresponding coordination number of water using SPC/E, and TIP3P models

Table 21. Comparison of the characteristic properties of various water models and experiment at 298K

Simulation	$g_{O-O}(r)$	$g_{O-H}(r)$	$\angle HOH$, deg	D(x10^{-5}cm^2/s)	ρ(g.cm^{-3})	Ref.
SPC/Fw	----	1.012	113.24	2.32	-----	[392]
SPC/E	----	1.0	109.47	2.41	----	[266]
TIPS 2	2.79	0.9572	104.52	3.2	0.927	[393]
TIP3P	2.74	0.9572	104.52	5.1	1.002	[393]
TIP4P	2.74	0.9572	104.52	3.22	1.001	[393]
TIP4P/EW	----	0.9572	104.52	2.4	0.9954	[394]
TIP4P/2005	----	0.9572	104.52	2.08	0.9979	[395]
TIP5P	----	0.9572	104.52	2.6	0.999	[393]
TIP4P-FQ	2.92	0.9572	104.52	1.9	1.000	[396]
TIP4P-QDP	2.91	0.9572	104.52	2.2	0.9951	[397]
SPC	2.75	1.0	109.47	3. 6	0.964	[398]
SPC/FQ	2.94	1.0	109.47	1.7	----	[396]
BF	2.72	0.96	105.7	4.3	1.181	[399]
SPC/E	2.75	1.8	----	2.6	0.326	[400]
GCPM	2.877	0.9572	104.52	2.26	1.004	[401]
Shell	2.97	0.98	104.5	1.15	1.30	[402]
SPC/E	2.98	0.98	---	2.24	0.945	present work
TIP3P	3.225	0.95	---	1.41	1.021	Present work
Exp.	2.97	0.98	104.5	2.30	0.997	[390], [391]

Since 1982, different potential functions have been developed to simulate liquid water. In order to compare our results obtained with those reported ones, different simulated water models and their characteristic RDF, diffusion coefficient, and density at 298K have been summarized in Table 21. In comparison, the results obtained herein show a very good agreement with the experimental and those reported ones [390], [391].

D.3. Molecular Dynamics simulation of ZnS molecules in water

After reproducing the ZnS sphalerite nanoparticles within a few percent of the experimental values, a ZnS nanosphere with diameter 2.5 nm has been immersed to the center of the simulated cubic box of water. While each box contains the same number of water molecules but different models are used. The interaction of 228 (ZnS) surrounded with 1689 water molecules has been tracked by MDs. No distinguishable difference has been observed in RDF and corresponding CN of systems containing TIP3P or SPC/E water models. Thereby, one of the calculated RDF is represented in Fig. 81 and in Table 22. As tabulated in Table 22, the radial distribution function of ZnS has been changed while it surrounded with water molecules. The RDF of Zn-Zn and Zn-S containes a sharp peak at 3.82 Å and 2.38 Å, respectively, followed by several small and broad peaks (Fig. 81). This chang can be attributed to the interaction of water molecules with Zn or S atoms.

Table 22. RDFs of ZnS interaction with water molecules

	ZnS in aqueous solution		ZnS	
1st peak	g(r)	n(r)	g(r)	n(r)
Zn-Zn	3.82	10.28	3.82	12
Zn-S	2.38	3.46	2.32	4
Zn-O	2.025	1.28	----	----
Zn-H	2.80	1.17	----	----
S-O	3.38	5.45	-----	----
S-H	2.73	1.91	-----	----

There are three possible ways for bonding of water molecules with ZnS nanoparticles, such as Zn-O, S-O, and S-H. RDF curves of Zn-H and S-H contain several low-intensity peaks with nonzero g(r) minimum, attributing to the labile interaction of Zn and S atoms with H atom of waters. While RDFof Zn-O and S-O containes one sharp peak followed by several low-intense peaks with nonzero minimum, ascribing to the rigid interaction between Zn and S

atoms with oxygen of waters in the first coordination sphere. As presented in Fig. 81, Zn-O pair contains one sharp peak at ~2.025 Å with a shoulder at 2.58 Å. While RDF of S-O pair in aqueous solution contain a relatively broad peak at ~3.38 Å. The results obtained from MDs suggest that the interaction between Zn atoms with water molecules are stronger than S atoms with water. This could be related to the larger Zn and O Pauline electronegativities (3.44-1.65=1.79) than S and H atoms (2.58-2.20=0.38) [267]. Thereby, the predominate interaction of water molecules and ZnS nanoparticles occurs between O and Zn atoms.

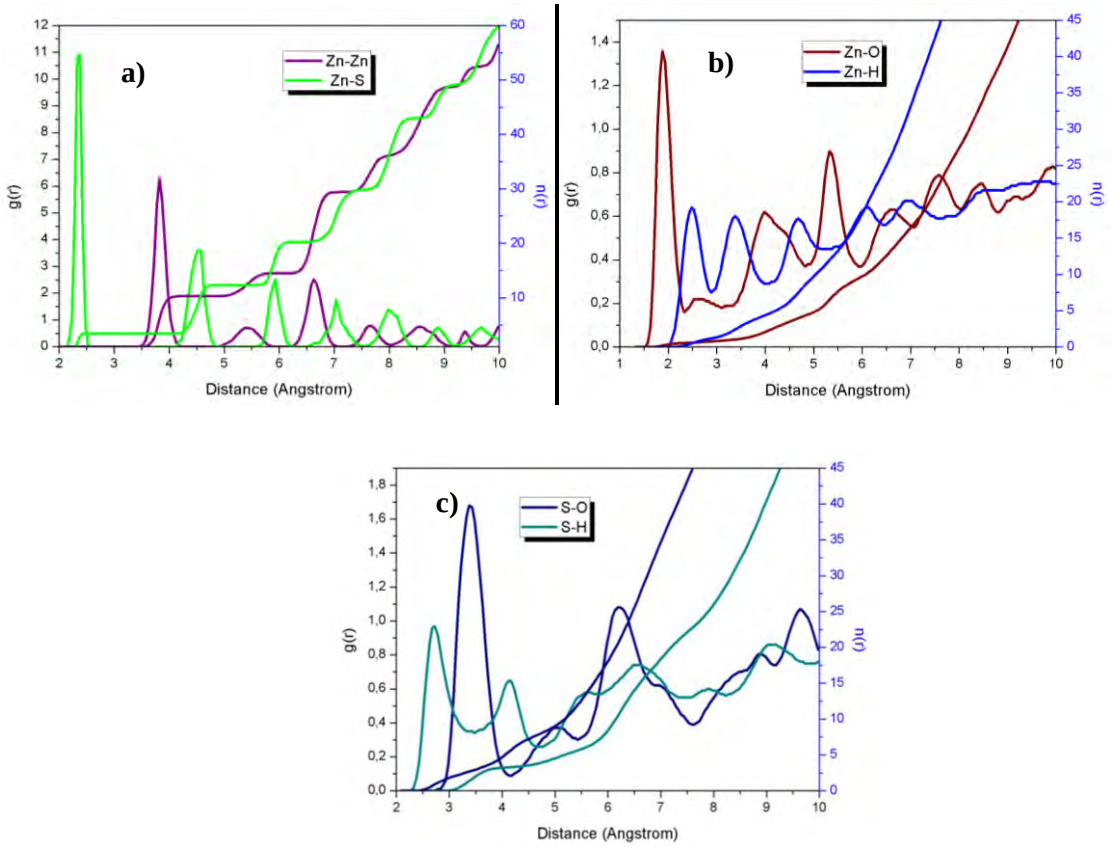

Figure 81. RDFs and corresponding integration of a) Zn-Zn, Zn-S, b)Zn-O, Zn-H, and c)S-H, S-O

From MDs results, we observed that surface Zn atoms could bond with an average of two water molecules. The interaction of ZnS nanoparticles with water molecules has also been studied by Zhang *et al.* using temperature-programmed desorption (TPD) and MDs [267]. They reported that Zn atoms could adsorb 1 to 4 water molecules which depends on local structure of Zn atoms in the surface of ZnS nanoparticles [267]. For instance, Zn atoms on the surface could interact with higher number of water molecules [267].

Furthermore, suspension of uncoated ZnS nanoparticles (diameter of 3 nm) in water has been characterized by EXAFS [403]. It has been reported that EXAFS spectrum of dispersed nanoparticles in water exhibited a peak at 2.348Å corresponding to Zn-S pair [403]. On the other hand, XRD studies of $ZnSO_4$ in aqueous solution demonstrated that Zn ion at 2.083Å could coordinate with 6 water molecules [404]–[406] and with 8-13 water molecules at the second coordination shell [407]. On the other hand, Kawada *et al.* have demonstrated that Zn ions of $ZnSO_4$ in aqueous solution coordinated with 2 water molecules at distance of 2.10Å referring to raman spectroscopy measurements [408]. In another research work, hydration of Zn ions in aqueous solution has been investigated by x-ray absorption spectroscopy [409]. The calculated multiple scattering and related EXAFS signals of Zn in aqueous solution revealed a first and second hydration shells at 2.06Å and 4.26Å with corresponding coordination number of 6.02 and 11.6, respectively. Referring to the experimental reported results, the first coordination of Zn-O pair is at the distance about 2.06 Å, which is close to our results (2.02 Å). The coordination number of Zn with water molecules in our study is close to reported Raman spectroscopy measurements.

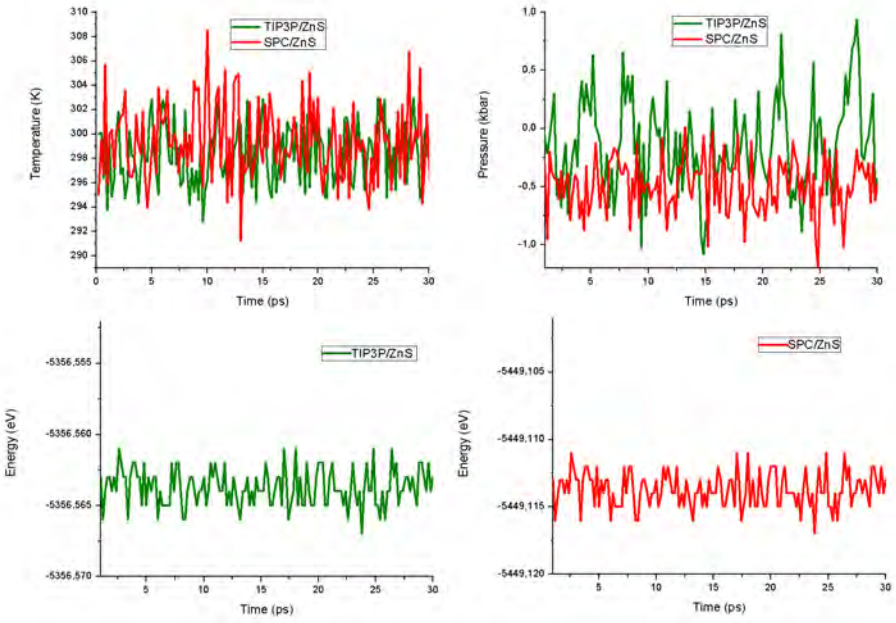

Figure 82. Time -dependent of potential energy (eV), Temperature (K), and pressure (kbar) of ZnS in aqueous solution

Time-dependence of temperature, pressure and potential energy of the system including ZnS nanoparticles and SPC/E or TIP3P water models have been exhibited in Fig. 82. The significant difference is observed in energy of the system. Energy of system with SPC/E water

(-5449,11) is ~ 100 eV lower than the one of TIP3P water (-5356,56). This difference in energy is attributed to the different water models.

D.4. Molecular dynamics simulation of Mn atoms interaction with water molecules

In order to study the structure of MnZnS within the liquid, we need to study the interaction between Mn ions and water molecules. Mn-H and Mn-O RDFs with their running integration have been presented in Fig. 83. The first RDF peak of Mn-O and Mn-H are centered at 2.12 Å and 2.67 Å, respectively. The second hydration shell of Mn atom appeared ranging from 3.08 Å to 5.63 Å with maximum at 4.075 Å. In RDF of Mn-H, the second peak appears in the range of 3.48-6.03 Å with the maximum at 4.72 Å. Compared to first shell, second RDF peak of both Mn-O and Mn-H pairs are much broader with nonzero value at the minimum.
Referring to running integration of Mn-O RDF, Mn atom is surrounded with the six water molecules at first hydration shell. Moreover, number of coordination at second shell exhibits a mean value of 18.5 water molecules. From Mn-H RDF integration, Mn atom surrounded with 12.03 and 38.26 hydrogen atoms at first and second shell, respectively.

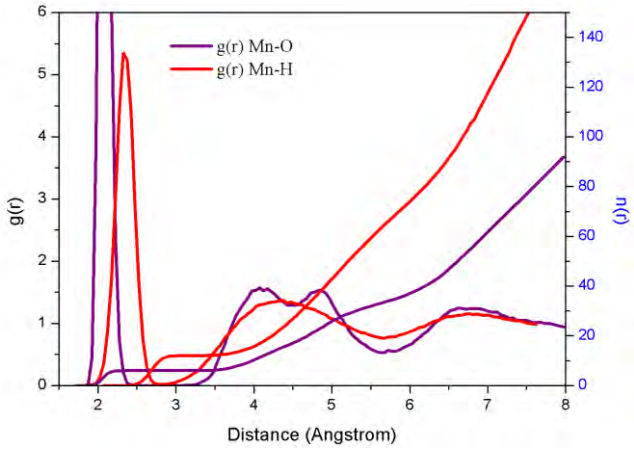

Figure 83. RDFs and corresponding coordination number of Mn-O, Mn-H

From RDF of Mn-O, the inter shell region between first and second shell maintains at zero with distinguishable distance. Thus, it could be inferred that no exchange occurred during simulation time between these hydration shells. The broad peak with nonzero g(r) minimum at second shell indicates rapid exchange between water molecules during simulation times.

From coordination number of Mn-O at first and second hydration shell, we could induce that each water molecule at first shell interacts with 3.08 water molecules at second shell.

The structure of Mn atom surrounded with water molecules has been little studied. The interaction of Mn atom with water molecules have been simulated via classical Monte Carlo (MC), Molecular dynamic simulation (MD), and Quantum mechanical and molecular mechanical (QM/MM) types [410]. The reported results are summarized in Table 23. Schewank and colleagues have also studied Mn-water interaction via QM/MM simulation including three body potential [411]. The first and second RDF of Mn-O has been reported at 2.25Å (CN= 6) and 4.4Å (CN=15.9), respectively [411]. Among the results obtained from different method of simulations, the results obtained from QM/MM simulations are reported to be much closer to the experimental values [410].

Table 23. The characteristic RDF obtained from MC, MD, QM/MM simulations

method	Pair atoms	r_1	n_1	r_2	n_2
MC[1]	Mn-O	2.23	8.90	4.59	22.83
	Mn-H	2.92	17.4	4.82	53.44
MD[2]	Mn-H	2.22	8.74	4.42	22.74
	Mn-O	2.94	19.11	4.98	53.13
QM/MM[3]	Mn-O	2.28	6.74	4.00	18.06
	Mn-H	2.84	13.67	4.80	48

1. One Mn(II) ion and 199 water molecules, 298.16 K, cutoff=9.117 Å, ρ=0.997 g cm^{-3}, NVT, CF2[412] potential for water-water interaction and MCY[413] for ion-water interaction
2 same as MC with time step=0.2fs
3 same as MC, system equilibrated at 4.2 ps, NVT ensemble, ab initio molecular orbital calculation, Hartee-Fock energy for many body effects

Furthermore, X-ray scattering spectroscopy studies of Mn ions in aqueous solution approves the octahedrally coordination of Mn ions with water molecules at first coordination shell at 2.20Å [414]. Compared with those published results, our results are in good agreement with RDF of QM/MM MD simulation. Thereby, the interaction of Mn ion with water molecules has been successfully simulated using Buckingham potential for describing the Mn-water interactions which agrees adequately with experimental values.

D.5. Molecular dynamics simulation of MnZnS molecules interaction with water molecules

Finally, the interaction of MnZnS with water molecules has been studied by MDs. The RDF calculated from MD is presented in Fig. 84 and in Table 24. By comparing the RDF of Mn:ZnS nanoparticles in water, RDF of all three systems are similar and RDF of all atomic pairs contain a sharp peak at the first coordination and small broad peaks at the second and third coordination spheres with nonzero g(r) minimum. Referring to RDF curves, Mn-Mn, Mn-Zn and Mn-S curves significantly change compared with those of MnZnS crystal Mn-Mn RDF contains one sharp peak following two broad peaks while each broad peak includes several low-intense peaks. In comparison with RDF of ZnS-surrounded with water molecules, Zn-O, S-H, and S-O RDF peaks of MnZnS-H_2O shifted to lower r-distance. Moreover, RDF peak of Zn-Zn, Zn-S, S-O, and S-H pairs did not significantly change in MnZnS-H_2O and ZnS- H_2O, Table 24. As listed in Table 24, the CN of Mn-Mn pair of MnZnS decreases to ~1 from solid state to aqueous systems. This could be attributed to strong interaction of Mn atoms on the surface with water molecules which reduces the Mn-Mn interactions.

Table 24. RDF and CN of first coordination shell obtained for $Mn_xZn_{1-x}S$ -H_20 (x=0.1, 0.2, 0.3) and ZnS+ H_2O

Atomic pairs	$Mn_{0.1}Zn_{0.9}S$ +H_2O		$Mn_{0.2}Zn_{0.8}S$ +H_2O		$Mn_{0.3}Zn_{0.7}S$ +H_2O		ZnS+ H_2O	
	1^{st} g(r)	1^{st} n(r)	1^{st} g(r)	1^{st} n(r)	1^{st} g(r)	1^{st} n(r)	g(r)	n(r)
Mn-Mn	3.87	1.04	3.77	0.57	3.87	1.59	----	----
Mn-Zn	3.77	5.22	3.77	5.92	3.77	6.22	----	----
Mn-S	2.37	2.74	2.37	2.74	2.37	2.74	----	----
Zn-S	2.20	3.68	2.27	3.65	2.32	3.59	2.38	3.46
Zn-Zn	3.79	8.41	3.77	8.49	3.72	8.58	3.82	10.28
Mn-H	2.62	7.25	2.72	7.25	2.77	7.25	----	----
Mn-O	2.37	2.74	2.37	2.74	2.37	2.74	----	----
Zn-H	2.62	0.82	2.62	0.82	2.62	0.82	1.88	0.55
Zn-O	1.97	0.36	1.97	0.36	1.97	0.36	2.48	1.17
S-O	3.27	3.07	3.27	3.07	3.27	3.07	3.38	5.45
S-H	2.62	2.70	2.62	2.70	2.62	2.70	2.73	1.91

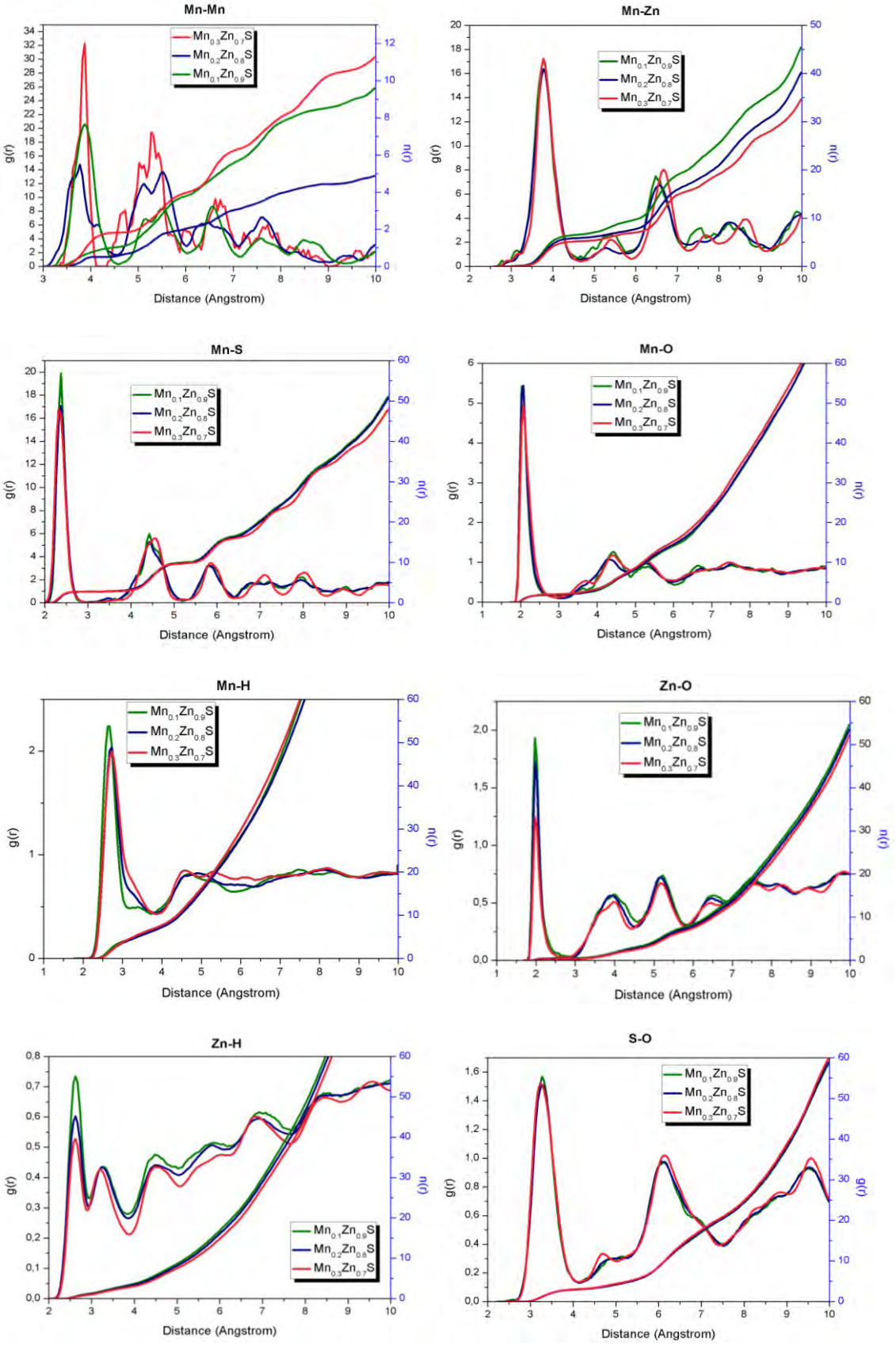

Figure 84. RDFs and corresponding CN of Mn-Mn, Mn-S, Mn-Zn, Mn-O, Mn-H, Zn-O, Zn-H, and S-O of $Mn_xZn_{1-x}S$ (x=0.1, 0.2, 0.3) nanoparticles in aqueous solution

Mn atoms at first coordination shell coordinated with ~3 oxygen and ~7 hydrogen atoms. The sharp and intense peak of Mn-O RDF could confirm the strong interaction between these two atomic pairs. If we consider the number of oxygen as the number of coordinated water molecules, Zn atoms at ~2Å coordinated with 0.5 water molecules while Mn atoms coordinated with ~3water molecules.

From a snapshot of MnZnS presented in Fig. 85, each Mn bonds with higher water molecules (1 to 3), compared with 1 to 2 water molecules bonded with Zn sites in ZnS-H_2O system. From the high CN and short distance of Mn-H_2O, the short relaxation time is acceptable. Moreover, the long distance of ~1Å between 1^{st} and 2^{nd} coordination sphere could confirm the strong bonding of Mn atoms with water molecules in 1^{st} sphere with long residency time while these water molecules are still in exchange with water molecules of 2^{nd} sphere due to nonzero g(r) minimum. On the other hand, 2^{nd} coordination sphere of Mn-O is very labile which leads to faster exchange rates with those of outer sphere referring to close 2^{nd} and 3^{rd} RDF peaks of Mn-O pairs. Although we need to improve the simulation conditions of nanoparticles by including the mercaptoacetic acid coating around nanoparticle to exactly predict the relaxation mechanism of MnZnS in aqueous solution, these primarily RDF results could explain very well the short relaxation times of MnZnS in aqueous solution (high relaxivity).

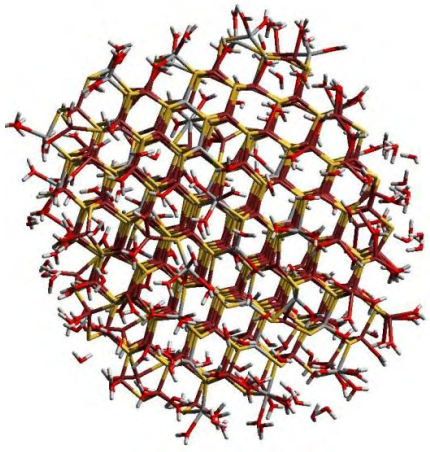

Figure 85. Snapshot of relaxed system containing water molecules and MnZnS nanoparticles

In Fig. 86, we have presented the energy of MnZnS-H_2O system over 30 ps (simulation time). Energy of system increases from -67691 eV to -66927 eV with increasing the Mn doping concentrations from 10% to 20% then reduce to -67685 eV for Mn=30%.

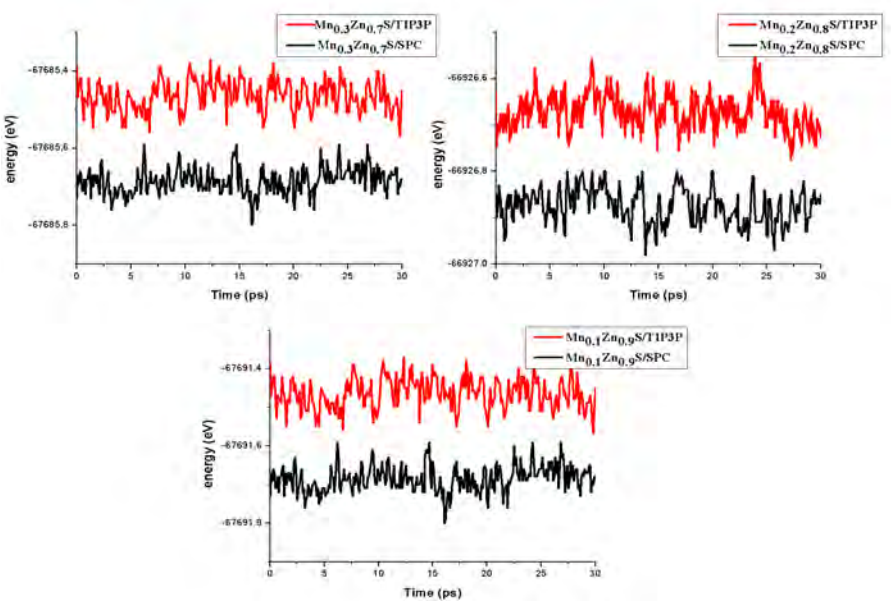

Figure 86. Time-dependent of potential energy (eV) of $Mn_{0.1}Zn_{0.9}S$, $Mn_{0.2}Zn_{0.8}S$, and $Mn_{0.3}Zn_{0.7}S$ surrounded with water molecules

Chapter V: Conclusion

A. Conclusion

Recently, molecular imaging has received tremendous attention referring to their ability to visualize the cellular function of organisms which could help in the diagnosis of disease, including cancer and neurodegenerative disease, meantime simultaneously providing biological information [415]. MRI is emerging as a powerful diagnostic tool by providing high resolution anatomical images. The source of the most of contrast observed in MRI is the relaxation time differences. One way to enhance the contrast of MR images is to administer the paramagnetic substances, which could alter the proton relaxation times. After the first report of administration of paramagnetic substance to enhance the relaxation of water protons in 1946 [416], great efforts have been spent on developing the paramagnetic MRI contrast agents providing high contrast, low toxicity, high stability, tumor targeting and longer imaging time window. On the other hand, due to increasing the interest towards high-field MRI, designing the CA, which possesses the high relaxivity at high magnetic field, is a crucial issue in designing the contrast agents referring to decrease the relaxivity of majority MRI CA at high magnetic field. The work presented in this thesis is the development of two novel MRI contrast agent such as macromolecules and nanoparticle paramagnetic contrast agents exhibiting high solubility, and high efficiency (high relaxivity) at high field (3T).

The first compound studied is Gd (III) meso-tetrakis (4-pyridyl) porphyrin (Gd(TPyP))(OAc). The potential of Gd(TPyP) in aqueous solution has been studied via NMR relaxometry (20 MHz) and MRI (60 MHz), meanwhile, its efficiency has been compared with those of cationic *iron*(III) meso-tetrakis(4-N-methyl-pyridiniumyl) (Fe(TMPyP)) and ionic manganese(III) meso-tetra(4-sulfonatophenyl)porphyrins (Mn(TSPP)) in aqueous media. Compared with evaluated relaxivity of Fe(TMPyP) and Mn(TSPP) in water, Gd(TPyP) has shown the highest relaxivity of 26 $mM^{-1}s^{-1}$ which is 8 times greater than r1 of commercial Gd-DOTA (~4.1 $mM^{-1}s^{-1}$) at 20 MHz. While with increasing magnetic field to 60 MHz, r1 of Gd(TPyP) did not change significantly (~24 $mM^{-1}s^{-1}$). The *in-vitro* relaxivity studies of Gd(TPyP) have shown the feasibility of Gd(TPyP) to be used as MRI CA. Thus, in order to enhance the biomedical application of Gd(TPyP) and its water solubility, Gd(TPyP) has been conjugated to synthesized chitosan nanoparticles (CNs). The potential of spherical Gd(TPyP)-CNs as MRI contrast enhancement, with a diameter in the range of 45-64 nm and hydrodynamic radius of 412 nm, has been investigated via MRI 3T. The nanoparticles of Gd(TPyP)-CNs exhibit r1 of 38 $mM^{-1}s^{-1}$with r1/r2 ratio of almost 1 (0.86). Thereby, conjugation of Gd(TPyP) complex with chitosan nanoparticles leads to enhanced water

solubility and relaxivity of Gd(TPyP) referring to increase the rotational correlation time, enhancing the accessibility of water, and an increase in the amount of paramagnetic ion loaded into a nanoparticle. Thus, this novel nanosized macromolecular contrast agent could be a good candidate as T1 contrast agents for further studies.

The second developed contrast agents is Mn-doped ZnS QDs that the majority of Mn atoms are localized on the surface of atoms. The relaxivities of Mn:ZnS with Mn dopant content in the range of 10% to 30% have been performed. $Mn_xZn_{1-x}S$ colloids (x=0.1, 0.2, 0.3) have shown great ability to enhancing the signal intensity on T1 images at low concentrations (less than 0.1 mM). Owing to the high r1 which increases from 20 to 84 $mM^{-1}s^{-1}$ with increasing Mn content is confirmation of our hypothesis to enhance the efficiency of nanoparticles by conjugating of metal ions close or on the surface of nanoparticles. Meanwhile, for further Mn dopant of 30% the r1 decreases to 75 $mM^{-1}s^{-1}$. This reduction could be attributed to the dipolar interaction of Mn atoms, causing the decrease of electronic relaxation times and reduction in the overall relaxivity. In order to study the effect of particle size of nanoparticles on reducing this dipolar interaction, different sizes of $Mn_{0.3}Zn_{0.7}S$ nanoparticles have been synthesized and their potential as enhancing MR contrast images has been studied. We observed that the volume to surface ratio has the predominant affect on their relaxivity which causes the decrease of r1 from 75 $mM^{-1}s^{-1}$ to 40 $mM^{-1}s^{-1}$ with increasing diameter of nanoparticles. Comparing with r1 of conventional Mn contrast agents (Mn-DPDP) (Teslascan®, r1=2.1 $mM^{-1}.s^{-1}$ at 1.5T), the relaxivities of synthesized Mn-doped ZnS are much higher (20 times). Thereby, the high relaxivity of Mn:ZnS nanoparticles could be attributed to the high surface to volume ratio, high accessibility to water molecules, and short distance between Mn ions and water molecules.

In order to obtain further insight into relaxivity mechanism of Mn:ZnS nanoparticles in solution, molecular dynamic simulation (MDs) has been carried out. The crystal structure Mn:ZnS with different Mn dopant in the range of 10% to 30%, incorporating on the outer surface of ZnS sites, has been reproduced very well using MDs. The calculated lattice parameter and cell volume of MnZnS crystal increase from 5.40 to 5.42Å and 156 to 160 $Å^3$ with Mn dopant which are in good agreement with the experimental reported ones [386]. After confirming the reliability of the modeled MnZnS crystal, we developed the potential to describe the interaction of MnZnS nanoparticles with water molecules. The simulated radial distribution and corresponding coordination number of MnZnS-H_2O system give us the preliminary explanation of relaxivity mechanism of MnZnS nanoparticles in aqueous solution. The water molecules could form the bond with MnZnS nanoparticles via formation of Mn-O,

S-O, S-H, Zn-O. Referring to the calculated RDF, the interaction between Mn and O atoms is the predominant. The Mn interacts with ~3 water molecules at shortest distance of 2.37Å for all three different MnZns nanoparticles. Due to the sharp RDF and distinguishable distance between 1st and 2nd hydration shells, it could be predicted that those water molecules in first sphere form strong bond with Mn atoms. Meanwhile, there is still an exchange between water molecules in 1st and 2nd sphere shell due to minimum nonzero RDF. The results obtained from MD could give us the primary insight about the short relaxation mechanism of MnZnS nanoparticles.

B. Prospective

Incorporation of metallated porphyrin into chitosan nanoparticles is a relatively new class of complex that is in the early stage of the research. Thereby, the extensive work shall be performed to promote this new type of complex to be used in molecular imaging and nanomedecine contexts. Several key parameters such as their toxicity, biodistribution, pharmacokinetics and ability in enhancing the tumor cell visualization could be considered as future work direction. The chitosan could interact with the negatively charged of neoplastic cells membrane due to its positive charge of amino group. This interaction leads to inhibit the growth of cancer cells, reduce the membrane permeability, and decrease the spread of cancer cells by metastasis. However, chitosan could interact with healthy and normal cell membrane without such effects. This is so interesting for cancer therapy. Thus, metallated porphyrin incorporated into chitosan nanoparticles could be considered as a diagnostic imaging and simultaneously as a therapeutic agent. Furthermore, the surface of the compound could be encapsulated with folic acid (FA) in order to improve their cellular uptake. Combination of targeting capability of FA and biocompatibility of chitosan [417] could greatly enhance the uptake of metalloporphyrin-conjugated chitosan nanoparticles into tumor cells combined with prolonged blood circulatory time of nanoparticles.

Although, localization of paramagnetic ions on the surface of QDs opens a new window in improving their potential as MRI CA, the study the toxicity, kinetic stability of nanoparticles and improving their tumor targeting would be stated as the second prospective. Moreover, in order to improve the reliability of the molecular dynamic simulation results with experimental *in-vitro* MRI studies, the future direction of the simulation studies could be conducted by studying the interaction of MnZnS-coated with mercaptoacetic acid with water molecules.

Bibliography

[1] R. Damadian, M. Goldsmith, and L. Minkoff, "NMR in cancer: XVI. FONAR image of the live human body.," *Physiol. Chem. Phys.*, vol. 9, no. 1, pp. 97–100, 108, 1977.

[2] W. S. HINSHAW, P. A. BOTTOMLEY, and G. N. HOLLAND, "Radiographic thin-section image of the human wrist by nuclear magnetic resonance," *Nature*, vol. 270, no. 5639, pp. 722–723, Dec. 1977.

[3] G. M. Lanza, P. M. Winter, S. D. Caruthers, A. M. Morawski, A. H. Schmieder, K. C. Crowder, and S. A. Wickline, "Magnetic resonance molecular imaging with nanoparticles," *J. Nucl. Cardiol.*, vol. 11, no. 6, pp. 733–743, 2004.

[4] R. Mewis and S. Archibald, "Biomedical applications of macrocyclic ligand complexes," *Coord. Chem. Rev.*, vol. 254, no. 15–16, pp. 1686–1712, 2010.

[5] D. N. Reinhoudt, *Supramolecular Materials and Technologies*. Wiley, 2008.

[6] C. Chen, J. S. J. Cohen, C. C. E. Myers, and M. Sohn, "Paramagnetic metalloporphyrins as potential contrast agents in NMR imaging," *FEBS Lett.*, vol. 168, pp. 70–74, 1984.

[7] J. H. Agondanou, I. Nicolis, E. Curis, J. Purans, G. A. Spyroulias, A. G. Coutsolelos, and S. Bénazeth, "Gadolinium Acetylacetonate Tetraphenyl Monoporphyrinate Complex and Some of Its Derivatives: EXAFS Study and Molecular Dynamics Simulation," *Inorg. Chem.*, vol. 46, no. 17, pp. 6871–6879, 2007.

[8] K. W. Bowman, Katherine; Leong, "Chitosan nanoparticles for oral drug and gene delivery," *Int. J. Nanomedicine*, vol. 2, no. 1, pp. 117–128, 2006.

[9] N. G. M. Schipper, K. M. Vårum, P. Stenberg, G. Ocklind, H. Lennernäs, and P. Artursson, "Chitosans as absorption enhancers of poorly absorbable drugs: 3: Influence of mucus on absorption enhancement," *Eur. J. Pharm. Sci.*, vol. 8, no. 4, pp. 335–343, 1999.

[10] S. Baruah, C. Ortinero, O. V Shipin, and J. Dutta, "Manganese doped zinc sulfide quantum dots for detection of Escherichia coli.," *J. Fluoresc.*, vol. 22, no. 1, pp. 403–8, Jan. 2012.

[11] A. Borel, F. Yerly, L. Helm, and A. E. Merbach, "Molecular Dynamics Simulations of the Internal Mobility of Gd3+-Based MRI Contrast Agents: Consequences for Water Proton Relaxivity," *Chim. Int. J. Chem.*, vol. 58, no. 4, pp. 200–203, Apr. 2004.

[12] M. Puddephat, "Principles of magnetic resonance imaging," 2013. .

[13] J. Ridgway, "Cardiovascular magnetic resonance physics for clinicians: part I," *J Cardiovasc Magn Reson*, 2010.

[14] C. Burtea, S. Laurent, L. Vander Elst, and R. N. Muller, “Contrast agents: magnetic resonance.,” *Handb. Exp. Pharmacol.*, no. 185 Pt 1, pp. 135–65, Jan. 2008.

[15] É. T. Andre S. Merbach, Lothar Helm, Ed., *The chemistry of contrast agents in medical magnetic resonance imaging*, Second edi. United Kingdom: John Wiley & Sons, Ltd., 2013.

[16] R. Muller, “Contrast agents in whole body magnetic resonance: operating mechanisms,” Encycloped., D. Grant and R. Harris, Eds. New York: Wiley, 1996, pp. 1438–1444.

[17] W. Krause, *Contrast Agents 1: Magnetic Resonance Imaging*, Springer-V. Heidelberg, 2002.

[18] E. L. Q. and C. J. Chang, “Responsive magnetic resonance imaging contrast agents as chemical sensors for metals in biology and medicine,” *Chem. Soc. Rev.*, vol. 39, pp. 51–60, 2010.

[19] N. Bloembergen and L. Morgan, “Proton Relaxation Times in Paramagnetic Solutions. Effects of Electron Spin Relaxation,” *J Chem Phys.*, vol. 34, pp. 842–850, 1961.

[20] M. Gueron, “Nuclear relaxation in macromolecules by paramagnetic ions: a novel mechanism,” *J. Magn. Reson.*, vol. 19, no. 1, pp. 58–66, 1975.

[21] P. Caravan and Z. Zhang, “Structure - relaxivity relationships among targeted MR contrast agents.,” *Eur. J. Inorg. Chem.*, vol. 12, 2012.

[22] Y. Gossuin, A. Roch, R. N. Muller, and P. Gillis, “An evaluation of the contributions of diffusion and exchange in relaxation enhancement by MRI contrast agents.,” *J. Magn. Reson.*, vol. 158, no. 1–2, pp. 36–42, 2002.

[23] J. H. Freed, “Dynamic effects of pair correlation functions on spin relaxation by translational diffusion in liquids. II. Finite jumps and independent T1 processes,” *J. Chem. Phys.*, vol. 68, no. 9, 1978.

[24] S. Aime, M. Chiaussa, G. Digilio, E. Gianolio, and E. Terreno, “Contrast agents for magnetic resonance angiographic applications: 1H and 17O NMR relaxometric investigations on two gadolinium(III) DTPA-like chelates endowed with high binding affinity to human serum albumin,” *JBIC J. Biol. Inorg. Chem.*, vol. 4, no. 6, pp. 766–774, 1999.

[25] P. Hermann, J. Kotek, V. Kubíček, and I. Lukeš, “Gadolinium (III) complexes as MRI contrast agents: ligand design and properties of the complexes,” *Dalt. Trans.*, 2008.

[26] H.-J. Weinmann, W. Ebert, B. Misselwitz, and H. Schmitt-Willich, “Tissue-specific MR contrast agents,” *Eur. J. Radiol.*, vol. 46, no. 1, pp. 33–44, Apr. 2003.

[27] S. A. Kirchin MA, Pirovano GP, “Gadobenate dimeglumine (Gd-BOPTA),” *Invest Radiol.*, vol. 33, pp. 798–809, 1998.

[28] S. Aime and P. Caravan, “Biodistribution of gadolinium- based contrast agents, including gadolinium deposition,” *J. Magn. Reson. Imaging*, 2009.

[29] M. Yu, J. Park, and S. Jon, “Targeting strategies for multifunctional nanoparticles in cancer imaging and therapy,” *Theranostics*, 2012.

[30] G. Orive, O. A. Ali, E. Anitua, J. L. Pedraz, and D. F. Emerich, “Biomaterial-based technologies for brain anti-cancer therapeutics and imaging,” *Biochim. Biophys. Acta - Rev. Cancer*, vol. 1806, no. 1, pp. 96–107, 2010.

[31] T. M. T. Allen and P. R. P. Cullis, “Drug delivery systems: entering the mainstream.,” *Science*, vol. 303, no. 5665, pp. 1818–22, Mar. 2004.

[32] T. M. Allen and P. R. Cullis, “Drug delivery systems: entering the mainstream.,” *Science*, vol. 303, no. 5665, pp. 1818–22, Mar. 2004.

[33] G. Orive, A. OA, A. E, P. JL, and E. DF, “Biomedical based technologies for brain anti cancer therapeutics and imaging,” *Biochim Biophys Acta*, vol. 1806, pp. 96–107, 2010.

[34] Y. Zhang and J. Lovell, “Porphyrins as theranostic agents from prehistoric to modern times,” *Theranostics*, 2012.

[35] C. F. G. C. Geraldes and S. Laurent, “Classification and basic properties of contrast agents for magnetic resonance imaging.,” *Contrast Media Mol. Imaging*, vol. 4, no. 1, pp. 1–23, 2009.

[36] P. Endres and K. MacRenaris, “Quantitative imaging of cell-permeable magnetic resonance contrast agents using x-ray fluorescence.,” *Mol. Imaging*, 2006.

[37] J. Lee, M. Gye, K. Choi, and J. Hong, “In vitro differentiation of germ cells from nonobstructive azoospermic patients using three-dimensional culture in a collagen gel matrix,” *Fertil. Steril.*, 2007.

[38] S. Knör, A. Modlinger, T. Poethko, M. Schottelius, H.-J. Wester, and H. Kessler, “Synthesis of novel 1,4,7,10-tetraazacyclodecane-1,4,7,10-tetraacetic acid (DOTA) derivatives for chemoselective attachment to unprotected polyfunctionalized compounds.,” *Chemistry*, vol. 13, no. 21, pp. 6082–90, Jan. 2007.

[39] V. Kubícek, J. Rudovský, J. Kotek, P. Hermann, L. Vander Elst, R. N. Muller, Z. I. Kolar, H. T. Wolterbeek, J. A. Peters, and I. Lukes, “A bisphosphonate monoamide analogue of DOTA: a potential agent for bone targeting.,” *J. Am. Chem. Soc.*, vol. 127, no. 47, pp. 16477–85, Nov. 2005.

[40] K. Smith and J. Falk, *Porphyrins and metalloporphyrins*. 1975.

[41] M. Hodgson, “Preparation , structure and spectra of meso-metalloporphyrins,” Qeensland university of technology, 2005.

[42] P. Rothemund, “A New Porphyrin Synthesis. The Synthesis of Porphin1,” *J. Am. Chem. Soc.*, 1936.

[43] P. Rothemund, “FORMATION OF PORPHYRINS FROM PYRROLE AND ALDEHYDES,” *J. Am. Chem. Soc.*, vol. 57, no. 10, pp. 2010–2011, Oct. 1935.

[44] P. Rothemund and A. R. Menotti, “Porphyrin Studies. IV. 1 The Synthesis of α, β, γ, δ-Tetraphenylporphine,” *J. Am. Chem. Soc.*, vol. 63, no. 1, pp. 267–270, 1941.

[45] P. Rothemund, “A New Porphyrin Synthesis. The Synthesis of Porphin1,” *J. Am. Chem. Soc.*, vol. 58, no. 4, pp. 625–627, Apr. 1936.

[46] A. S. Semeikin, O. I. Koifman, and B. D. Berezin, “Synthesis of tetraphenylporphins with active groups in the phenyl rings. 1. Preparation of tetrakis(4-aminophenyl)porphin,” *Chem. Heterocycl. Compd.*, vol. 18, no. 10, pp. 1046–1047, Oct. 1982.

[47] A. Butler, “The synthesis of meso-substituted porphyrins: reaction conditions and substituent effects,” University of Georgia, 2001.

[48] A. D. Adler, F. R. Longo, J. D. Finarelli, J. Goldmacher, J. Assour, and L. Korsakoff, “A simplified synthesis for meso-tetraphenylporphine,” *J. Org. Chem.*, vol. 32, no. 2, p. 476, Feb. 1967.

[49] J. Lindsey, H. Hsu, and I. Schreiman, “Synthesis of tetraphenylporphyrins under very mild conditions,” *Tetrahedron Lett.*, 1986.

[50] J. J. S. Lindsey, H. H. C. Hsu, and I. I. C. Schreiman, “Synthesis of tetraphenylporphyrins under very mild conditions,” *Tetrahedron Lett.*, vol. 27, no. 41, pp. 4969–4970, 1986.

[51] J. S. Lindsey, I. C. Schreiman, H. C. Hsu, P. C. Kearney, and A. M. Marguerettaz, “Rothemund and Adler-Longo reactions revisited: synthesis of tetraphenylporphyrins under equilibrium conditions,” *J. Org. Chem.*, vol. 52, no. 5, pp. 827–836, Mar. 1987.

[52] J. S. Lindsey, K. A. MacCrum, J. S. Tyhonas, and Y. Y. Chuang, “Investigation of a Synthesis of meso-Porphyrins Employing High Concentration Conditions and an Electron Transport Chain for Aerobic Oxidation,” *J. Org. Chem.*, vol. 59, no. 3, pp. 579–587, 1994.

[53] R. A. W. Johnstone, M. Luisa P. G. Nunes, M. M. Pereira, A. M. d’A. Rocha Gonsalves, and A. C. Serra, “Improved Syntheses of 5,10,15,20-Tetrakisaryl- and Tetrakisalkylporphyrins,” *Heterocycles*, vol. 43, no. 7, p. 1423, 1996.

[54] G. P. Arsenault, E. Bullock, and S. F. MacDonald, “Pyrromethanes and Porphyrins Therefrom 1,” *J. Am. Chem. Soc.*, vol. 82, no. 16, pp. 4384–4389, Aug. 1960.

[55] M. Gouterman, “Study of the Effects of Substitution on the Absorption Spectra of Porphin,” *J. Chem. Phys.*, vol. 30, no. 5, p. 1139, 1959.

[56] V. N. Nemykin and R. G. Hadt, “Interpretation of the UV−vis Spectra of the meso(Ferrocenyl)-Containing Porphyrins using a TDDFT Approach: Is Gouterman’s Classic Four-Orbital Model Still in Play?,” *J. Phys. Chem. A*, vol. 114, no. 45, pp. 12062–12066, 2010.

[57] L. Milgrom, “The colours of life: an introduction to the chemistry of porphyrins and related compounds,” 1997.

[58] L. Josefsen and R. Boyle, “Unique diagnostic and therapeutic roles of porphyrins and phthalocyanines in photodynamic therapy, imaging and theranostics,” *Theranostics*, 2012.

[59] J. Golab, D. Nowis, M. Skrzycki, H. Czeczot, A. Baranczyk-Kuzma, G. M. Wilczynski, M. Makowski, P. Mroz, K. Kozar, R. Kaminski, A. Jalili, M. Kopec’, T. Grzela, and M. Jakobisiak, “Antitumor effects of photodynamic therapy are potentiated by 2-methoxyestradiol. A superoxide dismutase inhibitor.,” *J. Biol. Chem.*, vol. 278, no. 1, pp. 407–14, Jan. 2003.

[60] O. Raab, “Ueber die wirkung fluorescierenden stoffe auf infusorien,” *Z. Biol.*, vol. 39, pp. 524–46, 1900.

[61] H. Von Tappeiner and A. Jesionek, “Therapeutische versuche mit fluoreszierenden stoffen,” *Münch Med Wochenschr*, 1903.

[62] M. Ethirajan, Y. Chen, P. Joshi, and R. Pandey, “The role of porphyrin chemistry in tumor imaging and photodynamic therapy,” *Chem. Soc. Rev.*, 2011.

[63] H. Von Tappeiner and A. Jodlbauer, “Uber die wirkung der photodynamischen (fluorescierenden) stoffe auf protozoen und enzyme,” *Dtsch Arch Klin Med*, 1904.

[64] N. James, T. Ohulchanskyy, and Y. Chen, “Comparative Tumor Imaging and PDT Efficacy of HPPH Conjugated in the Mono-and Di-Forms to Various Polymethine Cyanine Dyes: Part-2,” *Theranostics*, 2013.

[65] J. P. Celli, B. Q. Spring, I. Rizvi, C. L. Evans, K. S. Samkoe, S. Verma, B. W. Pogue, and T. Hasan, “Imaging and photodynamic therapy: mechanisms, monitoring, and optimization.,” *Chem. Rev.*, vol. 110, no. 5, pp. 2795–838, May 2010.

[66] A. Policard, “Etude sur les aspects offerts par des tumeurs expérimentales examinées à la lumière de Wood,” *C. R .Soc. Bio.*, vol. 91, pp. 1423–24, 1924.

[67] H. Auler and G. Banzer, “Untersuchungen über die Rolle der Porphyrine bei geschwulstkranken Menschen und Tieren,” *J. Cancer Res. Clin. Oncol.*, 1942.

[68] C. Chen, J. Cohen, C. Myers, and M. Sohn, “Paramagnetic metalloporphyrins as potential contrast agents in NMR imaging,” *FEBS Lett.*, 1984.

[69] P. Furmanski and C. Longley, “Metalloporphyrin enhancement of magnetic resonance imaging of human tumor xenografts in nude mice,” *Cancer Res.*, 1988.

[70] R. C. Lyon, P. J. Faustino, J. S. Cohen, A. Katz, F. Mornex, D. Colcher, C. Baglin, S. H. Koenig, and P. Hambright, “Tissue distribution and stability of metalloporphyrin MRI contrast agents,” *Magn. Reson. Med.*, vol. 4, no. 1, pp. 24–33, Jan. 1987.

[71] D. Shahbazi-Gahrouei, “Gadolinium-porphyrins: new potential magnetic resonance imaging contrast agents for melanoma detection,” *J. Res. Med. Sci.*, 2006.

[72] D. Shahbazi-Gahrouei, M. Williams, S. Rizvi, and B. J. Allen, “In vivo studies of Gd-DTPA-monoclonal antibody and gd-porphyrins: potential magnetic resonance imaging contrast agents for melanoma.,” *J. Magn. Reson. Imaging*, vol. 14, no. 2, pp. 169–74, Aug. 2001.

[73] J. L. Sessler, T. D. Mody, G. W. Hemmi, and V. Lynch, “Synthesis and structural characterization of lanthanide(III) texaphyrins,” *Inorg. Chem.*, vol. 32, no. 14, pp. 3175–3187, Jul. 1993.

[74] C. Bremer, J. Bankert, T. Filler, W. Ebert, B. Tombach, and P. Reimer, “High-dose Gd-DTPA vs. Bis-Gd-mesoporphyrin for monitoring laser-induced tissue necrosis,” *J. Magn. Reson. Imaging*, vol. 21, no. 6, pp. 801–808, 2005.

[75] B. Hofmann, a Bogdanov, E. Marecos, W. Ebert, W. Semmler, and R. Weissleder, “Mechanism of gadophrin-2 accumulation in tumor necrosis.,” *J. Magn. Reson. Imaging*, vol. 9, no. 2, pp. 336–41, Feb. 1999.

[76] G.-P. Yan, Z. Li, W. Xu, C.-K. Zhou, L. Yang, Q. Zhang, L. Li, F. Liu, L. Han, Y.-X. Ge, and J.-F. Guo, “Porphyrin-containing polyaspartamide gadolinium complexes as potential magnetic resonance imaging contrast agents.,” *Int. J. Pharm.*, vol. 407, no. 1–2, pp. 119–25, Apr. 2011.

[77] G. Marchal, Y. Ni, P. Herijgers, W. Flameng, C. Petr  , H. Bosmans, J. Yu, W. Ebert, C.-S. Hilger, D. Pfefferer, W. Semmler, and A. L. Baert, “Paramagnetic metalloporphyrins: infarct avid contrast agents for diagnosis of acute myocardial infarction by MRI,” *Eur. Radiol.*, vol. 6, no. 1, pp. 2–8, 1996.

[78] W. Cheng, I. E. Haedicke, J. Nofiele, F. Martinez, K. Beera, T. J. Scholl, H.-L. M. Cheng, and X.-A. Zhang, “Complementary strategies for developing Gd-free high-field T_1 MRI contrast agents based on Mn(III) porphyrins.,” *J. Med. Chem.*, vol. 57, no. 2, pp. 516–20, Jan. 2014.

[79] J. H. McMillan, G. G. Cox, B. F. Kimler, J. S. Spicer, and S. Batnitzky, “Mn[III] uroporphyrin I: A novel metalloporphyrin contrast agent for magnetic resonance imaging,” *Magn. Reson. Imaging*, vol. 9, no. 4, pp. 553–558, 1991.

[80] J. E. Bradshaw, K. A. Gillogly, L. J. Wilson, K. Kumar, X. Wan, M. F. Tweedle, G. Hernandez, and R. G. Bryant, “New non-ionic water-soluble porphyrins: evaluation of manganese(III) polyhydroxylamide porphyrins as MRI contrast agents,” *Inorganica Chim. Acta*, vol. 275–276, pp. 106–116, Jul. 1998.

[81] V. Mouraviev, T. N. Venkatraman, A. Tovmasyan, M. Kimura, M. Tsivian, V. Mouravieva, T. J. Polascik, H. Wang, T. J. Amrhein, I. Batinic-Haberle, and C. Lascola, “Mn porphyrins as novel molecular magnetic resonance imaging contrast agents.,” *J. Endourol.*, vol. 26, no. 11, pp. 1420–4, Nov. 2012.

[82] S. H. Koenig, R. D. Brown, and M. Spiller, “The anomalous relaxivity of Mn3+(TPPS4),” *Magn. Reson. Med.*, vol. 4, no. 3, pp. 252–260, Mar. 1987.

[83] D. A. Place, P. J. Faustino, K. K. Berghmans, P. C. van Zijl, A. S. Chesnick, and J. S. Cohen, “MRI contrast-dose relationship of manganese(III)tetra(4-sulfonatophenyl)

porphyrin with human xenograft tumors in nude mice at 2.0 T.," *Magn. Reson. Imaging*, vol. 10, no. 6, pp. 919–28, Jan. 1992.

[84] R. Fiel, D. Musser, E. Mark, R. Mazurchuk, and J. J. Alletto, "A comparative study of manganese meso-sulfonatophenyl porphyrins: Contrast-enhancing agents for tumors," *Magn. Reson. Imaging*, vol. 8, no. 3, pp. 255–259, Jan. 1990.

[85] S. Qazi, M. Uchida, R. Usselman, R. Shearer, E. Edwards, and T. Douglas, "Manganese(III) porphyrins complexed with P22 virus-like particles as T1-enhanced contrast agents for magnetic resonance imaging.," *J. Biol. Inorg. Chem.*, vol. 19, no. 2, pp. 237–46, Feb. 2014.

[86] W. Krause, Ed., *Contrast Agents I in Magnetic Resonance Imaging*. Springer Science & Business Media, 2002.

[87] W. Cheng, T. Ganesh, F. Martinez, J. Lam, H. Yoon, R. B. Macgregor, T. J. Scholl, H.-L. M. Cheng, and X. Zhang, "Binding of a dimeric manganese porphyrin to serum albumin: towards a gadolinium-free blood-pool T1 MRI contrast agent.," *J. Biol. Inorg. Chem.*, vol. 19, no. 2, pp. 229–35, Feb. 2014.

[88] D. Shahbazi-Gahrouei, M. Williams, S. Rizvi, and B. J. Allen, "In vivo studies of Gd-DTPA-monoclonal antibody and gd-porphyrins: potential magnetic resonance imaging contrast agents for melanoma.," *J. Magn. Reson. Imaging*, vol. 14, no. 2, pp. 169–74, Aug. 2001.

[89] A. N. Oksendal and P.-A. Hals, "Biodistribution and toxicity of MR imaging contrast media," *J. Magn. Reson. Imaging*, vol. 3, no. 1, pp. 157–165, Jan. 1993.

[90] Z. Zou, H. L. Zhang, G. H. Roditi, T. Leiner, W. Kucharczyk, and M. R. Prince, "Nephrogenic Systemic Fibrosis: Review of 370 Biopsy-Confirmed Cases," *JACC Cardiovasc. Imaging*, vol. 4, no. 11, pp. 1206–1216, Nov. 2011.

[91] A. K. Haemel, E. A. Sadowski, M. M. Shafer, and A. Djamali, "Update on nephrogenic systemic fibrosis: are we making progress?," *Int. J. Dermatol.*, vol. 50, no. 6, pp. 659–666, Jun. 2011.

[92] J. Lim, B. Turkbey, M. Bernardo, L. H. Bryant, M. Garzoni, G. M. Pavan, T. Nakajima, P. L. Choyke, E. E. Simanek, and H. Kobayashi, "Gadolinium MRI contrast agents based on triazine dendrimers: relaxivity and in vivo pharmacokinetics.," *Bioconjug. Chem.*, vol. 23, no. 11, pp. 2291–2299, Nov. 2012.

[93] B. Turkbey, H. Kobayashi, M. Ogawa, M. Bernardo, and P. L. Choyke, "Imaging of tumor angiogenesis: functional or targeted?," *AJR. Am. J. Roentgenol.*, vol. 193, no. 2, pp. 304–13, Aug. 2009.

[94] M. Spanoghe, D. Lanens, R. Dommisse, A. Van der Linden, and F. Alderweireldt, "Proton relaxation enhancement by means of serum albumin and poly-l-lysine labeled with DTPA-Gd3+: Relaxivities as a function of molecular weight and conjugation efficiency," *Magn. Reson. Imaging*, vol. 10, no. 6, pp. 913–917, Jan. 1992.

[95] S. Langereis, Q. G. de Lussanet, M. H. P. van Genderen, W. H. Backes, and E. W. Meijer, "Multivalent Contrast Agents Based on Gadolinium−Diethylenetriaminepentaacetic Acid-Terminated Poly(propylene imine) Dendrimers for Magnetic Resonance Imaging," *Macromolecules*, vol. 37, no. 9, pp. 3084–3091, Mar. 2004.

[96] É. Tóth, I. van Uffelen, L. Helm, A. E. Merbach, D. Ladd, K. Briley-Sæbø, and K. E. Kellar, "Gadolinium-based linear polymer with temperature-independent proton relaxivities: a unique interplay between the water exchange and rotational contributions," *Magn. Reson. Chem.*, vol. 36, no. S1, pp. S125–S134, Jun. 1998.

[97] L. D. Margerum, B. K. Campion, M. Koo, N. Shargill, J.-J. Lai, A. Marumoto, and P. Christian Sontum, "Gadolinium(III) DO3A macrocycles and polyethylene glycol coupled to dendrimers Effect of molecular weight on physical and biological properties of macromolecular magnetic resonance imaging contrast agents," *J. Alloys Compd.*, vol. 249, no. 1–2, pp. 185–190, Mar. 1997.

[98] J. Tang, Y. Sheng, H. Hu, and Y. Shen, "Macromolecular MRI contrast agents: Structures, properties and applications," *Prog. Polym. Sci.*, 2013.

[99] N. Csaba, M. Garcia-Fuentes, and M. Alonso, "The performance of nanocarriers for transmucosal drug delivery," 2006.

[100] J. J. Wang, Z. W. Zeng, R. Z. Xiao, T. Xie, G. L. Zhou, X. R. Zhan, and S. L. Wang, "Recent advances of chitosan nanoparticles as drug carriers.," *Int. J. Nanomedicine*, vol. 6, pp. 765–74, Jan. 2011.

[101] D. L. Ladd, R. Hollister, X. Peng, D. Wei, G. Wu, D. Delecki, R. A. Snow, J. L. Toner, K. Kellar, J. Eck, V. C. Desai, G. Raymond, L. B. Kinter, T. S. Desser, and D. L. Rubin, "Polymeric Gadolinium Chelate Magnetic Resonance Imaging Contrast Agents: Design, Synthesis, and Properties," *Bioconjug. Chem.*, vol. 10, no. 3, pp. 361–370, 1999.

[102] R. L. Lucas, M. Benjamin, and T. M. Reineke, "Comparison of a Tartaric Acid Derived Polymeric MRI Contrast Agent to a Small Molecule Model Chelate," *Bioconjug. Chem.*, vol. 19, no. 1, pp. 24–27, 2008.

[103] S. Aime, M. Botta, M. Fasano, S. Paoletti, P. L. Anelli, F. Uggeri, and M. Virtuani, "NMR Evidence of a Long Exchange Lifetime for the Coordinated Water in Ln(III)-Bis(methyl amide)-DTPA Complexes (Ln = Gd, Dy)," *Inorg. Chem.*, vol. 33, no. 21, pp. 4707–4711, 1994.

[104] M. G. Duarte, M. H. Gil, J. a Peters, J. M. Colet, L. V Elst, R. N. Muller, and C. F. Geraldes, "Synthesis, characterization, and relaxivity of two linear Gd(DTPA)-polymer conjugates.," *Bioconjug. Chem.*, vol. 12, no. 2, pp. 170–7, 2001.

[105] Y. Zong, J. Guo, T. Ke, A. M. Mohs, D. L. Parker, and Z.-R. Lu, "Effect of size and charge on pharmacokinetics and in vivo MRI contrast enhancement of biodegradable polydisulfide Gd(III) complexes," *J. Control. Release*, vol. 112, no. 3, pp. 350–356, May 2006.

[106] A. M. Mohs, Y. Zong, J. Guo, D. L. Parker, and Z.-R. Lu, "PEG-g-poly(GdDTPA-co-l-cystine): Effect of PEG Chain Length on in Vivo Contrast Enhancement in MRI," *Biomacromolecules*, vol. 6, no. 4, pp. 2305–2311, Jun. 2005.

[107] S. Nazir, T. Hussain, A. Ayub, U. Rashid, and A. J. MacRobert, "Nanomaterials in combating cancer: therapeutic applications and developments.," *Nanomedicine*, vol. 10, no. 1, pp. 19–34, Jan. 2014.

[108] P. Giunchedi, I. Genta, B. Conti, R. A. A. Muzzarelli, and U. Conte, "Preparation and characterization of ampicillin loaded methylpyrrolidinone chitosan and chitosan microspheres," *Biomaterials*, vol. 19, no. 1–3, pp. 157–161, 1998.

[109] P. Calvo, C. Remuñán-López, J. L. Vila-Jato, and M. J. Alonso, "Novel hydrophilic chitosan-polyethylene oxide nanoparticles as protein carriers," *J. Appl. Polym. Sci.*, vol. 63, no. 1, pp. 125–132, Jan. 1997.

[110] S. Nazir, T. Hussain, A. Ayub, U. Rashid, and A. J. MacRobert, "Nanomaterials in combating cancer: therapeutic applications and developments.," *Nanomedicine*, vol. 10, no. 1, pp. 19–34, Jan. 2014.

[111] L. Ilium, "Chitosan and Its Use as a Pharmaceutical Excipient," *Pharm. Res.*, vol. 15, no. 9, 1998.

[112] I. Aranaz, R. Harris, and A. Heras, "Chitosan Amphiphilic Derivatives. Chemistry and Applications," *Curr. Org. Chem.*, vol. 14, no. 3, pp. 308–330, Feb. 2010.

[113] Y. Ohya, M. Shiratani, H. Kobayashi, and T. Ouchi, "Release Behavior of 5-Fluorouracil from Chitosan-Gel Nanospheres Immobilizing 5-Fluorouracil Coated with Polysaccharides and Their Cell Specific Cytotoxicity," *J. Macromol. Sci. Part A*, vol. 31, no. 5, pp. 629–642, May 1994.

[114] A. Grenha, "Chitosan nanoparticles: a survey of preparation methods," *J. Drug Target.*, 2012.

[115] H. Tokumitsu, H. Ichikawa, and Y. Fukumori, "Chitosan-gadopentetic acid complex nanoparticles for gadolinium neutron-capture therapy of cancer: preparation by novel emulsion-droplet coalescence technique," *Pharm. Res.*, 1999.

[116] A. Shering, "Formulation of 5-fluorouracil loaded chitosan nanoparticles by emulsion droplet coalescence method for cancer therapy," *Int. J. Pharm. Biol. Arch.*, 2011.

[117] R. Manchanda and S. Nimesh, "Controlled size chitosan nanoparticles as an efficient, biocompatible oligonucleotides delivery system," *J. Appl. Polym. Sci.*, 2010.

[118] T. Banerjee, S. Mitra, A. Kumar Singh, R. Kumar Sharma, and A. Maitra, "Preparation, characterization and biodistribution of ultrafine chitosan nanoparticles.," *Int. J. Pharm.*, vol. 243, no. 1–2, pp. 93–105, Aug. 2002.

[119] M. A. Mitra S, Gaur U, Ghosh PC, "Tumor targeted delivery of encapsulated dextran doxorubicin conjugate using chitosan nanoparticles as carriers," *J. Control. Release*, vol. 74, pp. 317–323, 2001.

[120] M. El-Shabouri, “Positively charged nanoparticles for improving the oral bioavailability of cyclosporin-A,” *Int. J. Pharm.*, 2002.

[121] W. Fan, W. Yan, Z. Xu, and H. Ni, “Formation mechanism of monodisperse, low molecular weight chitosan nanoparticles by ionic gelation technique,” *Colloids Surfaces B Biointerfaces*, 2012.

[122] S. Sajeesh and C. Sharma, “Cyclodextrin–insulin complex encapsulated polymethacrylic acid based nanoparticles for oral insulin delivery,” *Int. J. Pharm.*, 2006.

[123] Y. Hu, X. Jiang, Y. Ding, H. Ge, Y. Yuan, and C. Yang, “Synthesis and characterization of chitosan–poly (acrylic acid) nanoparticles,” *Biomaterials*, 2002.

[124] F. Atyabi, F. Talaie, and R. Dinarvand, “Thiolated chitosan nanoparticles as an oral delivery system for Amikacin: in vitro and ex vivo evaluations.,” *J. Nanosci. Nanotechnol.*, vol. 9, no. 8, pp. 4593–603, Aug. 2009.

[125] H. Q. Mao, K. Roy, V. L. Troung-Le, K. A. Janes, K. Y. Lin, Y. Wang, J. T. August, and K. W. Leong, “Chitosan-DNA nanoparticles as gene carriers: synthesis, characterization and transfection efficiency.,” *J. Control. Release*, vol. 70, no. 3, pp. 399–421, Feb. 2001.

[126] O. Borges, G. Borchard, J. C. Verhoef, A. de Sousa, and H. E. Junginger, “Preparation of coated nanoparticles for a new mucosal vaccine delivery system.,” *Int. J. Pharm.*, vol. 299, no. 1–2, pp. 155–66, Aug. 2005.

[127] E. L. S. Carvalho, A. Grenha, C. Remuñán-López, M. J. Alonso, and B. Seijo, “Mucosal delivery of liposome-chitosan nanoparticle complexes.,” *Methods Enzymol.*, vol. 465, pp. 289–312, Jan. 2009.

[128] A. Grenha, B. Seijo, and C. Remuñán-López, “Microencapsulated chitosan nanoparticles for lung protein delivery.,” *Eur. J. Pharm. Sci.*, vol. 25, no. 4–5, pp. 427–37, 2005.

[129] M. Dash, F. Chiellini, R. Ottenbrite, and E. Chiellini, “Chitosan—A versatile semi-synthetic polymer in biomedical applications,” *Prog. Polym. Sci.*, vol. 36, no. 8, pp. 981–1014, Aug. 2011.

[130] J. Zoldners, T. Kiseleva, and I. Kaiminsh, “Influence of ascorbic acid on the stability of chitosan solutions,” *Carbohydr. Polym.*, 2005.

[131] T. Kean and M. Thanou, *Renewable Resources for Functional Polymers and Biomaterials*. Cambridge: Royal Society of Chemistry, 2011.

[132] J. Xu, S. McCarthy, R. Gross, and D. Kaplan, “Chitosan film acylation and effects on biodegradability,” *Macromolecules*, 1996.

[133] C. Chatelet, O. Damour, and A. Domard, “Influence of the degree of acetylation on some biological properties of chitosan films,” *Biomaterials*, 2001.

[134] W. Malette, H. Q. Jr, and E. Adickes, “Chitosan effect in vascular surgery, tissue culture and tissue regeneration,” *Chitin Nat. Technol.*, 1986.

[135] Y. Elçin, V. Dixit, K. Lewin, and G. Gitnick, “Xenotransplantation of fetal porcine hepatocytes in rats using a tissue engineering approach,” *Artif. Organs*, 1999.

[136] A. Denuziere, D. Ferrier, O. Damour, and A. Domard, “Chitosan–chondroitin sulfate and chitosan–hyaluronate polyelectrolyte complexes: biological properties,” *Biomaterials*, 1998.

[137] H. Onishi and Y. Machida, “Biodegradation and distribution of water-soluble chitosan in mice,” *Biomaterials*, 1999.

[138] S. Chae, M. Jang, and J. Nah, “Influence of molecular weight on oral absorption of water soluble chitosans,” *J. Control. release*, 2005.

[139] M. Thanou, J. Verhoef, and H. Junginger, “Oral drug absorption enhancement by chitosan and its derivatives,” *Adv. Drug Deliv. Rev.*, 2001.

[140] S. B. Rao and C. P. Sharma, “Use of chitosan as a biomaterial: studies on its safety and hemostatic potential.,” *J. Biomed. Mater. Res.*, vol. 34, no. 1, pp. 21–8, Jan. 1997.

[141] S. C. Richardson, H. V Kolbe, and R. Duncan, “Potential of low molecular mass chitosan as a DNA delivery system: biocompatibility, body distribution and ability to complex and protect DNA.,” *Int. J. Pharm.*, vol. 178, no. 2, pp. 231–43, Mar. 1999.

[142] C. Zhang, G. Qu, Y. Sun, X. Wu, Z. Yao, and Q. Guo, “Pharmacokinetics, biodistribution, efficacy and safety of N-octyl- O-sulfate chitosan micelles loaded with paclitaxel,” *Biomaterials*, 2008.

[143] K. Sonaje, Y. Lin, J. Juang, and S. Wey, “In vivo evaluation of safety and efficacy of self-assembled nanoparticles for oral insulin delivery,” *Biomaterials*, 2009.

[144] Z. Shi, K. G. Neoh, E. T. Kang, B. Shuter, S.-C. Wang, C. Poh, and W. Wang, “(Carboxymethyl)chitosan-modified superparamagnetic iron oxide nanoparticles for magnetic resonance imaging of stem cells.,” *ACS Appl. Mater. Interfaces*, vol. 1, no. 2, pp. 328–35, Feb. 2009.

[145] C. E. Smith, A. Shkumatov, S. G. Withers, B. Yang, J. F. Glockner, S. Misra, E. J. Roy, C.-H. Wong, S. C. Zimmerman, and H. Kong, “A polymeric fastener can easily functionalize liposome surfaces with gadolinium for enhanced magnetic resonance imaging.,” *ACS Nano*, vol. 7, no. 11, pp. 9599–610, Nov. 2013.

[146] Y. Huang, B. Cao, X. Yang, Q. Zhang, X. Han, and Z. Guo, “Gd complexes of diethylenetriaminepentaacetic acid conjugates of low-molecular-weight chitosan oligosaccharide as a new liver-specific MRI contrast agent.,” *Magn. Reson. Imaging*, vol. 31, no. 4, pp. 604–9, May 2013.

[147] K. Nwe, C. Huang, and A. Tsourkas, “Gd-Labeled Glycol Chitosan as a pH-Responsive Magnetic Resonance Imaging Agent for Detecting Acidic Tumor Microenvironments,” *J. Med. Chem.*, 2013.

[148] X. Zhang, Y. Zhao, T. Han, and Q. Zhang, “Synthesis of Novel Magnetic Water-Soluble Chitosan as Potential Magnetic Resonance Imaging Contrast Agents,” *Asian J. Chem.*, vol. 25, no. 9, pp. 4953–4956, 2013.

[149] L. Zhang, Y. Liu, D. Yu, and N. Zhangl, “Gadolinium-loaded chitosan nanoparticles as magnetic resonance imaging contrast agents for the diagnosis of tumor.,” *J. Biomed. Nanotechnol.*, vol. 9, no. 5, pp. 863–9, May 2013.

[150] I. Hajdu, M. Bodnár, G. Trencsényi, T. Márián, G. Vámosi, J. Kollár, and J. Borbély, “Cancer cell targeting and imaging with biopolymer-based nanodevices.,” *Int. J. Pharm.*, vol. 441, no. 1–2, pp. 234–41, Jan. 2013.

[151] S. Aime, E. Gianolio, F. Uggeri, S. Tagliapietra, A. Barge, and G. Cravotto, “New paramagnetic supramolecular adducts for MRI applications based on non-covalent interactions between Gd(III)-complexes and beta- or gamma-cyclodextrin units anchored to chitosan.,” *J. Inorg. Biochem.*, vol. 100, no. 5–6, pp. 931–8, May 2006.

[152] I. Pashkunova-Martic, C. Kremser, M. Galanski, V. Arion, P. Debbage, W. Jaschke, and B. Keppler, “Lectin-Gd-loaded chitosan hydrogel nanoparticles: a new biospecific contrast agent for MRI.,” *Mol. Imaging Biol.*, vol. 13, no. 1, pp. 16–24, Feb. 2011.

[153] L. Vander Elst, S. Laurent, H. M. Bintoma, and R. N. Muller, “Albumin-bound MRI contrast agents: the dilemma of the rotational correlation time,” *MAGMA.*, vol. 12, pp. 135–40, 2001.

[154] T. P. Roberts, H. C. Roberts, and R. C. Brasch, “Optimizing imaging techniques to reduce errors in microvascular quantitation with macromolecular MR contrast agents,” *Acad Radiol.*, vol. 5, 1998.

[155] Y. Huang, X. Zhang, Q. Zhang, X. Dai, and J. Wu, “Evaluation of diethylenetriaminepentaacetic acid–manganese(II) complexes modified by narrow molecular weight distribution of chitosan oligosaccharides as potential magnetic resonance imaging contrast agents,” *Magn. Reson. Imaging*, vol. 29, no. 4, pp. 554–560, 2011.

[156] S. Hong, Y. Chang, and I. Rhee, “Chitosan-coated Ferrite (Fe3O4) nanoparticles as a T-2 contrast agent for magnetic resonance imaging,” *J. Korean Phys. Soc*, 2010.

[157] Z.-T. Tsai, J.-F. Wang, H.-Y. Kuo, C.-R. Shen, J.-J. Wang, and T.-C. Yen, “In situ preparation of high relaxivity iron oxide nanoparticles by coating with chitosan: A potential MRI contrast agent useful for cell tracking,” *J. Magn. Magn. Mater.*, vol. 322, no. 2, pp. 208–213, Jan. 2010.

[158] D.-J. Yu, M.-Z. Li, X.-Z. Huang, W.-H. Zhu, Y. Huang, Q. Zhang, and Q. Liu, “Preparation of and study on magnetic resonance imaging performance of metal porphyrin modified by low molecular weight chitosan,” *Guang Pu Xue Yu Guang Pu Fen Xi*, vol. 33, no. 10, pp. 2736–9, Oct. 2013.

[159] A. L. EFROS, “Interband absorption of light in a semiconductor sphere,” *SPIE milestone Ser.*, vol. 180, pp. 71–74.

[160] A. F. E. Hezinger, J. Teßmar, and A. Göpferich, “Polymer coating of quantum dots – A powerful tool toward diagnostics and sensorics,” *Eur. J. Pharm. Biopharm.*, vol. 68, no. 1, pp. 138–152, 2008.

[161] S. Kim, B. Fisher, H.-J. Eisler, and M. Bawendi, “Type-II Quantum Dots: CdTe/CdSe(Core/Shell) and CdSe/ZnTe(Core/Shell) Heterostructures,” *J. Am. Chem. Soc.*, vol. 125, no. 38, pp. 11466–11467, Aug. 2003.

[162] T. Jamieson, R. Bakhshi, D. Petrova, R. Pocock, M. Imani, and A. M. Seifalian, “Biological applications of quantum dots,” *Biomaterials*, vol. 28, no. 31, pp. 4717–4732, 2007.

[163] F. A. Esteve-Turrillas and A. Abad-Fuentes, “Applications of quantum dots as probes in immunosensing of small-sized analytes,” *Biosens. Bioelectron.*, vol. 41, no. 0, pp. 12–29, 2013.

[164] A. M. Smith and S. Nie, “Chemical analysis and cellular imaging with quantum dots,” *Analyst*, vol. 129, no. 8, pp. 672–7, 2004.

[165] W. R. Algar, A. J. Tavares, and U. J. Krull, “Beyond labels: A review of the application of quantum dots as integrated components of assays, bioprobes, and biosensors utilizing optical transduction,” *Anal. Chim. Acta*, vol. 673, no. 1, pp. 1–25, 2010.

[166] S. J. Rosenthal, J. C. Chang, O. Kovtun, J. R. McBride, and I. D. Tomlinson, “Biocompatible Quantum Dots for Biological Applications,” *Chem. Biol.*, vol. 18, no. 1, pp. 10–24, 2011.

[167] X. Peng, J. Wickham, and A. P. Alivisatos, “Kinetics of II-VI and III-V Colloidal Semiconductor Nanocrystal Growth: ‘Focusing’ of Size Distributions,” *J. Am. Chem. Soc.*, vol. 120, no. 21, pp. 5343–5344, May 1998.

[168] A. P. Alivisatos, “Perspectives on the Physical Chemistry of Semiconductor Nanocrystals,” *J. Phys. Chem.*, vol. 100, no. 31, pp. 13226–13239, Jan. 1996.

[169] U. Banin and O. Millo, “TUNNELING AND OPTICAL SPECTROSCOPY OF SEMICONDUCTOR NANOCRYSTALS,” *Annu. Rev. Phys. Chem.*, vol. 54, no. 1, pp. 465–492, Oct. 2003.

[170] F. V Mikulec, M. Kuno, M. Bennati, D. A. Hall, R. G. Griffin, and M. G. Bawendi, “Organometallic Synthesis and Spectroscopic Characterization of Manganese-Doped CdSe Nanocrystals,” *J. Am. Chem. Soc.*, vol. 122, no. 11, pp. 2532–2540, Mar. 2000.

[171] R. E. Bailey and S. Nie, “Alloyed Semiconductor Quantum Dots: Tuning the Optical Properties without Changing the Particle Size,” *J. Am. Chem. Soc.*, vol. 125, no. 23, pp. 7100–7106, May 2003.

[172] M. E. Akerman, W. C. W. Chan, P. Laakkonen, S. N. Bhatia, and E. Ruoslahti, “Nanocrystal targeting in vivo.,” *Proc. Natl. Acad. Sci. U. S. A.*, vol. 99, no. 20, pp. 12617–21, Oct. 2002.

[173] J. B. Delehanty, K. Boeneman, C. E. Bradburne, K. Robertson, and I. L. Medintz, "Quantum dots: a powerful tool for understanding the intricacies of nanoparticle-mediated drug delivery," *Expert Opin. Drug Deliv.*, vol. 6, no. 10, pp. 1091–1112, 2009.

[174] A. M. Smith, H. Duan, A. M. Mohs, and S. Nie, "Bioconjugated quantum dots for in vivo molecular and cellular imaging," *Adv. Drug Deliv. Rev.*, vol. 60, no. 11, pp. 1226–1240, 2008.

[175] D. Bera, L. Qian, T.-K. Tseng, and P. H. Holloway, "Quantum Dots and Their Multimodal Applications: A Review," *Materials (Basel).*, vol. 3, no. 4, pp. 2260–2345, 2010.

[176] A. Valizadeh, H. Mikaeili, M. Samiei, S. M. Farkhani, N. Zarghami, M. Kouhi, A. Akbarzadeh, and S. Davaran, "Quantum dots: synthesis, bioapplications, and toxicity.," *Nanoscale Res. Lett.*, vol. 7, no. 1, p. 480, Jan. 2012.

[177] E. Chason, S. T. Picraux, J. M. Poate, J. O. Borland, M. I. Current, T. Diaz de la Rubia, D. J. Eaglesham, O. W. Holland, M. E. Law, C. W. Magee, J. W. Mayer, J. Melngailis, and A. F. Tasch, "Ion beams in silicon processing and characterization," *J. Appl. Phys.*, vol. 81, no. 10, p. 6513, 1997.

[178] L. Spanhel, M. Haase, H. Weller, and A. Henglein, "Photochemistry of colloidal semiconductors. 20. Surface modification and stability of strong luminescing CdS particles," *J. Am. Chem. Soc.*, vol. 109, no. 19, pp. 5649–5655, 1987.

[179] P. H. Bang, J.; Yang, H.; Holloway, J. Bang, H. Yang, and P. H. Holloway, "Enhanced and stable green emission of ZnO nanoparticles by surface segregation of Mg.," *Nanotechnology*, vol. 17, no. 4, pp. 973–8, Feb. 2006.

[180] L. Spanhel and M. A. Anderson, "Semiconductor clusters in the sol-gel process: quantized aggregation, gelation, and crystal growth in concentrated zinc oxide colloids," *J. Am. Chem. Soc.*, vol. 113, no. 8, pp. 2826–2833, 1991.

[181] D. Bera and L. Qian, "Time-evolution of photoluminescence properties of ZnO/MgO core/shell quantum dots," *J. Phys. D. Appl. Phys.*, vol. 41, 2008.

[182] P. H. Bang, J.; Yang, H.; Holloway, "Enhanced and stable green emission of ZnO nanoparticles by surface segregation of Mg.," *Nanotechnology*, vol. 17, 2006.

[183] A. Sashchiuk, A.; Lifshitz, E.; Reisfeld, R.; Saraidarov, T.; Zelner, M.; Willenz, "Optical and conductivity properties of PbS nanocrystals in amorphous zirconia sol-gel films.," *J. Sol-Gel Sci.Technol.*, vol. 24, pp. 31–38, 2002.

[184] V. L. Colvin, A. N. Goldstein, and A. P. Alivisatos, "Semiconductor nanocrystals covalently bound to metal surfaces with self-assembled monolayers," *J. Am. Chem. Soc.*, vol. 114, no. 13, pp. 5221–5230, 1992.

[185] H. Yang, P. H. Holloway, G. Cunningham, and K. S. Schanze, "CdS:Mn nanocrystals passivated by ZnS: Synthesis and luminescent properties," *J. Chem. Phys.*, vol. 121, no. 20, 2004.

[186] H. Yang and P. H. Holloway, “Efficient and Photostable ZnS-Passivated CdS:Mn Luminescent Nanocrystals,” *Adv. Funct. Mater.*, vol. 14, no. 2, pp. 152–156, 2004.

[187] H. Yang, S. Santra, and P. H. Holloway, “Syntheses and Applications of Mn-Doped II-VI Semiconductor Nanocrystals,” *J. Nanosci. Nanotechnol.*, vol. 5, no. 9, pp. 1364–1375, Sep. 2005.

[188] A. R. Kortan, R. Hull, R. L. Opila, M. G. Bawendi, M. L. Steigerwald, P. J. Carroll, and L. E. Brus, “Nucleation and growth of cadmium selendie on zinc sulfide quantum crystallite seeds, and vice versa, in inverse micelle media,” *J. Am. Chem. Soc.*, vol. 112, no. 4, pp. 1327–1332, 1990.

[189] C. F. Hoener, K. A. Allan, A. J. Bard, A. Campion, M. A. Fox, T. E. Mallouk, S. E. Webber, and J. M. White, “Demonstration of a shell-core structure in layered cadmium selenide-zinc selenide small particles by x-ray photoelectron and Auger spectroscopies,” *J. Phys. Chem.*, vol. 96, no. 9, pp. 3812–3817, 1992.

[190] G. N. Karanikolos, P. Alexandridis, G. Itskos, A. Petrou, and T. J. Mountziaris, “Synthesis and Size Control of Luminescent ZnSe Nanocrystals by a Microemulsion−Gas Contacting Technique,” *Langmuir*, vol. 20, no. 3, pp. 550–553, 2004.

[191] S. Ogawa, K. Hu, F.-R. F. Fan, and A. J. Bard, “Photoelectrochemistry of Films of Quantum Size Lead Sulfide Particles Incorporated in Self-Assembled Monolayers on Gold,” *J. Phys. Chem. B*, vol. 101, no. 29, pp. 5707–5711, 1997.

[192] C. B. Murray, D. J. Norris, and M. G. Bawendi, “Synthesis and characterization of nearly monodisperse CdE (E = sulfur, selenium, tellurium) semiconductor nanocrystallites,” *J. Am. Chem. Soc.*, vol. 115, no. 19, pp. 8706–8715, 1993.

[193] A. B. Nepomnyashchii and A. J. Bard, “Electrochemistry and Electrogenerated Chemiluminescence of BODIPY Dyes,” *Acc. Chem. Res.*, vol. 45, no. 11, pp. 1844–1853, 2012.

[194] H. Lee, P. H. Holloway, H. Yang, L. Hardison, and V. D. Kleiman, “Synthesis and characterization of colloidal ternary ZnCdSe semiconductor nanorods.,” *J. Chem. Phys.*, vol. 125, no. 16, p. 164711, Oct. 2006.

[195] M. A. Hines and P. Guyot-Sionnest, “Bright UV-Blue Luminescent Colloidal ZnSe Nanocrystals,” *J. Phys. Chem. B*, vol. 102, no. 19, pp. 3655–3657, 1998.

[196] W. W. Yu, Y. A. Wang, and X. Peng, “Formation and Stability of Size-, Shape-, and Structure-Controlled CdTe Nanocrystals: Ligand Effects on Monomers and Nanocrystals,” *Chem. Mater.*, vol. 15, no. 22, pp. 4300–4308, 2003.

[197] H. S. Chen, S. J. J. Wang, C. J. Lo, and J. Y. Chi, “White-light emission from organics-capped ZnSe quantum dots and application in white-light-emitting diodes,” *Appl. Phys. Lett.*, vol. 86, no. 13, p. -, 2005.

[198] L. Bakueva, S. Musikhin, M. A. Hines, T.-W. F. Chang, M. Tzolov, G. D. Scholes, and E. H. Sargent, “Size-tunable infrared (1000–1600 nm) electroluminescence from PbS

quantum-dot nanocrystals in a semiconducting polymer," *Appl. Phys. Lett.*, vol. 82, no. 17, 2003.

[199] D. Battaglia and X. Peng, "Formation of High Quality InP and InAs Nanocrystals in a Noncoordinating Solvent," *Nano Lett.*, vol. 2, no. 9, pp. 1027–1030, 2002.

[200] P. Zrazhevskiy, M. Sena, and X. Gao, "Designing multifunctional quantum dots for bioimaging, detection, and drug delivery," *Chem. Soc. Rev.*, vol. 39, no. 11, pp. 4326–54, 2010.

[201] W. C. Chan, "Quantum Dot Bioconjugates for Ultrasensitive Nonisotopic Detection," *Science (80-.).*, vol. 281, no. 5385, pp. 2016–2018, Sep. 1998.

[202] S. K. Choi, N. Arnheim, and M. E. Thompson, "Hydroxylated quantum dots as luminescent probes for in situ hybridization," *J Am Chem Soc*, vol. 123, no. 17, pp. 4103–4, 2001.

[203] J. C. Chang, O. Kovtun, J. R. McBride, and I. D. Tomlinson, "Biocompatible quantum dots for biological applications.," *Chem. Biol.*, vol. 18, no. 1, pp. 10–24, 2011.

[204] W. Liu, M. Howarth, A. B. Greytak, Y. Zheng, D. G. Nocera, A. Y. Ting, and M. G. Bawendi, "Compact Biocompatible Quantum Dots Functionalized for Cellular Imaging," *J. Am. Chem. Soc.*, vol. 130, no. 4, pp. 1274–1284, Jan. 2008.

[205] A. Sukhanova, J. Devy, L. Venteo, H. Kaplan, M. Artemyev, V. Oleinikov, D. Klinov, M. Pluot, J. H. M. Cohen, and I. Nabiev, "Biocompatible fluorescent nanocrystals for immunolabeling of membrane proteins and cells," *Anal. Biochem.*, vol. 324, no. 1, pp. 60–67, 2004.

[206] W. Jiang, S. Mardyani, H. Fischer, and W. C. W. Chan, "Design and Characterization of Lysine Cross-Linked Mercapto-Acid Biocompatible Quantum Dots," *Chem. Mater.*, vol. 18, no. 4, pp. 872–878, Jan. 2006.

[207] A. M. Smith and S. Nie, "Minimizing the Hydrodynamic Size of Quantum Dots with Multifunctional Multidentate Polymer Ligands," *J. Am. Chem. Soc.*, vol. 130, no. 34, pp. 11278–11279, Aug. 2008.

[208] D. Gerion, F. Pinaud, S. C. Williams, W. J. Parak, D. Zanchet, S. Weiss, and A. P. Alivisatos, "Synthesis and Properties of Biocompatible Water-Soluble Silica-Coated CdSe/ZnS Semiconductor Quantum Dots†," *J. Phys. Chem. B*, vol. 105, no. 37, pp. 8861–8871, Jun. 2001.

[209] X. Wu, H. Liu, J. Liu, K. N. Haley, J. A. Treadway, J. P. Larson, N. Ge, F. Peale, and M. P. Bruchez, "Immunofluorescent labeling of cancer marker Her2 and other cellular targets with semiconductor quantum dots," *Nat. Biotechnol.*, vol. 21, no. 1, pp. 41–6, 2003.

[210] T. Pellegrino, L. Manna, S. Kudera, T. Liedl, D. Koktysh, A. L. Rogach, S. Keller, J. Rädler, G. Natile, and W. J. Parak, "Hydrophobic Nanocrystals Coated with an Amphiphilic Polymer Shell: A General Route to Water Soluble Nanocrystals," *Nano Lett.*, vol. 4, no. 4, pp. 703–707, Mar. 2004.

[211] Y. Cui, R. M. Levenson, L. W. K. Chung, and S. Nie, “In vivo cancer targeting and imaging with semiconductor quantum dots,” *Nat. Biotechnol.*, vol. 22, no. 8, pp. 969–76, 2004.

[212] D. Bera, L. Qian, and P. H. Holloway, “Semiconducting Quantum Dots for Bioimaging,” in *Drug Delivery Nanoparticles Formulation and Characterization*, pp. 349–366.

[213] A. M. Smith, X. Gao, and S. Nie, “Quantum Dot Nanocrystals for In Vivo Molecular and Cellular Imaging,” *Photochem. Photobiol.*, vol. 80, no. 3, pp. 377–385, 2004.

[214] R. E. Bailey, A. M. Smith, and S. Nie, “Quantum dots in biology and medicine,” *Phys. E Low-dimensional Syst. Nanostructures*, vol. 25, no. 1, pp. 1–12, 2004.

[215] S. Santra, J. Xu, K. Wang, and W. Tan, “Luminescent nanoparticle probes for bioimaging,” *J. Nanosci. Nanotechnol.*, vol. 4, no. 6, pp. 590–9, 2004.

[216] P. Sharma, S. Brown, G. Walter, S. Santra, and B. Moudgil, “Nanoparticles for bioimaging,” *Adv. Colloid Interface Sci.*, vol. 123–126, no. 0, pp. 471–485, 2006.

[217] W. J. Parak, T. Pellegrino, and C. Plank, “Labelling of cells with quantum dots,” *Nanotechnology*, vol. 16, no. 2, p. R9, 2005.

[218] Z.-B. Li, W. Cai, and X. Chen, “Semiconductor quantum dots for in vivo imaging,” *J. Nanosci. Nanotechnol.*, vol. 7, no. 8, pp. 2567–81, 2007.

[219] S. Kumar and R. Richards-Kortum, “Optical molecular imaging agents for cancer diagnostics and therapeutics.,” *Nanomedicine*, vol. 1, no. 1, pp. 23–30, 2006.

[220] G. Shan, R. Weissleder, and S. Hilderbrand, “Upconverting organic dye doped core-shell nano-composites for dual-modality NIR imaging and photo-thermal therapy,” *Theranostics*, 2013.

[221] U. Resch-Genger, M. Grabolle, S. Cavaliere-Jaricot, R. Nitschke, and T. Nann, “Quantum dots versus organic dyes as fluorescent labels.,” *Nat. Methods*, vol. 5, no. 9, pp. 763–75, Sep. 2008.

[222] K. Remaut, B. Lucas, K. Raemdonck, K. Braeckmans, J. Demeester, and S. C. De Smedt, “Can we better understand the intracellular behavior of DNA nanoparticles by fluorescence correlation spectroscopy?,” *J. Control. Release*, vol. 121, no. 1–2, pp. 49–63, Aug. 2007.

[223] M. Correa-Duarte, M. Giersig, and L. Liz-Marzán, “Stabilization of CdS semiconductor nanoparticles against photodegradation by a silica coating procedure,” *Chem. Phys. Lett.*, 1998.

[224] K. E. Sapsford, T. Pons, I. L. Medintz, and H. Mattoussi, “Biosensing with Luminescent Semiconductor Quantum Dots,” *Sensors*, vol. 6, no. 8, pp. 925–953, 2006.

[225] M. Dahan, S. Lévi, C. Luccardini, P. Rostaing, B. Riveau, and A. Triller, "Diffusion dynamics of glycine receptors revealed by single-quantum dot tracking.," *Science*, vol. 302, no. 5644, pp. 442–5, Oct. 2003.

[226] L. Jing, K. Ding, S. Kalytchuk, Y. Wang, R. Qiao, S. V. Kershaw, A. L. Rogach, and M. Gao, "Aqueous Manganese-Doped Core/Shell CdTe/ZnS Quantum Dots with Strong Fluorescence and High Relaxivity," *J. Phys. Chem. C*, vol. 117, no. 36, pp. 18752–18761, Sep. 2013.

[227] S. Wang, B. R. Jarrett, S. M. Kauzlarich, and A. Y. Louie, "Core/shell quantum dots with high relaxivity and photoluminescence for multimodality imaging.," *J. Am. Chem. Soc.*, vol. 129, no. 13, pp. 3848–56, Apr. 2007.

[228] F. Ye, Å. Barrefelt, and H. Asem, "Biodegradable polymeric vesicles containing magnetic nanoparticles, quantum dots and anticancer drugs for drug delivery and imaging," *Biomaterials*, 2014.

[229] Y.-K. Peng, C.-W. Lai, C.-L. Liu, H.-C. Chen, Y.-H. Hsiao, W.-L. Liu, K.-C. Tang, Y. Chi, J.-K. Hsiao, K.-E. Lim, H.-E. Liao, J.-J. Shyue, and P.-T. Chou, "A new and facile method to prepare uniform hollow MnO/functionalized $mSiO_2$ core/shell nanocomposites.," *ACS Nano*, vol. 5, no. 5, pp. 4177–87, May 2011.

[230] G. Stasiuk, S. Tamang, and D. Imbert, "Cell-permeable Ln (III) chelate-functionalized InP quantum dots as multimodal imaging agents," *ACS Nano*, 2011.

[231] X. Wei, W. Wang, and K. Chen, "ZnO: Er, Yb, Gd Particles Designed for Magnetic-Fluorescent Imaging and Near-Infrared Light Triggered Photodynamic Therapy," *J. Phys. Chem. C*, 2013.

[232] Y. Liu, K. Ai, Q. Yuan, and L. Lu, "Fluorescence-enhanced gadolinium-doped zinc oxide quantum dots for magnetic resonance and fluorescence imaging," *Biomaterials*, 2011.

[233] H. Yang, S. Santra, G. A. Walter, and P. H. Holloway, "GdIII-Functionalized Fluorescent Quantum Dots as Multimodal Imaging Probes," *Adv. Mater.*, vol. 18, no. 21, pp. 2890–2894, 2006.

[234] G. Stasiuk, S. Tamang, D. Imbert, and C. Gateau, "Optimizing the relaxivity of Gd (III) complexes appended to InP/ZnS quantum dots by linker tuning," *Dalt. Trans.*, 2013.

[235] X. Wei, W. Wang, and K. Chen, "Preparation and characterization of ZnS:Tb{,}Gd and ZnS:Er{,}Yb{,}Gd nanoparticles for bimodal magnetic-fluorescent imaging," *Dalt. Trans.*, vol. 42, no. 5, pp. 1752–1759, 2013.

[236] C.-Y. Cheng, K.-L. Ou, W.-T. Huang, J.-K. Chen, J.-Y. Chang, and C.-H. Yang, "Gadolinium-Based CuInS2/ZnS Nanoprobe for Dual-Modality Magnetic Resonance/Optical Imaging," *ACS Appl. Mater. Interfaces*, vol. 5, no. 10, pp. 4389–4400, Apr. 2013.

[237] J.-C. Hsu, C.-C. Huang, K.-L. Ou, N. Lu, F.-D. Mai, J.-K. Chen, and J.-Y. Chang, "Silica nanohybrids integrated with CuInS2/ZnS quantum dots and magnetite

nanocrystals: multifunctional agents for dual-modality imaging and drug delivery," *J. Mater. Chem.*, vol. 21, no. 48, pp. 19257–19266, 2011.

[238] J. Jung, M. Kim, J. Cho, S. Lee, I. Yang, and J. Cho, "Europium-doped gadolinium sulfide nanoparticles as a dual-mode imaging agent for T 1-weighted MR and photoluminescence imaging," *Biomaterials*, 2012.

[239] B. Alder and T. Wainwright, "Studies in molecular dynamics. I. General method," *J. Chem. Phys.*, 1959.

[240] A. Rahman, "Correlations in the motion of atoms in liquid argon," *Phys. Rev.*, 1964.

[241] X. Chen, X. Li, L. Cai, and J. Zhu, "Pressure induced phase transition in ZnS," *Solid State Commun.*, 2006.

[242] C. Hu, L. Sun, Z. Zeng, and X. Chen, "Pressure and temperature induced phase transition of ZnS from first-principles calculations," *Chinese Phys. Lett.*, 2008.

[243] J. F. Huang, F.; Zhang, H.; Gilbert, B.; Banfield, "Surface State Controlled Nanocrystalline ZnS Structure Transformation," in *225th National Meeting of the American Chemical Society*, 2003.

[244] J. F. Zhang, H.; Gilbert, B.; Huang, F.; Banfield, "Water-driven transformation of nanoparticle structure at room temperature," *Nature*, vol. 424, p. 1025, 2003.

[245] S. P. R. and A. S. B. C. Feigl, "Safe, stable and effective nanotechnology: phase mapping of ZnS nanoparticles," *J. Mater. Chem.*, vol. 20, pp. 4971–4980, 2010.

[246] K. Wright and R. Jackson, "Computer simulation of the structure and defect properties of zinc sulfide," *J. Mater. Chem.*, 1995.

[247] K. Wright and G. Watson, "Simulation of the structure and stability of sphalerite (ZnS) surfaces," *Am. Mineral.*, 1998.

[248] H. Zhang and J. F. Banfield, "Aggregation, Coarsening, and Phase Transformation in ZnS Nanoparticles Studied by Molecular Dynamics Simulations," *Nano Lett.*, vol. 4, no. 4, pp. 713–718, Apr. 2004.

[249] K. Wright and J. D. Gale, "interatomic potentials for the simulation of the zinc-blende and wurzite forms of ZnS and CdS: Bulk structure, properties, and phase stability," *Phys. Rev. B*, vol. 70, p. 035211, 2004.

[250] K. Wright, "The incorporation of Cadmium, Manganese, and Ferrous iron in sphalerite/ Insights from computer simulations," *Can. Mineral.*, vol. 47, pp. 615–623, 2009.

[251] S. Hamad, S. Cristol, and C. R. A. Catlow, "Simulation of the embryonic stage of ZnS formation from aqueous solution.," *J. Am. Chem. Soc.*, vol. 127, no. 8, pp. 2580–90, Mar. 2005.

[252] E. Spanó, S. Hamad, and C. R. A. Catlow, "Computational Evidence of Bubble ZnS Clusters," *J. Phys. Chem. B*, vol. 107, no. 38, pp. 10337–10340, Sep. 2003.

[253] A. Adler, “On the preparation of metalloporphyrins,” *J. Inorg. Nucl. Chem.*, vol. 32, no. 7, pp. 2443–2445, 1970.

[254] M. A. Friedman and B. J. Wood, “Precipitation of Gadolinium and Ethanol during Nerve Block,” *Journal of vascular and interventional radiology : JVIR*, vol. 14, no. 3. Society of Cardiovascular and Interventional Radiology,, p. 394, 01-Mar-2003.

[255] D. Nanz, G. Andreisek, J. M. Fröhlich, D. Weishaupt, K. Treiber, S. Ess, and T. Pfammatter, “Contrast Material–enhanced Visualization of the Ablation Medium for Magnetic Resonance– monitored Ethanol Injection Therapy: Imaging and Safety Aspects,” *J. Vasc. Interv. Radiol.*, vol. 17, no. 1, pp. 95–102, 2006.

[256] M. G. Wysoki and R. I. White, “Crystallization When Mixing Contrast Materials with Ethanol for Embolization of Venous Malformations,” *Journal of vascular and interventional radiology : JVIR*, vol. 12, no. 2. Society of Cardiovascular and Interventional Radiology,, p. 264, 01-Feb-2001.

[257] W. Fan, W. Yan, Z. Xu, and H. Ni, “Formation mechanism of monodisperse, low molecular weight chitosan nanoparticles by ionic gelation technique,” *Colloids Surfaces B Biointerfaces*, vol. 90, no. 0, pp. 21–27, 2012.

[258] M. Gaceur, M. Giraud, M. Hemadi, S. Nowak, N. Menguy, J. P. Quisefit, K. David, T. Jahanbin, S. Benderbous, M. Boissière, and S. Ammar, “Polyol-synthesized Zn0.9Mn0.1S nanoparticles as potential luminescent and magnetic bimodal imaging probes: synthesis, characterization, and toxicity study,” *J. Nanoparticle Res.*, vol. 14, no. 7, p. 932, Jun. 2012.

[259] S. Hamad, S. Cristol, and C. R. A. Catlow, “Surface Structures and Crystal Morphology of ZnS: Computational Study,” *J. Phys. Chem. B*, vol. 106, no. 42, pp. 11002–11008, 2002.

[260] K. Wright and R. A. R. Jackson, “Computer simulation of the structure and defect properties of zinc sulfide,” *J. Mater. Chem.*, vol. 5, no. 11, pp. 2037–2040, 1995.

[261] F. Benkabou, H. Aourag, and M. Certier, “Atomistic study of zinc-blende CdS, CdSe, ZnS, and ZnSe from molecular dynamics,” *Mater. Chem. Phys.*, vol. 66, no. 1, pp. 10–16, Sep. 2000.

[262] I. T. Todorov, W. Smith, and K. T. M. T. Doveb, “DL_POLY_3: new dimensions in molecular dynamics simulations via massive parallelism,” *J. Mater. Chem.*, vol. 16, pp. 1911–1918, 2006.

[263] R. W. G. Wyckoff, *Crystal Structures*, 2nd ed. New York: Interscience, 1924.

[264] K. Wright, “An X-ray absorption study of doped sphalerites,” *Can. Mineral.*, 2009.

[265] W. L. Jorgensen, J. Chandrasekhar, J. D. Madura, R. W. Impey, and M. L. Klein, “Comparison of simple potential functions for simulating liquid water,” *J. Chem. Phys.*, vol. 79, no. 2, p. 926, 1983.

[266] H. J. C. Berendsen, J. R. Grigera, and T. P. Straatsma, “The missing term in effective pair potentials,” *J. Phys. Chem.*, vol. 91, no. 24, pp. 6269–6271, Nov. 1987.

[267] H. Zhang, J. R. Rustad, and J. F. Banfield, “Interaction between water molecules and zinc sulfide nanoparticles studied by temperature-programmed desorption and molecular dynamics simulations.,” *J. Phys. Chem. A*, vol. 111, no. 23, pp. 5008–14, Jun. 2007.

[268] E. Fagadar-Cosma and C. Enache, “Comparative investigations of the absorption and fluorescence spectra of tetrapyridylporphyrine and Zn (II) tetrapyridylporphyrine,” *Dig. J. Nanomater. Biostructures*, vol. 2, no. 1, pp. 175–183, 2007.

[269] S. Abdo, M. I. Cruz, and J. J. Fripiat, “Metallation-demetallation reaction of Tin-Tetra(4-Pyridyl) Porphyrin in Na-HECTORITE,” *Clays Clay Miner.*, vol. 28, no. 2, pp. 125–129, 1980.

[270] D. F. Marsh and L. M. Mink, “Microscale Synthesis and Electronic Absorption Spectroscopy of Tetraphenylporphyrin H 2 (TPP) and Metalloporphyrins Zn II (TPP) and Ni II (TPP),” vol. 73, no. 12, pp. 1188–1190, 1996.

[271] Z.-C. Sun, Y.-B. She, Y. Zhou, X.-F. Song, and K. Li, “Synthesis, Characterization and Spectral Properties of Substituted Tetraphenylporphyrin Iron Chloride Complexes,” *Molecules*, vol. 16, no. 4, pp. 2960–2970, 2011.

[272] M. Dongol, a. El-Denglawey, a. F. Elhady, and a. a. Abuelwafa, “Structural properties of nano 5, 10, 15, 20-Tetraphenyl-21H,23H-porphine nickel (II) thin films,” *Curr. Appl. Phys.*, vol. 12, no. 5, pp. 1334–1339, Sep. 2012.

[273] M. D. M. D. OGAN, D. REVEL, and R. C. R. C. Brasch, “Metalloporphyrin Contrast Enhancement of Tumors in Magnetic Resonance Imaging A Study of Human Carcinoma, Lymphoma, and Fibrosarcoma in Mice,” *Invest. Radiol.*, vol. 22, no. 10, 1987.

[274] P. Hambright, A. Turner, J. S. Cohen, R. C. Lyon, A. Katz, P. Neta, and A. Adeyemo, “An iron(III) porphyrin that exhibits minimal dimerization in aqueous solution,” *Inorganica Chim. Acta*, vol. 128, no. 1, pp. L11 – L14, 1987.

[275] S. C. M. Gandini, E. a. Vidoto, O. R. Nascimento, and M. Tabak, “Spectroscopic study of a water-soluble iron(III) meso-tetrakis(4-N-methylpyridiniumyl) porphyrin in aqueous solution: effects of pH and salt,” *J. Inorg. Biochem.*, vol. 94, no. 1–2, pp. 127–137, Feb. 2003.

[276] R. Lauffer, “Paramagnetic Metal Complexes as Water Proton Relaxation Agents for NMR Imaging: Theory and Design,” *Chem Rev.*, vol. 87, pp. 901–927, 1987.

[277] A. Budimir, J. Kalmár, I. Fábián, G. Lente, I. Bányai, I. Batinić-Haberle, and M. Birus, “Water exchange rates of water-soluble manganese(III) porphyrins of therapeutical potential.,” *Dalton Trans.*, vol. 39, no. 18, pp. 4405–10, May 2010.

[278] K. E. Kellar and N. Foster, “Relaxation enhancement of water protons by manganese(III) porphyrins: influence of porphyrin aggregation,” *Inorg. Chem.*, vol. 31, no. 8, pp. 1353–1359, 1992.

[279] A. De Cian, M. Moussavi, J. Fischer, and R. Weiss, “Synthesis, structure, and spectroscopic and magnetic properties of lutetium(III) phthalocyanine derivatives: LuPc2.CH2Cl2 and [LuPc(OAc)(H2O)2].H2O.2CH3OH,” *Inorg. Chem.*, vol. 24, no. 20, pp. 3162–3167, 1985.

[280] E. Terreno, D. D. Castelli, A. Viale, and S. Aime, “Challenges for Molecular Magnetic Resonance Imaging,” *Chem. Rev.*, vol. 110, no. 5, pp. 3019–3042, 2010.

[281] P. Hermann, J. Kotek, V. Kubicek, and I. Lukes, “Gadolinium(iii) complexes as MRI contrast agents: ligand design and properties of the complexes,” *Dalt. Trans.*, no. 23, pp. 3027–3047, 2008.

[282] F. Yerly, K. I. Hardcastle, L. Helm, S. Aime, M. Botta, and A. E. Merbach, “Molecular dynamics simulation of [Gd(egta)(H(2)O)](-) in aqueous solution: internal motions of the poly(amino carboxylate) and water ligands, and rotational correlation times.,” *Chemistry*, vol. 8, no. 5, pp. 1031–9, Mar. 2002.

[283] L. Frullano and P. Caravan, “Rational Design of a High Relaxivity MR probe 1,” *Proc. Intl. Soc. Mag. Reson. Med*, vol. 17, p. 2009, 2009.

[284] J. L. Sessler and R. a Miller, “Texaphyrins: new drugs with diverse clinical applications in radiation and photodynamic therapy.,” *Biochem. Pharmacol.*, vol. 59, no. 7, pp. 733–9, Apr. 2000.

[285] C. F. Geraldes, A. D. Sherry, P. Vallet, F. Maton, R. N. Muller, T. D. Mody, G. Hemmi, and J. L. Sessler, “Nuclear magnetic relaxation dispersion studies of water-soluble gadolinium(III)-texaphyrin complexes,” *J. Magn. Reson. imaging*, vol. 5, no. 6, 1995.

[286] S. W. YOUNG and Q. FAN, “Imaging of Human Colon Cancer Xenograft with Gadolinium- Texaphyrin,” *Invest. Radiol.*, vol. 31, no. 5, 1996.

[287] F. Hindré, M. Le Plouzennec, J. D. de Certaines, M. T. Foultier, T. Patrice, and G. Simonneaux, “Tetra-p-aminophenylporphyrin conjugated with Gd-DTPA: Tumor-specific contrast agent for MR imaging,” *J. Magn. Reson. Imaging*, vol. 3, no. 1, pp. 59–65, 1993.

[288] P. Caravan, C. T. Farrar, L. Frullano, and R. Uppal, “Influence of molecular parameters and increasing magnetic field strength on relaxivity of gadolinium- and manganese-based T1 contrast agents,” *Contrast Media Mol. Imaging*, vol. 4, no. 2, pp. 89–100, 2009.

[289] S. Bhuniya, H. Moon, H. Lee, K. S. Hong, S. Lee, D.-Y. Yu, and J. S. Kim, “Uridine-based paramagnetic supramolecular nanoaggregate with high relaxivity capable of detecting primitive liver tumor lesions,” *Biomaterials*, vol. 32, no. 27, pp. 6533–6540, 2011.

[290] P. Caravan, G. Parigi, J. M. Chasse, N. J. Cloutier, J. J. Ellison, R. B. Lauffer, C. Luchinat, S. A. McDermid, M. Spiller, and T. J. McMurry, "Albumin Binding, Relaxivity, and Water Exchange Kinetics of the Diastereoisomers of MS-325, a Gadolinium(III)-Based Magnetic Resonance Angiography Contrast Agent," *Inorg. Chem.*, vol. 46, no. 16, pp. 6632–6639, 2007.

[291] A. Jedlovszky-Hajdú, E. Tombácz, I. Bányai, M. Babos, and A. Palkó, "Carboxylated magnetic nanoparticles as {MRI} contrast agents: Relaxation measurements at different field strengths," *J. Magn. Magn. Mater.*, vol. 324, no. 19, pp. 3173–3180, 2012.

[292] W. Wang, H. Dong, V. Pacheco, D. Willbold, Y. Zhang, A. Offenhaeusser, R. Hartmann, T. E. Weirich, P. Ma, H.-J. Krause, and Z. Gu, "Relaxation behavior study of ultrasmall superparamagnetic iron oxide nanoparticles at ultralow and ultrahigh magnetic fields.," *J. Phys. Chem. B*, vol. 115, no. 49, pp. 14789–93, Dec. 2011.

[293] J. S. Troughton, M. T. Greenfield, J. M. Greenwood, S. Dumas, A. J. Wiethoff, J. Wang, M. Spiller, T. J. McMurry, and P. Caravan, "Synthesis and Evaluation of a High Relaxivity Manganese(II)-Based MRI Contrast Agent," *Inorg. Chem.*, vol. 43, no. 20, pp. 6313–6323, 2004.

[294] L. Helm, "Optimization of gadolinium-based MRI contrast agents for high magnetic-field applications," *Future Med. Chem.*, vol. 2, no. 3, pp. 385–396, Mar. 2010.

[295] J. Garcia, A. N. W. Kuda-Wedagedara, and M. J. Allen, "Physical Properties of Eu(2+)-Containing Cryptates as Contrast Agents for Ultra-High Field Magnetic Resonance Imaging.," *Eur. J. Inorg. Chem.*, vol. 2012, no. 12, pp. 2135–2140, Apr. 2012.

[296] Y. Gossuin, A. Hocq, Q. L. Vuong, S. Disch, R. P. Hermann, and P. Gillis, "Physico-chemical and NMR relaxometric characterization of gadolinium hydroxide and dysprosium oxide nanoparticles.," *Nanotechnology*, vol. 19, no. 47, p. 475102, Nov. 2008.

[297] P. Caravan, J. J. Ellison, T. J. McMurry, and R. B. Lauffer, "Gadolinium(III) Chelates as MRI Contrast Agents: Structure, Dynamics, and Applications," *Chem. Rev.*, vol. 99, no. 9, pp. 2293–2352, 1999.

[298] R. M. Anderton and J. F. Kauffman, "Temperature-Dependent Rotational Relaxation of Diphenylbutadiene in n-Alcohols: A Test of the Quasihydrodynamic Free Space Model," *J. Phys. Chem.*, vol. 98, no. 47, pp. 12117–12124, Nov. 1994.

[299] S. Gao, J. Chen, L. Dong, Z. Ding, Y.-H. Yang, and J. Zhang, "Targeting delivery of oligonucleotide and plasmid DNA to hepatocyte via galactosylated chitosan vector.," *Eur. J. Pharm. Biopharm.*, vol. 60, no. 3, pp. 327–34, Aug. 2005.

[300] G. Borchard, "Chitosans for gene delivery.," *Adv. Drug Deliv. Rev.*, vol. 52, no. 2, pp. 145–50, Nov. 2001.

[301] A. Geçer, N. Yıldız, A. Çalımlı, and B. Turan, “Trimethyl chitosan nanoparticles enhances dissolution of the poorly water soluble drug Candesartan-Cilexetil,” *Macromol. Res.*, vol. 18, no. 10, pp. 986–991, 2010.

[302] A. Portero, C. Remuñán-López, and J. L. Vila-Jato, “Effect of chitosan and chitosan glutamate enhancing the dissolution properties of the poorly water soluble drug nifedipine,” *Int. J. Pharm.*, vol. 175, no. 1, pp. 75–84, 1998.

[303] D.-G. Kim, Y.-I. Jeong, C. Choi, S.-H. Roh, S.-K. Kang, M.-K. Jang, and J.-W. Nah, “Retinol-encapsulated low molecular water-soluble chitosan nanoparticles,” *Int. J. Pharm.*, vol. 319, no. 1–2, pp. 130–138, 2006.

[304] E. Buhler and M. Rinaudo, “Structural and Dynamical Properties of Semirigid Polyelectrolyte Solutions: A Light-Scattering Study,” *Macromolecules*, vol. 33, no. 6, pp. 2098–2106, 2000.

[305] C. Schatz, C. Pichot, T. Delair, C. Viton, and A. Domard, “Static Light Scattering Studies on Chitosan Solutions: From Macromolecular Chains to Colloidal Dispersions,” *Langmuir*, vol. 19, no. 23, pp. 9896–9903, 2003.

[306] M. W. Anthonsen, K. M. Vårum, A. M. Hermansson, O. Smidsrød, and D. A. Brant, “Aggregates in acidic solutions of chitosans detected by static laser light scattering,” *Carbohydr. Polym.*, vol. 25, no. 1, pp. 13–23, 1994.

[307] M. M. Amiji, “Pyrene fluorescence study of chitosan self-association in aqueous solution,” *Carbohydr. Polym.*, vol. 26, no. 3, pp. 211–213, 1995.

[308] Q. Gan, T. Wang, C. Cochrane, and P. McCarron, “Modulation of surface charge, particle size and morphological properties of chitosan–TPP nanoparticles intended for gene delivery,” *Colloids Surfaces B Biointerfaces*, vol. 44, no. 2–3, pp. 65–73, 2005.

[309] Y. Wu, W. Yang, C. Wang, J. Hu, and S. Fu, “Chitosan nanoparticles as a novel delivery system for ammonium glycyrrhizinate,” *Int. J. Pharm.*, vol. 295, no. 1–2, pp. 235–245, 2005.

[310] P. He, S. S. Davis, and L. Illum, “Chitosan microspheres prepared by spray drying,” *Int. J. Pharm.*, vol. 187, no. 1, pp. 53–65, 1999.

[311] M. L. Tsaih and R. H. Chen, “Effect of molecular weight and urea on the conformation of chitosan molecules in dilute solutions,” *Int. J. Biol. Macromol.*, vol. 20, no. 3, pp. 233–240, 1997.

[312] P. Sorlier, C. Viton, and A. Domard, “Relation between Solution Properties and Degree of Acetylation of Chitosan: Role of Aging,” *Biomacromolecules*, vol. 3, no. 6, pp. 1336–1342, 2002.

[313] M. W. Anthonsen, K. M. Vårum, and O. Smidsrød, “Solution properties of chitosans: conformation and chain stiffness of chitosans with different degrees of N-acetylation,” *Carbohydr. Polym.*, vol. 22, no. 3, pp. 193–201, 1993.

[314] M. H. Ottøy, K. M. Vårum, and O. Smidsrød, “Compositional heterogeneity of heterogeneously deacetylated chitosans,” *Carbohydr. Polym.*, vol. 29, no. 1, 1996.

[315] N. Errington, S. E. Harding, K. M. Vårum, and L. Illum, “Hydrodynamic characterization of chitosans varying in degree of acetylation,” *Int. J. Biol. Macromol.*, vol. 15, no. 2, pp. 113–117, 1993.

[316] W. Wang, S. Bo, S. Li, and W. Qin, “Determination of the Mark-Houwink equation for chitosans with different degrees of deacetylation,” *Int. J. Biol. Macromol.*, vol. 13, no. 5, pp. 281–285, 1991.

[317] M. Rinaudo, M. Milas, and P. Le Dung, “Characterization of chitosan. Influence of ionic strength and degree of acetylation on chain expansion,” *Int. J. Biol. Macromol.*, vol. 15, no. 5, pp. 281–285, 1993.

[318] M. Terbojevich, A. Cosani, G. Conio, E. Marsano, and E. Bianchi, “Chitosan: chain rigidity and mesophase formation,” *Carbohydr. Res.*, vol. 209, no. 0, pp. 251–260, 1991.

[319] G. Berth and H. Dautzenberg, “The degree of acetylation of chitosans and its effect on the chain conformation in aqueous solution,” *Carbohydr. Polym.*, vol. 47, no. 1, pp. 39–51, 2002.

[320] C. Schatz, C. Viton, T. Delair, C. Pichot, and A. Domard, “Typical Physicochemical Behaviors of Chitosan in Aqueous Solution,” *Biomacromolecules*, vol. 4, no. 3, pp. 641–648, 2003.

[321] P. Sorlier, A. Denuzière, C. Viton, and A. Domard, “Relation between the Degree of Acetylation and the Electrostatic Properties of Chitin and Chitosan,” *Biomacromolecules*, vol. 2, no. 3, pp. 765–772, 2001.

[322] C. J. Van Oss, M. K. Chaudhury, and R. J. Good, “Interfacial Lifshitz-van der Waals and polar interactions in macroscopic systems,” *Chem. Rev.*, vol. 88, no. 6, pp. 927–941, 1988.

[323] G. Qun and W. Ajun, “Effects of molecular weight, degree of acetylation and ionic strength on surface tension of chitosan in dilute solution,” *Carbohydr. Polym.*, vol. 64, no. 1, pp. 29–36, 2006.

[324] W. Yang, J. Fu, T. Wang, and N. He, “Chitosan/Sodium Tripolyphosphate Nanoparticles: Preparation, Characterization and Application as Drug Carrier,” *Journal of Biomedical Nanotechnology*, vol. 5, no. 5. pp. 591–595, 2009.

[325] S. Y. S. Chae, M.-K. M. Jang, and J.-W. J. Nah, “Influence of molecular weight on oral absorption of water soluble chitosans,” *J. Control. release*, vol. 102, no. 2, pp. 383–394, 2005.

[326] S. W. C. Richardson, H. J. V Kolbe, and R. Duncan, “Potential of low molecular mass chitosan as a DNA delivery system: biocompatibility, body distribution and ability to complex and protect DNA.,” *Int. J. Pharm.*, vol. 178, no. 2, pp. 231–43, Mar. 1999.

[327] J. Li and Q. Huang, “Rheological properties of chitosan–tripolyphosphate complexes: From suspensions to microgels,” *Carbohydr. Polym.*, vol. 87, no. 2, pp. 1670–1677, 2012.

[328] L. Qi, Z. Xu, X. Jiang, C. Hu, and X. Zou, “Preparation and antibacterial activity of chitosan nanoparticles,” *Carbohydr. Res.*, vol. 339, no. 16, pp. 2693–2700, 2004.

[329] Z. Jin, W. Li, H. Cao, X. Zhang, G. Chen, H. Wu, C. Guo, Y. Zhang, H. Kang, Y. Wang, and K. Zhao, “Antimicrobial activity and cytotoxicity of N-2-HACC and characterization of nanoparticles with N-2-HACC and {CMC} as a vaccine carrier,” *Chem. Eng. J.*, vol. 221, no. 0, pp. 331–341, 2013.

[330] Y. Xu and Y. Du, “Effect of molecular structure of chitosan on protein delivery properties of chitosan nanoparticles,” *Int. J. Pharm.*, vol. 250, no. 1, pp. 215–226, 2003.

[331] J. Yu, Y. Du, and H. Zheng, “Blend films of chitosan-gelatin,” *Wuhan Univ. J. Nat. Sci.*, vol. 4, no. 4, p. 476, 1999.

[332] J. Z. Knaul, S. M. Hudson, and K. A. M. Creber, “Improved mechanical properties of chitosan fibers,” *J. Appl. Polym. Sci.*, vol. 72, no. 13, pp. 1721–1732, 1999.

[333] S. Vimal, G. Taju, K. S. N. Nambi, S. A. Majeed, V. S. Babu, M. Ravi, and A. S. S. Hameed, “Synthesis and characterization of CS/TPP nanoparticles for oral delivery of gene in fish,” *Aquaculture*, vol. 358–359, no. 0, pp. 14–22, 2012.

[334] S. W. Ali, S. Rajendran, and M. Joshi, “Synthesis and characterization of chitosan and silver loaded chitosan nanoparticles for bioactive polyester,” *Carbohydr. Polym.*, vol. 83, no. 2, pp. 438–446, 2011.

[335] C. Reichardt, *Solvents and Solvent Effects in Organic Chemistry*, Second edi. Weinheim: VCH, 1988.

[336] Y. G. Sıdır and İ. Sıdır, “Solvent effect on the absorption and fluorescence spectra of 7-acetoxy-6-(2,3-dibromopropyl)-4,8-dimethylcoumarin: Determination of ground and excited state dipole moments,” *Spectrochim. Acta Part A Mol. Biomol. Spectrosc.*, vol. 102, no. 0, pp. 286–296, 2013.

[337] P. Tallury, S. Santra, P. Sharma, B. M. D. C. Matos, N. Bengtsson, S. Biswas, A. K. Saha, G. A. Walter, E. A. Scott, and B. M. Moudgil, “Fluorescent and paramagnetic chitosan nanoparticles that exhibit high magnetic resonance relaxivity: synthesis, characterization and in vitro studies,” *J Biomed Nanotechnol*, vol. 7, no. 5, pp. 724–9, 2011.

[338] S. Aime, E. Gianolio, F. Uggeri, S. Tagliapietra, A. Barge, and G. Cravotto, “New paramagnetic supramolecular adducts for MRI applications based on non-covalent interactions between Gd(III)-complexes and beta- or gamma-cyclodextrin units anchored to chitosan.,” *J. Inorg. Biochem.*, vol. 100, no. 5–6, pp. 931–8, May 2006.

[339] A. Szpak, G. Kania, T. Skórka, W. Tokarz, S. Zapotoczny, and M. Nowakowska, “Stable aqueous dispersion of superparamagnetic iron oxide nanoparticles protected by charged chitosan derivatives.,” *J. Nanopart. Res.*, vol. 15, no. 1, p. 1372, Jan. 2013.

[340] N. Lee and T. Hyeon, “Designed synthesis of uniformly sized iron oxide nanoparticles for efficient magnetic resonance imaging contrast agents.,” *Chem. Soc. Rev.*, vol. 41, no. 7, pp. 2575–89, Apr. 2012.

[341] S. Kar and S. Biswas, “Rapid Synthesis of Core/Shell ZnS:Mn/Si Nanotetrapods by a Catalyst-Free Thermal Evaporation Route,” *ACS Appl. Mater. Interfaces*, vol. 1, no. 7, pp. 1420–1426, 2009.

[342] V. Wood, J. E. Halpert, M. J. Panzer, M. G. Bawendi, and V. Bulović, “Alternating Current Driven Electroluminescence from ZnSe/ZnS:Mn/ZnS Nanocrystals,” *Nano Lett.*, vol. 9, no. 6, pp. 2367–2371, 2009.

[343] R. Zhang, Y. Liu, and S. Sun, “Synthesis and characterization of high-quality colloidal Mn2+-doped ZnS nanoparticles,” *Opt. Mater. (Amst).*, vol. 34, no. 11, pp. 1788–1794, Sep. 2012.

[344] L. Peng and Y. Wang, “Effects of the Template Composition and Coating on the Photoluminescence Properties of ZnS:Mn Nanoparticles.,” *Nanoscale Res. Lett.*, vol. 5, no. 5, pp. 839–45, Jan. 2010.

[345] X. Lü, J. Yang, Y. Fu, Q. Liu, B. Qi, C. Lü, and Z. Su, “White light emission from Mn2 + doped ZnS nanocrystals through the surface chelating of 8-hydroxyquinoline-5-sulfonic acid.,” *Nanotechnology*, vol. 21, no. 11, p. 115702, Mar. 2010.

[346] J. Cao, J. Yang, Y. Zhang, L. Yang, Y. Wang, M. Wei, Y. Liu, M. Gao, X. Liu, and Z. Xie, “Optimized doping concentration of manganese in zinc sulfide nanoparticles for yellow-orange light emission,” *J. Alloys Compd.*, vol. 486, no. 1–2, pp. 890–894, 2009.

[347] G. Murugadoss, B. Rajamannan, and V. Ramasamy, “Synthesis, characterization and optical properties of water-soluble ZnS:Mn2+ nanoparticles,” *J. Lumin.*, vol. 130, no. 11, pp. 2032–2039, 2010.

[348] R. Kripal, A. K. Gupta, S. K. Mishra, R. K. Srivastava, A. C. Pandey, and S. G. Prakash, “Photoluminescence and photoconductivity of ZnS:Mn2+ nanoparticles synthesized via co-precipitation method,” *Spectrochim. Acta Part A Mol. Biomol. Spectrosc.*, vol. 76, no. 5, pp. 523–530, 2010.

[349] G. Murugadoss, “Synthesis and optical characterization of {PVP} and SHMP-encapsulated Mn2+-doped ZnS nanocrystals,” *J. Lumin.*, vol. 130, no. 11, pp. 2207–2214, 2010.

[350] S. Nazerdeylami, E. Saievar-Iranizad, Z. Dehghani, and M. Molaei, “Synthesis and photoluminescent and nonlinear optical properties of manganese doped ZnS nanoparticles,” *Phys. B Condens. Matter*, vol. 406, no. 1, pp. 108–111, 2011.

[351] T. T. Q. Hoa, N. D. The, S. McVitie, N. H. Nam, L. Van Vu, T. D. Canh, and N. N. Long, "Optical properties of Mn-doped ZnS semiconductor nanoclusters synthesized by a hydrothermal process," *Opt. Mater. (Amst).*, vol. 33, 2011.

[352] M. Marandi, G. Hajisalem, N. Taghavinia, and M. Houshiar, "Fast two-step microwave-activated synthesis of Mn doped ZnS nanocrystals: Comparison of the luminescence and doping process with thermochemical approach," *J. Lumin.*, vol. 131, no. 4, pp. 721–726, 2011.

[353] H. P. Soni, D. Parmar, N. Patel, M. Chawda, and D. Bodas, "Formation of ZnS nanorods entrapped in polyacrylic acid (PAA) film," *Mater. Lett.*, vol. 62, no. 17–18, pp. 2700–2703, 2008.

[354] B. Bhattacharjee and C.-H. Lu, "Multicolor luminescence of undoped zinc sulfide nanocrystalline thin films at room temperature," *Thin Solid Films*, vol. 514, no. 1–2, pp. 132–137, 2006.

[355] R. Bhargava, D. Gallagher, X. Hong, and A. Nurmikko, "Optical properties of manganese-doped nanocrystals of ZnS," *Phys. Rev. Lett.*, vol. 72, no. 3, pp. 1–4, 1994.

[356] N. Dixit, H. Soni, M. Chawda, and D. Bodas, "Study of electrical and optical properties of Mn doped ZnS clusters," *Mater. Lett.*, vol. 63, no. 30, pp. 2669–2671, 2009.

[357] N. Pradhan, D. M. Battaglia, Y. Liu, and X. Peng, "Efficient, Stable, Small, and Water-Soluble Doped ZnSe Nanocrystal Emitters as Non-Cadmium Biomedical Labels," *Nano Lett.*, vol. 7, no. 2, pp. 312–317, 2007.

[358] J. Aldana, Y. A. Wang, and X. Peng, "Photochemical Instability of CdSe Nanocrystals Coated by Hydrophilic Thiols," *J. Am. Chem. Soc.*, vol. 123, no. 36, pp. 8844–8850, 2001.

[359] S. F. Wuister, C. de Mello Donegá, and A. Meijerink, "Influence of Thiol Capping on the Exciton Luminescence and Decay Kinetics of CdTe and CdSe Quantum Dots," *J. Phys. Chem. B*, vol. 108, no. 45, pp. 17393–17397, 2004.

[360] M. Gao, J. Sun, E. Dulkeith, N. Gaponik, U. Lemmer, and J. Feldmann, "Lateral Patterning of CdTe Nanocrystal Films by the Electric Field Directed Layer-by-Layer Assembly Method," *Langmuir*, vol. 18, no. 10, pp. 4098–4102, 2002.

[361] H. Hu and W. Zhang, "Synthesis and properties of transition metals and rare-earth metals doped ZnS nanoparticles," *Opt. Mater. (Amst).*, vol. 28, no. 5, pp. 536–550, Apr. 2006.

[362] W. Chen, R. Sammynaiken, Y. Huang, J.-O. Malm, R. Wallenberg, J.-O. Bovin, V. Zwiller, and N. a. Kotov, "Crystal field, phonon coupling and emission shift of Mn[sup 2+] in ZnS:Mn nanoparticles," *J. Appl. Phys.*, vol. 89, no. 2, p. 1120, 2001.

[363] T. A. Kennedy, E. R. Glaser, P. B. Klein, and R. N. Bhargava, "Symmetry and electronic structure of the Mn impurity in ZnS nanocrystals," *Phys. Rev. B*, vol. 52, no. 20, 1995.

[364] I. Yu, T. Isobe, M. Senna, and S. Takahashi, “Optical properties and characteristics of ZnS:Mn prepared by Mn coating method,” *Mater. Sci. Eng. B*, vol. 38, no. 1–2, pp. 177–181, 1996.

[365] K. Sooklal, B. S. Cullum, S. M. Angel, and C. J. Murphy, “Photophysical Properties of ZnS Nanoclusters with Spatially Localized Mn2+,” *J. Phys. Chem.*, vol. 100, no. 11, pp. 4551–4555, 1996.

[366] N. Tsujii, H. Kitazawa, and G. Kido, “Magnetic properties of Mn- and Eu-doped ZnS nanocrystals,” *J. Appl. Phys.*, vol. 93, no. 10, p. 6957, 2003.

[367] M. Wei, J. Yang, Y. Yan, L. Yang, J. Cao, H. Fu, B. Wang, and L. Fan, “Influence of Mn ions concentration on optical and magnetic properties of Mn-doped ZnS nanowires,” *Phys. E Low-dimensional Syst. Nanostructures*, vol. 52, no. 0, pp. 144–149, 2013.

[368] V. P. Sirkeli, D. D. Nedeoglo, N. D. Nedeoglo, I. V. Radevici, R. L. Sobolevskaia, K. D. Sushkevich, E. Lähderanta, A. V. Lashkul, R. Laiho, J.-P. Biethan, O. Yilmazoglu, D. Pavlidis, and H. L. Hartnagel, “Magnetic and luminescent properties of manganese-doped ZnSe crystals,” *Phys. B Condens. Matter*, vol. 407, no. 18, pp. 3802–3807, Sep. 2012.

[369] M. J. Baek, J. Y. Park, W. Xu, K. Kattel, H. G. Kim, E. J. Lee, A. K. Patel, J. J. Lee, Y. Chang, T. J. Kim, J. E. Bae, K. S. Chae, and G. H. Lee, “Water-soluble MnO nanocolloid for a molecular T1 MR imaging: a facile one-pot synthesis, in vivo T1 MR images, and account for relaxivities.,” *ACS Appl. Mater. Interfaces*, vol. 2, no. 10, pp. 2949–55, Oct. 2010.

[370] J. Huang, J. Xie, K. Chen, L. Bu, S. Lee, Z. Cheng, X. Li, and X. Chen, “HSA coated MnO nanoparticles with prominent MRI contrast for tumor imaging,” *Chem. Commun. (Camb).*, vol. 46, no. 36, 2010.

[371] E. Wiener, K. Woertler, G. Weirich, E. J. Rummeny, and M. Settles, “Contrast enhanced cartilage imaging: Comparison of ionic and non-ionic contrast agents,” *Eur. J. Radiol.*, vol. 63, no. 1, pp. 110–119, 2007.

[372] G. Elizondo, C. J. Fretz, D. D. Stark, S. M. Rocklage, S. C. Quay, D. Worah, Y. M. Tsang, M. C. Chen, and J. T. Ferrucci, “Preclinical evaluation of MnDPDP: new paramagnetic hepatobiliary contrast agent for MR imaging,” *Radiology*, vol. 178, 1991.

[373] A. Colins, *Nanotechnology Cookbook: Practical, Reliable and Jargon-free Experimental Procedures*, 1st ed. Elsevier, 2012.

[374] M. P. Lowe, D. Parker, O. Reany, S. Aime, M. Botta, G. Castellano, E. Gianolio, and R. Pagliarin, “pH-Dependent Modulation of Relaxivity and Luminescence in Macrocyclic Gadolinium and Europium Complexes Based on Reversible Intramolecular Sulfonamide Ligation,” *J. Am. Chem. Soc.*, vol. 123, no. 31, pp. 7601–7609, 2001.

[375] J. Deruiter, “Carboxylic Acid Structure and Chemistry : Part 2,” in *Principles of drug action I*, Auburn University, 2005, pp. 1–11.

[376] V. Jacques, S. Dumas, W.-C. Sun, J. S. Troughton, M. T. Greenfield, and P. Caravan, “High-relaxivity magnetic resonance imaging contrast agents. Part 2. Optimization of inner- and second-sphere relaxivity.,” *Invest. Radiol.*, vol. 45, 2010.

[377] C. Platas-Iglesias, L. Vander Elst, W. Zhou, R. N. Muller, C. F. G. C. Geraldes, T. Maschmeyer, and J. A. Peters, “Zeolite GdNaY nanoparticles with very high relaxivity for application as contrast agents in magnetic resonance imaging.,” *Chemistry*, vol. 8, no. 22, pp. 5121–31, Nov. 2002.

[378] Y.-S. Lin, Y. Hung, J.-K. Su, R. Lee, C. Chang, M.-L. Lin, and C.-Y. Mou, “Gadolinium(III)-Incorporated Nanosized Mesoporous Silica as Potential Magnetic Resonance Imaging Contrast Agents,” *J. Phys. Chem. B*, vol. 108, no. 40, pp. 15608–15611, Oct. 2004.

[379] J. Huang, “Improving the Magnetic Resonance Imaging Contrast and Detection Methods with Engineered Magnetic Nanoparticles,” *Theranostics*, vol. 2, no. 1, pp. 86–102, 2012.

[380] H. Bin Na, J. H. Lee, K. An, Y. Il Park, M. Park, I. S. Lee, D.-H. Nam, S. T. Kim, S.-H. Kim, S.-W. Kim, K.-H. Lim, K.-S. Kim, S.-O. Kim, and T. Hyeon, “Development of a T1 Contrast Agent for Magnetic Resonance Imaging Using MnO Nanoparticles,” *Angew. Chemie*, vol. 119, no. 28, pp. 5493–5497, 2007.

[381] L. Faucher, Y. Gossuin, A. Hocq, and M.-A. Fortin, “Impact of agglomeration on the relaxometric properties of paramagnetic ultra-small gadolinium oxide nanoparticles.,” *Nanotechnology*, vol. 22, no. 29, p. 295103, Jul. 2011.

[382] a T. M. Anishur Rahman, P. Majewski, and K. Vasilev, “Gd2O3 nanoparticles: size-dependent nuclear magnetic resonance.,” *Contrast Media Mol. Imaging*, vol. 8, no. 1, pp. 92–5, 2013.

[383] L. M. Parkes, R. Hodgson, L. T. Lu, L. D. Tung, I. Robinson, D. G. Fernig, and N. T. K. Thanh, “Cobalt nanoparticles as a novel magnetic resonance contrast agent--relaxivities at 1.5 and 3 Tesla.,” *Contrast Media Mol. Imaging*, vol. 3, no. 4, pp. 150–6, 2008.

[384] F. Roohi, J. Lohrke, A. Ide, G. Schütz, and K. Dassler, “Studying the effect of particle size and coating type on the blood kinetics of superparamagnetic iron oxide nanoparticles.,” *Int. J. Nanomedicine*, vol. 7, pp. 4447–58, Jan. 2012.

[385] C.-Y. Yeh, Z. Lu, S. Froyen, and A. Zunger, “Zinc-blende–wurtzite polytypism in semiconductors,” *Phys. Rev. B*, vol. 46, no. 16, pp. 10086–10097, Oct. 1992.

[386] B. H. Van, P. Van Ben, T. M. Thi, and H. N. Nhat, “Absorption and Radiation Transitions in Configuration of Mn-Doped ZnS Nanoparticles Synthesized by a Hydrothermal Method,” *J. Mater.*, vol. 2013, pp. 1–9, 2013.

[387] V. D. Mote, Y. Purushotham, and B. N. Dole, “Structural, morphological and optical properties of Mn doped ZnS nanocrystals,” *Cerâmica*, vol. 59, no. 352, pp. 614–619, Dec. 2013.

[388] T. G. A. Youngs, “Aten--an application for the creation, editing, and visualization of coordinates for glasses, liquids, crystals, and molecules.,” *J. Comput. Chem.*, vol. 31, no. 3, pp. 639–48, Feb. 2010.

[389] C. B. Duke, “The atomic geometries of GaP(110) and ZnS(110) revisited: A structural ambiguity and its resolution,” *J. Vac. Sci. Technol. A Vacuum, Surfaces, Film.*, vol. 2, no. 2, p. 515, 1984.

[390] L. A. Curtiss, D. J. Frurip, and M. Blander, “Studies of molecular association in H2O and D2O vapors by measurement of thermal conductivity,” *J. Chem. Phys.*, vol. 71, no. 6, 1979.

[391] J. A. Odutola and T. R. Dyke, “Partially deuterated water dimers: Microwave spectra and structure,” *J. Chem. Phys.*, vol. 72, no. 9, 1980.

[392] Y. Wu, H. L. Tepper, and G. A. Voth, “Flexible simple point-charge water model with improved liquid-state properties,” *J. Chem. Phys.*, vol. 124, 2006.

[393] W. L. Jorgensen and J. Tirado-Rives, “Potential energy functions for atomic-level simulations of water and organic and biomolecular systems,” *PNAS*, vol. 102, no. 19, pp. 6665– 6670, 2005.

[394] H. W. Horn, W. C. Swope, J. W. Pitera, J. D. Madura, T. J. Dick, G. L. Hura, and T. Head-Gordon, “Development of an improved four-site water model for biomolecular simulations: TIP4P-Ew,” *J. Chem. Phys.*, vol. 120, 2004.

[395] J. L. F. Abascala and C. Vega, “A general purpose model for the condensed phases of water: TIP4P/2005,” *J. Chem. Phys.*, vol. 123, 2005.

[396] S. W. Rick, S. J. Stuart, and B. J. Berne, “Dynamical fluctuating charge force fields: Application to liquid water,” *J. Chem. Phys.*, vol. 101, 1994.

[397] B. A. Bauer, G. L. Warren, and S. Patel, “Incorporating Phase-Dependent Polarizability in Nonadditive Electrostatic Models for Molecular Dynamics Simulations of the Aqueous Liquid-Vapor Interface,” *J. Chem. Theory Comput.*, vol. 5, pp. 359–373, 2009.

[398] J. J. de Pablo, J. M. Prausnitz, H. J. Strauch, and P. T. Cummings, “Molecular simulation of water along the liquid-vapor coexistence curve from 25 °C to the critical point,” *J. Chem. Phys.*, vol. 93, 1990.

[399] J. D. Bernal and R. H. Fowler, “A Theory of Water and Ionic Solution, with Particular Reference to Hydrogen and Hydroxyl Ions,” *J. Chem. Phys.*, vol. 1, no. 8, 1933.

[400] Y. Guissani and B. Guillot, “A computer simulation study of the liquid-vapor coexistence curve of water,” *J Chem Phys.*, vol. 98, 1983.

[401] P. Paricaud, M. Predota, A. A. Chialvo, and P. T. Cummings, “From dimer to condensed phases at extreme conditions: accurate predictions of the properties of water by a Gaussian charge polarizable model.,” *J. Chem. Phys.*, vol. 122, no. 24, p. 244511, Jun. 2005.

[402] N. H. de Leeuw and S. C. Parker, “Molecular-dynamics simulation of MgO surfaces in liquid water using a shell-model potential for water,” *Phys. Rev. B*, vol. 58, no. 20, 1998.

[403] B. Gilbert, H. Zhang, F. Huang, J. F. Banfield, Y. Ren, D. Haskel, J. C. Lang, G. Srajer, A. Jürgensen, and G. a Waychunas, “Analysis and simulation of the structure of nanoparticles that undergo a surface-driven structural transformation.,” *J. Chem. Phys.*, vol. 120, no. 24, pp. 11785–95, Jun. 2004.

[404] G. Licheri and G. Paschina, “X-Ray Diffraction Study of Aqueous Solutions of ZnSO4,” *Naturforsch. Tl. A*, vol. 37, p. 1205, 1982.

[405] A. Musinu and G. Paschina, “The sulphate ion in aqueous solution: an X-ray diffraction study of a ZnSO4 solution,” *J. Appl. Crystallogr.*, pp. 1–16, 1982.

[406] T. Radnai, G. Palinkas, and R. Caminiti, “X-Ray Diffraction Study on Hydration and Ion-Pairing in Aqueous ZnSO4 Solution,” *Naturforsch. Tl. A*, 1982.

[407] W. Bol, G. J. A. Gerrits, and C. L. van Panthaleon Eck, “The hydration of divalent cations in aqueous solution. An X-ray investigation with isomorphous replacement,” *J. Appl. Crystallogr.*, vol. 3, no. 6, pp. 486–492, Dec. 1970.

[408] T. Kawada, B. D. Mookherjee, and S. S. Chang, “Chemical reactions involved in the catalytic hydrogenation of oils. III. Further identification of volatile by-products,” *J. Am. Oil Chem. Soc.*, vol. 43, no. 4, pp. 237–241, Apr. 1966.

[409] A. Kuzmin, S. Obst, and J. Purans, “X-ray absorption spectroscopy and molecular dynamics studies of hydration in aqueous solutions,” *J. Phys. Condens. Matter*, vol. 9, no. 46, pp. 10065–10078, Nov. 1997.

[410] J. I. Yagu, H. L. Ahmed M. Mohammed, and B. M. Rode, “Classical and Mixed Quantum Mechanical/Molecular Mechanical Simulation of Hydrated Manganous Ion,” *J. Phys. Chem. A*, vol. 105, pp. 7646–7650, 2001.

[411] C. F. Schwenk, H. H. Loeffler, and B. M. Rode, “Structure and dynamics of metal ions in solution: QM/MM molecular dynamics simulations of Mn(2+) and V(2+).,” *J. Am. Chem. Soc.*, vol. 125, no. 6, pp. 1618–24, Feb. 2003.

[412] G. Jancsó, K. Heinzinger, and P. A. Bopp, “Molecular Dynamics Study of the Effect of Pressure on an Aqueous NaCl Solution,” *Z.Naturforsch 40a*, vol. 1235, 1985.

[413] O. Matsuoka1, E. Clementi1, and M. Yoshimine, “CI study of the water dimer potential surface,” *J. Chem. Phys.*, vol. 64, 1976.

[414] H. Ohtaki, T. Yamaguchi, M. Maeda, and M. M. Toshio Yamaguchi, “X-Ray Diffraction Studies of the Structures of Hydrated Divalent Transition-Metal Ions in Aqueous Solution,” *Bull. Chem. Soc. Jpn.*, vol. 49, pp. 701–708, 1976.

[415] H. Bin Na, I. C. Song, and T. Hyeon, “Inorganic Nanoparticles for MRI Contrast Agents,” *Adv. Mater.*, vol. 21, no. 21, pp. 2133–2148, Jun. 2009.

[416] F. Bloch, W. Hansen, and M. Packard, “The Nuclear Induction Experiment,” *Phys. Rev.*, vol. 70, no. 7–8, pp. 474–485, Oct. 1946.

[417] Z. Hou, C. Zhan, Q. Jiang, Q. Hu, and L. Li, “Both FA-and mPEG-conjugated chitosan nanoparticles for targeted cellular uptake and enhanced tumor tissue distribution,” *Nanoscale Res. Lett.*, 2011.

Synthèse de la thèse en Français

1. Introduction

L'imagerie par résonance magnétique (IRM) est une technique de diagnostic très utilisée. Malheureusement, la différence entre tissus sains et altérés est souvent insuffisante pour provoquer une variation sensible de l'intensité du signal, ce qui a motivé le développement des agents de contraste (AC) d'augmenter le contraste entre les parties saines et malades des tissus. Un effort considérable a été consacré à la conception des agents de contraste, qui présente à la fois une relaxivité élevée, une haute stabilité, une faible toxicité , et une grande spécificité tissulaire.

Le ligand macrocyclique est un chélateurs de métaux intéressant en raison de sa stabilité thermodynamique et cinétique élevée [1]. Parmi le chélateur macrocyclique étudié en préclinique, la porphyrine a été très analysée en raison de sa fonction de capture préférentielle par les cellules tumorales (y compris les sarcomes , les carcinomes, et la plaque d'athérome) [2] , alors que les mécanismes de cette sélectivité restent un obscur jusqu'à maintenant. Après le premier travaux sur l'efficacité élevée de la Mn (II)–méso-porphyrine soluble dans l'eau [3] , le potentiel de divers Mn (II) et Fe (II) méso-porphyrins soluble dans l'eau comme agents de contraste IRM a été exploré. Néanmoins, la faible stabilité de la Gd (III)–méso-porphyrine soluble dans l'eau a limité le développement de ces complexes [4]. La métallo-méso-tétra-pyridyle porphyrine (MMTPyP) comprend un étirement axial ligand du fait de la coordination du métal avec un atome d'azote provenant d'une molécule de porphine adjacente [5]. La solubilité du complexe MMTPyP pourrait être obtenue chimiquement par encapsulation ou par liaison covalente à la surface des nano vecteurs, conduisant à améliorer la biocompatibilité et à éviter la libération d'ions paramagnétiques. Parmi les polymères étudiés pour réaliser un ciblage cellulaire, le chitosane a reçu beaucoup d'attention dans les domaines de la délivrance ciblée de médicaments et de l'imagerie moléculaire [6]. Nous proposons d'utiliser des nanoparticules de chitosane formant un complexe conjugué de la Gd(III) méso - tétra- pyridyle porphyrine pour améliorer sa biocompatibilité médicale, sa solubilité dans l'eau et d'augmenter son efficacité en IRM.

Le développement actuel de sondes d'imagerie multifonctionnelles permet d'avoir accès à des sources d'information complémentaires. Les quantum dots (QD) dopés par des ions paramagnétiques sont particulièrement étudiés pour être utilisés dans ce cas. Les QD dopé par des ions Mn(II) est l'un des QD les plus étudiés dans le domaine d'imagerie médicale. Bien que, la recherche a surtout été axée sur son potentiel comme un bio-marqueur fluorescent [7],

son efficacité comme un agent de contraste IRM est moins bien étudié. En plus, la majorité des QD dopés par Mn(II) se présentent sous la forme de particules constituées d'un cœur recouvert d'une coquille. Envisager le griffage des ions sur la surface des nanoparticules constituerait une nouvelle approche de conception des sondes multimodales (IRM et fluorescence) qui pourraient améliorer l'efficacité des nanoparticules en IRM et parallèlement ne pas changer les propriétés de fluorescence de QDs.

Outre les études expérimentales, l'utilisation de simulations pourraient être une technique utile pour obtenir des informations détaillées sur la structure, le comportement intramoléculaire en solution aqueuse et la dynamique des molécules [8]. La simulation en Dynamique Moléculaire (DM) est une des techniques numériques les plus utilisées pour rapprocher les propriétés macroscopiques du système en permettant de simuler son évolution. Par conséquent, la modélisation de l'eau au voisinage des AC par Dynamique Moléculaire aide à l'obtention d'un aperçu fiable sur leur relaxivité grâce à l'interaction entre les ions paramagnétiques et l'eau.

Objectif de la thèse

Ma thèse a été consacrée à concevoir et à développer deux classes d'agents de contraste (AC) intrinsèquement efficace en IRM.

1. Développer un complexe de Gd-méso-tétra-pyridyle porphyrine conjugué avec des nanoparticules de chitosan, susceptible d'avoir des applications biomédicales grâce au chitosane capable d'améliorer la biocompatibilité, la biodégradabilité, et muco-adhésif *in-vivo.*
2. Développer le concept de greffage de Mn dopé à la surface de nanoparticules ZnS, avec des concentrations de Mn élevés, afin d'améliorer l'accessibilité de l'eau au moment magnétique du Mn**.** Afin d'obtenir un aperçu significatif sur l'interaction de Mn: ZnS avec des molécules d'eau environnantes, la simulation dynamique moléculaire sera effectuée pour mieux comprendre les mécanismes de relaxation de nanoparticules de Mn :ZnS dispersés dans l'eau. Les résultats de la relaxivité r1 expérimentale en fonction de la concentration de la teneur en Mn sont mis en corrélation avec les résultats obtenus par dynamique moléculaire.

2. Protocole

2.1. Synthèse de Gd(TPyP)-NC

Les Gd(TPyP) ont été synthétisées selon la méthode développée par Adler [9]. Les nanoparticules de chitosane (NC) ont été préparées à partir de la méthode décrite par Fan et al. [10]. Ensuite, la Gd(TPyP) a été encapsulée par des nanoparticules de chitosane (NC) par conjugaison chimique et absorption passive. En conjugaison chimique, la Gd(TPyP) peut être directement ajoutée à la solution de chitosane ou de sodium triphosphate pentabasic (TPP), précédant la procédure de formation des NC. Le chargement passif a été étudié en mélangeant les NC avec la métalloporphyrine pendant 15 minutes. Le mélange a été dissout dans l'eau distillée sous agitation magnétique pendant 15 minutes à 4°C. La centrifugation a été utilisée pour séparer la Gd(TPyP) et ainsi recueillir le complexe Gd(TPyP)-NC.

2.1.1. La Caractérisation du Gd(TPyP)-NC

L'efficacité de la Gd(TPyP) dans l'éthanol a été étudiée par relaxométrie RMN à 20 MHz (37°C) et IRM à 60 MHz (25°C). Leurs relaxivités ont été comparées avec deux produits de référence : la Mn(III)-méso-tétra(4-sulfonatophenyl) porphyrine (Mn(III)TSPP) et la Fe(II)-méso-tétra(N-methylpyridinium) porphyrine (Fe(II)TMPyP). Les dimensions et la morphologie de surface des NC et de la Gd(TPyP) ont été caractérisées par diffusion dynamique de la lumière et microscopie électronique à balayage (MEB). Un spectromètre d'absorption ultraviolet-visible et un spectromètre de masse couplé à un plasma inductif ont été utilisés pour déterminer les concentrations de Gd(TPyP) dans les particules. Les types de liaisons dans le Gd(TPyP)-NC ont été étudiés à l'aide de la spectroscopie d'absorption infrarouge en comparant les spectres IR à ceux des Gd(TPyP) et des NC. Les pourcentages d'efficacité (%LE), de capacité de chargement (%LC), et du rendement des nanoparticules ont été calculés en utilisant les équations (4), (5), (6) suivantes :

$$\text{Efficacité de chargement (\%)} = \left(\frac{A-B}{A}\right) x100 \quad (4)$$

$$\text{Capacité de chargement (\%)} = \left(\frac{A-B}{C}\right) x100 \quad (5)$$

$$\text{Rendement (\%)} = \frac{W1}{W2} x100 \quad (6)$$

A, B, et C sont respectivement la quantité initiale de Gd(TPyP), la quantité de Gd(TPyP) après centrifugation, et le poids de NC. W1 correspond au poids du Gd(TPyP)-NC récupéré après lyophilisation alors que W2 réfère à la somme du poids sec initial de NC et Gd (TPyP). L'IRM de Gd(TPyP)-NC dispersés dans l'eau a été réalisée avec un appareil IRM 3T (Philips ACHIEVA TX) à 25°C. Les relaxivités longitudinale et transversale des colloïdes préparés

ont été évaluées à partir des images pondérées en T1 et T2. Les images pondérées en T1 et T2 sont obtenues à partir de la séquence en spin écho.

2.2. Nanoparticules de Mn : ZnS

Les nanoparticules de $Mn_xZn_{1-x}S$ avec x= 0,1 ; 0,2 ; 0,3 ont été synthétisées par la méthode de polyol en utilisant le protocole décrit en [10]. Les différentes tailles de $Mn_{0.3}Zn_{0.7}S$ ont été recueillies par centrifugation à différentes vitesses de rotation.

2.2.1. La caractérisation

La structure cristalline et la microstructure de Mn:ZnS ont été caractérisées en diffraction des rayons X (DRX) avec un rayonnement Cu Ka (λ=1,54 Å) et par microscopie électronique en transmission à haute résolution (TEM). L'efficacité du dopage et les variations de composition chimique de l'échantillon ont été vérifiées à l'aide d'un spectromètre à dispersion d'énergie (EDX) et d'un spectromètre de fluorescence X. Ensuite, l'efficacité des nanoparticules de Mn:ZnS pour l'IRM et la fluorescence optique a été étudiée en utilisant la spectroscopie de fluorescence et l'IRM 3T à 25°C.

2.3. Simulation de Dynamique Moléculaire

La dynamique moléculaire nous donne la possibilité d'étudier la dynamique réelle du système pendant le temps de la simulation. En dynamique moléculaire, la position atomique du système est prévue en appliquant les équations du mouvement de Newton. Par conséquent, l'état du système à tout moment peut être prédit à partir de son état actuel. Une discrétisation du temps permet de calculer, à chaque pas et pour chaque atome, les forces d'interaction qui résultent de potentiels préétablis. Ainsi, le principe fondamental de la dynamique donne accès aux accélérations, aux vitesses et donc aux déplacements de chaque atome. Il est par ailleurs possible de contrôler la température et/ou la pression du système simulé en corrigeant les vitesses et trajectoires sur des périodes limitées. Une telle technique de simulation peut donc permettre d'aboutir à une meilleure compréhension de la dynamique microscopique de MnZnS en solution aqueuse. C'est pourquoi nous avons simulé par dynamique moléculaire le système MnZnS, d'une part dans le vide, et d'autre part dans l'eau.

La configuration initiale des atomes MnZnS a été construite à partir des coordonnées atomiques de la structure crystalline de ZnS-blende. On a utilisé les potentiels interatomiques de Wright pour l'incorporation des impuretés dans la structure ZnS. Deux modèles tels que la

TIP3P (transferable intermolecular potential 3 potentiel) [11], et la SPC / E (extended simple point charge) [12] ont été utilisés pour la simulation des molécules d'eau.

Dans le modèle cœur-coquille de MnZnS, Zn et S atomes dans la molécule ont été modélisés par un cœur avec la masse nulle (ou très léger) relié à un coquille, qui contient toute la masse atomique, par un ressort harmonique. La somme des charges de cœur-coquille doit être égale à la charge totale des atomes. Le potentiel est décrit comme suit

$$u_{ij} = \frac{1}{2} K r_{ij}^2$$

Où K est la force constante et r_{ij} est la distance entre l'atome i et j. L'interaction des termes à courte portée entre l'atome i et j atome a été démontrée par le potentiel de Buckingham

$$u_{ij} = A_{ij} \exp(-\frac{R_{ij}}{\rho_{ij}}) - \frac{C_{ij}}{R_{ij}^6}$$

Où R_{ij} est la distance entre deux atomes i et j, et A_{ij}, ρ_{ij}, C_{ij} sont trois paramètres fixés du modèle dépendent des atomes en interaction. Le potentiel des trois corps a été considéré entre S-Zn-S

$$u_{ij} = \frac{1}{2} K_{ijk} (\theta - \theta_{ijk})^2$$

Lorsque θ_{ijk} est l'angle formé par un atome de S_i et Zn_j (au centre) et S_k, θ est la valeur de l'angle à l'équilibre (109,4 °), et k est le paramètre du modèle. Ces paramètres ont été répertoriés dans le tableau 1.

Tableau 1. Paramètres du potentiel pour la simulation de la structure blende MnZnS.

Buckingham				
Atomic Pair	A (eV)	ρ(Å)	C(eVÅ^6)	Cutoff(Å)
Mn-S	750.686175	0.390889	0.0	12.0
S-S	1200.0	0.149	0.0	12.0
Zn-S	528.8990	0.4110	0.0	12.0
Trois Coeur				
Atomic Pair	K(eVrad^{-2})	Θ_0(deg)	ρ_1/ρ_2(Å)	Cutoff(Å)
SS-Zn-SS	9.4283e-6	109.47	0.3	6.0
cœur-coquille				
Atomic Pair	Mass	Charge	K(eVÅ^{-2})	
S(Core)	30.0	1.357	--	
S(Shell)	2.0	-3.357	13.302743	
Mn	54.0	2.0	--	
Zn	65.0	2.0	--	

Enfin, les interactions des nanoparticules $Mn_xZn_{1-x}S$ (x = 0,1 ; 0,2 ; 0,3) avec les molécules d'eau ont été simulées en utilisant le potentiel de Buckingham dont les valeurs sont indiquées dans le tableau 2.

Tableau 2. Valeurs du potentiel pour modéliser les interactions entre les nanoparticules de MnZnS et les molécules d'eau.

Atomic pair	A(eV)	r(Å)	C(eVÅ^6)
S-O	41399.49	0.2039	0
S-H	4268.15	0.3686	965.33
Zn-O	14974.51	0.186011	0.0
Mn-O	25974.51	0.188011	20

3. Résultats

3.1. Efficacité de Gd(TPyP) en IRM

L'efficacité de la Gd(TPyP) dans l'éthanol a été évaluée par relaxométrie RMN à 20 MHz (37°C) et IRM à 60 MHz (25°C) en comparant les résultats avec les produits de référence : Mn(TSPP), Fe(TMPyP), et Gd-Dota. Les résultats de relaxométrie RMN obtenus sont représentés dans le tableau ci-dessous (tableau 4). Parmi les complexes étudiés, le T1 et le T2 de la Gd(TPyP) sont plus courts à ceux du Mn(TSPP), du Fe(TMPyP) et du Gd-Dota. Le T1 varie de 194 ms à 33 ms pour une concentration Gd(III) allant de 0,1 mm à 1 mm. Les relaxivités de Fe(TMPyP), Mn(TSPP) et Gd(TPyP) ont été regroupées dans le tableau 4. Parmi les trois métalloporphyrines étudiées, la Gd(TPyP) montre la r1 la plus élevée, 26 $mM^{-1}s^{-1}$, tandis que la Fe(TMPyP) exhibe la r1 la plus basse avec 3,7 $mM^{-1}s^{-1}$.

Tableau 4. Valeurs de T1, T2, r1 et R2 pour les porphyrines Mn(TSPP), Fe(TMPyP) et Gd(TPyP) et Gd-Dota à 20 MHz.

Mn(TSPP) dans l'eau			Fe(TMPyP) dans l'eau			Gd(TPyP) dans l'éthanol			Gd-Dota dans l'eau			Gd-Dota dans Les mélanges eau-éthanol		
mM	T1(ms)	T2(ms)	mM	T1(ms)	T2(ms)	mM	T1(ms)	T2(ms)	mM	T1(ms)	T2(ms)	mM	T1(ms)	T2(ms)
0.1	244	226	1	1190	428	0.1	194	167	0.6	484	395	1	446	381
0.3	149	137	2	467	148	0.3	66	55.4	5	41.1	34.1	5	75.3	53.7
0.5	81.6	74.6	3.5	283	87.5	0.6	45	22.4	7	28.6	23.6	7	48.8	39.4
1	27.1	24.4	10	147	46.2	1	33	15.6	9	24.3	20.2	9	32.1	27.3
Relaxivité ($mM^{-1}s^{-1}$)														
r1		r2	r1		r2	r1		r2	r1		r2	r1		r2
6.63		21.43	3.70		4.12	**26.43**		**68.47**	4.1		5.02	3.51		4.12

D'autres études de l'efficacité de trois métalloporphyrines ont été réalisées en utilisant l'IRM à 3T. Les images pondérées en T1 et T2 de Mn (TSPP) et Fe (TMPyP) en solution aqueuse ont été présentés à la figure 1. On peut noter une augmentation de l'intensité des signaux en T1 avec la concentration d'ions paramagnétiques, inversement pour T2.

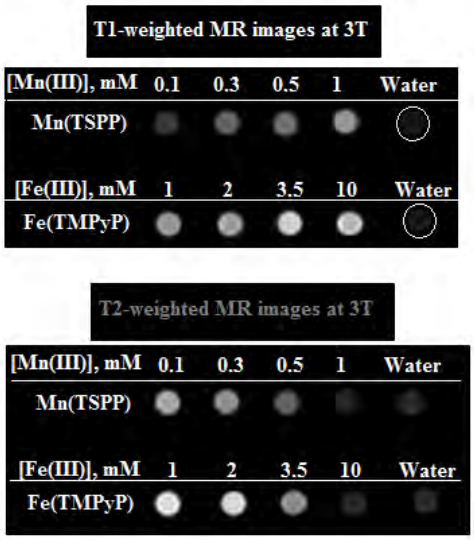

Figure 1. Écho de spin pondérée T1 (TR = 400 ms, TE = 8 ms) et T2 (TR = 1500 ms, TE = 40 ms) de concentration différente de Mn (TSPP) et Fe (TMePyP) dans l'eau à 3T

Aussi bien, figure 2 représente T1 et T2 pondérés de Gd(TPyP) et Gd-Dota dans des milieux aqueux. Nous avons observé (figure 2) que la Gd(TPyP) avec une concentration faible (10 fois) produit des signaux plus intenses en T1 et plus bas en T2, par rapport à ceux des Gd-DOTA.

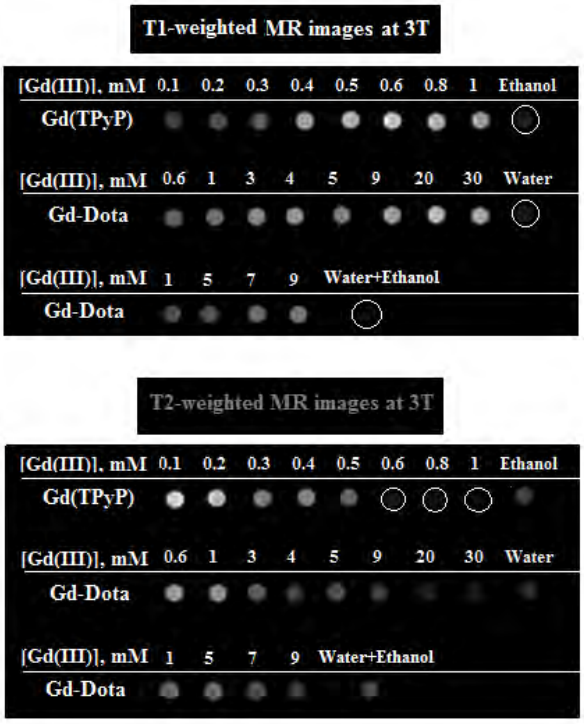

Figure 2. Écho de spin pondérée T1 (TR = 400 ms, TE = 8 ms) et T2 (TR = 1500 ms, TE = 40 ms) de concentration différente de Gd(TPyP) dans l'éthanol, Gd-Dota dans l'eau et dans le mélange de l'eau et l'éthanol à 3T

Par ailleurs, comme la relaxivité dépend des paramètres comme le champ magnétique appliqué et la température. On a évalué les valeurs de r1 et r2 de Gd(TPyP) en milieu aqueux en comparant avec ceux de Gd-Dota à 3T (figure 3). Ces valeurs sont comparées à celles mesurées à 0.47T (37°C) à la figure 3. On a observé une diminution (très petit) de r1 et une augmentation de r2 avec le champ magnétique.

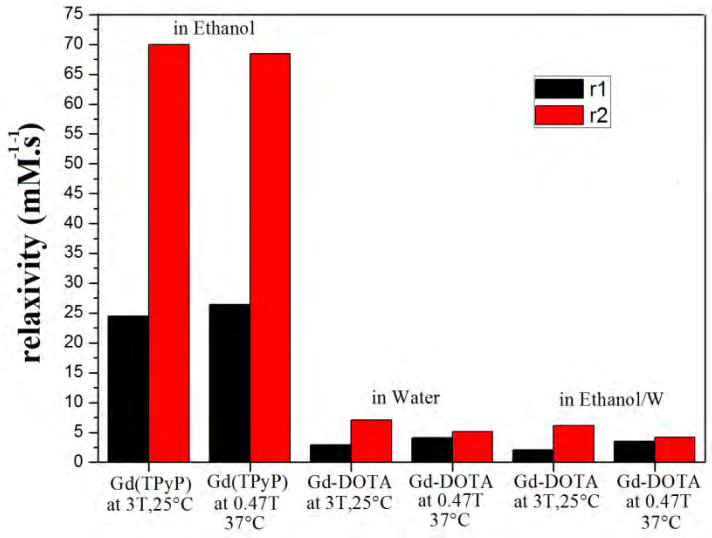

Figure 3. r1 et r2 relaxivité de Gd (TPyP) et Gd-DOTA solution à 3T (25 °C) et 0.47 T (37 °C)

Dans la littérature, la r1 de Fe(TMPyP) a été rapporté dans la gamme entre 4,4 et 1,3 $mM^{-1}s^{-1}$ (à 10 MHz) avec une augmentation respectée du pH de 1 à 10 [13]. Cette dépendance est liée aux moments de spin de la Fe(TMPyP) pour différents pH. Elle possède un spin de 5/2 à pH <5 et le spin chute à 1/2 à un pH supérieur de 7 à cause de la formation de Fe-O-Fe et de la dimérisation de la substance [13]. Nos résultats sont situés dans la plage des valeurs rapportées avec une faible différence qui est liée aux variations du champ magnétique appliqué. Le nombre de molécules d'eau coordonnées au Fe(II) en première sphère dépend du pH de la solution qui peut varier entre 1 et 2. Dans nos conditions d'étude (pH), le Fe(II) coordonne avec une molécule d'eau si on en compare son spectre UV-visible avec celui mentionné par Gandini *et al.* [14]. De plus, en raison de la charge positive de la position ortho de la Fe(TMPyP), les électrons ont tendance à être retirer et à renforcer les liaisons eau-métal. Cela risque de provoquer l'augmentation du temps de résidence d'une molécule d'eau jusqu'à 1,3s à température ambiante [15] Ainsi, une molécule d'eau coordonnée en première sphère avec un temps de résidence long entraine une valeur de r1 de 3,7 $mM^{-1}s^{-1}$ à 0.47T et 37°C.

Mn (TSPP) présente une forte r1 de 6,63 $mM^{-1}s^{-1}$, conformes à celles déclarées antérieurement [16],[17]. Mn (III) ion coordonnées axialement avec deux molécules d'eau en 1 ^{iére} sphère [18]. Surtout, grâce à la grande densité électronique au centre de Mn(TSPP), les liaisons de l'eau au centre métallique (Mn) labialise qui promeut le mécanisme de l'échange chimique de la molécule d'eau entre la 1 ^{iére} sphère de coordination et du solvant. Cela conduit à avoir un temps de résidence court, déclarée de 36 ns à température ambiante [18]. De plus, la courte distance minimale d'approche entre entre le Mn(II) et le proton d'une molécule d'eau (~ de 2.26Å) pourrait pousser à augmenter l'interaction dipolaire [14].

La r1 de Gd-DOTA dilué dans le mélange eau/éthanol (3,51 $mM^{-1}s^{-1}$) est légèrement inférieur à celle de Gd-Dota dilué dans l'eau, qui est en bon accord avec celle rapportée [19]. Cette petite différence pourrait être liée à la structure de l'éthanol. Dans le mélange eau/éthanol, quatre sites distincts chimiquement existent qui étaient occupées par l'hydrogène, tels que les groupes méthyle (CH3), méthylène (CH2), une liaison H-O polaire de l'éthanol et un hydrogène de l'éthanol avec un oxygène de l'eau. Par conséquent, il est signalé l'artefact de déplacement chimique du méthyle et méthylène est du à un décalage de la fréquence de résonance qui provoque l'augmentation de la relaxation [19].

La structure moléculaire de Gd(TPyP) a déjà été étudié par la spectroscopie infrarouge et la diffractométrie de rayons X, en supposant que on a une molécule d'eau coordonnée avec Gd (III) [20]. Par ailleurs, sa masse moléculaire de 833 g/mol n'est pas assez haute pour avoir une haute relaxivité. Ainsi, la masse moléculaire et une molécule d'eau en 1^{iére} sphère de Gd(TPyP) ne pouvaient pas les seuls paramètres déterminant la relaxivité. Cette r1 haute peut être attribuée à d'autres paramètres comme le temps de résidence de l'eau, la distance entre Gd (III) et de la molécule d'eau coordonnée, ainsi que le temps de corrélation de la rotation. De plus, d'autres propriétés de la structure moléculaire, comme bien situés de l'ion métallique au centre de chélate [21],[22], l'isotrope de complexe [21],[22], et la rigidité de la liaison entre des ions métalliques et des chélates [23] pourrait influencer la relaxivité de Gd (TPyP).

Par ailleurs, la diminution de r1 de Gd(TPyP) et Gd-Dota avec le champs magnétique a été associée à une contribution négligeable du temps de relaxation électronique à champ magnétique élevé (au-dessus 1.5T) [24]. De plus, l'accroissement de leur r2 avec le champ magnétique est dû à l'augmentation linéaire de l'aimantation [25]. La température peut aussi avoir un effet significatif sur la relaxivité. Il est connu que la relaxivité diminue lorsque la température augmente [26]. Sur la base de l'équation Stoke-Einstein-Debye, la baisse de la r1 est due à la relation entre le temps de corrélation de la rotation avec la température [27]. Ce temps croît avec la température, ce qui provoque une diminution de relaxivité [28]. Un autre

paramètre dépendant de la température est le temps d'échange de la molécule d'eau au voisinage du Gd. A basse température, la r1 serait limitée tandis que la vitesse d'échange d'eau est assez rapide [26].

3.2. Caractérisation physico-chimique de Gd(TPyP)-NC

Nous avons étudié le chargement de Gd(TPyP) en NC par conjugaison chimique. Comme décrit dans le protocole, la conjugaison chimique de Gd(TPyP) avec NC a été effectuée en ajoutant 1 ml de Gd(TPyP) soit dans l'acide acétique (NP-1) ou dans la PPT (NP-2) solution. Les spectres UV-visible des nanoparticules préparées (NP-1) et (NP-2) ont été présentés dans la figure 4, en comparant avec celui de Gd(TPyP) dans l'éthanol. Le spectre de NP-2 est similaire au spectre des NP-1. Le spectre de NP-1 contient la bande de Soret intense à 445 nm suivie par 3 bandes Q (522 nm, 552 nm et 588 nm), tandis que le spectre de NP-2 presente une bande de Soret large et basse à 416 nm suivie par 3Q bandes (516, 556, et 587 nm). Dans les deux spectres de NP-1 et NP-2, la disparition de la *bande caractéristique* de Gd(TPyP) à 554 nm et simultanément l'accroissant du pic de la bande Q de H2(TPyP) à 517 nm ont été observée, qui pourraient être marqué comme structurelle déformation de Gd (TPyP). Se référant à la probabilité de démétallation de Gd(TPyP) cours de la conjugaison chimique de Gd(TPyP) à NC, cette technique n'est pas bonne pour l'encapsulation de Gd(TPyP) par NC. D'après la figure 4, le spectre de Gd(TPyP) chargé à NC via la méthode passive est semblable à celui de Gd(TPyP) dans l'éthanol qui affiche une bande de Soret intense à 419 nm suivie par une bande Q à 552 nm. Le léger décalage observé du pic de Soret devrait être liée à la différence de solvant utilisé.

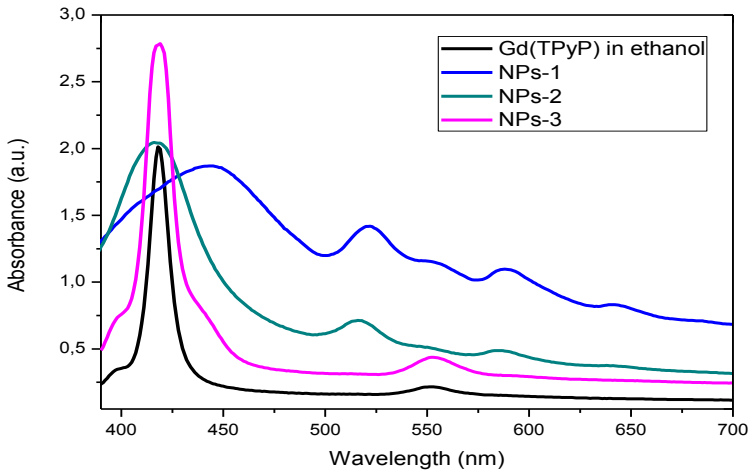

Figure 4. Les spectres UV-Vis de Gd (TPyP) dans l'éthanol, les NP-1 et NP-2 : Gd (TPyP) -NC par conjugaison chimique, NP-3: Gd (TPyP) -NC via la méthode passive

Comme présenté dans la figure 5, tous les échantillons ont montré solubilité dans l'eau. Les échantillons 1, 2, 3, et 4 respectivement correspondent à 2, 4, 8, et 12 mg de Gd(TPyP) chargés à 4 mg de NC. La spectroscopie UV-visible a été utilisée pour déterminer la concentration de la Gd(TPyP) en NC. Figure 5 expose l'absorption de Gd(TPyP)–NC après charger quantité différente de Gd(TPyP) à NC. On peut voir que l'intensité de la bande de Soret de Gd(TPyP) -NC augmente avec la concentration de Gd (TPyP).

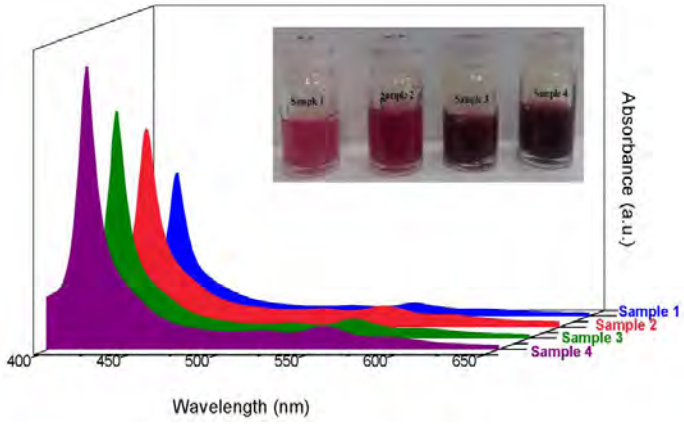

Figure 5. Les spectres UV-visible de Gd (TPyP) -NC après le chargement de la quantité différente de Gd(TPyP) en NC

En outre, des mesures quantitatives avec spectrométrie de masse couplée à un plasma inductif ICP-MS) ont été effectuées. Cette méthode donne la valeur réelle de Gd chargé en NC. La corrélation linéaire entre la valeur obtenue par mesure UV et ICP-MS a été observée. Le pourcentage de l'efficacité (%LE) et de la capacité de chargement (%LC), et du rendement des nanoparticules ont été évalués. Effet de différentes concentrations de Gd(TPyP) sur l'LE, LC et le rendement (%) de Gd(TPyP) -NC a été présenté à la Figure 6. Il a été observé que LE maximal (87%) était réalisés au taux 1/2 cependant LC et le rendement (%) atteignent leur maximum à un rapport de 1/ 3.

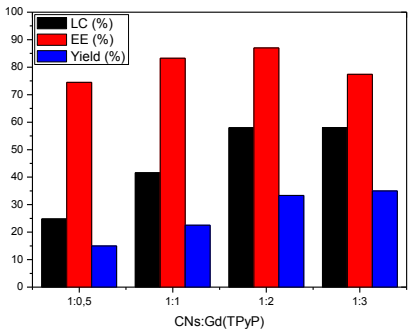

Figure 6. Le pourcentage de l'efficacité (%LE) et de la capacité de chargement (%LC), et du rendement des nanoparticules pour différents rapports de Gd (TPyP) -NC

L’efficacité des échantillons avec le chargement de différant contenu dans l'eau distillée ont été étudiés par IRM à 3T. Les images pondérées en T1 et T2 de Gd (TPyP) -NC dans l'eau ont été présentés à la figure 7. L’intensité du signal en T1 accroît, alors que le signal en T2 diminue avec le chargement de Gd(TPyP) ainsi que les concentrations de Gd(III).

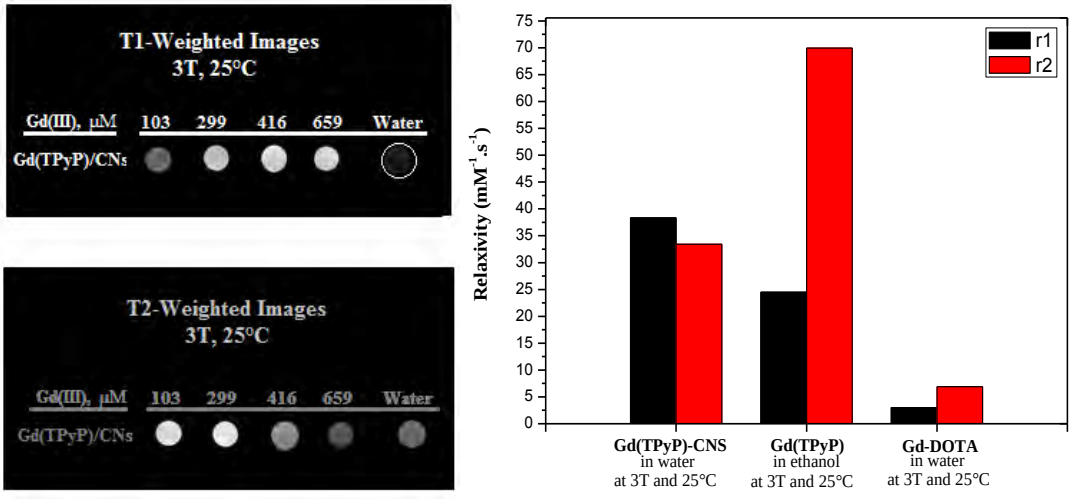

Figure 7. Écho de spin pondérée T1 (TR = 400 ms, TE = 8 ms) et T2 (TR = 1500 ms, TE = 40 ms) de concentration différente de Gd(TPyP)-NC dans l'eau à 3T, et r1 et R2 relaxivité de Gd (TPyP)-NC, Gd(TPyP) et Gd-DOTA solution

En comparant les valeurs r1 et r2 de Gd(TPyP)-NC avec celle de DOTA-Gd, une valeur de r1 haute de 38 $mM^{-1}s^{-1}$ à 60 MHz a été obtenue qui est 12 fois plus élevée que celle de Dota-Gd. Ainsi, la mise en valeur de la valeur de r1 avec la conjugaison de Gd(TPyP) à NC est conforme à ceux que l'on a publiés. Le renforcement de la relaxivité avec la conjugaison de AC avec NC pourrait être expliqué comme : une diminution du temps de corrélation de rotation par attachement du complexe à NC, une augmentation de la vitesse d'échange des molécules d'eau et une augmentation de la quantité d'ions paramagnétique chargé dans une nanoparticule.

Nous avons observé que la r2 est baissée de 69,97 $mM^{-1}s^{-1}$ à 33,43 $mM^{-1}s^{-1}$ après conjugaison de Gd(TPyP) avec NC. La diffusion de la molécule de l'eau en présence de particules hydrophiles diminue ce qui augmente la valeur de r2 [20]. En outre, nous pourrions supposer que plus d’un ion de Gd (III) est chargé dans les nanoparticules qui sont dû une augmentation de r2. Notre résultat obtenu est incompatible avec ces explications. La r2 élevée de Gd(TPyP) dans l'éthanol pourrait être attribuée à son agrégation pendant les mesures a cause de sa peine soluble dans un solvant organique. Cela pourrait conduire à la formation de l'agrégation

moléculaire, qui cause un accroissement de la r2. Alors que, la formation de l'agrégation diminue avec le chargement Gd(TPyP) à NC.

3.3. Mn :ZnS quantum dots

L'étude structurale de nanoparticules Mn :ZnS a montré, à partir des pics du diagramme de DRX, que toutes les nanopartiucles sont parfaitement indexables dans la structure belnde sans aucune impureté crystalline ni amorphe. Par ailleurs, la taille de nanoparticules est estimée par affinement des diagrammes en utilisant le logiciel MAUD. Les résultats obtenus sur la taille de nanoparticules par DRX et MEB et d'analyse des teneurs en Mn (II) par EDX et XRF sont regroupés et présentés dans le tableau 4.

Tableau 4. Caractéristiques physico-chimiques de $Mn_xZn_{1-x}S$ tels que la composition chimique mesurée par la fluorescence X et l' analyse EDX , et la taille moyenne des cristaux < L_{XRD} > mesurée par DRX < D_{TEM} > et à partir des images MEB

Samples	Mn/(Zn+Mn) at.-%		Zn/(Zn+Mn) at.-%		Nanoparticles size	
	EDX	XRF	EDX	XRF	$<L_{XRD}>$ (nm)	$<D_{TEM}>$ (nm)
$Mn_{0.1}Zn_{0.9}S$	10	9.2	90	90.8	1.6	1.54 ± 0.15
$Mn_{0.2}Zn_{0.9}S$	20	17.0	80	83	1.8	1.63 ± 0.26
$Mn_{0.3}Zn_{0.7}S$	30	26.0	70	74	1.9	1.55± 0.25

L'analyse EDX et XRF confirme clairement la présence du Mn. Notons que la composition des nanoaprticules mesurée par EDX est pratiquement identique à celle par XRF. La variation de la composition en Mn n'incite pas de différences structurales et de tailles notables par rapport aux résultats de MEB et DRX.

Les spectres de photoluminescence (PL) des trois échantillons de Mn :ZnS ont été présentés dans la figure 8 . De Figure 66, les trois échantillons présentaient une large bande d'émission bleue avec un pic distinct autour de 465 nm. Notons que l'intensité du pic diminue lorsque la concentration de dopage en Mn augmente. Normalement, le spectre PL est constitué des émissions bleu et jaune respectivement, dans les intervalles 400-500 nm et 580 à 600 nm. L'émission bleue de MnZnS doit être associée à la lutte contre les émissions de défauts de ZnS hôte [29] alors que l'émission jaune est incorporée à $^4T_1$ - $^6A_1$ transition de Mn (II). Théoriquement, des Mn (II) ions prennent la place des ions Zn^{2+} à condition de posséder la même taille et la charge ainsi que les mêmes propriétés chimiques [30]. Il a été rapporté qu'une partie de Mn (II) pourrait être située en surface, ou plus exactement en interface des

cristallites [31]. Sooklal et al. [32] ont reporté que l'émission orange de Mn :ZnS nanoparticules est associée au Mn ion qui est incorporé dans une matrice ZnS et l'émission bleue associée à celle qui est sur la surface de ZnS. Des photographies d'émission de $Mn_{0.1}Zn_{0.9}S$ et ZnS sous excitation UV (325 nm) ont été présentées dans la figure 8. Nous avons observé l'émission bleue pour Mn: ZnS qui indique l'incorporation de Mn (II) sur la surface de ZnS. De ce fait, une émission orange-jaune à 590 nm n'est pas toujours observée dans le spectre de PL des Mn: ZnS de nos études.

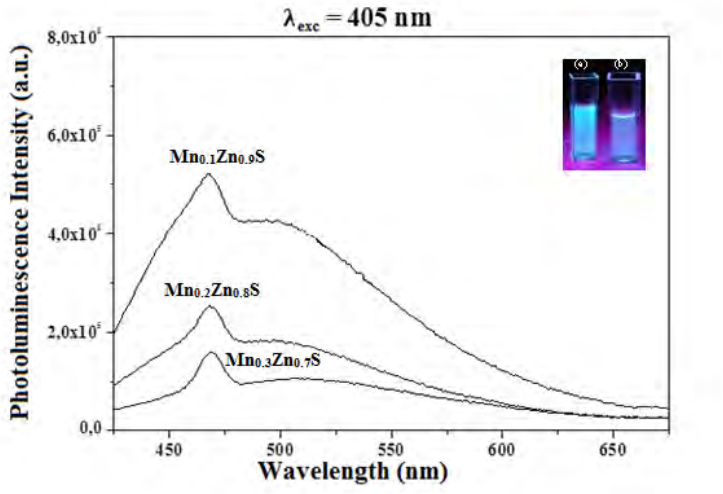

Figure 8. Les spectres d'émission de photoluminescence de $Mn_xZn_{1-x}S$ ($0.1 \leq x \leq 0.3$) enregistré à 300K, le médaillon émission observée pour a) ZnS et b) $Mn_{0.1}Zn_{0.9}S$) à λ=325

La capacité de MnZnS colloïdes à accélérer ainsi les vitesses de relaxation des protons de l'eau a été étudiée à l'aide d'un scanner IRM à 3T. Les concentrations de Mn (II) ont été mesurées par la spectroscopie de masse couplée à un plasma inductif (ICP-MS). Le T1 et T2 pondérés de Mn: ZnS (dans l'eau) sont présentés dans la Figure 9. L'IRM montre en T1 et en T2 l'augmentation du signal en présence du Mn :ZnS nanoparticules par rapport à la solution ZnS. L'intensité des signaux en T1 pour trois colloïdes augmente progressivement avec la concentration de Mn (II). La relaxation est l'un des paramètres le plus important pour montrer l'efficacité de colloïdes préparés comme un agent de contraste IRM. Ainsi, r1 et r2 de $Mn_xZn_{1-x}S$ (x = 0,1, 0,2, et 0,3) en solution à différentes concentrations ont été évaluées.

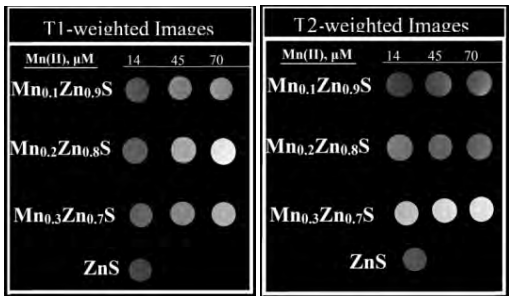

Figure 9. Écho de spin pondérée T1 (TR = 400 ms, TE = 8 ms) et T2 (TR = 1500 ms, TE = 40 ms) de concentration différente de $Mn_xZn_{1-x}S$ (x = 0,1 ; 0,2 ; 0,3) dans l'eau à 3T

Les temps de relaxation longitudinale et transversale (T1 et T2) de $Mn_xZn_{1-x}S$ (x = 0,1 ; 0,2 ; 0,3) des solutions à différentes concentrations ont été montrés dans la figure 10. Une augmentation de r1 de 20,34 à 86,09 $mM^{-1}.s^{-1}$ et r2 de 37,37 à 54,95 $mM^{-1}.s^{-1}$ avec l'accroissement de Mn(II) de 10% à 20%. Pour une teneur en Mn plus élevée (Mn = 0,3), r1 et r2 diminuent.

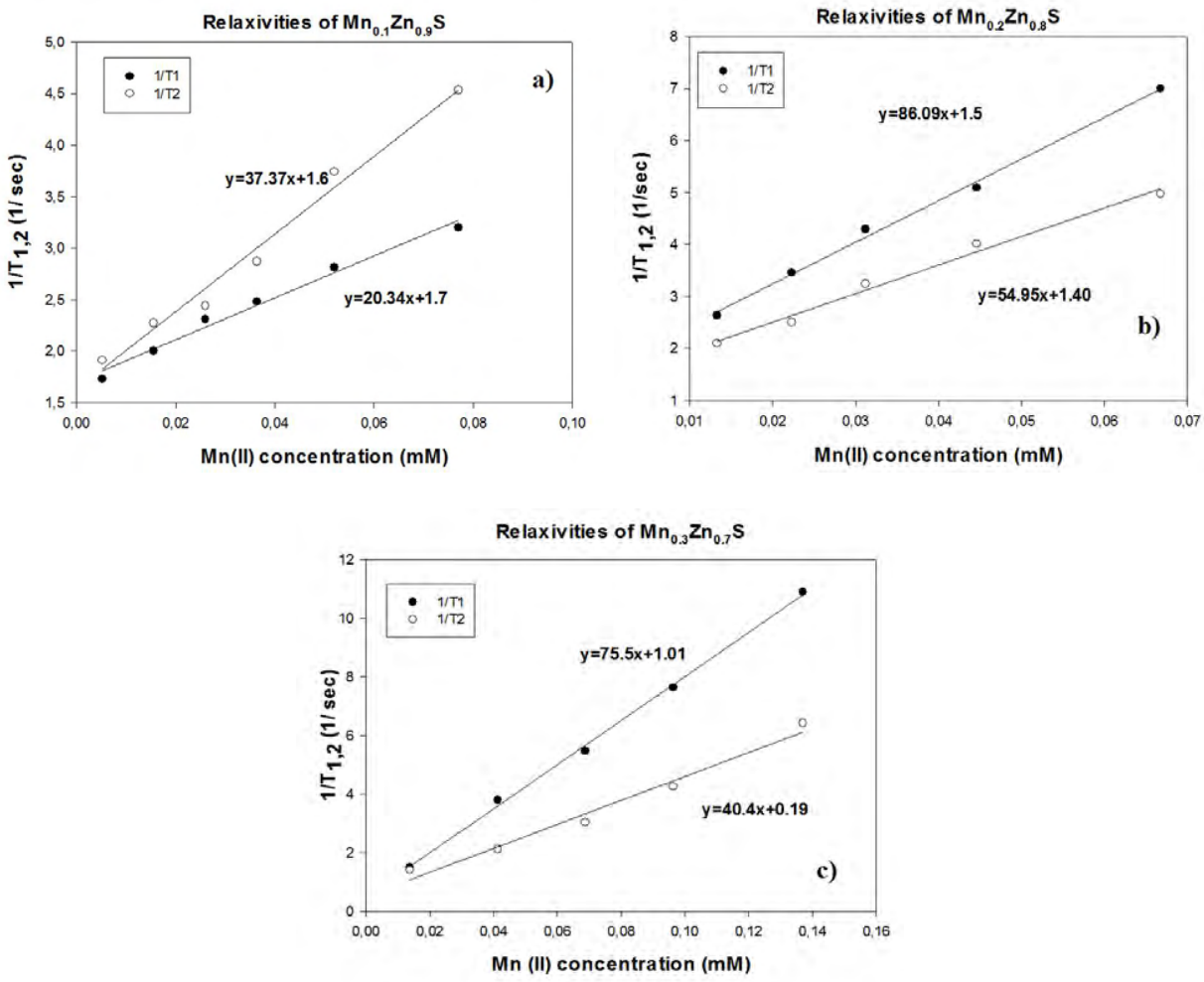

Figure 10. La r1 et la r2 de $Mn_xZn_{1-x}S$ (x=0,1 ; 0,2 ; 0,3) à 3T

La haute relaxivité r1 de tous les trois nanoparticules de Mn :ZnS variant de 20 à 75 $mM^{-1}s^{-1}$ peut être attribuer à la taille petite ($\leq$ 2 nm) des nanoparticules qui a provoqué l'accumulation des ions Mn(II) sur la surface de ZnS. La localisation de Mn (II) sur la surface de ZnS provoquerait la réduction de la distance (r) entre les molécules d'eau et Mn(II). La distance entre les ions paramagnétiques et molécule d'eau joue un rôle important sur la relaxivité. D'autre part, l'enrobage des nanoparticules pourrait également avoir un impact sur la relaxivité. L'acide thioglycolique hydrophile permet à l'eau de pénétrer à la sphère intérieure de Mn: ZnS [33], et contribue l'amélioration de r1. Ainsi, la grande valeur r1 de Mn: ZnS dans notre étude pourrait être liée à des ions Mn localisées sur la surface de ZnS, qui est grande par rapport au volume, l'enrobage avec l'acide thioglycolique et le nombre élevé de surface coopérative de Mn(II). En outre, la contribution des sphères secondaires et externes est importante dans la relaxation totale de nanoparticules [5]. Le groupe carboxylique de l'acide thioglycolique est fortement polaire [34]. Par conséquent, favorablement il fait des liaisons hydrogène fortes avec les molécules d'eau [35]. Ces interactions fortes entraînent l'augmentation de temps résidence des molécules d'eau en sphère secondaire [35]. De ce fait, le groupe carboxylique de l'acide thioglycolique peut favoriser la contribution de sphère secondaire qui va améliorer la relaxivité du Mn: ZnS. Nous avons observé un abaissement de r1 et r2 de Mn:ZnS pour le dopage de Mn de 30%. Cela pourrait être lié à une interaction dipôle-dipôle significative à cette concentration de la teneur en Mn (30%) qui raccourcit les temps de relaxation électronique et de réduire la relaxation globale.

Après avoir observé la diminution de r1 et r2 pour $Mn_{0.3}Zn_{0.7}S$ par rapport à celles de $Mn_{0.1}Zn_{0.9}S$ et $Mn_{0.2}Zn_{0.8}S$; $Mn_{0.3}Zn_{0.7}S$ a été choisi pour les études ultérieures. Les $Mn_{0.3}Zn_{0.7}S$ nanoparticules de taille différentes (dans le tableau 5) ont été synthétisés et recueillies par la centrifugeuse. Les tailles de nanoparticules ont été estimées à partir de l'image MEB et les spectres DRX. Les résultats obtenus ont été répertoriés dans le tableau 5. Le diamètre moyen des particules $Mn_{0.3}Zn_{0.7}S$ évalué par MEB montre un accord raisonnable avec les données de DRX.

Tableau 5. La taille des particules de $Mn_{0.3}Zn_{0.7}S$ évalué à partir de MEB et DRX

Sample	Particle size by TEM	Particle size by XRD
$Mn_{0.3}Zn_{0.7}S$ (S1)	1.55	1.8
$Mn_{0.3}Zn_{0.7}S$ (S2)	1.85	1.9
$Mn_{0.3}Zn_{0.7}S$ (S3)	2.1	2.3
$Mn_{0.3}Zn_{0.7}S$ (S4)	2.6	2.5

Les images pondérées en T1 et T2 des quatre échantillons (S1, S2, S3, et S4), comme indiqué dans le tableau 5, en solution aqueuse à 3T ont été présentées dans la figure 11. Les images pondérées en T1, les nanoparticules induisent une amélioration de l'intensité du signal avec l'augmentation des concentrations de Mn (II) et la taille de nanoparticules.

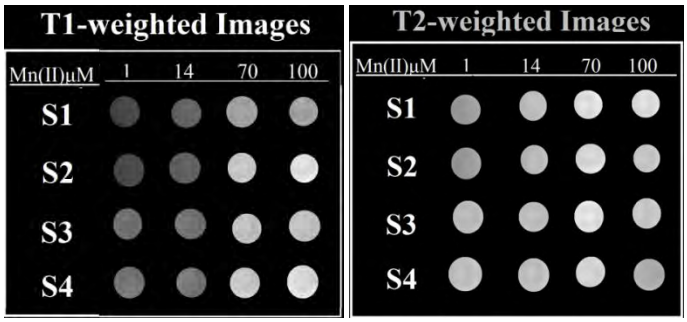

Figure 11. Écho de spin pondérée T1 (TR = 400 ms, TE = 8 ms) et T2 (TR = 1500 ms, TE = 40 ms) de $Mn_{0.3}Zn_{0.7}S$ avec granulométrie différente

Les r1 et r2 de la taille différente de $Mn_{0.3}Zn_{0.7}S$ ont été exhibées dans la figure 12. La r1 diminue considérablement avec l'accroissement de la taille des particules, à partir d'une valeur de 75,5 $mM^{-1}.S^{-1}$ pour les plus petites particules (1,55 nm) à 42,81 $mM^{-1}.s^{-1}$ pour les plus grandes particules (2,5 nm). Parallèlement, la r2 diminue de 40,4 pour S1 à 31,4 $mM^{-1}.s^{-1}$ pour S2 colloïdes, alors qu'aucun changement observé pour celle de S3 et S4.

L'abaissement de r1 avec la taille des particules est en accord avec ceux rapportés précédemment. La réduction du rapport surface/volume des particules pourrait être responsable de cette diminution. En raison de la dépendance des relaxivités r1 et r2 avec la taille de nanoparticules, le changement de r2 est moins prononcée que r1. La diminution de r2 de S1 à S2 pourrait être attribuée à la diminution du rapport surface sur volume. Bien que, la r2 de S3 et S4 n'a pas changé. Roohi et al. ont également observé la même tendance pour la r2 de SPIO [36] qui change avec l'augmentation de rayon hydrodynamique de SPIO jusqu'à 60 nm alors que pour celles qui sont plus grandes, la r2 reste constante [36].

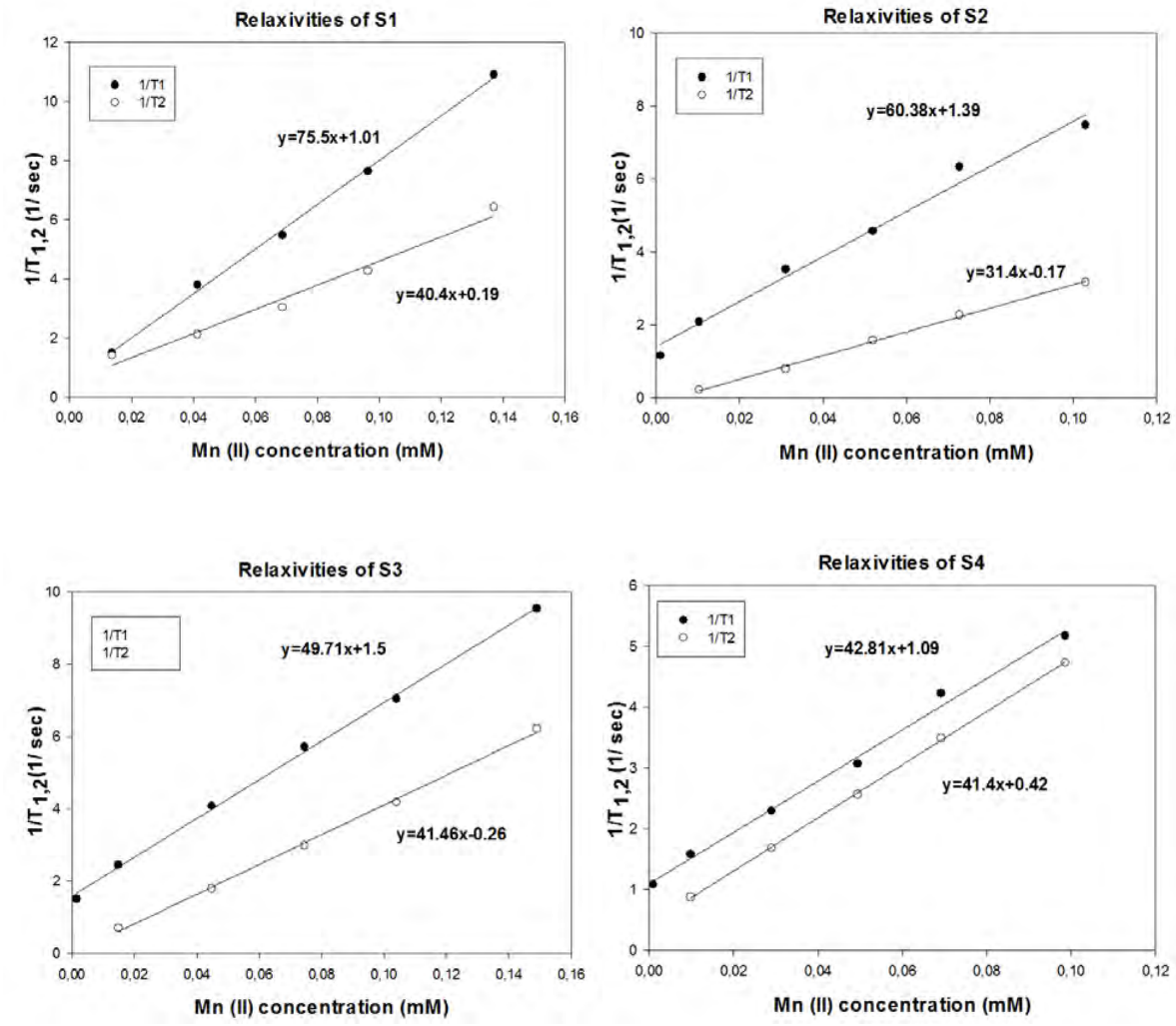

Figure 12. la r1 et la r2 de $Mn_{0.3}Zn_{0.7}S$ avec granulométrie différente

3.4. Simulation par dynamique moléculaire (DM)

3.4.1. DM de nanoparticules Mn :ZnS

Dans un premier temps, nous avons simulé la structure blende de MnZnS. Les caractéristiques structurales peuvent s'analyser au moyen de fonctions de distribution radiale g(r) et fonctions de distribution cumulée n(r), lesquelles sont évaluées pour chaque paire de types d'atome. Elles sont représentées dans la figure 13 et les valeurs caractéristiques synthétisées dans le tableau 5.

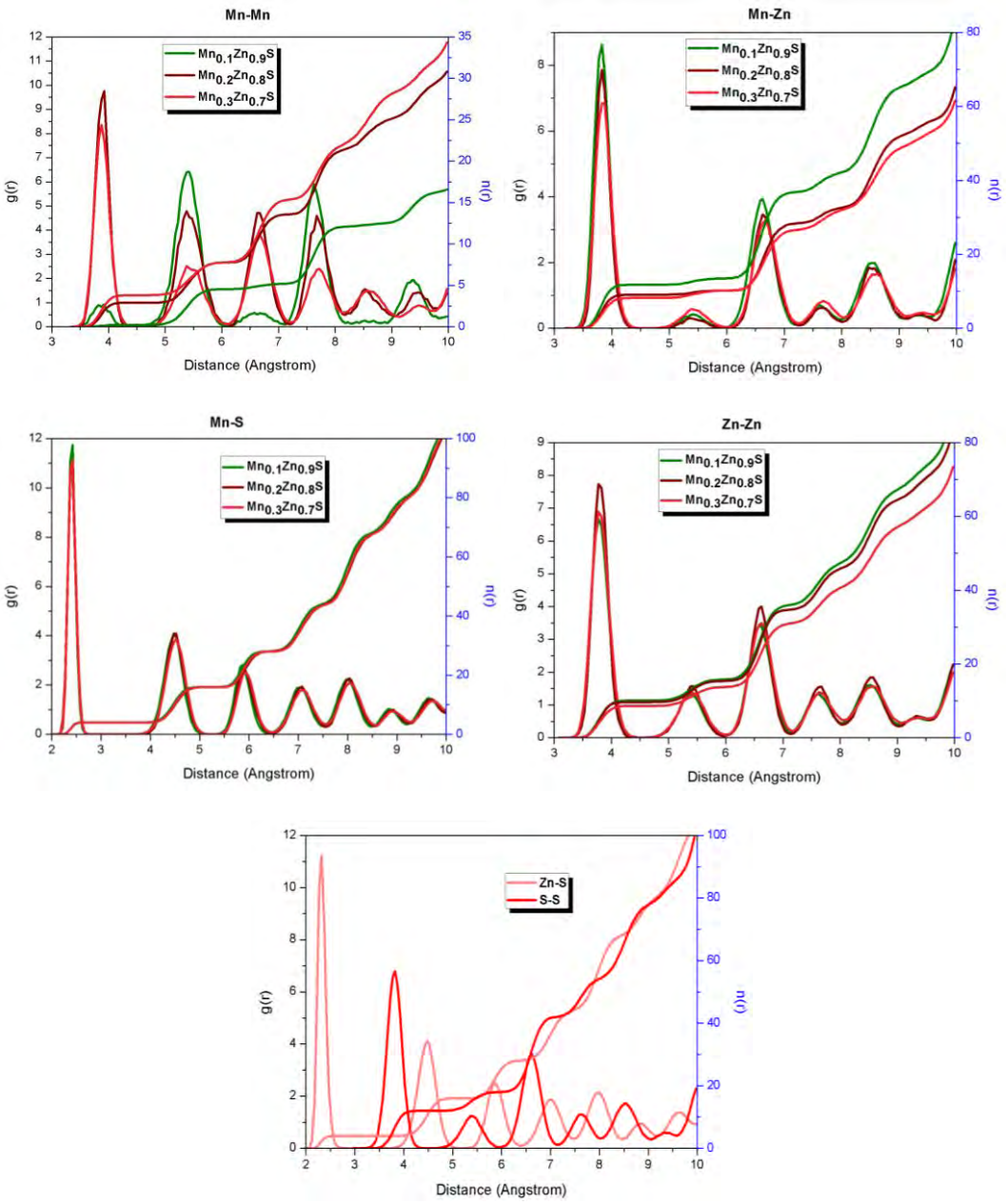

Figure 13. g(r) et n(r) de la structure blende de $Mn_xZn_{1-x}S$ (x=0,1 ; 0,2 ; 0,3) dans le vide

Tableau 5. Les caractéristiques structurales de $Mn_xZn_{1-x}S$ (x=0,1 ; 0,2 ; 0,3) simulées tels que : les fonctions de distribution radiale g(r), les fonctions de distribution cumulée n(r) pour chaque paire de types d'atome, paramètre de maille et le volume de maille

	$Mn_{0.1}Zn_{0.9}S$		$Mn_{0.2}Zn_{0.8}S$		$Mn_{0.3}Zn_{0.7}S$		ZnS		Expt.	
Pair atoms	1^{st} g(r)	1^{st} n(r)	1^{st} g(r)	1^{st} n(r)	1^{st} g(r)	1^{st} n(r)	1^{st} g(r)	1^{st} n(r)	1^{st} g(r)	1^{st} n(r)
Mn-Mn	3.87	0.22	3.87	2.90	3.87	3.80	----	----		
Mn-Zn	3.82	11.77	3.82	9.09	3.82	8.19	----	----		
Mn-S	2.42	4	2.42	4	2.42	4	----	----		
Zn-S	2.32	4	2.32	4	2.32	4	2.32	4	2.34	4
Zn-Zn	3.77	10.08	3.77	9.67	3.77	8.62	3.78	12	3.82	12
a (Å)	5.394		5.407		5.429		5.39		5.409	
Unit cell Volume ($Å^3$)	156.99		158.10		160.04		156.68		158.34	

Comme indiqué dans le tableau 5, la coordination de Zn par Zn diminue légèrement avec l'augmentation de la teneur en Mn. Par ailleurs, la plus courte distance pour la paire Mn-S est relevée à 2,42 Å, ce qui est en bon accord avec la distance Mn-S mesurée par spectroscopie d'absorption des rayons X (2,43 à 2,45 Å) [12]. Dans la structure cristalline de Mn:ZnS, et pour différentes concentrations de Mn (10 à 30%), la première interaction d'atomes de Mn-Mn est à 3,87 Å. En se référant à la RDF calculée, l'incorporation d'atomes de Mn dans ZnS n'affecte pas la structure blende de ZnS et provoque seulement l'expansion de la structure de tétraèdre de ZnS. Cette expansion a un effet sur le paramètre de maille, comme observé avec son augmentation de 5,394 Å pour $Mn_{0.1}Zn_{0.9}S$ à 5.429 Å pour $Mn_{0.3}Zn_{0.7}S$. Wright *et al.* ont étudié la structure cristalline de ZnS dans laquelle Mn est introduit comme impureté dans les sites ZnS [37]. Ils ont rapporté une distance Mn-S de 2,41 Å et une augmentation du paramètre de maille de 0,00064 Å par % de MnS, c'est-à-dire pour la substitution d'un atome Mn dans $(ZnS)_4$ [37]. Alors que pour l'incorporation d'un deuxième Mn dans $(ZnS)_4$, ils ont rapporté moins de distorsion avec une distance entre les Mn qui évolue jusqu'à 3,87 Å [37]. De ce fait, l'accroissement du paramètre de maille avec l'augmentation du dopage en Mn dans notre étude est cohérent. En outre, des études expérimentales ont également rapporté l'augmentation du paramètre de maille et du volume des cellules de Mn:ZnS avec la teneur en Mn. En raison des paramètres cristallins rapportés de ZnS: Mn, soit à partir de simulations ou de caractérisations expérimentales, les nanoparticules MnZnS simulées avec différentes teneurs en Mn sont donc fiables.

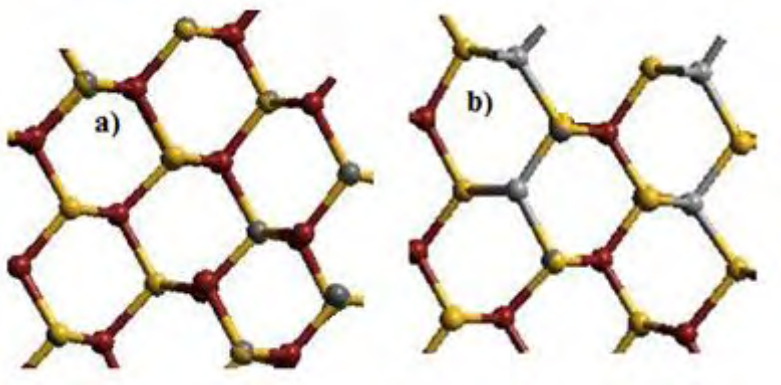

Figure 14. Les structures de surface (110) de a) ZnS et b) MnZnS , Zn : rouge , S : jaune , et Mn : gris

Une visualisation des structures simulées par DM a pu être obtenue en utilisant le logiciel ATEN [38]. Les structures de surface (110) de ZnS et MnZnS après relaxation sont illustrées dans la Figure 14. Comme on l'observe dans la figure 14, les atomes de S s'écartent de leurs

positions naturelles avant relaxation, et ceci dans les deux structures. Le mouvement des atomes de Zn et S après relaxation de la structure des cristaux de ZnS a été étudié par Wright *et al.* [39]et Duke *et al.* [40]. Tous deux ont rapporté ce décalage des atomes de S par rapport à Zn.

3.4.2. DM de nanoparticules Mn :ZnS en solution

L'interaction de MnZnS avec des molécules d'eau, SPC/E et TIP3P, a été étudiée par DM. Les fonctions de distribution radiale et cumulées obtenues à partir de la simulation sont présentées dans la figure 15. Les valeurs caractéristiques sont reportées dans le tableau 6. Avec l'évolution de la teneur en Mn, on note toutefois que les fonctions de distribution radiale relatives aux paires Mn-Mn, Mn-Zn et Mn-S présentent des différences notables avec celles obtenues pour la structure solides sans eau. Ainsi, on constate que l'hydratation de la nanoparticule altère sensiblement sa structure cristalline. Plus particulièrement, la distribution radiale de la paire Mn-Mn présente un pic fort après deux larges pics tandis que chaque pic comprend plusieurs pics de faible intensité. Et pour toutes les paires atomiques, la fonction de distribution radiale présente un premier grand pic relatif à la première coordination et des pics moins intenses et plus larges correspondant à la deuxième ou à la troisième sphère de coordination sphère. On note aussi que les minima sont non nuls. Ces indications sont la signature d'une légère déstructuration du cristal qui, a priori, doit prendre lieu à l'interface avec l'eau.

Tableau 6. Les fonctions de distribution radiale g(r), les fonctions de distribution cumulée n(r) simulées de $Mn_xZn_{1-x}S$ (x=0,1 ; 0,2 ; 0,3) dans l'eau pour chaque paire de types d'atome comparant avec ceux de ZnS dans l'eau

Atomic pairs	$Mn_{0.1}Zn_{0.9}S + H_2O$		$Mn_{0.2}Zn_{0.8}S + H_2O$		$Mn_{0.3}Zn_{0.7}S + H_2O$		$ZnS + H_2O$	
	1^{st} g(r)	1^{st} n(r)	1^{st} g(r)	1^{st} n(r)	1^{st} g(r)	1^{st} n(r)	g(r)	n(r)
Mn-Mn	3.87	1.04	3.77	0.57	3.87	1.59	----	----
Mn-Zn	3.77	5.22	3.77	5.92	3.77	6.22	----	----
Mn-S	2.37	2.74	2.37	2.74	2.37	2.74	----	----
Zn-S	2.20	3.68	2.27	3.65	2.32	3.59	2.38	3.46
Zn-Zn	3.79	8.41	3.77	8.49	3.72	8.58	3.82	10.28
Mn-H	2.62	7.25	2.72	7.25	2.77	7.25	----	----
Mn-O	2.37	2.74	2.37	2.74	2.37	2.74	----	----
Zn-H	2.62	0.82	2.62	0.82	2.62	0.82	1.88	0.55
Zn-O	1.97	0.36	1.97	0.36	1.97	0.36	2.48	1.17
S-O	3.27	3.07	3.27	3.07	3.27	3.07	3.38	5.45
S-H	2.62	2.70	2.62	2.70	2.62	2.70	2.73	1.91

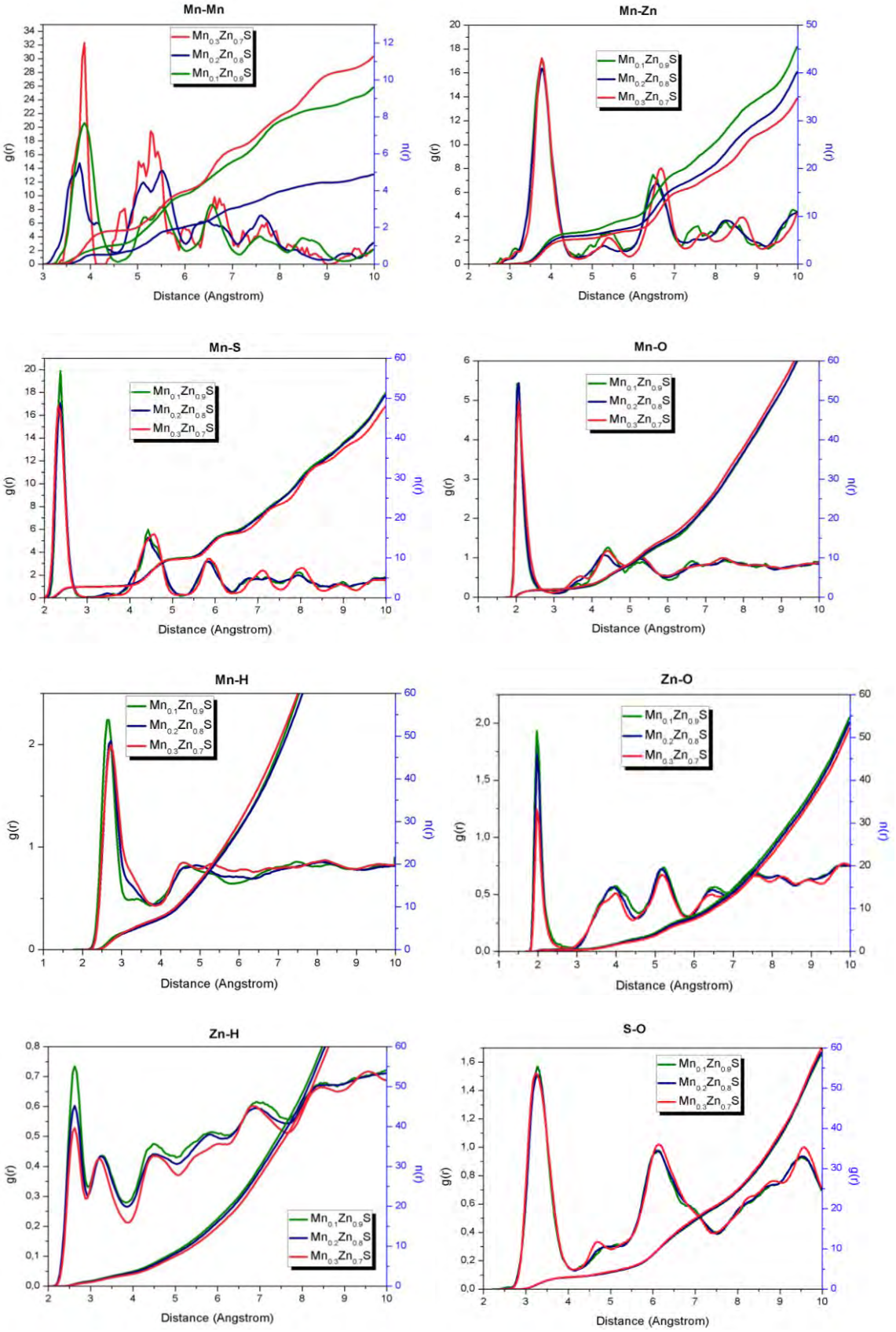

Figure 15. g(r) et n(r) de nanoparticule de $Mn_xZn_{1-x}S$ (x=0,1 ; 0,2 ; 0,3) dans l'eau

En outre, le pic intense de RDF de Mn-O pourrait confirmer l'interaction forte entre ces deux types d'atome. Si l'on considère le nombre d'oxygène comme le nombre de molécules d'eau coordonnées, les atomes de Zn sont en moyenne coordonnées avec 0,5 molécules d'eau à 2 Å, tandis que des atomes Mn se coordonnent avec ~ 3 molécule d'eau à la même distance.

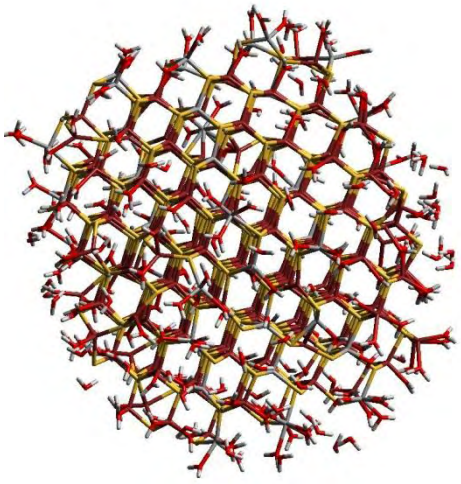

Figure 16. la vue 3D de nanoparticules de Mn :ZnS dans l'eau

Comme indiqué dans le tableau 6, la coordination de Mn en Mn au sein des nanoparticules MnZnS est diminuée de ~ 1 de dans le système hydraté par rapport dans la structure blende non hydratée. Cela pourrait être dû à l'interaction forte des atomes de Mn positionnés à l'interface avec l'eau, réduisant d'autant les interactions Mn-Mn. A partir de la vue 3D de MnZnS hydraté (figure 16), on peut constater que chacun des Mn situés à l'interface fait des liaisons avec de 1 à 4 molécules d'eau.

La longue distance (~ 1 Å) entre la 1ère et la 2ème sphère de coordination de Mn pourrait confirmer la liaison forte des atomes de Mn avec les molécules d'eau en 1ère sphère. Cela prolongerait le temps de résidence des molécules d'eau en 1ère sphère alors que ces molécules d'eau sont toujours en échange avec des molécules d'eau situées dans la 2ème sphère puisque le minimum de g(r) est non nul sur cet intervalle. Par ailleurs, le recouvrement des deuxième et troisième pics, correspondant respectivement à la 2nde et 3^{e} sphère d'hydratation autorise à penser que les échanges de molécules d'eau entre ces deux sphères sont très favorisés. Donc a priori le temps de résidence des molécules d'eau dans la seconde sphère d'hydratation doit être court. Bien que nous pourrions rendre plus réalistes ces simulations en envisageant un enrobage d'acide thioglycolique autour de nanoparticules afin, dans l'idéal, de pouvoir prédire exactement le mécanisme de relaxation des nanoparticules MnZnS en solution aqueuse, ces

résultats expliquent déjà très bien les temps de relaxation courts de MnZnS en solution aqueuse.

4. Conclusion

Cette thèse est réalisée sous la direction du Pr Soraya Benderbous au laboratoire INSERM-U825 Imagerie Cérébrale et Handicap Neurologique au sein de l'équipe 1 Neuro- Imagerie Clinique et Cognitive de l'université de Toulouse. Elle concerne le développement de deux nouveaux agents de contraste IRM macromoléculaires et nanoparticulaires présentant une solubilité élevée, et une efficacité élevée (haute relaxivité) à haut champ (3T).

Les travaux ont fait l'objet de plusieurs collaborations scientifiques :

- Pour le développement des nanoparticules, avec le laboratoire chimie des matériaux, Nanoscience de l'université de Paris-7 sous la direction du Prof Souad Ammar Merah,

- Pour le développement des complexes de Gd-Porphyrrines liées au chitosan, avec le laboratoire de chimie bioorganique et bioinorganique de l'université de Paris-sud sous la direction du Dr Hafsa Korri-Youssoufi

- Pour les simulations en dynamique moléculaire avec laboratoire de Photonique LPHIA | UPRES EA 4464 (université d'Angers) sous la direction du Pr Stéphane Chaussedent.

La première substance développée est la Gd (III)-méso-tétra (4-pyridyl) porphyrine (Gd (TPyP)) macromoléculaire. Le complexe obtenu présente une grande relaxivité r1 de 24 $mM^{-1}s^{-1}$à 60 MHz soit une efficacité au moins 6 fois plus importante que celles des agents conventionnels. Afin d'améliorer sa biocompatibilité médicale, sa solubilité de l'eau, et augmenter son efficacité en IRM, la Gd-porphyrine a été conjuguée avec les nanoparticules de chitosan. Ainsi, une valeur de 38 $mM^{-1}s^{-1}$ à 60 MHz 9 fois plus élevée que celle de Dota-Gd a été obtenue.

Parallèlement, nous avons développé le concept de greffage de Mn dopé à la surface de nanoparticules ZnS afin d'améliorer l'accessibilité de l'eau au moment magnétique du Mn. Les nanoparticules ont une relaxivité r1 variant de 20 à 75 $mM^{-1}s^{-1}$ pour un taux de Mn passant de 0.1 à 0.3, par rapport au produit commercial Mn DPDP (r1=2.8 $mM^{-1}.s^{-1}$ à 42 MHz). Par la suite, l'influence de la granulométrie de $Mn_{0.3}Zn_{0.7}S$ sur son efficacité a été

étudiée. Leur r1 a diminué de 75 à 42 $mM^{-1}s^{-1}$ avec l'augmentation de la dimension particulaire.

Pour expliquer le mécanisme, une simulation numérique de la dynamique moléculaire de l'eau au voisinage des nanoparticules de MnZnS a été développée pour aboutir à une meilleure compréhension du mécanisme de relaxivité de MnZnS en solution aqueuse. En se référant à la RDF calculée, l'incorporation d'atomes de Mn dans ZnS n'affecte pas la structure blende de ZnS et provoque seulement l'expansion de la structure de tétraèdre de ZnS. Cette expansion a un effet sur le paramètre de maille, comme observé avec son augmentation de 5,394 Å pour $Mn_{0.1}Zn_{0.9}S$ à 5.429 Å pour $Mn_{0.3}Zn_{0.7}S$. En outre, des études expérimentales ont également rapporté l'augmentation du paramètre de maille et du volume des Mn:ZnS avec la teneur en Mn. En raison des paramètres cristallins rapportés de ZnS: Mn, soit à partir de simulations ou de caractérisations expérimentales, les nanoparticules MnZnS simulées avec différentes teneurs en Mn sont donc fiables. L'interaction de MnZnS avec des molécules d'eau, SPC/E et TIP3P, a été étudiée par DM. On constate que l'hydratation de la nanoparticule altère sensiblement sa structure cristalline. En outre, le pic intense de RDF de Mn-O pourrait confirmer l'interaction forte et la liaison forte entre ces deux types d'atome. Cela prolongerait le temps de résidence des molécules d'eau en $1^{ère}$ sphère alors que ces molécules d'eau sont toujours en échange avec des molécules d'eau situées dans la $2^{ème}$ sphère puisque le minimum de g(r) est non nul sur cet intervalle. Par ailleurs, le recouvrement des deuxième et troisième pics, correspondant respectivement à la 2^{nde} et $3^{ème}$ sphère d'hydratation autorise à penser que les échanges de molécules d'eau entre ces deux sphères sont très favorisés. Si l'on considère le nombre d'oxygène comme représentatif du nombre de molécules d'eau coordonnées, des atomes Mn se coordonnent avec ~ 3 molécule d'eau à 2 Å. A partir de la vue 3D de MnZnS hydraté, on peut constater que chacun des Mn situés à l'interface fait des liaisons avec de 1 à 4 molécules d'eau.

5. Bibliographies

[1] R. Mewis and S. Archibald, "Biomedical applications of macrocyclic ligand complexes," *Coord. Chem. Rev.*, vol. 254, no. 15–16, pp. 1686–1712, 2010.

[2] D. N. Reinhoudt, *Supramolecular Materials and Technologies*. Wiley, 2008.

[3] C. Chen, J. S. Cohen, C. E. Myers, and M. Sohn, "Paramagnetic metalloporphyrins as potential contrast agents in {NMR} imaging," *{FEBS} Lett.*, vol. 168, no. 1, pp. 70–74, 1984.

[4] R. C. Lyon, P. J. Faustino, J. S. Cohen, A. Katz, F. Mornex, D. Colcher, C. Baglin, S. H. Koenig, and P. Hambright, "Tissue distribution and stability of metalloporphyrin MRI contrast agents," *Magn. Reson. Med.*, vol. 4, no. 1, pp. 24–33, Jan. 1987.

[5] J. H. Agondanou, I. Nicolis, E. Curis, J. Purans, G. A. Spyroulias, A. G. Coutsolelos, and S. Bénazeth, "Gadolinium Acetylacetonate Tetraphenyl Monoporphyrinate Complex and Some of Its Derivatives: EXAFS Study and Molecular Dynamics Simulation," *Inorg. Chem.*, vol. 46, no. 17, pp. 6871–6879, 2007.

[6] K. W. Bowman, Katherine; Leong, "Chitosan nanoparticles for oral drug and gene delivery," *Int. J. Nanomedicine*, vol. 2, no. 1, pp. 117–128, 2006.

[7] S. Baruah, C. Ortinero, O. V Shipin, and J. Dutta, "Manganese doped zinc sulfide quantum dots for detection of Escherichia coli.," *J. Fluoresc.*, vol. 22, no. 1, pp. 403–8, Jan. 2012.

[8] A. Borel, F. Yerly, L. Helm, and A. E. Merbach, "Molecular Dynamics Simulations of the Internal Mobility of Gd3+-Based MRI Contrast Agents: Consequences for Water Proton Relaxivity," *Chim. Int. J. Chem.*, vol. 58, no. 4, pp. 200–203, Apr. 2004.

[9] B. Alder and T. Wainwright, "Studies in molecular dynamics. I. General method," *J. Chem. Phys.*, 1959.

[10] S. Gaceur, Meriem;Giraud, Marion, Hemadi, Miryana; Novak, Sophie; Menguy, Nicolas Quisefit, Jean-Paul;David, Karine; Jahanbin, Tania; Benderbous, Soraya; Boissiere, Michel, Ammar, "Polyol-synthesized Zn0.9Mn0.1S nanoparticles as potential luminescent and magnetic bimodal imaging probes: synthesis, characterization, and toxicity study," *J. Nanoparticle Res.*, vol. 14, no. 7, 2012.

[11] W. L. Jorgensen, J. Chandrasekhar, J. D. Madura, R. W. Impey, and M. L. Klein, "Comparison of simple potential functions for simulating liquid water," *J. Chem. Phys.*, vol. 79, no. 2, p. 926, 1983.

[12] H. J. C. Berendsen, J. R. Grigera, and T. P. Straatsma, "The missing term in effective pair potentials," *J. Phys. Chem.*, vol. 91, no. 24, pp. 6269–6271, Nov. 1987.

[13] S. H. Koenig and R. D. Brown, "Relaxation of solvent protons by paramagnetic ions and its dependence on magnetic field and chemical environment: implications for NMR imaging.," *Magn. Reson. Med.*, vol. 1, no. 4, pp. 478–95, Dec. 1984.

[14] K. E. Kellar and N. Foster, “Relaxation enhancement of water protons by manganese(III) porphyrins: influence of porphyrin aggregation,” *Inorg. Chem.*, vol. 31, no. 8, pp. 1353–1359, 1992.

[15] R. Lauffer, “Paramagnetic Metal Complexes as Water Proton Relaxation Agents for NMR Imaging: Theory and Design,” *Chem Rev.*, vol. 87, pp. 901–927, 1987.

[16] S. H. Koenig, R. D. Brown, and M. Spiller, “The anomalous relaxivity of Mn3+(TPPS4),” *Magn. Reson. Med.*, vol. 4, no. 3, pp. 252–260, Mar. 1987.

[17] A. Budimir, J. Kalmár, I. Fábián, G. Lente, I. Bányai, I. Batinić-Haberle, and M. Birus, “Water exchange rates of water-soluble manganese(III) porphyrins of therapeutical potential.,” *Dalton Trans.*, vol. 39, no. 18, pp. 4405–10, May 2010.

[18] A. Budimir, J. Kalmár, I. Fábián, G. Lente, I. Bányai, I. Batinić-Haberle, and M. Birus, “Water exchange rates of water-soluble manganese(III) porphyrins of therapeutical potential.,” *Dalton Trans.*, vol. 39, no. 18, pp. 4405–10, May 2010.

[19] D. Nanz, G. Andreisek, J. M. Fröhlich, D. Weishaupt, K. Treiber, S. Ess, and T. Pfammatter, “Contrast Material–enhanced Visualization of the Ablation Medium for Magnetic Resonance– monitored Ethanol Injection Therapy: Imaging and Safety Aspects,” *J. Vasc. Interv. Radiol.*, vol. 17, no. 1, pp. 95–102, 2006.

[20] A. De Cian, M. Moussavi, J. Fischer, and R. Weiss, “Synthesis, structure, and spectroscopic and magnetic properties of lutetium(III) phthalocyanine derivatives: LuPc2.CH2Cl2 and [LuPc(OAc)(H2O)2].H2O.2CH3OH,” *Inorg. Chem.*, vol. 24, no. 20, pp. 3162–3167, 1985.

[21] E. Terreno, D. D. Castelli, A. Viale, and S. Aime, “Challenges for Molecular Magnetic Resonance Imaging,” *Chem. Rev.*, vol. 110, no. 5, pp. 3019–3042, 2010.

[22] P. Hermann, J. Kotek, V. Kubíček, and I. Lukeš, “Gadolinium (III) complexes as MRI contrast agents: ligand design and properties of the complexes,” *Dalt. Trans.*, 2008.

[23] F. Yerly, K. I. Hardcastle, L. Helm, S. Aime, M. Botta, and A. E. Merbach, “Molecular dynamics simulation of [Gd(egta)(H(2)O)](-) in aqueous solution: internal motions of the poly(amino carboxylate) and water ligands, and rotational correlation times.,” *Chemistry*, vol. 8, no. 5, pp. 1031–9, Mar. 2002.

[24] L. Helm, “Optimization of gadolinium-based MRI contrast agents for high magnetic-field applications,” *Future Med. Chem.*, vol. 2, no. 3, pp. 385–396, Mar. 2010.

[25] P. Caravan, C. T. Farrar, L. Frullano, and R. Uppal, “Influence of molecular parameters and increasing magnetic field strength on relaxivity of gadolinium- and manganese-based T1 contrast agents,” *Contrast Media Mol. Imaging*, vol. 4, no. 2, pp. 89–100, 2009.

[26] J. Garcia, A. N. W. Kuda-Wedagedara, and M. J. Allen, “Physical Properties of Eu(2+)-Containing Cryptates as Contrast Agents for Ultra-High Field Magnetic Resonance Imaging.,” *Eur. J. Inorg. Chem.*, vol. 2012, no. 12, pp. 2135–2140, Apr. 2012.

[27] P. Caravan, J. J. Ellison, T. J. McMurry, and R. B. Lauffer, “Gadolinium(III) Chelates as MRI Contrast Agents: Structure, Dynamics, and Applications,” *Chem. Rev.*, vol. 99, no. 9, pp. 2293–2352, 1999.

[28] R. M. Anderton and J. F. Kauffman, “Temperature-Dependent Rotational Relaxation of Diphenylbutadiene in n-Alcohols: A Test of the Quasihydrodynamic Free Space Model,” *J. Phys. Chem.*, vol. 98, no. 47, pp. 12117–12124, Nov. 1994.

[29] J. Aldana, Y. A. Wang, and X. Peng, “Photochemical Instability of CdSe Nanocrystals Coated by Hydrophilic Thiols,” *J. Am. Chem. Soc.*, vol. 123, no. 36, pp. 8844–8850, 2001.

[30] B. Dong, L. Cao, G. Su, and W. Liu, “Synthesis and characterization of Mn doped ZnS d-dots with controllable dual-color emissions,” *J. Colloid Interface Sci.*, vol. 367, no. 1, pp. 178–82, Mar. 2012.

[31] D. Venkatesan, D. Deepan, J. Ramkumar, S. Moorthy Babu, and R. Dhanasekaran, “Synthesis and Characterization of Sodium Bis(2-ethylhexyl) Sulfonsuccinate (AOT) Capped Pure and Mn-Doped CdS Nanoparticles,” *J. Nanomater.*, vol. 2012, pp. 1–8, 2012.

[32] V. P. Sirkeli, D. D. Nedeoglo, N. D. Nedeoglo, I. V. Radevici, R. L. Sobolevskaia, K. D. Sushkevich, E. Lähderanta, A. V. Lashkul, R. Laiho, J.-P. Biethan, O. Yilmazoglu, D. Pavlidis, and H. L. Hartnagel, “Magnetic and luminescent properties of manganese-doped ZnSe crystals,” *Phys. B Condens. Matter*, vol. 407, no. 18, pp. 3802–3807, Sep. 2012.

[33] Y.-S. Lin, Y. Hung, J.-K. Su, R. Lee, C. Chang, M.-L. Lin, and C.-Y. Mou, “Gadolinium(III)-Incorporated Nanosized Mesoporous Silica as Potential Magnetic Resonance Imaging Contrast Agents,” *J. Phys. Chem. B*, vol. 108, no. 40, pp. 15608–15611, Oct. 2004.

[34] H. Bin Na, J. H. Lee, K. An, Y. Il Park, M. Park, I. S. Lee, D.-H. Nam, S. T. Kim, S.-H. Kim, S.-W. Kim, K.-H. Lim, K.-S. Kim, S.-O. Kim, and T. Hyeon, “Development of a T1 Contrast Agent for Magnetic Resonance Imaging Using MnO Nanoparticles,” *Angew. Chemie*, vol. 119, no. 28, pp. 5493–5497, 2007.

[35] J. Shin, R. M. Anisur, M. K. Ko, G. H. Im, J. H. Lee, and I. S. Lee, “Hollow Manganese Oxide Nanoparticles as Multifunctional Agents for Magnetic Resonance Imaging and Drug Delivery,” *Angew. Chemie Int. Ed.*, vol. 48, no. 2, pp. 321–324, 2009.

[36] C.-Y. Yeh, Z. Lu, S. Froyen, and A. Zunger, “Zinc-blende–wurtzite polytypism in semiconductors,” *Phys. Rev. B*, vol. 46, no. 16, pp. 10086–10097, Oct. 1992.

[37] E. Spanó, S. Hamad, and C. R. A. Catlow, “Computational Evidence of Bubble ZnS Clusters,” *J. Phys. Chem. B*, vol. 107, no. 38, pp. 10337–10340, Sep. 2003.

[38] Y. Wu, H. L. Tepper, and G. A. Voth, “Flexible simple point-charge water model with improved liquid-state properties,” *J. Chem. Phys.*, vol. 124, 2006.

[39] K. Wright and J. D. Gale, “interatomic potentials for the simulation of the zinc-blende and wurzite forms of ZnS and CdS: Bulk structure, properties, and phase stability,” *Phys. Rev. B*, vol. 70, p. 035211, 2004.

[40] W. L. Jorgensen and J. Tirado-Rives, “Potential energy functions for atomic-level simulations of water and organic and biomolecular systems,” *PNAS*, vol. 102, no. 19, pp. 6665– 6670, 2005.

AUTHOR : Tania Jahanbin
Thesis Title : Design and development of highly effective MRI contrast agents *in-vitro*. contribution of molecular dynamics simulation on NMR signal
THESIS SUPERVISOR : Soraya Benderbous
PLACE AND DATE OF DEFENCE : Toulouse, INSERM U825, Imagerie Cérébrale et Handicaps Neurologiques, CHU Purpan-Pavillon BAUDOT, Place du Dr Joseph Baylac, 31024 TOULOUSE CEDEX 3- et le 13 Novembre

RESUME en englais

The objective of this thesis is design and development of two types of MRI contrast agents (CA) with high efficiency, including macromolecule and nanoparticles. The first substance is Gd(III)-meso-tetra(4-pyridyl)porphyrin (Gd(TPyP)). Its efficiency has been compared with two metalloporphyrin compounds, Mn(III)-meso-tetra(4-sulfonatophenyl) porphyrin (Mn(TSPP)) and Fe(II)-meso-tetra(N-methylpyridiniumyl)porphyrin (Fe(TMPyP)) in presence of two magnetic field of 20 and 60 MHz. Among the metallated porphyrins, Gd(TPyP) exhibits the highest r1 of 24 $mM^{-1}s^{-1}$ (6-fold higher compared to r1 of Gd-DOTA). In the next step, Gd(TPyP) has been conjugated to chitosan nanoparticles in order to improve its biocompatibility and water solubility. The small water-soluble Gd(TPyP)-conjugated chitosan nanoparticles (~40 nm) show higher (56%) r1 of 38 $mM^{-1}.s^{-1}$ at 3T than the one of Gd(TPyP) in ethanol and 9-fold greater than r1 of Gd-DOTA.

The second complex developed as CA is $Mn_xZn_{1-x}S$ ($0.1 \leq x \leq 0.3$) nanoparticles while the majority of Mn atoms localized on/ or close to the surface of ZnS nanoparticles to enhance their efficiency as MRI CA. Mn:ZnS nanoparticles exhibits higher r1 compared with the one of commercial Mn-DPDP (r1=2.8 $mM^{-1}s^{-1}$ at 42 MHz), which significantly increases from 20.34 to 75.5 $mM^{-1}s^{-1}$ with Mn content in the range of 0.1-0.3. Thereafter, effect of particle size on relaxivity of $Mn_{0.3}Zn_{0.7}S$ has been investigated. We observed that r1 decreases with increasing particle size due to decreasing the surface to volume ratio from 75.5 to 42.81 $mM^{-1}s^{-1}$. In order to obtain the insight through the relaxivity of Mn:ZnS nanoparticles, computational technique has been carried out to predict the interaction and dynamic of Mn:ZnS and solvent (water) via molecular dynamic simulations (MDs). Thereby, $Mn_xZn_{1-x}S$ with different dopnat contents ($0.1 \leq x \leq 0.3$) has been modeled via MDs. We achieved to reproduce the crystal structure of MnZnS precisely, within a few percent of experimental values. The study has been completed successfully by adding MnZnS nanoparticles in aqueous solution.

KEYWORDS : Relaxivity, macromolecule, porphyrin, chitosan, quantum dots, molecular dynamic simulation

DISCIPLINE ADMINISTRATIVE: Radio-physique et Imagerie Médicale

INTITULE ET ADRESSE DE L'U.F.R. OU DU LABORATOIRE : INSERM-U825, Imagerie Cérébrale et Handicaps Neurologiques, CHU Purpan-Pavillon BAUDOT, Place du Dr Joseph Baylac, 31024 TOULOUSE CEDEX 3

AUTEUR : Tania Jahanbin
TITRE : *Conception et développement in vitro d'agents de contraste hautement efficace en IRM Apport de la dynamique moléculaire sur le signale de RMN*
DIRECTEUR DE THESE : Soraya Benderbous
LIEU ET DATE DE SOUTENANCE : Toulouse, INSERM U825, Imagerie Cérébrale et Handicaps Neurologiques, CHU Purpan-Pavillon BAUDOT, Place du Dr Joseph Baylac, 31024 TOULOUSE CEDEX 3- et le 13 Novembre

RESUME en français

L'objectif du travail de thèse est de concevoir et développer 2 classes d'agent de contraste (AC) intrinsèquement efficace en IRM. La première classe comprend le Gd (III)-méso-tétra (4-pyridyl) porphyrine (Gd (TPyP)) macromoléculaire. Son efficacité a été comparé avec deux produits de référence : la Mn(III)-méso-tétra(4-sulfonatophenyl)porphyrine (Mn(III)TSPP), et Fe(II)-méso-tétra(N-methylpyridinium)porphyrine (Fe(II)TMPyP) à de deux champs magnétiques de 20 MHz et 60 MHz. En particulier, la relativité r1 la plus grande est obtenue pour le complexe Gd(TPyP) (24 $mM^{-1}s^{-1}$à 60 MHz) soit une efficacité au moins 6 fois plus importante que pour les complexes de Gd conventionnels. Afin d'améliorer sa biocompatibilité médicale, sa solubilité de l'eau, et augmenter son efficacité en IRM, la Gd-porphyrine a été conjuguée avec les nanoparticules de chitosan. Ainsi, une valeur de 38 $mM^{-1}s^{-1}$ à 60 MHz 9 fois plus élevée que celle de Dota-Gd a été obtenue dans l'eau.

Dans la 2ème partie de la thèse, nous avons développé le concept de greffage de Mn dopé à la surface de nanoparticules ZnS afin d'améliorer l'accessibilité de l'eau au moment magnétique du Mn. Les nanoparticules ont une relaxivité r1 variant de 20.34 à 75.5 $mM^{-1}s^{-1}$ pour un taux de Mn passant de 0.1 à 0.3, par rapport au produit commercial Mn DPDP (r1=2.8 $mM^{-1}.s^{-1}$ à 42 MHz). Par la suite, l'influence de la granulométrie de $Mn_{0.3}Zn_{0.7}S$ sur son efficacité a été étudiée. Leur r1 a diminué de 75.5 à 42.81 $mM^{-1}s^{-1}$ avec l'augmentation de la dimension particulaire. Pour expliquer le mécanisme, une simulation numérique de la dynamique moléculaire de l'eau au voisinage des nanoparticules de MnZnS a été développée. Les résultats de la simulation de la structure cristalline de MnZnS sont concordent avec les valeurs expérimentales par la cristallographie aux rayons X. Le modèle a été amélioré en incluant un effet de la concentration variable au Mn dans un environnement aqueux.

MOTS-CLES : La relaxivité, macromoléculaire, porphyrine, chitosan, quantum dots, la simulation par dynamique moléculaire

DISCIPLINE ADMINISTRATIVE: Radio-physique et Imagerie Médicale

INTITULE ET ADRESSE DE L'U.F.R. OU DU LABORATOIRE : INSERM-U825, Imagerie Cérébrale et Handicaps Neurologiques, CHU Purpan-Pavillon BAUDOT, Place du Dr Joseph Baylac, 31024 TOULOUSE CEDEX 3